



HAL
open science

The trade-wind boundary layer and climate sensitivity

Anna Lea Albright

► **To cite this version:**

Anna Lea Albright. The trade-wind boundary layer and climate sensitivity. Meteorology. Sorbonne Université, 2022. English. NNT : 2022SORUS207 . tel-03828209

HAL Id: tel-03828209

<https://theses.hal.science/tel-03828209>

Submitted on 25 Oct 2022

HAL is a multi-disciplinary open access archive for the deposit and dissemination of scientific research documents, whether they are published or not. The documents may come from teaching and research institutions in France or abroad, or from public or private research centers.

L'archive ouverte pluridisciplinaire **HAL**, est destinée au dépôt et à la diffusion de documents scientifiques de niveau recherche, publiés ou non, émanant des établissements d'enseignement et de recherche français ou étrangers, des laboratoires publics ou privés.

École doctorale 129 : Sciences de l'Environnement

THÈSE

pour obtenir le grade de docteur délivré par

Sorbonne Université

Spécialité doctorale "Sciences de l'Environnement"

*qui sera
présentée et soutenue publiquement par*

Anna Lea ALBRIGHT

le 18 mars 2022

The trade-wind boundary layer and climate sensitivity

Directrice de thèse : **Sandrine BONY**
Co-Directeur de thèse : **Bjorn STEVENS**

Jury

Sandrine BONY	Laboratoire de Météorologie Dynamique, CNRS	Directrice
Florent BRIENT	Sorbonne Université	Examinateur
Francis CODRON	Sorbonne Université	Examinateur
Kerry EMANUEL	Massachusetts Institute of Technology	Rapporteur
Cathy HOHENEGGER	Max Planck Institute for Meteorology	Rapporteur
Marie LOTHON	Laboratoire d'Aérodynamique, CNRS	Examinatrice
Bjorn STEVENS	Max Planck Institute for Meteorology	Co-Directeur

Abstract

The response of clouds in the trades to warming remains uncertain, raising the specter of a high climate sensitivity. Decreases in cloud fraction are thought to relate to couplings among convective mixing, turbulence, radiation, and the large-scale environment. The EUREC⁴A (*Elucidating the role of cloud-circulation coupling in climate*) field campaign made extensive measurements that allow for deeper physical understanding and the first process-based constraint on the trade cumulus feedback, as described in this thesis, in two parts.

The first part (Chapters 2–5) uses EUREC⁴A observations to improve understanding of the characteristic vertical structure of trade-wind air and the processes that determine it. The second part (Chapters 6–7) applies an improved physical understanding of the trade-wind boundary layer to the evaluation of trade cumulus feedbacks. Ideas developed in these chapters support new conceptual models of the structure of the lower trade-wind atmosphere and a more active role of clouds in maintaining this structure, and show little evidence for a strong trade cumulus feedback to warming.

Chapt. 3 calculates clear-sky radiative profiles from 2580 *in situ* soundings launched during EUREC⁴A, which are then used to observationally close subcloud layer moisture and heat budgets in Chapt. 4. Chapt. 4 shows that mixed layer theory, evaluated with EUREC⁴A observations and with uncertain parameters constrained in a Bayesian approach, provides a closed description of subcloud layer thermodynamic variability. Monthly-mean residuals are 3.6 Wm^{-2} for moisture and 2.9 Wm^{-2} for heat, and synoptic residuals are small and unbiased. Mixed layer theory is therefore a useful framework for characterizing subcloud layer variability and the processes controlling it. Surface wind speed variability is found to influence the subcloud layer depth and fluxes, yet thermodynamic variability above the subcloud layer top emerges as the primary control on subcloud layer moisture and heat variability. Observed thermodynamic profiles and effective entrainment parameters constrained in the Bayesian methodology show evidence of an about 150 m thick transition layer separating the well-mixed part of the subcloud layer from the subcloud layer top.

Contrary to previous theory, Chapt. 5 shows that the canonical structure of strong jumps at the subcloud layer top is rare and occurs only in large cloud-free areas. A population of small clouds is shown to be responsible for smoothing vertical gradients over the transition layer. These findings suggest a new conceptual picture that the dissipation of small clouds modulates the transition layer structure. This analysis allows for positing an interplay between shallow and deeper trade-wind convection and a more active role for clouds in mixing processes that determine the subcloud layer structure.

Chapt. 6 traces how, in a representative subset of CMIP6 models, differing trade-wind cloud radiative responses can explain about 70% of the spread in global cloud feedbacks, and differences in trade-wind cloud responses discriminate between high and low climate sensitivity models. Chapt. 7 presents analysis supporting a weak trade cumulus feedback. Observations support a positive relationship between cloudi-

ness and convective mixing, which is opposite to the negative relationship thought to underlie strongly positive trade cumulus feedbacks. Three metrics related to the couplings among clouds, convective mixing, and relative humidity are presented that can be applied to both observations and climate models and yield a probabilistic estimate of the trade cumulus feedback.

Acknowledgments

The last three and a half years as a graduate student at the Laboratory of Dynamic Meteorology in Paris have been a wonderful adventure. I would like to warmly thank Sandrine Bony for sharing her brilliance and joy of doing science, and for the independence she gave me in developing my research projects. When I sent her an email one crisp fall day in Cambridge, asking how to apply to her group, I could not have imagined how much of the world she would open to me, both concretely¹ and more metaphorically. With the constraints of the covid-19 pandemic, our group meetings moved outside to underneath the canopy of the Lebanese cedar in the Jardin des Plantes², which felt a fitting parallel for her poetic, yet strong and guiding influence.

A heartfelt thank you also goes to Bjorn Stevens. I first met Bjorn whilst swiftly walking to a panel discussion he was giving at AGU in New Orleans in 2017. This feeling of dynamism³ has always remained. I have never met someone who could develop such good metaphors, so quickly — which symbolizes, for me, at once his expansive knowledge, quick wit, and ability to distill complex ideas to their essence. I feel grateful to have joined such a positive and collaborative research environment that Sandrine and Bjorn brought to life, in particular around the EUREC⁴A field campaign.

Many thanks to fellow cloud enthusiasts — you made the last years such a lot of fun. Ben Fildier and Ludovic Touzé-Peiffer, thank you for being the best roommates in Barbados and outreach team, or ‘équipe de choc’. Our radiative profiles project helped me through the first covid-19 lockdown, and Ben’s initiative to grow tomatoes on the ENS rooftop was a reminder to pause and enjoy small delights. Raphaela Vogel and Jessica Vial helped me process and work with *in situ* observations and GCM output, sometimes while canoeing through Hamburg’s canals or hiking in Barbados. Thank

¹e.g., moving to Paris and traveling to Boulder, Barcelona, Mykonos, Barbados, Hamburg, and the Provence.

²https://commons.wikimedia.org/wiki/File:P1260407_Paris_V_jardin_des_Plantes_cedre_du_Liban_1734_rwk.jpg

³Meetings included but were not limited to: meetings while cycling, meetings in the MPI ‘birch forest’, and group chats while swimming in the ocean around Barbados.

you to Hauke Schulz for smooth sailing on the Schlei to balance less-smooth days writing these chapters. Un grand merci und herzlichen Dank also to Caroline Muller, Max Popp, Nicolas Rochetin, Marius Léna, Addisu Semie, Thibaut Dauhut, Geet George, Tobias Kölling, Theresa Mieslinger, Marc Prange, Jule Radtke, Theresa Lang, Hans Segura, Jiawei Bao, and Julia Windmiller for knowledge and happy moments shared – in Paris and Hamburg, or as neighbors on Coverly Drive in Barbados.

A few years ago, in 2016, it was a stroke of luck to walk into Mike McElroy's class, 'Energy and Climate: Vision for the Future' one snowy January day. This class and an ensuing research project with Mike led me to pursue a master's in Earth and Planetary Sciences during my fourth year at Harvard. A year of research with Peter Huybers after graduation taught me the ropes of scientific research and writing. His creativity and ability to meaningfully contribute to a vast arc of questions have been a steady source of inspiration over the past few years. I am grateful to have continued to work together throughout my PhD.

Financially, this thesis was largely supported by the European Research Council (ERC) under the European Union's Horizon 2020 research and innovation programme (grant agreement #694768).

For my grandfather, Harald Weinrich

Contents

1	Why look to the trades?	13
1.1	A defining challenge of our time	13
1.2	Climate questions traced to the trades	17
1.2.1	Role of trades in climate	18
1.3	Thesis outline	26
1.4	A door in the sky — learning to see clouds	27
2	Can EUREC⁴A answer climate questions?	31
2.1	Why organize EUREC ⁴ A?	31
2.2	Building a cloud laboratory in the trades	34
2.2.1	Primary measurement platforms	35
2.2.2	Relevance for climate questions	35
2.3	Flying	38
2.4	Organizing outreach	41
3	Atmospheric radiative profiles during EUREC⁴A	45
3.1	Abstract	45
3.2	Introduction	46
3.3	Data and methods	48
3.3.1	Radiosonde and dropsonde data	48
3.3.2	Radiative transfer calculation	50
3.4	Preliminary results and discussion	52
3.4.1	Variability across soundings	52
3.4.2	Diurnal cycle and day-to-day variability	54
3.4.3	Radiative signatures of mesoscale patterns of cloud organization	56
3.4.4	Effect of sharp moisture gradients on radiative heating profiles	60
3.5	Uncertainty assessment	60

3.6	Conclusions	65
4	Observed subcloud layer moisture and heat budgets in the trades	67
4.1	Abstract	67
4.2	Introduction	68
4.3	EUREC ⁴ A field campaign data	71
4.4	Describing the subcloud layer structure and its variability	74
4.4.1	Defining the subcloud layer height	74
4.4.2	Evidence that vertical thermodynamic gradients are small	78
4.4.3	Moisture variability is the primary mode of subcloud layer thermodynamic variability	79
4.5	Mixed layer theory for subcloud layer moisture and heat	82
4.5.1	Theory and closure assumptions	82
4.5.2	Observational estimates of terms in mixed layer theory budgets	88
4.5.3	Bayesian inversion of uncertain terms in entrainment fluxes	91
4.6	Resulting moisture and temperature budgets	97
4.7	How do these subcloud layer properties relate to the large-scale environment?	101
4.7.1	Wind speed variability	101
4.7.2	Predictive skill of mixed layer theory	103
4.8	Conclusions	105
4.9	Appendix A: Methodology for various boundary and subcloud layer height estimates	108
4.9.1	Thermodynamic variable gradient method	108
4.9.2	Parcel method	109
4.9.3	Linearized relative humidity profile	110
4.10	Appendix B: Vertical thermodynamic profiles	111
4.11	Appendix C: Derivation for entrainment efficiency parameter, A_e	114
5	A new conceptual picture of the transition layer	117
5.1	Abstract	117

5.2	Introduction	118
5.3	EUREC ⁴ A data	121
5.4	Building a new conceptual picture of the transition layer with EUREC ⁴ A observations	123
5.4.1	Transition layer depth	124
5.4.2	Transition layer stability	126
5.4.3	Cloud bases form within the transition layer	128
5.5	Physical origins of transition layer structure	129
5.5.1	Two populations of clouds	132
5.5.2	Shallow clouds appear to produce transition layer structure	133
5.6	The effects of a cloudy transition layer	135
5.6.1	Mixing diagrams and mixed layer theory	135
5.7	Discussion and conclusions	142
6	Uncertainty in trade cumulus feedbacks still contributes to uncertainty in global cloud feedbacks in CMIP6	147
6.1	Outline	147
6.2	Methods	148
6.2.1	Estimating equilibrium climate sensitivity	148
6.2.2	Quantifying cloud radiative responses	151
6.3	Uncertainty in ECS still driven by spread in global and tropical cloud feedbacks	153
6.4	Trade-wind cloud responses differ between high and low climate sensitivity models	154
6.4.1	Conceptualizing the tropical circulation	154
6.4.2	Different thermodynamic and dynamic cloud radiative responses for high and low ECS models	158
6.4.3	Global influence of spread in trade cumulus feedbacks	161
6.4.4	Vertical cloud fraction changes in high and low ECS models	163
6.5	Analysis of climate sensitivity in the IPSL-CM6A-LR model	164

6.6	Initial conclusions	168
7	Constraining trade cumulus feedbacks with EUREC^{4A}	169
7.1	Introduction	169
7.2	Mixing-desiccation hypothesis	170
7.3	First observational test of this mechanism	172
7.3.1	Measurements and methods	172
7.3.2	Observed relationships	174
7.4	Comparison with GCMs	174
7.5	Can present-day variability constrain future cloud changes?	177
7.5.1	Observational constraints	181
7.5.2	Comparison with other cloud feedback estimates	182
7.6	Discussion and initial conclusions	185
8	Conclusions and perspectives	187
8.1	Summary of key results	188
8.1.1	Clear-sky radiation in the trades	188
8.1.2	Observed subcloud layer moisture and heat budgets	189
8.1.3	A new conceptual picture of the transition layer	190
8.1.4	Towards the first process-based constraint on trade cumulus feedbacks	191
8.2	Perspectives	193
8.2.1	Short-term perspectives	193
8.2.2	Bias correction using atmospheric radiative profiles from <i>in situ</i> measurements and machine learning approaches	196
8.2.3	How do tropical forests modulate atmospheric moisture trans- ports?	197
8.2.4	Final thoughts	199
9	Additional materials	201

Chapter 1

Why look to the trades?

“We were still sailing in the blue zone of the trade winds. And it was every day, every day, every night, the same regular breath, warm, exquisite to breathe; and the same transparent sea, and the same small white clouds, speckled, calmly passing across the deep sky; ...” –Pierre Loti, *My Brother Yves*, 1883.

“Climate change is a question of our world’s destiny — it will determine the well-being of everyone on Earth”. –Angela Merkel, 2017.

1.1 A defining challenge of our time

Climate prediction is a defining challenge of our time. It is long-established that greenhouse gases lead to a warming of the atmosphere (e.g., Arrhenius, 1908; Charney et al., 1979). A central open question, which motivates much of the research in this thesis, is what sets the speed and intensity of warming at the global scale. How much and how quickly will global temperatures rise due to greenhouse gas forcing? A subsequent question is what effects are produced by a certain amount of warming. Heating provides the energy to drive winds, evaporate moisture, form rain, and melt ice. Global warming is thus expected to influence extreme weather events, such as storms, floods, and droughts, and increase sea level. These regional changes have attendant consequences for human health, water resources, agriculture, migration, and biodiversity. As expressed by former German chancellor Angela Merkel, climate

change is a question of Earth’s destiny and will affect the well-being of everyone on Earth.

Economically, climate change is an externality that is unprecedentedly large and uncertain (Tol, 2009). Estimates of the social cost of carbon range in magnitude (e.g., Stern, 2006; Weitzman, 2011; Nordhaus, 2018), yet they all project large consequences. These estimates, however, likely remain an incomplete representation of the possible effects of climate change, in particular heavy-tailed structural uncertainties associated with low-probability, high-impact scenarios (e.g., Weitzman, 2011, 2014; Wagner and Weitzman, 2016). There is thus a need for advancing knowledge about how much the Earth will warm and the implications of a given level of warming.

A primary lens for studying future climate is General Circulation Models (GCMs), also called global climate models. In 1963, Joseph Smagorinsky published a seminal paper describing numerical experiments using the primitive equations, a set of fluid equations that describe global atmospheric flows (Smagorinsky, 1963). This first GCM was based on the premise that studying the atmospheric circulation required a model capable of resolving heat transport from the equator to the poles. Smagorinsky’s work paved the way to a vast research effort to couple the atmospheric circulation to different physical processes, such as moist convection and cloud formation, which have long been appreciated as important for the energetics of the atmosphere (e.g., Arakawa and Schubert, 1974; Stevens and Bony, 2013).

GCMs are a powerful tool for understanding how the climate system works, yet they remain an imprecise lens into the future. These models must make a number of approximations and simplifications, in particular to represent small-scale processes below the 100–200 km resolution of typical GCMs. Most processes related to moist convection and cloud formation cannot, for instance, be simulated explicitly and are instead represented indirectly by so-called parametrizations, which relate subgrid-scale processes to the large-scale variables explicitly resolved by the model (e.g., Siebesma et al., 2020). Representing tropical diabatic responses, in particular, relies heavily upon such parametrizations, whereas in the mid-latitudes, much of the energy and moisture transport is accomplished by baroclinic eddies that are better

resolved by GCMs (Smagorinsky, 1963; Stevens and Bony, 2013; Siebesma et al., 2020). Beyond these structural uncertainties, there are additional parametric uncertainties that result from inadequately sampling the high-dimensional parameter spaces of these models; a model with only 20 free parameters is, for instance, already a hypercube with around one million corners (Carslaw et al., 2018).

Due to these uncertainties, GCMs lay out a broad swath of futures in response to greenhouse gas forcing. A common metric for quantifying the response of the climate system to carbon dioxide (CO_2) radiative forcing is the equilibrium climate sensitivity (ECS). ECS is defined as the amount of surface warming at equilibrium following a doubling of atmospheric CO_2 concentrations. Knutti et al. (2017) write that ECS “has reached almost iconic status as the single number that describes how severe climate change will be”. This idealized metric also serves as a way to compare model predictions.

Despite a long history of recognizing the influence of carbon dioxide on Earth’s temperature, ECS has proven stubbornly challenging to estimate. In the 1820s, the French physicist Joseph Fourier suggested that the Earth traps heat (Fleming, 1999). In 1896, in developing a theory to explain the Ice Ages, Swedish physicist and chemist Svante Arrhenius first estimated how increases in atmospheric CO_2 are responsible for increases in Earth’s temperature. In 1908, Arrhenius wrote, “Although the sea, by absorbing carbonic acid [resulting from carbon dioxide interacting with water], acts as a regulator of huge capacity, which takes up about five-sixths of the produced carbonic acid, we yet recognize that the slight percentage of carbonic acid in the atmosphere may by the advances of industry be changed to a noticeable degree in the course of a few centuries” (Arrhenius, 1908). Arrhenius was the first person to recognize the potential for anthropogenic CO_2 to change Earth’s temperature and estimated a temperature increase of 4°C in response to a CO_2 doubling (Arrhenius, 1908). In the 1960s, Charles Keeling presented observational evidence of increasing atmospheric CO_2 concentrations due to human activities, relative to preindustrial levels trapped in ice cores. Climate models developed beginning in the 1960s provided a physical-numerical framework for studying the relationship between radiative forcing by CO_2

and surface temperature (e.g., Smagorinsky, 1963; Manabe and Strickler, 1964; Manabe and Wetherald, 1967). In 1979, the United States National Academy of Sciences convened a group of scientists, led by Jule Charney, to assess the potential influences of CO₂ on climate. The ensuing report, “Carbon Dioxide and Climate: A Scientific Assessment” became known as the ‘Charney Report’ and popularized the concept of equilibrium climate sensitivity. Drawing on results from two early climate models and physical insights, the Charney report put forward a best estimate of ECS of 3°C and range from 1.5–4.5°C (Charney et al., 1979), known as the ‘Charney range’.

Tightening the Charney range of ECS is one of climate science’s most enduring problems. The most recent assessment of climate sensitivity, across multiple lines of evidence gives a narrower range of 2.6–3.9°C (Sherwood et al., 2020). Notably, the tighter upper bound is not directly constrained by the latest generation of GCMs in the Coupled Model Intercomparison Project phase 6 (CMIP6) whose range is 1.8–5.6°C (Zelinka et al., 2020; Meehl et al., 2020). The upper bound is instead constrained by process-based and paleoclimate constraints, though paleoclimate constraints also use GCMs (Sherwood et al., 2020). Despite the apparent tighter upper bound, there are still open questions regarding the influence of changing spatial patterns of warming (‘pattern effect’), long timescale feedbacks, and cloud feedbacks, which could still allow for a more positive upper bound on ECS (Sherwood et al., 2020).

The increase in complexity of GCMs has expanded the number of physical processes that can be studied with these tools, yet uncertainties in climate sensitivity remain similar to those that emerged from early modeling studies. In his landmark study, Smagorinsky concluded, “In pursuing the objective to generalize theoretical models we must ask ourselves whether greater detail in formulating the contributing processes is warranted by truncation errors, by sensitivity of the results to detail, by the resulting increase in computational complexity and time, and by ignorance of the way these processes really work. Very often this cannot be determined in advance, but must wait for computational experiments to be performed”. Stevens and Bony (2013) respond, writing, “Although the drive to complexity has not reduced key un-

certainties, it has addressed Smagorinsky’s question as to what level of process detail is necessary to understand the general circulation. There is now ample evidence that an inadequate representation of clouds and moist convection, or more generally the coupling between atmospheric water and circulation, is the main limitation in current representations of the climate system”. The Charney report already discussed that a primary obstacle to better climate predictions was uncertainty in the radiative feedbacks associated with clouds (e.g., Charney et al., 1979; Bony et al., 2013b). These obstacles remain in CMIP6, with the response of clouds and convection still representing a primary uncertainty in constraining climate sensitivity (e.g., Zelinka et al., 2020; Meehl et al., 2020). This chain of research casts into relief that in addition to increasing the complexity of models, it is equally important to deepen physical, process understanding using observations and simpler modeling frameworks.

1.2 Climate questions traced to the trades

In the novel, *My Brother Yves*, the French naval officer and writer, Pierre Loti, writes about a journey in the trade winds, as cited in the opening quotation. The trade-wind zones extend from about 10–30° north and south of the equator. In both hemispheres, these zones are dominated by the trades, which are steady easterly winds with an equatorward component, blowing from the subtropical high to the equatorial low.

The etymology of the trade winds in different languages gives insight to their nature and perception. In 14th century English, ‘trades’ denoted a regular path or track, but by the 18th century, the importance of the trade winds for exchanges of goods led to the association with foreign commerce (Dictionary). In German, the winds are known as *Passatwinde*, coming from Portuguese, *passar*, or Italian *passata*, both meaning to ‘go through’, highlighting their steady movement. In French, the trades are *les vents d’alizés*, similar to Portuguese, *ventos alísios*. The French name is speculated to relate to the Latin root *lixare*, which was used in medieval French to qualify the “smooth, delicate, gentle character of these measured winds that blow regularly” (Bellec, 2003). The serenity and steadiness of this etymology and Loti’s

description appear at odds with the urgency of climate change. How can such a calm and steady region play a role in determining how much the Earth will warm?

1.2.1 Role of trades in climate

A first answer comes by way of their large statistical weight: trade-wind regions are the most frequent tropical regime, and trade-wind cumuli are, moreover, the most frequent cloud type on Earth (e.g., Norris, 1998; Bony and Dufresne, 2005). Trade-cumulus regions cover approximately 20% of the Earth (e.g., Myers et al., 2021). Small changes in these regions with warming, such as associated with their cloudiness, therefore have a large global impact. Their geographic extent provides an intrinsic motivation to better understand the trades.

In the vertical, trade-wind air exhibits a characteristic layered structure (Riehl et al., 1951; Malkus, 1958; Augstein et al., 1974; Stevens, 2006). A robust vertical structure also allows for developing conceptual models, which are useful frameworks for developing process understanding (e.g., Stevens, 2006). In its most general form, the trade-wind atmosphere is divided into a shallow, moist layer typically extending to 2–3 km in height, topped by a much drier free troposphere. Near the equator, deep convection forms in response to the destabilizing effect of radiative cooling from water vapor (e.g., Emanuel et al., 1994b). This deep, precipitating convection effectively dehydrates the atmosphere, such that air subsiding in the subtropics is very dry. Large-scale subsidence in the subtropics also suppresses deep convection, explaining why the trade-wind moist layer does not grow beyond few kilometer depth.

This shallow, moist layer is often referred to as the ‘planetary boundary layer’ and is itself divided into additional layers. Previous descriptions of these layers, primarily from Malkus (1958) and Augstein et al. (1974), are briefly summarized:

1. *surface layer*: the lowest 50–100 m over the ocean that are characterized by mechanical turbulence.
2. *mixed layer*: a neutrally stable, vertically well-mixed layer from the top of the surface layer up to approximately 600 m.

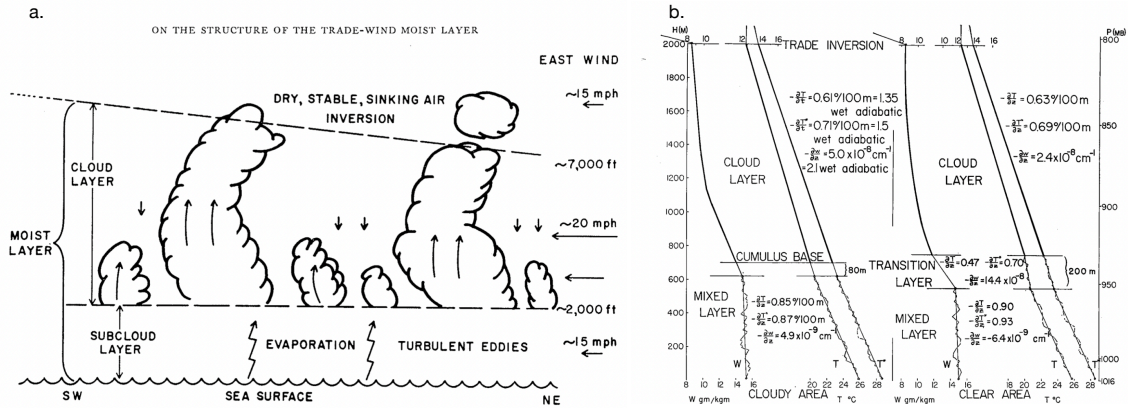


Figure 1-1: Reproducing two figures from Malkus (1958), one of the first papers to analyze the vertical structure of the trade-wind atmosphere. Panel (a) plots a cartoon of the vertical levels in the moist layer, from the sea surface to the cloud top, overlain by a dry, subsiding free troposphere, and (b) mean sounding profiles in cloudy (nine soundings) and clear areas (sixteen soundings) for the mixing ratio (W), temperature (T), and virtual temperature (T^*). These profiles are annotated with estimates of the different vertical levels introduced above: mixed layer, transition layer, cloud layer, and inversion layer.

3. *transition layer*: a layer of approximately 100 m thickness that is thought to separate dry convection and mechanical mixing below from cloud convection above the transition layer top. Together the mixed layer and transition layer are often referred to as the *subcloud layer*.
4. *cloud layer*: a layer wherein shallow trade cumuli are embedded. This layer typically has decreasing specific humidity and a temperature gradient that is slightly stronger than the moist adiabat. Cloudiness typically peaks around cloud-base and again near the trade-wind inversion. Trade-wind cumuli are shallow in height because they are capped by subsiding air and a stable inversion layer.
5. *trade-wind inversion layer*: a layer of strongly decreasing humidity ('hydro-lapse') and increasing temperature around 2–3 km in height, which separates the moist layer from the dry free troposphere. The mean height of this inter-facial zone is determined by the opposing balance between compression due to large-scale subsidence and expansion due to convection.

In the following sections, three vignettes are discussed that describe the implications of this characteristic vertical structure and motivate a closer examination of the trade-wind planetary boundary layer.

Link in the global energy budget

One motivation to study the trade-wind planetary boundary layer is its role as an early link in the global energy budget (e.g., Riehl et al., 1951; Malkus, 1958). The trade-wind subcloud layer couples the surface to the cloud layer, and in doing so, regulates the import of energy and moisture from the ocean (e.g., Malkus, 1958; LeMone and Pennell, 1976; Stevens, 2007). Subcloud layer moisture and temperature variability control moist static energy variability, which influences the convective potential and thus cloudiness (e.g., Emanuel, 1986; Neelin et al., 1987; Lindzen and Hou, 1988; Emanuel, 1993). Clouds, however, also influence the subcloud layer. Clouds bring down drier air from aloft, which can then be entrained into the subcloud layer (Stevens, 2006). They can also influence the radiative budget of the subcloud layer and of the surface.

The export of latent heat from the trades to the equator is accomplished by advection of moisture by the trades. The trades can be interpreted in a number of ways. They can be interpreted, for example, as the return flow of the Hadley circulation, or, from a boundary layer perspective, as the result of the boundary layer momentum budget that is driven by pressure gradients induced by sea-surface temperature differences, leading to a flow from the subtropics to the equatorial regions (Lindzen and Nigam, 1987). After being exported to equatorial regions, latent heat that originally accumulated in the trade-wind boundary layer has numerous downstream effects. The advection of moisture into the deep tropics favors high values of boundary layer moist static energy and thus deep convection (Emanuel et al., 1994b) near the equator rather than in the trade wind regions (Oueslati and Bellon, 2013; Popp and Silvers, 2017). Upper-level divergence in the deep tropics is consistent with the poleward mass flux in the Hadley circulation that exports energy poleward, thus helping to maintain an approximate thermal equilibrium globally (e.g., Riehl

et al., 1951; Malkus, 1958; Pierrehumbert, 1995). Outside the tropics, the poleward energy transport is dominated by eddies, which influence large-scale circulations and the global hydrological cycle through their transport of latent and sensible heat and angular momentum (e.g., Riehl, 1954; Heckley, 1985; Tiedtke, 1989).

Given its role in global energy transports, primarily by funneling latent and sensible heat to the tropics, subtle thermodynamic variations in the trades can have significant global reverberations (e.g., Malkus, 1958; Augstein et al., 1974; Tiedtke, 1989). These considerations motivate an investigation of the vertical structure of the trade-wind atmosphere, as well as its thermodynamic variability and vertical mixing processes.

Earth’s ‘radiator fins’

The vertical structure of trade-wind air also has implications for radiative processes. Fig. 1-2 shows that Earth is a water planet. It depicts upper-atmospheric water vapor absorption above about 4 km observed from the Meteosat satellite in the water vapor channel. Areas with a dry upper atmosphere are rare globally but emerge in the subtropics (e.g., Spencer and Braswell, 1997; Soden, 1998).

The trade-wind atmosphere is effective at cooling to space because of the large infrared transmissivity of the dry free troposphere and, typically, lack of high clouds. Strong radiant energy loss to space occurs from the top of the shallow moist layer, whereas the dry atmosphere above does not return much downwelling radiation. The loss of infrared energy to space increases nonlinearly with decreases in relative humidity (Spencer and Braswell, 1997; Soden, 1998). For instance, a free troposphere with 10% mean relative humidity radiates about 320 Wm^{-2} , whereas an atmosphere with 30% relative humidity radiates only 300 Wm^{-2} (e.g., Fig. 2 in Spencer and Braswell (1997)). The key to allowing the tropics to lose its heat is thus to have vast dry areas. Evocatively, Pierrehumbert (1995) calls the subtropics the ‘radiator fins’, in contrast with the equatorial regions being like a ‘furnace’ or a ‘hothouse’. Through their dryness, the trades thus increase the efficiency of radiant heat loss, stabilize tropical temperatures, and reduce the amount of energy that must be exported to the

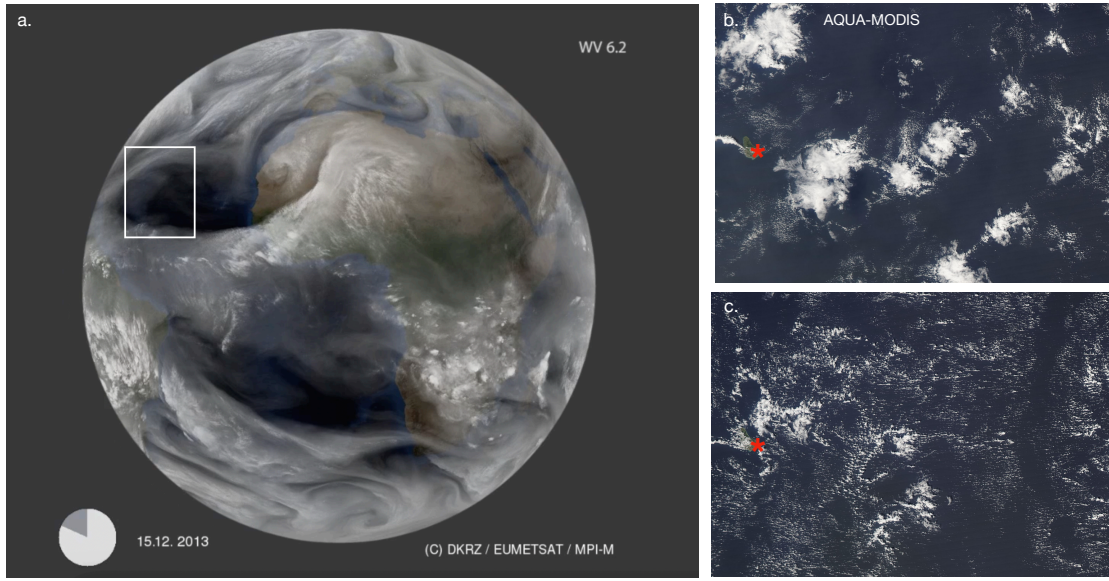


Figure 1-2: (a) the 6.2 micron METEOSAT channel, which measures atmospheric water vapor absorption above about 600 hPa. Darker shades indicate lower humidity and thus greater transparency to emitted longwave radiation. One such area with a dry free troposphere is highlighted by a white box. (b) Two AQUA MODIS GOES-E views of a trade-wind cloud field east of Barbados (indicated by a red star) on February 2, 2020 and (c) February 9, 2020.

poles.

A less cloudy future?

Besides its dry free troposphere, the trades further cool tropical temperatures through the presence of shallow cumuli, which have a negative radiative effect (e.g., Hartmann et al., 1992). Regarding these shallow trade-wind clouds, the question is not how much longwave radiation do the subtropics lose to space. It is, rather, how much shortwave energy do the subtropics absorb, with more shallow clouds implying a larger albedo and less heat gain, and vice versa. Trade-wind cumuli are, as introduced previously, the most frequent cloud type on Earth (e.g., Norris, 1998; Bony et al., 2017). The ‘small white clouds’, as described by Loti, are not as spectacular as cumulonimbus clouds that can grow higher than the tallest mountains or the expansive decks of stratocumulus clouds off western continental coasts. Yet they constitute the ‘silent’,

or humble majority of Earth’s clouds whose changes are greatly amplified by their frequency.

Climate change experiments with GCMs show that there is a propensity of trade-wind cloudiness, in particular at its base, to decrease with warming, raising the specter of high ECS values. In a pioneering study, Bony and Dufresne (2005) showed that cloud radiative responses in GCMs diverged most in shallow cumulus regimes, and these responses discriminate between high and low climate sensitivity models (Fig. 1-3a). This analysis also highlights how climate models, despite their known deficiencies, allow us to form hypotheses — for instance, that the sensitivity of trade-wind clouds to environmental conditions is a large source of uncertainty in global cloud feedbacks and ECS (Bony and Dufresne, 2005). Ensuing research has further supported the Bony and Dufresne (2005) findings, such as using different CMIP ensembles (e.g., Webb et al., 2006; Vial et al., 2013; Zelinka et al., 2020) and more idealized aquaplanet configurations (e.g., Medeiros et al., 2008). Fig. 1-2 shows two trade-wind cloud fields from the GOES-E satellite. This uncertainty can be rephrased pictorially: how will the views in Fig. 1-2 change with warming, towards a cloudier or less cloudy future in the trades?

Process-based studies, on the other hand, suggest that trade-wind clouds are less sensitive to changing environmental conditions than GCMs predict. In large-eddy simulations (LES), trade-wind clouds at cloud-base are resilient to changing environmental conditions both in the current climate (Nuijens et al., 2015a) and idealized climate change experiments (Rieck et al., 2012; Blossey et al., 2013; Bretherton, 2015; Vogel et al., 2016). These process-based studies suggest a neutral or slightly positive trade-wind cloud feedback. Two recent studies, Myers et al. (2021) and Cesana and Del Genio (2021), use satellite measurements and also find evidence for a near-zero trade-wind cloud feedback (Fig. 1-3d.). Myers et al. (2021) also find that trade cumulus feedbacks estimated using CMIP models are markedly higher than their satellite-constrained estimate. In CMIP6 relative to CMIP5, a too-negative midlatitude cloud feedback, compared to satellite constraints, was corrected (e.g., Zelinka et al., 2020). This correction is argued to have unmasked a compensating too-positive

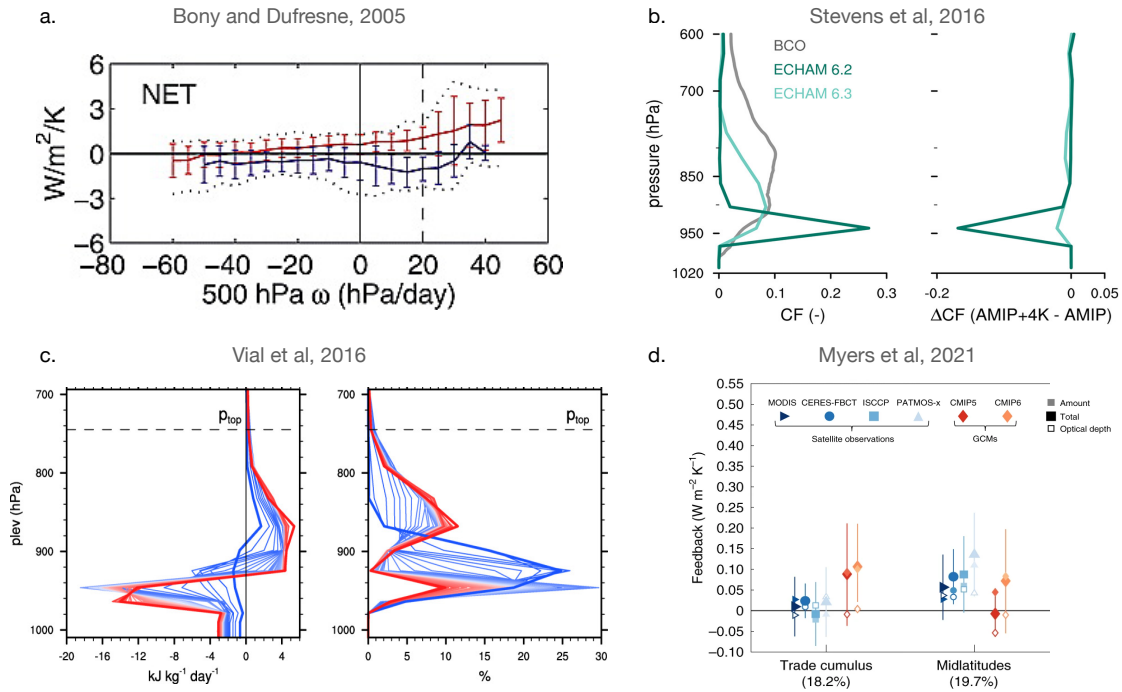


Figure 1-3: Figures illustrating the discrepancy between a large sensitivity of cloud-base cloudiness to changing environmental conditions in GCMs (a, b, c) and greater resilience in satellites (d) and LES (not shown). (a) Reproduction of Fig. 2 from Bony and Dufresne (2005) showing the change in the net cloud radiative effect with warming as a function of dynamical regimes. Red (blue) points correspond to models predicting a positive (negative) tropical-mean cloud radiative response. Markers show the mean, lines the standard deviation, and dotted lines the range of 15 coupled GCMs. (b) Reproduction of Fig. 1 in Stevens et al. (2016b) showing cloud fraction (left) and change in cloud fraction (right) for two model versions differing in a single shallow convective mixing parameter. Also shown is an observed cloud fraction profile at the Barbados Cloud Observatory as described in this study (grey). (c) Reproduction of Fig. 1 in Vial et al. (2016) showing the vertical distribution of the moist static energy flux convergence due to convection (left, in %) and cloud fraction (right, in %) for a range of convective mixing strengths, with minimum in thick blue, and maximum in thick red. (d) Adapted from Fig. 3 in Myers et al. (2021) showing observationally-constrained marine low cloud feedbacks scaled by regime frequency globally. Error bars for observations span 90% confidence intervals estimated from observational uncertainty and inter-model uncertainty in cloud-controlling factors. Bars for CMIP models span the range of simulated feedbacks associated with changes in low cloud properties.

cloud feedback in the trades, which then led to much higher ECS values in CMIP6, outside the Charney range (Myers et al., 2021), again emphasizing the importance of testing the credibility of strongly positive trade cumulus feedbacks simulated by GCMs.

There is thus a discrepancy to resolve — why are trade-wind clouds in GCMs much more sensitive to changing environmental conditions than in LES or satellite-derived studies? On the one hand, there are reasons to interpret results from LES and satellite-based studies with caution. In LES, the cloud amount is not linked to the large-scale circulations in which the clouds form, and cloud fraction is known to be sensitive to microphysics scheme, resolution, or domain size (e.g., Vogel et al., 2016; Vial et al., 2017; Radtke et al., 2021). Cloud fraction estimates from satellites were shown to diverge widely across passive remote sensors (Stubenrauch et al., 2013). Another consideration is that due to their coarse spatial resolution, satellite retrievals could, in principle, underestimate the number of cloudy pixels and overestimate the clear-sky fraction (e.g., Mieslinger et al., 2019, 2021); this would lead to an underestimate of the cloud feedback, which is proportional to the difference between the all-sky and clear-sky cloud radiative effect. The satellite-based studies also rely upon reanalysis data to estimate environmental conditions, yet these reanalysis data are known to exhibit biases in the trades (e.g., Stevens et al., 2016b). More fundamentally, the question remains why these lines of evidence suggest a small trade cumulus feedback. That is, the physical mechanism explaining the resilience of trade cumulus cloud fraction to changing environmental conditions remains unknown.

Growing evidence suggests that the diversity of GCM trade cumulus feedbacks can, on the other hand, be traced to a specific idea: how models represent lower-tropospheric vertical mixing (e.g., Sherwood et al., 2014; Bony et al., 2017). Fig. 1-3b,c. highlight two case studies from GCMs that differ in the strength of convective mixing, with large implications for changes in cloudiness and ECS. The general idea, which will be discussed in Chapt. 7, is that increased convective mixing brings dry air down from the free troposphere, drying the large-scale environment near cloud-base and decreasing cloud-base cloudiness. Greater mixing therefore reduces cloudiness at

cloud base. In GCMs, differences in this vertical mixing are thought to result from different representations of the interplay among surface turbulent fluxes, convective mixing, and low-level radiative effects (e.g., Tomassini et al., 2014; Vial et al., 2016).

These processes are thought to explain large differences in the trade-wind cloud feedback, yet they have never been tested observationally. During the EUREC⁴A (*Elucidating the role of cloud-circulation coupling in climate*) field campaign, we collected data to measure these interplays, such as among cloudiness, shallow convective mixing, radiative heating, and the large-scale environment, in order to constrain cloud feedbacks (Bony et al., 2017; Stevens et al., 2021). The campaign took place in January and February 2020 in the downstream trades of the North Atlantic. The original aim of EUREC⁴A to constrain cloud feedbacks opened a broader set of questions to improve fundamental understanding of the trades. The Charney report stated that climate prediction may be “expected to improve gradually as greater scientific understanding is acquired and faster computers are built” (Charney et al., 1979). Since this report, faster computers have been built, but there are still numerous open questions regarding scientific understanding of the trades, several of which this thesis, using EUREC⁴A data, tries to answer.

1.3 Thesis outline

From a methodological perspective, this thesis has two parts. In the first part (Chapters 2–5), *in situ* EUREC⁴A observations are introduced (Chapt. 2) and analyzed to deepen physical understanding of the characteristic vertical structure of trade-wind air and the processes that maintain it. Chapt. 4 closes subcloud layer moisture and heat budgets for the first time with *in situ* observations, using radiative heating profiles calculated and studied in Chapt. 3 and bulk models of surface and entrainment fluxes constrained in a Bayesian approach. The EUREC⁴A observations also provide a basis for reconceptualizing the transition layer, which contrasts with previous views based on theory for cloud-free boundary layers (Chapt. 5).

Better understanding how the trades behave in the present-day using EUREC⁴A



Figure 1-4: Artistic of clouds and turbulence from different time periods and cultures: (a) knight on horseback hidden in the clouds Andrea Mantegna’s (1456–1459) painting of St. Sebastian, (b) figure hiding in the clouds in a 13th century fresco by Giotto di Bondone, (c) sketch of turbulence by Leonardo da Vinci (1452–1519), (d) *Starry Night* by Vincent van Gogh (1853–1890), (e) *L’Embellie*, or *The Upswing* by René Magritte (1898–1967), (f) the *The Great Wave off Kanagawa* by Hokusai (1760–1849), and (g) *La corde sensible*, or *The Heartstring* by René Magritte.

observations allows for better evaluating how trade-wind clouds will change in the future. In the second part (Chapters 6–7), this improved physical understanding is applied to the evaluation of general circulation models. Chapt. 6 traces how, in CMIP6, uncertainties in trade cumulus feedbacks are strongly associated with uncertainties in the global cloud feedback and, to a lesser extent, in equilibrium climate sensitivity. Chapt. 7 shows analysis supporting the first process-based constraint on the trade cumulus cloud feedback. This constraint draws upon extensive EUREC⁴A observations, mixed layer theory as evaluated in Chapt. 4, and output from ten GCMs. Conclusions and perspectives following from ideas presented in this thesis are discussed in Chapt. 8. Chapt. 9 presents additional materials.

1.4 A door in the sky — learning to see clouds

Clouds, while remaining the subject of rich scientific inquiry, have also long fascinated artists and writers. One can argue that there are a number of parallels between observing art and observing nature. Both involve noticing and connecting particular elements with the entirety. Art and nature evoke a sense of beauty and wonder that are thought-provoking. Seeing artwork, like observing nature, is enriched by

being with people of various backgrounds, as each person brings different perspectives and experiences to bear. Works of art, such as poetry, painting, or dance, also foster concision and intensity in communicating ideas, which is not unlike a scientific equation or explanation.

Looking at art, moreover, sharpens our senses and encourages close examination. The precise observer Andrea Mantegna's (1456–1459) painting of St. Sebastian is rewarded with a knight on horseback hidden in the turbulent clouds (Fig. 1-4a). Similarly, if looking closely at a 13th century fresco by Florentine artist, Giotto di Bondone, a profile of a smirking devil, or alternatively the artist himself, emerges in the vaporous clouds (Fig. 1-4b). In both cases, once you see the hidden figure a first time, you cannot fail to see it the following times. These vignettes raise the question of how we learn to see, as one often sees what one is conditioned to see. How often do we miss surprises hidden in plain sight? One way that EUREC⁴A avoids potential blind spots is by bringing together a vast community. By merging differing, complementary perspectives, one can hope to overcome our blind spots and discover some of the surprises that have remained hidden in the clouds.

These cloud mysteries have long fascinated the human imagination. Art has often depicted clouds and turbulent motion, as illustrated in Fig. 1-4. Painter René Magritte writes about his research on “the problem of the cloud”: “I feel a drive to paint a cloud, perhaps a hundred” (Sylvester, 1992). Indeed, his painting *L'Embellie*, or *The Upswing*, (1962) depicts a door in the sky that opens onto a field of shallow clouds (Fig. 1-4e). The Barbadian poet, Kamau Brathwaite (1930–2020), uses the same visual language as Magritte, writing, “from under the clouds where I write the first poem ... a door opening in the sky” (Brathwaite, 2005). To return to the questions introduced in this chapter, Magritte and Brathwaite's images of a door in the sky evoke the history of climate model analysis of the trades. These model analyses revealed limitations in our physical understanding about shallow convective processes in the trades, which represent bottlenecks for climate predictions. That is, they have shown us the door to deeper physical understanding and improved climate prediction. Now, EUREC⁴A has allowed us to walk through this door. The German

physicist, Max Planck, writes about the scientific process of formulating questions and then posing them to nature that is at the heart of EUREC^{4A}: “An experiment is a question which science poses to Nature, and a measurement is the recording of Nature’s answer. But before an experiment can be performed, it must be planned — the question to Nature must be formulated before being posed” (Planck, 2014). The ‘recordings’ of nature’s answers from EUREC^{4A} invite us to deepen our physical understanding, all the while being filled with a sense of wonder and curiosity about these questions in the sky.

Chapter 2

Can EUREC⁴A answer climate questions?

At the time of EUREC⁴A, the scientific study of the trades had progressed to the point of formulating specific questions that, if tested observationally, could lead to a step-change in understanding, as discussed in Chapt. 1. Before transitioning to the research chapters, this chapter discusses additional motivations for organizing the EUREC⁴A field campaign (Sec. 2.1) and presents the primary measurement platforms (Sec. 2.2.1). An argument is also given why these measurements are amenable to answering climate questions (Sec. 2.2.2). I had the opportunity to take part in EUREC⁴A and briefly describe my research flight experiences (Sec. 2.3) and contributions to the campaign (Sec. 2.4).

2.1 Why organize EUREC⁴A?

The EUREC⁴A (*Elucidating the role of cloud-circulation coupling in climate*) field study took place in January and February 2020 in the north Atlantic trades, east of Barbados (see Fig. 2-1 for experiment location). As introduced in Chapt. 1, it is the most extensive field campaign ever performed in the trades, and the first campaign to measure both clouds and their large-scale environment, including circulations (Bony et al., 2017; Stevens et al., 2021). EUREC⁴A was originally conceived to observationally test trade cumulus feedback mechanisms thought to explain large differences in climate sensitivity and to provide benchmark measurements for a new generation of models and satellite observations (Bony et al., 2017; Stevens et al., 2021).

These aims require jointly characterizing the micro- and macrophysical environment of clouds, and the cloud field itself. Yet the question arises, why organize such a campaign, given the large number of previous field campaigns and the wealth of data from satellites?

Advancing understanding on the questions raised in Chapt. 1 requires observational data, but such data is lacking in the trades. The last major field studies focusing on the trades took place about 50 years ago, before climate change was considered a salient issue. They include the *Atlantic Expedition* from September to October 1965 (Augstein et al., 1973), the *Atlantic Tradewind EXperiment*, ATEX, in February 1969 (Augstein et al., 1974), the *Barbados Oceanographic and Meteorological Experiment*, BOMEX, from May to July 1969 (Holland, 1970), and the Puerto-Rico Experiment in December 1972 (LeMone and Pennell, 1976). These campaigns took place at the advent of the satellite era, so they were not yet accompanied by observations from space. Despite occurring half a century ago, these studies continue to act as reference data sets for studying and simulating cloudiness in the trades (e.g., Stevens et al., 2001; Siebesma et al., 2003).

More recent field campaigns focused on different cloud regimes and other questions than jointly characterizing trade-wind clouds and their large-scale environment. Some field studies sampled primarily stratocumulus regimes (e.g., Stevens et al., 2003b; Bretherton et al., 2004; Wood et al., 2011; Russell et al., 2013), or regions of deeper convection (e.g., Betts, 1974; Raymond et al., 2003), such as the Global Atmospheric Research Program’s (GARP) Atlantic Tropical Experiment (GATE) (e.g., Kuettner, 1974) or the Tropical Ocean Global Atmosphere Coupled Ocean–Atmosphere Response Experiment (TOGA-COARE) (e.g., Webster and Lukas, 1992; Johnson et al., 1999). Other field campaigns made measurements in the trades, such as *Rain in shallow cumulus over the ocean* (RICO, Rauber et al., 2007), *Cloud System Evolution in the Trades* (CSET, Albrecht et al., 2019) and *Organization of Tropical East Pacific Convection* (OTREC, Fuchs-Stone et al., 2020), yet their scientific motivations were targeted towards more specific physical processes, such as precipitation and the stratocumulus-to-cumulus transition.

Since early field campaigns in the trades, the expansion of satellite measurements has provided global views of Earth and extensive new data. Yet as alluded to in Chapt. 1, the coarse vertical resolution of passive remote sensing measurements leads to biases in their representation of vertical moisture profile features, such as the sharp decrease at the planetary boundary layer top or elevated moisture layers (e.g., Loeb et al., 2009; Chepfer et al., 2010; Stevens et al., 2017; Prange et al., 2021), especially in the lowest three kilometers, corresponding to the weakest absorption lines (Chazette et al., 2014). Regarding cloudiness, biases in cloud detection among different passive remote sensors lead to large discrepancies in estimates of trade-wind cloud fraction and related quantities (Stubenrauch et al., 2013). The highest-resolution satellite measurements better resolve trade-wind clouds (e.g. the ASTER instrument has up to 15 m spatial resolution), yet these high-resolution sensors have limited temporal sampling (e.g., Mieslinger et al., 2019, 2021). Cloudiness is often studied in mesoscale large-eddy simulations, yet cloud fraction and cloud organization are sensitive to resolution, domain size, and microphysics scheme (e.g., Bretherton and Blossey, 2017a; Vogel et al., 2016; Radtke et al., 2021).

Given these limitations, *in situ* observations are critical for testing ideas about trade-wind cumuli. To begin filling this measurement gap, in 2010, the Max Planck Institute for Meteorology and the Caribbean Institute for Meteorology and Hydrology established the Barbados Cloud Observatory (BCO) on the windward side of Barbados, at the easternmost point of the island (Stevens et al., 2016b). The BCO intercepts air that has been undisturbed by land influence since the western coast of Africa. Other long-term ground-based measurement stations are located in the extratropics, such as *Cloudnet* (Illingworth et al., 2007) and the U.S. Department of Energy’s ARM (Atmospheric Radiation Measurement) climate research facilities (e.g., Moran et al., 1998; Long et al., 2013). The BCO is unique, however, in being the only long-term observational site in the trades. The BCO was also the anchor for two Next-Generation Aircraft Remote Sensing for Validation Studies airborne field campaigns (NARVAL and NARVAL2), held in December 2013 and August 2016 in preparation for EUREC⁴A (Stevens et al., 2016b; Konow et al., 2019).

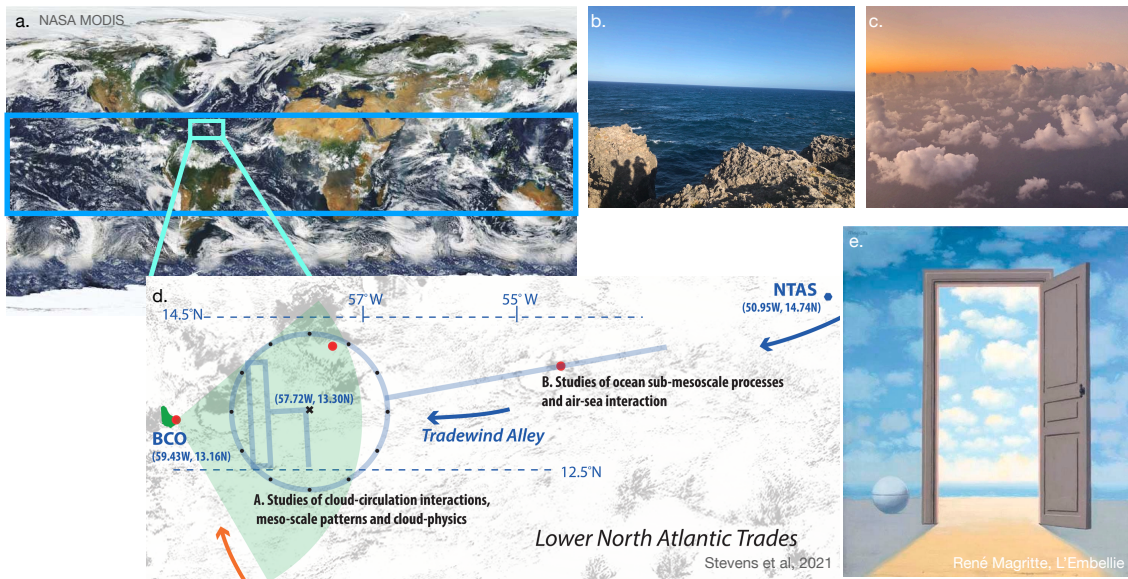


Figure 2-1: Location of EUREC⁴A field study in the North Atlantic trades, east of Barbados, as shown in (a) and (d). (b) shows the view from the Barbados Cloud Observatory in a rare cloud-free moment, and (c) depicts a cloud field seen from flying on the WP-3D aircraft. In (e) is René Magritte’s painting, *L’embellie* or *The Upswing* (1962), as if opening the door to the trade winds that blow from the east, as illustrated schematically in (d).

2.2 Building a cloud laboratory in the trades

Growing from these observational foundations, EUREC⁴A brought together four ships, five aircraft, the Barbados Cloud Observatory, a C-band rain radar, and a multitude of uncrewed aerial and seagoing systems, including fixed-wing aircraft, quadcopters, drifters, buoys, underwater gliders, and Saildrones (Stevens et al., 2021). EUREC⁴A also launched an extensive sounding array consisting of 1068 dropsondes and 1512 radiosondes. This ‘symphony’ of measurements can be thought of as building a transient cloud laboratory in the trades. This cloud laboratory can then be used to observationally test the questions raised in the previous chapter.

2.2.1 Primary measurement platforms

In the following section, the four measurement platforms whose data are used throughout the following chapters are briefly outlined. Further information is given in later chapters regarding particular analyses. The high-flying aircraft, HALO (High Altitude and Long Range Research Aircraft), (Konow et al., 2021) characterized clouds and the environment from approximately 9–10 km, both with remote-sensing instruments and by launching approximately 800 dropsondes around the perimeter of a fixed, mesoscale circle (Stevens et al., 2021). It followed a circular flight pattern known as the ‘EUREC⁴A circle’ (Fig. 2-2). This EUREC⁴A circle was centered at 13.3° N, 57.7° W and had an about 220 km diameter, roughly comparable to the meso- β scale from Orlanski (1975) or the size of a typical GCM grid box. A second aircraft, the ATR-42, primarily followed a 120x15 km rectangular, or racetrack, flight pattern below 3–4 km within the EUREC⁴A circle (Fig. 2-2) (Bony et al., 2022). One particularity of the ATR-42 was its sideways-pointing lidar and radars that, notably, measured the cloud fraction at cloud base. Flight legs below cloud base also characterized turbulent structures, microphysics (aerosols and clouds), and thermodynamic variability in the subcloud layer and near-to-surface. A third aircraft, the WP-3D Orion, augmented this sampling of clouds and their environment with additional dropsondes and remote sensing (Pincus et al., 2021). Within the EUREC⁴A circle, a research vessel, the R/V Meteor, complemented the three aircraft by providing sea temperature estimates, surface-based remote sensing, and surface flux measurements along an about 200 km transect in the same domain, from 12.5–14.5° N along the 57.255° W meridian (Fig. 2-2). Measurements from the Barbados Cloud Observatory provide additional data.

2.2.2 Relevance for climate questions

A common denominator of the platforms described in Sec. 2.2.1 is that they undertook intense, unbiased statistical sampling. That is, they did not ‘cloud chase’, or seek out specific meteorological conditions, as did other platforms, such as the Twin Otter

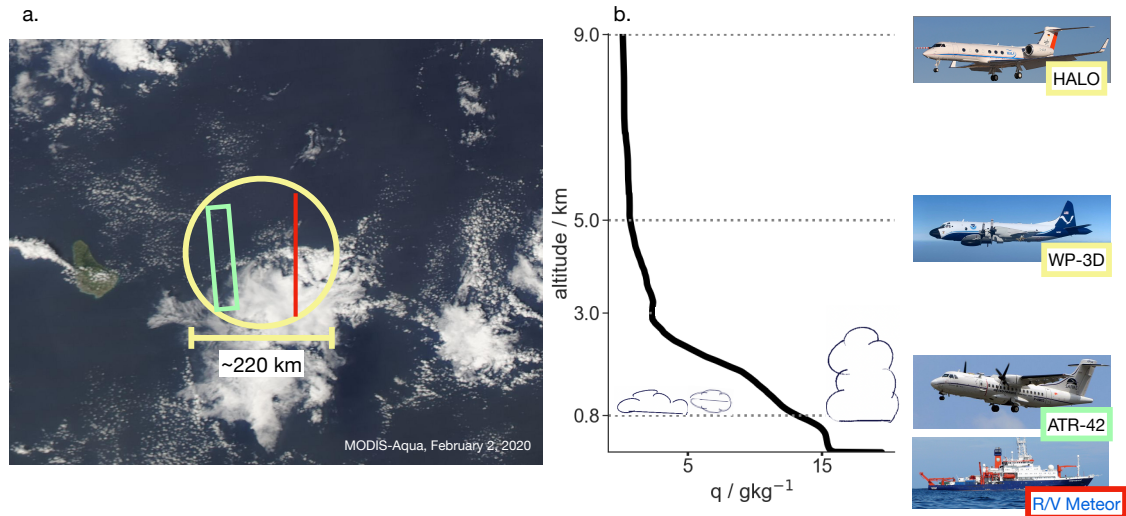


Figure 2-2: (a) MODIS-AQUA satellite image overlain with approximate tracks for HALO and the WP-3D in the EUREC⁴A circle (yellow), ATR-42 rectangular pattern (green), and R/V Meteor ship tracks (red), and (b) the campaign-mean specific humidity profile annotated with the approximate flight levels of the different aircraft, noting that HALO dropsondes yield data from 9–10 km and WP-3D dropsondes from about 5–7 km downwards.

aircraft that was also part of the campaign. Instead, the platforms followed prescribed flight patterns – the EUREC⁴A circle for HALO, and to a lesser extent, the WP-3D, the racetrack for the ATR-42, and the transect for the R/V Meteor. These measurements therefore yield unbiased realizations of the large-scale environment. As a result, measurements from the different platforms are assumed to be consistent and comparable, despite sampling at slightly offset locations and times.

For the relevance of EUREC⁴A measurements to climate questions, the measurements need to fulfill two additional conditions beyond being unbiased samples. First, measurements must be representative of the broader trade wind regions, such that inferences from EUREC⁴A generalize to the trades as a whole. Second, inferences from short timescales must be relevant for longer climate timescales.

For the first condition, Medeiros and Nuijens (2016) show that in GCMs and observations (from the BCO and Calipso), shallow cumulus clouds near Barbados exhibit similar structure and variability to clouds across the entire trade wind belt. Medeiros and Nuijens (2016) also show that errors simulated by GCMs near Barbados

– regarding the vertical structure of clouds, the planetary boundary layer, covariance with environmental conditions, and turbulent and convective mixing processes that give rise to clouds – are similar to errors simulated in other trade-wind regions. Rasp et al. (2020) find, similarly, that patterns of shallow cumulus cloud organization present near Barbados are also present through the trades as a whole. These studies lay an empirical foundation that clouds near Barbados are representative of trade-wind clouds across the tropics.

The second condition is that short timescale variability is informative of variability expressed on longer scales. Clouds and many associated processes, such as turbulence, entrainment, and convective mixing, are ‘fast physics’. Over the past two decades, numerous studies have shown that climatological biases in GCMs, in particular regarding moist convection, are already evident on shorter timescales, even within a few days of model simulation, motivating the evaluation of GCMs in ‘weather mode’ (e.g., Rodwell and Palmer, 2007; Williams et al., 2013). Regarding changes in tropical circulation and precipitation associated with the direct adjustments to CO₂, Bony et al. (2013a) show that about half of the 30-year mean change from a quadrupling of CO₂ occurs within five days, showing that these changes rely upon fast physical processes. Based on these considerations, it therefore appears a reasonable ansatz that EUREC⁴A observations can provide a window into understanding these fast physical processes, which can then inform longer-term responses. Indeed, in Chapt. 7, the relationships among convective mixing, cloudiness, and relative humidity are shown to be similar at the three-hourly and monthly timescales in GCM output. These results indicate that three-hourly processes are informative for explaining longer timescale variability. Vial et al, in review also demonstrate that variability on the diurnal timescale is representative of variability on monthly and annual timescales. Previous studies also indicate that cloud feedbacks are similar whether calculated from inter-annual, or longer timescale variability (e.g., Zhou et al., 2015; Sherwood et al., 2020).

2.3 Flying

I had the remarkable opportunity to take part in the EUREC⁴A campaign in January and February 2020. The *in situ* data that I analyze in the following chapters is thus data that I helped collect. The benefits of being immersed in the natural environment one wishes to study is perhaps best expressed by the renowned American mathematician and meteorologist, Edward Lorenz. Regarding atmospheric circulations, Lorenz wrote, “Before one can make any serious attempt to explain the circulation of the atmosphere, he must become familiar with the circulation which he wishes to explain... experience suggests that the investigator who attempts to deduce the atmospheric circulation without first observing it is placing himself at a considerable disadvantage” (Lorenz, 1967). This sentiment certainly holds for observing and making an attempt to better understand processes in the trades. There is also a unique spirit of discovery, joy, and camaraderie in participating in a field campaign that brings together people from numerous institutions and countries in a shared pursuit.

While in Barbados, I took part in two research flights: one on the ATR-42, and another on the WP-3D, known informally as the ‘hurricane hunter’ or ‘Miss Piggy’. These were my first research aircraft experiences and gave me different perspectives of the trade-wind clouds. The ATR flew through clouds near their base around 800 m, and the WP-3D flew higher, around 5–6 km on average. On the French ATR-42, I sat next to Marie Lothon who was already analyzing *in situ* thermodynamic data in real-time and initiated me as a first-timer into the workings of a flight. On this day, February, 5, 2020, there were many clouds at cloud base (Fig. 2-3a,d). On other days, the meteorological situation was quite different, and given the unbiased (vs. cloud-chasing) nature of the sampling, the crew found themselves flying through long stretches of nearly clear-sky. After hours of flat lines on different measurement devices designed to measure clouds and humidity, one can understand when Nicolas Rochetin, a French scientist, exclaimed, “Holy mackerel, we missed the stratiform zone again!” (“Saperlipopette, on a encore raté la zone stratiforme !”). Even when the skies were clear, a rapid descent down to 60 m provided an adrenaline rush.



Figure 2-3: Photos from flying in the ATR-42 (left) near (a,d) the maximum in cloud-base cloudiness and (e) near the surface around 60 m, and (right, b,c,f) in the WP-3D, depicting (b.,c.) wisps of clouds detrainning condensate at cloud top and (f) a field of shallow cumuli.

During this flight leg, it felt as though the airplane was skimming along the ocean surface. One was close enough to spot wave crests breaking into whitecaps in the strong wind and the sargassum seaweed that is so troublesome for Barbadian tourism. Within the ATR aircraft, it was still possible to appreciate the coordination of the EUREC⁴A experiment. The online *Planet* interface allowed for tracking, for instance, the Twin Otter aircraft that zigzagged around, chasing clouds, and the Poldirad rain radar, which we had helped build a few days earlier and that now measured precipitation. One could also track how the HALO aircraft flew above us in circles. On our headphones, the French pilots joked about the Germans who throw “800 lithium batteries in the sea”. (That is, the about 800 dropsondes launched from HALO.) The concurrence of the ATR-42 and HALO flight patterns (Fig. 2-2) and their unbiased sampling suggest that their measurements should be coherent. Indeed, after the campaign, strong agreement was found between the two platforms across the campaign, such as regarding their thermodynamic variability at different heights, indicating that measurements indeed reflect large-scale variability (Bony et al., 2022).

My flight on NOAA’s hurricane hunter was also a poetic, fascinating experience. The hurricane hunter, as its name implies, normally flies in much more trying conditions. The evening before my flight, Kerry Emanuel was telling us about the first and only crash of a hurricane hunter plane during Hurricane Janet in 1955, and another harrowing, near-crash during Hurricane Hugo in 1989. In the pre-flight meeting prior to our take-off, unusually strong wind shear was forecast for the flight area. We were then instructed to put on safety suits whose pockets contained essentials in case of an emergency, such as a flashlight, knife, and warming blanket. These aspects certainly added to the mystique and excitement, tinged with very slight fear, when stepping on board for the flight.

The WP-3D flight on February 9, 2020 was an all-night flight during full moon. Even deep in the night, the moonlight illuminated a panorama of cloud formations: billowing cumuli, cloud arcs, decks of clouds, veil clouds that appear like flying carpets, and a handful of extremely narrow cloud towers that grew to 7–8 km. I sat in the cockpit during take-off and parts of the flight. Despite the illusion of gliding

across a tactile or well-defined surface of the clouds, there is no such obvious boundary between clouds and their environment. Encountering the cloud edge is, of course, not like walking through a door, but rather like encountering a gradient of water vapor that would be easier to observe in infrared light. Stevens et al. (2017) expresses it evocatively and succinctly: “If it did not have to condense to become visible, water vapor would fuel the fascination of many more scientists. Imagine seeing with the naked eyes how elevated layers of water vapor, and its radiative effects, engender shallow circulations, or how pockets of humidity surround and socialize cumulus convection. Imagination is indeed necessary because water vapor’s mysteries arise as much from its visible transparency as from the opulence of its infrared opacity”.

One frequently-occurring cloud formation was small wisps of clouds that detached from cloud tops and then drifted and dissipated into the drier environment (Fig. 2-3b,c). This detrainment moistens and cools the surrounding environment. Observing these clouds out the window was the initial spark for proposing a new conceptual model of the transition layer in Chapt. 5.

2.4 Organizing outreach

Before concluding this chapter and transitioning to the research chapters, I summarize two contributions to the campaign. The first contribution is outreach work that we organized in collaboration with Barbadian colleagues Rebecca Chewitt-Lucas, Branden Spooner, Shanice Whitehall from the Caribbean Institute for Meteorology and Hydrology (CIMH), and French colleagues, Benjamin Fildier and Ludovic Touzé-Peiffer. Ulrike Kirchner and Dörte de Graaf from the Max Planck Institute for Meteorology also helped us organize outreach. The outreach initiatives included a two-day scientific symposium, about 20 visits to local schools, a weekly seminar series with local institutes, and an open house for the broader community to visit different measurement platforms. The second contribution was calculating clear-sky, aerosol-free atmospheric radiative profiles from 2580 soundings (1068 dropsondes and 1512 radiosondes) launched during the campaign (Albright et al., 2021a). This analysis is

presented in Chapt. 3.

The research symposium, ‘From BOMEX to EUREC⁴A’, brought together 24 local and visiting scientists and about 100 participants to consider the advances since BOMEX, a major field campaign that took place 50 years before EUREC⁴A (Fig. 2-4). While BOMEX had many similarities with EUREC⁴A, involving several ships and research aircraft, the main difference lies in their objectives. For BOMEX, the main objective was studying the exchange of moisture, heat, and momentum between the ocean and the atmosphere. At the time, climate change was not yet a topical issue, so the main goal of the campaign was to improve weather forecasting. For EUREC⁴A, by contrast, better understanding and constraining the magnitude of future climate change is at the heart of the campaign.

Two ‘alumni’ of the BOMEX campaign, 50 years before, spoke during the symposium: Clyde Outram, former director of Civil Aviation on Barbados, and Pat Callender, then the head of the Barbadian airport. They vividly recounted their experiences, even bringing an insignia from BOMEX that they had kept for five decades. Callender raised further points of contrast between BOMEX and EUREC⁴A, describing how he had to negotiate on behalf of local air traffic controllers seeking compensation for managing United States aircraft during the BOMEX campaign, and local scientists were not often co-authors on the papers published with BOMEX data. EUREC⁴A, on the other hand, is a Barbadian-German-French-American initiative with strong Barbadian involvement and expertise.

Together with the Barbadian Ministry of Education, we also organized visits to about 20 local elementary and secondary schools (Fig. 2-4). The Barbadian government has strongly invested in education, and our efforts sought to reinforce their environmental education. We interactively explored the scientific method by conducting small experiments using simple materials. Using commonly-found materials made it easier for students to recreate the experiments at home. The experiments included creating a cloud in a bottle, observing surface tension, and asking how stratification affects mixing and overturning (e.g., by observing whether an ice cube melts more quickly in fresh or salty water). During the school visits, we also tried to vi-



Figure 2-4: Photographs from outreach activities organized, including (a) the two-day symposium, ‘From BOMEX to EUREC⁴A and (b.,c.) a school visit where Ludovic Touzé-Peiffer and I perform experiments with local students. Photo a. is taken by Frédéric Batier, and photos b.,c., are taken by Marius Léna.

sualize questions asked during EUREC⁴A and benefited from cloud animations and presenting tips provided by Tim Cronin and Pier Siebesma. We also organized an outreach day, wherein a number of facilities opened to the general public, such as for the launching of radiosondes and drones. Our outreach activities are summarized in the EUREC⁴A overview paper, Stevens et al. (2021).

Chapter 3

Atmospheric radiative profiles during EUREC⁴A

This chapter presents the method to calculate atmospheric radiative profiles from EUREC⁴A soundings and presents initial results. Calculating these radiative profiles is a necessary step for analyses in later chapters, namely closing subcloud layer thermodynamic budgets (Chapt. 4) and reconceptualizing the transition layer (Chapt. 5).

3.1 Abstract

The couplings among clouds, convection, and circulation in trade-wind regimes remain a fundamental puzzle that limits our ability to constrain future climate change. Radiative heating plays an important role in these couplings. Here we calculate clear-sky radiative profiles from 2580 in situ soundings (1068 dropsondes and 1512 radiosondes) collected during the EUREC⁴A field campaign, which took place in the downstream trades of the western tropical Atlantic in January-February 2020. We describe the method used to calculate these cloud-free, aerosol-free radiative profiles. We then present preliminary results sampling variability at multiple scales, from the variability across all soundings to groupings by diurnal cycle and mesoscale organization, as well as individual soundings associated with elevated moisture layers. We also perform an uncertainty assessment and find that the errors resulting from uncertainties in observed sounding profiles, and ERA5 reanalysis employed as upper and lower boundary conditions are small. The present radiative profile data set

This chapter was published in *Earth System Science Data* in February 2021 (Albright et al., 2021a).

can provide important additional detail missing from calculations based on passive remote sensing and aid in understanding the interplay of radiative heating with dynamic and thermodynamic variability in the trades. The data set can also be used to investigate the role of low-level radiative cooling gradients in generating shallow circulations. All data are archived and freely available for public access on AERIS at <https://doi.org/10.25326/78>.

3.2 Introduction

The EUREC⁴A field campaign, which took place in January and February 2020 in the downstream trades of the western tropical Atlantic, was designed to elucidate the couplings among clouds, convection, and circulation in trade-wind regimes and understand the role of this interplay in climate change (Bony et al., 2017). Shallow trade-wind clouds cover large parts of tropical oceans (Wood, 2012), yet their response to warming remains largely unknown, and uncertainty in shallow convective processes are the cause for large uncertainties in climate projections (Bony and Dufresne, 2005; Vial et al., 2013; Sherwood et al., 2014; Zelinka et al., 2020). Among all physical processes involved in shallow convection, atmospheric radiative cooling emerges as key to the coupling between low-level circulations and convection. Understanding the dynamics driven by variations in radiative heating rates, and potential relationship to the mesoscale organization of clear and cloudy regions, was one motivation for the campaign (Bony et al., 2017).

A characteristic feature of the trade-wind vertical moisture profile is a sharp humidity gradient between the moist marine boundary layer and dry, subsiding free troposphere around two kilometers Riehl et al. (1951); Malkus (1958). This characteristic vertical moisture structure has important implications for radiative cooling profiles, but it is difficult to observe with satellite remote sensing (Stevens et al., 2017). Indeed, moisture profile features, such as the sharp decreases in moisture at the top of the marine boundary layer or elevated moisture layers, are smaller than typical weighting functions of even hyperspectral instruments (e.g. Maddy and Barnet, 2008;

Schmit et al., 2009; Menzel et al., 2018), especially in the lowest three kilometers, corresponding to the weakest absorption lines (Chazette et al., 2014). The lack of informative observations means that the vertical profile of water vapor in large-scale atmospheric analyses do not represent the fine-scale moisture structure indicated by soundings (Pincus et al., 2017). Errors in the vertical moisture structure estimated from passive remote sensing produce corresponding errors in radiative cooling profiles computed from retrievals and/or analyses, making *in situ* soundings especially valuable.

Here we calculate radiative profiles from 2580 *in situ* soundings (1068 dropsondes and 1512 radiosondes) collected during EUREC⁴A, whose network of observations provided extensive sampling of the tropical trade-wind environment. Similar studies have been conducted over continents as part of the Atmospheric Radiation Measurement program (Kato et al., 1997; Mlawer et al., 1998), over the western Pacific warm-pool region as part of the TOGA COARE (Coupled Ocean–Atmosphere Response Experiment) (Guichard et al., 2000), and over the western tropical Atlantic, albeit focused on transported Saharan dust layers (Gutleben et al., 2019). The present radiative profiles have the potential to complement and further what can be learned from calculations based on passive remote sensing. In addition, this data set may help in understanding how low-level gradients in radiative cooling fuel shallow circulations, as observed to emerge in remote sensing and large eddy simulations (L’Ecuyer et al., 2008; Stephens et al., 2012; Seifert et al., 2015). These shallow circulations are speculated to influence the mesoscale spatial organization of shallow convection, a question at the core of EUREC⁴A (Bony et al., 2020; Stevens et al., 2020b).

In Sec. 3.3, we describe the data, the radiative transfer code, and the procedure underlying the calculation of the radiative profiles. We then present initial results to open the discussion on questions that could be explored with these radiative profiles (Sec. 3.4). Lastly, we perform an uncertainty assessment (Sec. 3.5) and find that errors resulting from uncertainties in the sea surface skin temperature, *in situ* soundings, and ERA5 reanalysis used as boundary conditions are modest.

3.3 Data and methods

3.3.1 Radiosonde and dropsonde data

From January 8 to February 19, over 2500 atmospheric soundings were conducted using dropsondes and radiosondes over the western tropical Atlantic ocean south and east of Barbados. As the sondes fall or ascend, their simple autonomous sensors, equipped with a GPS receiver, measure the vertical profiles of pressure, temperature, relative humidity, and instantaneous horizontal wind. To calculate radiative profiles, we employ data (‘level-3’) that have been interpolated into a common altitude grid with 10 meter spacing (Stephan et al., 2020; George et al., 2021). We select dropsondes and radiosondes that have measurements on more than ten atmospheric levels in total; this crude filter suffices to remove failed soundings and results in an input data set consisting of 1068 atmospheric profiles from dropsondes and 1436 profiles from radiosondes. The minimum and maximum levels z_{min} and z_{max} measured by each sonde are reported in the final data set.

Figure 3-1a shows the geographic and temporal distributions of the sondes used to calculate the radiative profiles. Radiosondes were launched from a network of one land station and four research vessels, within a region ranging from 51–60°W to 6–16°N. On land, radiosondes were launched from the Barbados Cloud Observatory (BCO), located on a promontory on the easternmost point of Barbados called Deebles Point (13.16°N, 59.43°W), where it is exposed to relatively undisturbed easterly trade-winds. The fleet of four research vessels includes the French research vessel L’Atalante, two German research vessels Maria S. Merian (MS-Merian) and Meteor, and the American research vessel from the National Oceanic and Atmospheric Administration (NOAA) Ronald H. Brown (RH-Brown). Dropsondes were launched from both the German High Altitude and Long Range Research Aircraft (HALO) and the United States Lockheed WP-3D Orion from NOAA (WP-3D). HALO typically flew at an altitude of 30,000 ft (approximately 9 km), following a circular flight pattern with 90 km radius centered at 13.3°N, 57.7°W. When launching sondes, the WP-3D flew

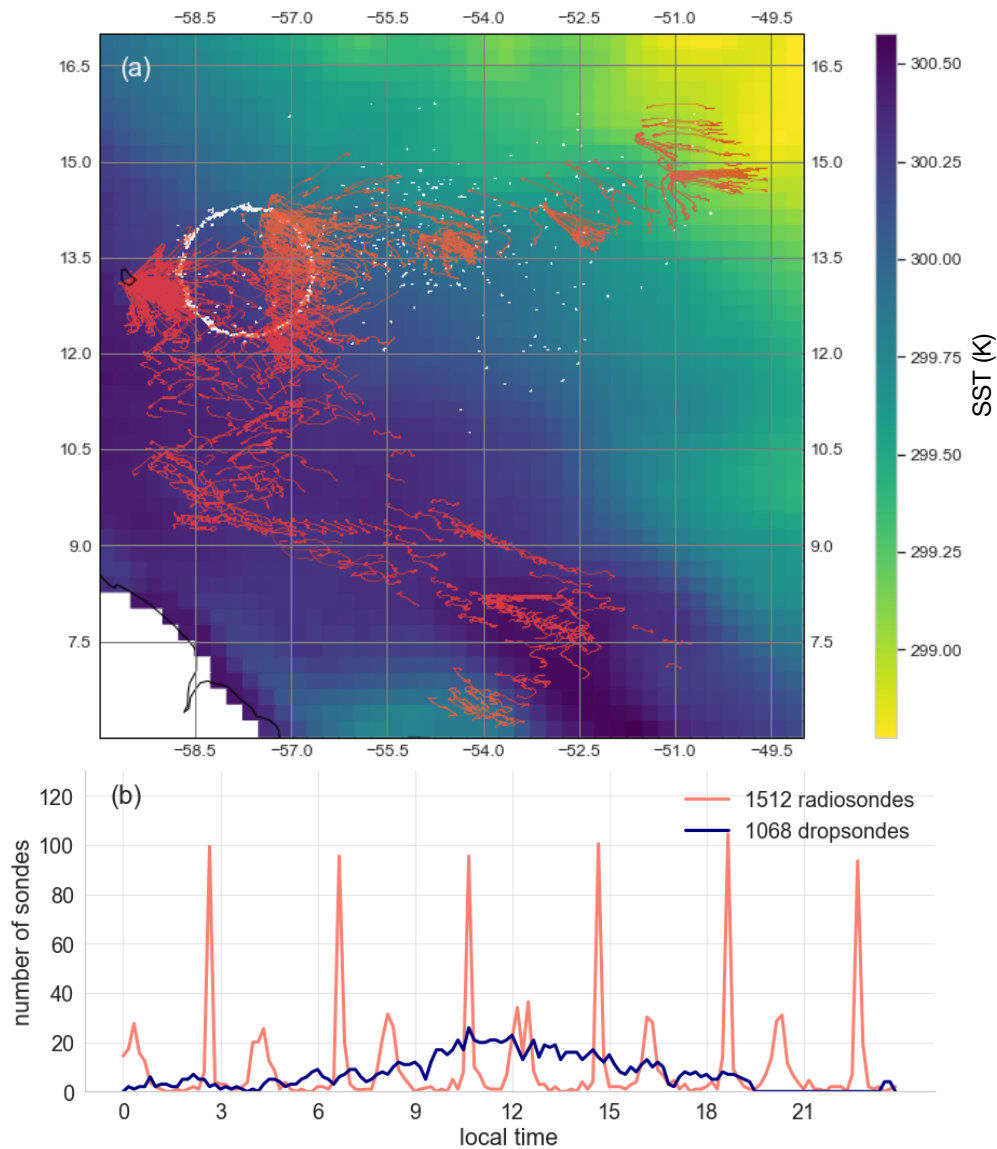


Figure 3-1: (a) The EUREC⁴A sounding network: 1068 soundings from dropsondes (white) and 1512 from radiosondes (coral). We employ 810 dropsondes launched from HALO and 258 dropsondes from the WP-3D to calculate radiative profiles, as well as 325, 344, 156, 377, and 310 radiosondes launched from L’Atalante, BCO, MS-Merian, Meteor, and RH-Brown, respectively. Background colors show sea surface skin temperature (SST_{skin}) from ERA5 reanalysis at 0.25° resolution averaged over January and February. (b) The diurnal distribution of the 1068 dropsondes (blue) and 1512 radiosondes (coral) with sonde launch time are binned in 10 min intervals.

at 24,000 ft (approximately 7 km), releasing sondes along both linear and circular patterns in the region covered by HALO, as well as further to the east close to the nominal position of the RH-Brown.

Radiosondes were launched every four hours, daily from January 8–February 19, 2020, approximately synchronously from each platform. Given that the time-lag between ascending and descending radiosondes is on the order of hours, and that there is substantial horizontal drift between the ascent and descent, we chose to compute separate radiative profiles for ascending and descending radiosondes. For dropsondes, HALO flight takeoffs were staggered at 5, 8, and 11 am local time, with flights lasting approximately eight hours, yielding roughly 72 sondes per flight. The WP-3D undertook three night flights, which allows for a better characterization of the diurnal cycle, together with the radiosondes launched during the night (Figure 3-1b).

We refer the reader to Stephan et al. (2020) and George et al. (2021) for a complete description of the radiosonde and dropsonde data sets, respectively, and Bony et al. (2017) and Stevens et al. (2021) for an overview of the campaign scientific motivations and measurement strategy.

3.3.2 Radiative transfer calculation

The radiative transfer code used here, RRTMGP (Rapid Radiative Transfer Model for GCMs, Parallel) (Pincus et al., 2019), is a plane-parallel correlated- k two-stream model based on state-of-the-art spectroscopic data for gas and condensate optics. It is based on line parameters from Atmospheric and Environmental Research and the MT_CKD water vapor continuum absorption model (Mlawer et al., 2012). The calculation of radiative profiles from radiosonde and dropsonde data then proceeds in the following way:

1. vertical soundings of temperature, pressure, and water vapor specific humidity at 10 meter resolution are interpolated onto a 1 hPa vertical grid and then merged with temperature and specific humidity from ERA5 reanalyses in the

following manner. Sonde measurements below 40 m are first truncated for all sondes: radiosondes do not provide data in this surface layer because of deck heating effects on ships (Stephan et al., 2020), and we apply the same filter to dropsondes for consistency. The ERA5 profiles at hourly and 0.25° resolution (European Centre for Medium-Range Weather Forecasts, 2017) are linearly interpolated temporally and spatially to the time, latitude, and longitude of the sounding. ERA5 values are used above the highest level measured by each sonde to extend the observed soundings vertically to 0.1hPa and account for the effect of high-altitude thermodynamic variability on the radiative cooling profiles below. To obtain the lower boundary condition, we linearly interpolate the ERA5 sea surface skin temperature (SST_{skin}), also at hourly and 0.25° resolution (European Centre for Medium-Range Weather Forecasts, 2017), to the time, longitude and latitude where the sounding was launched;

2. CO_2 concentrations are set to the present day value of 414 ppm while CH_4 , O_3 and N_2O concentrations are taken from the standard tropical atmosphere profile of Garand et al. (2001);
3. the set of resulting profiles is then used as input to RRTMGP to derive upwelling and downwelling clear-sky radiative fluxes in the shortwave and longwave ranges of the spectrum. The calculation uses a spectrally-uniform surface albedo of 0.07 and a spectrally-uniform surface emissivity of 0.98, typical values for tropical oceans.

Dropsondes and radiosondes drift horizontally as they rise and/or fall (Figure 3-1a), which could give slight errors due to aliasing of horizontal moisture variability into vertical variability. This potential error source is less pronounced for dropsondes than radiosondes due to their faster travel speed through the troposphere.

We compute radiative fluxes and heating rates only for the gaseous component of the atmosphere, without explicitly taking into account cloud or aerosol properties. These radiative profiles are therefore clear-sky and aerosol-free. The soundings do, however, capture the water vapor structure, including regions of high humidity in

cloud areas and aerosol layers. Cloud cover in trade-wind regimes is relatively low, between 10% (Nuijens et al., 2015a) and 20% (Medeiros and Nuijens, 2016) for active clouds, so cloud-free, or clear-sky, profiles are representative of the thermodynamic environment. Taking into account the influence of cloud liquid water would require a number of *ad hoc* assumptions about microphysical and optical properties within clouds (see for instance Guichard et al., 2000). Similarly, we do not directly represent the radiative effect of mineral dust aerosols. The dominant aerosol radiative effect in this region has been shown to result from the covariance of aerosols with water vapor, such that aerosols tend to be associated with elevated moisture layers Gutleben et al. (2019, 2020). Dust aerosol layers are, moreover, more common in the summer than in winter (Lonitz et al., 2015). We leave open the possibility that direct scattering by dust aerosols has an additional role on radiative heating rates, but do not have the coincident data to appropriately address this question for all soundings.

3.4 Preliminary results and discussion

This section includes a first exploration of the data set. We examine radiative variability at different scales – across all soundings, at the diurnal timescale, and according to different patterns of mesoscale organization – as well as in individual profiles showing the influence of sharp vertical moisture gradients on radiative heating rates.

3.4.1 Variability across soundings

A distribution of longwave, shortwave, and net heating rates, as well as large-scale thermodynamic quantities, are shown in Fig. 3-2. Local extrema in the median shortwave, longwave, and net heating rates occur near 2 km (Fig. 3-2d,e,f), associated with the rapid decrease in specific and relative humidity at this level (Fig. 3-2b,c). The top of the planetary boundary layer, or interface between the moist marine boundary layer and dry free troposphere above, is expected to occur around 2 km in the trades (Malkus, 1958; Cao et al., 2007; Stevens et al., 2017). The spread in specific and relative humidity is greater than that in temperature, suggesting a

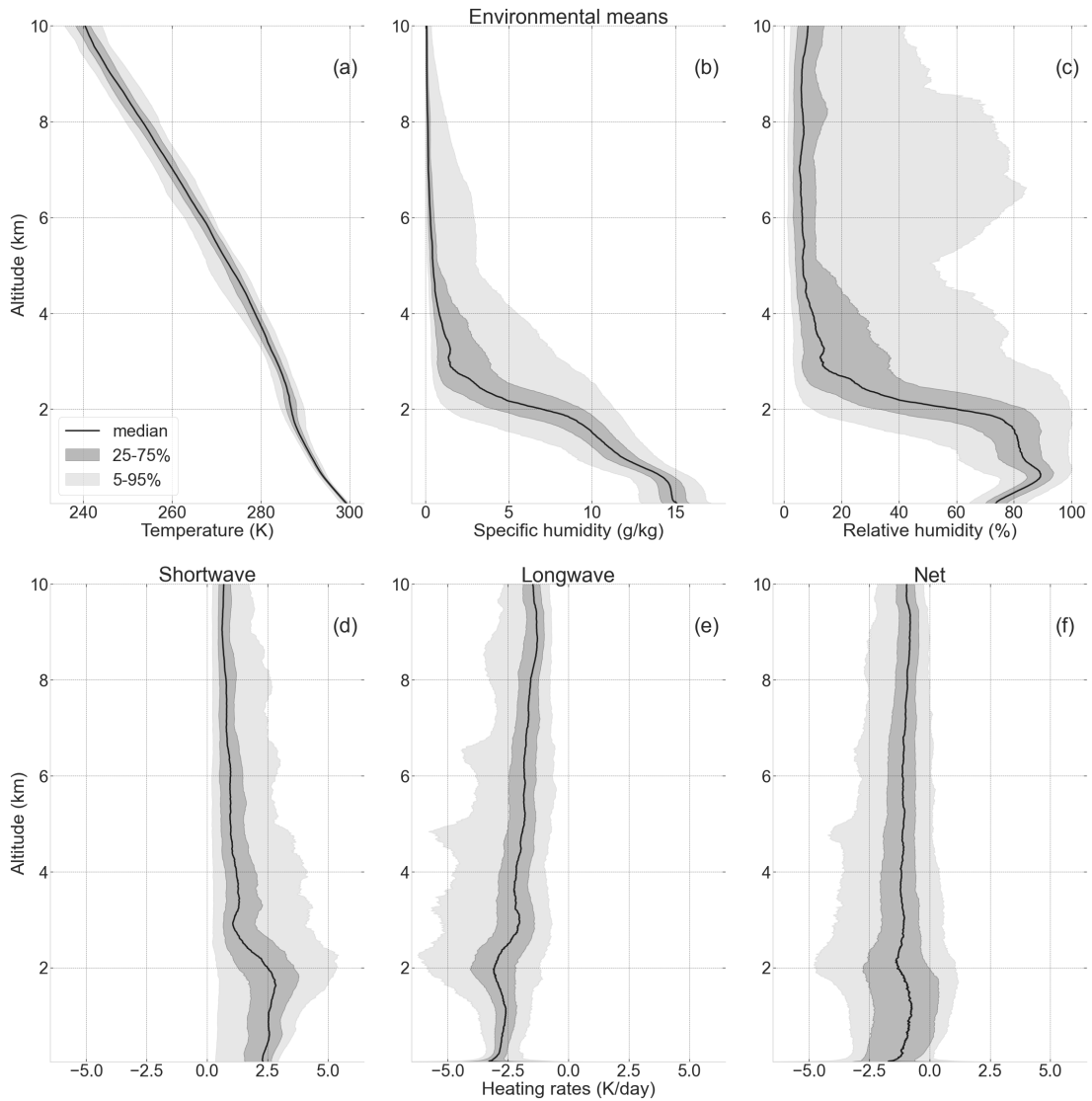


Figure 3-2: Top: Temperature (a), specific humidity (b) and relative humidity (c) (with respect to ice for $T < 0^\circ\text{C}$) from EUREC⁴A dropsonde and radiosonde data. Bottom: Shortwave (d), longwave (e) and net (f) heating rates calculated from EUREC⁴A dropsonde and radiosonde data using the radiative transfer code RRT-MGP. The center traces are the median profiles, and the medium and light grey shadings indicate the 25–75% and 5–95% intervals, respectively. For the shortwave, the median and the interquartile range are calculated using daytime values only.

strong role for moisture variability on the variability in radiative heating rates. On average, longwave cooling is stronger than shortwave heating, such that net heating rates are largely negative from the surface up to 10 km, with a median value around -1 K/day. Additional local minima in longwave heating are observed around 3, 5, and 7 km between the 5% and 25% quantiles. These local minima could, for instance, correspond to the radiative effect of elevated moisture layers arising from convection detraining moisture at these higher levels, albeit less frequently, or aerosol layers associated with increased water vapor concentrations (Stevens et al., 2017; Wood et al., 2018a,b; O et al., 2018; Gutleben et al., 2019).

We next partition radiative heating variability into its variability in time (e.g. diurnal cycle, day-to-day variability) and regarding the spatial characteristics of the convection field (e.g. the spatial distribution of clear and cloudy regions).

3.4.2 Diurnal cycle and day-to-day variability

Figure 3-3 gives an overview of the diurnal variability of radiative heating, which has been implicated in the diurnal cycle of convection and cloudiness (e.g., Gray and Jacobson Jr, 1977; Randall and Tjemkes, 1991; Ruppert and Johnson, 2016). Shortwave radiative heating follows the solar cycle. Longwave heating rates show less diurnal variability and have approximately the same amplitude (with an opposite sign) as shortwave heating rates during daytime. This compensation between longwave cooling and shortwave heating results in a daytime net heating rate that is slightly positive in the lower 2 km. The daytime heating within the cloud layer could contribute to stabilizing the lower atmosphere, disfavoring convection. At night, strong radiative cooling destabilizes the lower troposphere and strengthens convective fluxes. The maximum nighttime longwave cooling occurs slightly above 2 km. During daytime, the peak in stabilizing radiative heating appears slightly below 2 km. This difference in the height of peak radiative heating, albeit of different sign, could reflect differences in the height of the moist, convecting layer over the diurnal cycle: a shallower marine boundary layer during the day that deepens at night (Vial et al., 2019). These considerations highlight the potential for subtle interactions among radiation, convection,

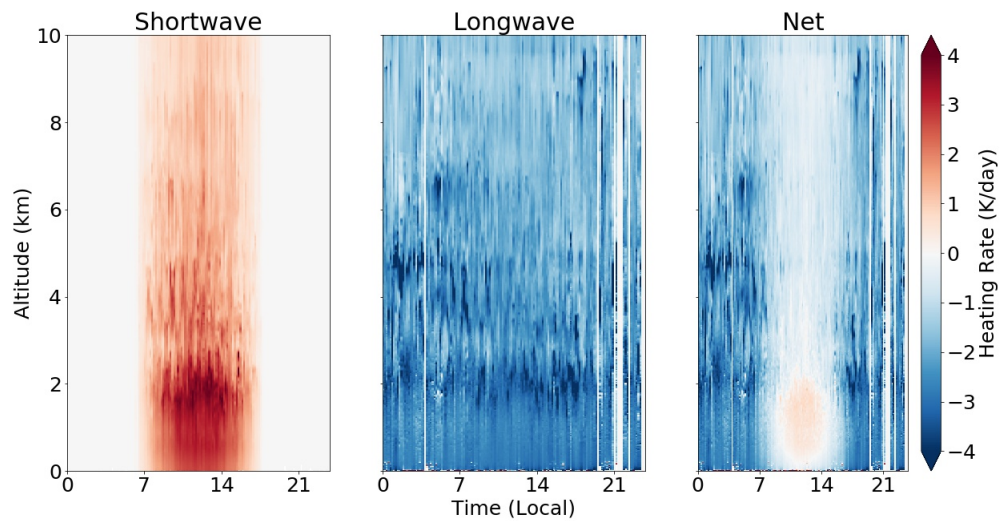


Figure 3-3: Diurnal composite of shortwave (left), longwave (middle), and net (right) clear-sky heating rates binned in 10-minute intervals. Colored shadings indicate heating rates in units of K/day. The data are plotted with respect to local solar time to simplify interpretation of the diurnal cycle. White indicates the absence of data. We note that some variability, such as in the nighttime longwave radiative cooling variability, could result from different numbers of sondes launched throughout the diurnal cycle (as illustrated in Fig. 3-1b).

and cloudiness on the diurnal timescale.

Fig. 3-4 shows the day-to-day evolution of the shortwave (top), longwave (middle) and net (bottom) heating rates derived from radiosondes launched at BCO. In the shortwave and net heating rates, the daily stripes are due to zero shortwave heating during the night. In the longwave component alone, the amplitude of the diurnal cycle is less evident. Regarding the day-to-day variability, both in the shortwave and the longwave components, trends in the height-evolution of the radiative heating maxima appear to persist over several days. These trends are likely due to variations in humidity (e.g. Dopplick, 1972; Jeevanjee and Fueglistaler, 2020) and are consistent with the presence of multi-day trends in moisture observed at BCO during the campaign (see Figure 13 in Stevens et al., 2021). At the end of the campaign, the rise in the peak of longwave cooling appears to correspond to the rising location of the interface between the moist, convecting layer below and dry free troposphere above (not shown). The persistence and evolution of radiative heating patterns could be tied to larger-scale synoptic moisture activity or to the evolution of mesoscale organization patterns.

3.4.3 Radiative signatures of mesoscale patterns of cloud organization

We next aggregate radiative heating rates spatially. Fig. 3-5 illustrates four representative cases of the Fish-Gravel-Flower-Sugar classification established previously for mesoscale (20-2,000 km) organization patterns of clear and cloudy regions (Bony et al., 2020; Stevens et al., 2020b). These cloud organization patterns were identified visually from satellite imagery and correspond to differences in large-scale environmental conditions (Bony et al., 2020). They are also observed to have different top-of-the-atmosphere radiative effects (Bony et al., 2020). As outlined in Stevens et al. (2020b), Sugar refers to a ‘dusting’ of small, shallow clouds with low reflectivity and a random spatial distribution. Gravel clouds tend to be deeper than Sugar (up to 3-4 km), have little stratiform cloudiness, precipitate, and organize along apparent

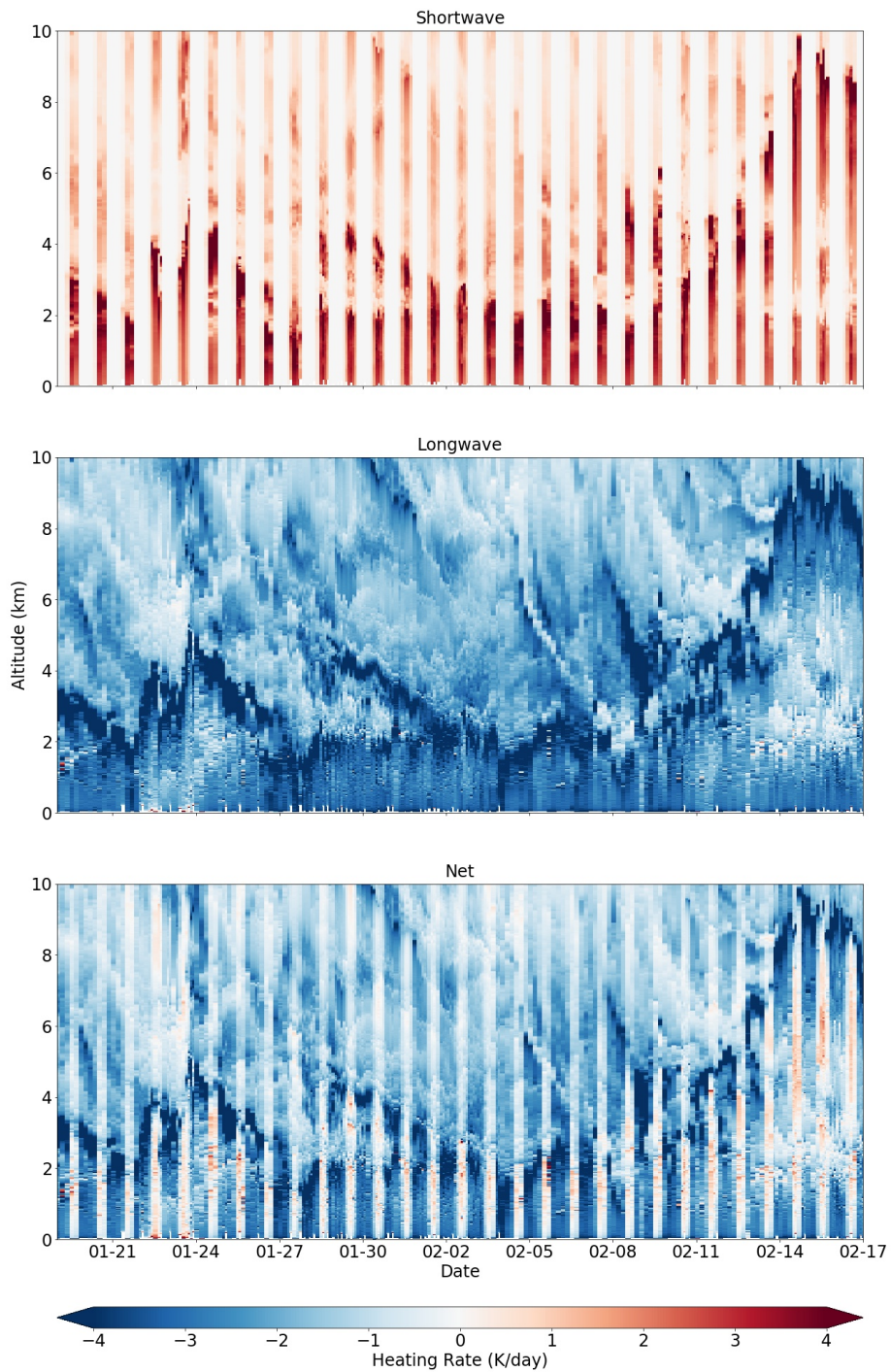


Figure 3-4: Shortwave (top), longwave (middle), and net (bottom) heating rates at BCO during EUREC⁴A, from January 19 to February 17. The heating rates are calculated from radiosondes launched at BCO. In colors are heating rates with units of K/day. White indicates the absence of data.

gust fronts or cold pools at the 20-200 km scales. Fish are skeletal networks (often fishbone-like) of clouds at the 200-2,000 km scale with stratiform cloud layers; the Fish pattern is often associated with extratropical intrusions. Flowers are circular features defined by their stratiform cloud elements. Both Fish and Flowers are surrounded by large swaths of clear air.

We choose four days as an example of the large-scale environmental and radiative signature of each pattern, given the spatial pattern observable in the GOES-16 satellite images in the HALO flight path shown by the white circle. We plot daily-mean profiles for temperature, specific humidity, and relative humidity (Fig. 3-5a,b,c), as well as shortwave, longwave, and net radiative heating rates (Fig. 3-5d,e,f). These profiles were calculated from approximately 70 HALO dropsondes launched during the eight-hour flight on each day. We also plot the standard deviation of radiative heating for each flight (Fig. 3-5g,h,i). As a first approximation, the standard deviation of daily radiative heating profiles acts as a proxy for spatial variability in radiative heating rates.

Spatial variability in radiative heating has been shown to drive shallow circulations (e.g. Naumann et al., 2019) and affect convective organization (e.g. Bretherton et al., 2005; Muller and Held, 2012). In this illustrative example, the differences in the mean and standard deviation of the radiative heating rates hint at a role for differences in radiative cooling rates in the onset or maintenance of mesoscale patterns of organization. For instance, the ‘Fish’ pattern on January 22, 2020 appears to have a moister lower troposphere between 1 and 3 km and slightly drier free troposphere above 4 km. This vertical moisture distribution may give rise to the observed vertical variability in radiative heating rates, with larger peaks in the mean profile (Fig. 3-5e) and standard deviation (Fig. 3-5h) in radiative heating observable between 2 and 4 km, likely corresponding to strong humidity gradients at these levels.

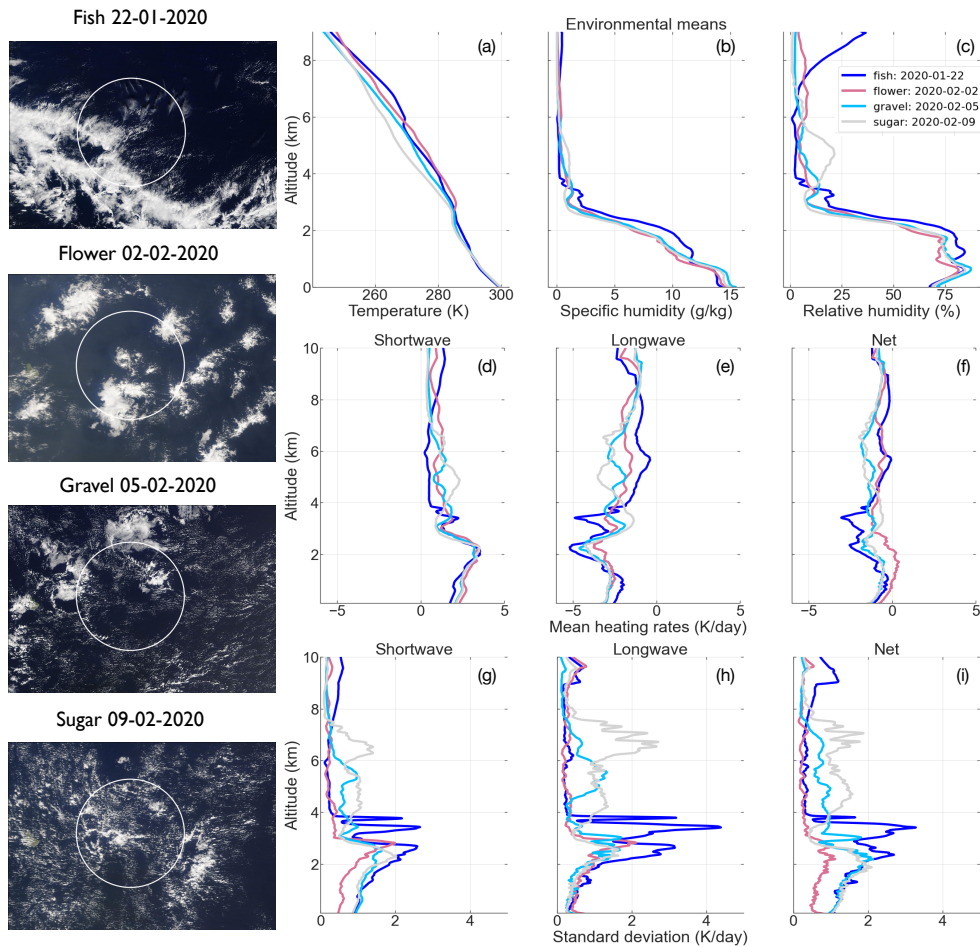


Figure 3-5: Thermodynamic (a-c), daily mean radiative heating (d-f), and daily standard deviation of radiative heating (g-i) profiles classified by mesoscale organization pattern, using a characteristic example of each type as diagnosed from snapshots from GOES-16 infrared channel (left column). This figure employs HALO dropsondes launched in the circular flight pattern (shown by the white circle) on the chosen day, corresponding to roughly 70 dropsondes each. We focus on the spatial extent of the HALO flight pattern because the cloud organization pattern does not necessarily extend across the entire sampling domain Figure 3-1a, nor have the patterns been shown to be scale-invariant.

3.4.4 Effect of sharp moisture gradients on radiative heating profiles

Figure 3-6 highlights the radiative signatures of elevated moisture layers, which can persist for multiple hours at inversion levels (Stevens et al., 2017; Wood et al., 2018a; Gutleben et al., 2019). We focus in detail on two thermodynamic and radiative heating profiles of a particular elevated moisture layer extending to 4 kilometers, alongside GOES-16 images (Fig. 3-6i,j) corresponding to these soundings. This structure persisted for at least four hours on January 24, 2020, and we plot thermodynamic conditions and radiative heating profiles sampled three hours apart, at 12:55 and 15:55 UTC (see Fig. 3-6). A striking feature is the sharp peak in longwave cooling at the top of the moisture layer of nearly -20 K/day at 15:55 UTC, corresponding to the strong humidity gradient, with relative humidity decreasing by nearly 70% in 100 meters (Fig. 3-6c,d).

Although we calculate clear-sky profiles only, the present work could be extended to account for radiative effect of cloud liquid water, which could be used, for instance, to investigate the radiative effect of geometrically- and optically-thin ‘veil clouds’ persisting at inversion levels (Wood et al., 2018a,b; O et al., 2018), such as those illustrated by the flight photographs (Fig. 3-6a,e). Over global oceans, approximately half of low clouds do not fully attenuate space-borne lidar, suggesting that these optically-thin clouds contribute significantly to total cloud cover estimates (?) and could have an important radiative impact (e.g., Wood et al., 2018b).

3.5 Uncertainty assessment

To evaluate the robustness of our results and ensure good use of this data set, we performed several uncertainty assessments by perturbing the SST_{skin} , *in situ* moisture data, and ERA profiles used. We also included in the data set the minimum and maximum levels z_{min} and z_{max} measured by each sonde. Unless indicated otherwise, the errors reported below correspond to a subset of profiles with valid data starting

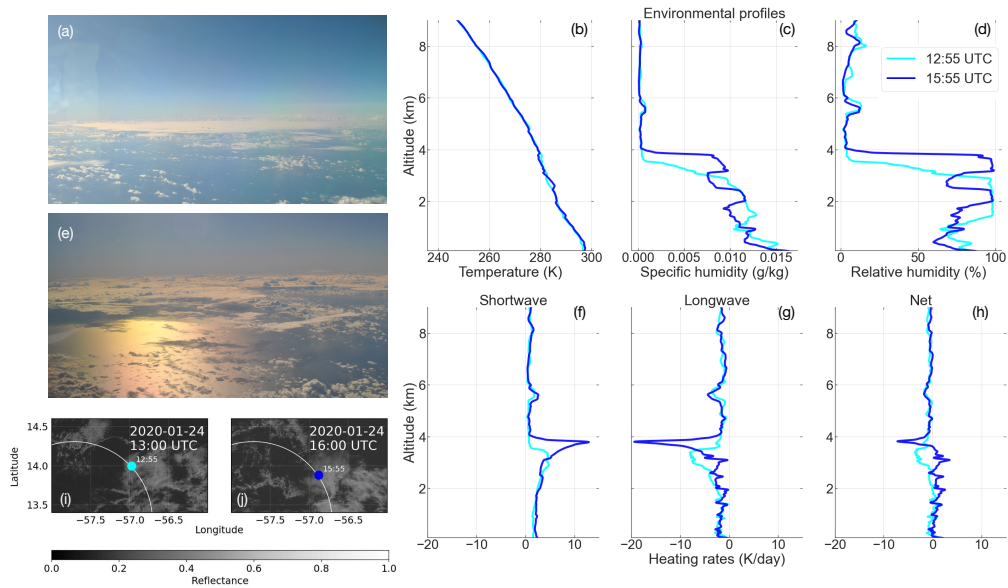


Figure 3-6: Thermodynamic and radiative heating profiles associated with an elevated moisture layer persisting for multiple hours on January 24, 2020 in the HALO flight pattern. Plotted here are the temperature (b), specific humidity (c), relative humidity (d), as well as shortwave, longwave, and net radiative heating rate (f-h) profiles for two soundings sampled three hours apart, at 12:55 and 15:55 UTC. Alongside these profiles are photographs (a,b) taken from the HALO aircraft during the flight and GOES-16 satellite images (i,j), with the dropsonde location and launch time indicated by a circle along the circular flight pattern. Credit for the two flight photographs: J. Vial.

at 40 m (ie. $z_{min} \leq 40$ m) and during daytime, which corresponds to 1314 profiles. The daytime filter was required for relevant calculation of the error in the shortwave, and then kept for consistency for the longwave, but the magnitude of errors in the longwave is not affected by this filter (not shown).

We first test the sensitivity to the ERA5 SST_{skin}. To this end, we perturbed the original SST_{skin} by ± 0.42 K and recalculate all heating rates. This value is chosen as it corresponds to the root-mean-square-error (RMSE) between ERA5 SST_{skin} and Marine-Atmosphere Emitted Radiance Interferometers (M-AERI) measures taken during a series of cruises in the Caribbean Sea from 2014 to 2019 (Luo and Minnett, 2020). Figure 3-7 shows the RMSE between the original and perturbed radiative profiles (blue-green curves). In the longwave and net, the effect of the perturbation is strong in the first atmospheric layer, but then decreases rapidly and becomes negligible after a few hundred meters. Except for the first few atmospheric layers, the uncertainty around the SST_{skin} can therefore be safely neglected.

We then investigate the sensitivity to the uncertainty of sounding measurements by perturbing all soundings by a vertically-uniform relative error and redoing all radiative transfer calculations. The manufacturer predicts an uncertainty of ± 0.1 K for the temperature and $\pm 3\%$ for relative humidity (Vaisala, 2018). The temperature uncertainty has virtually no effect on radiative profiles (not shown). The effect of $\pm 3\%$ uncertainty on the specific humidity profiles is shown in Fig. 3-7 in red. The highest RMSE for this specific humidity perturbation occurs in the cloud layer, between 800 m and 2 km, with a magnitude of 0.05 K/day for net radiative heating. A secondary peak with a magnitude of 0.03 K/day is also evident near the inversion, at about 3 km. Given a median radiative heating value of -1 K/day throughout the lower troposphere (Sec. 3.4.1), these errors are roughly 3-5% for the net radiative heating. These maxima likely correspond to the cumulative errors at the altitude of large vertical humidity gradients, which lead to peaks in longwave, and to a lesser extent shortwave heating rates for individual profiles.

Finally, we explore the uncertainty associated with ERA5 temperature and humidity data employed as an upper boundary condition. Similarly to the uncertainty

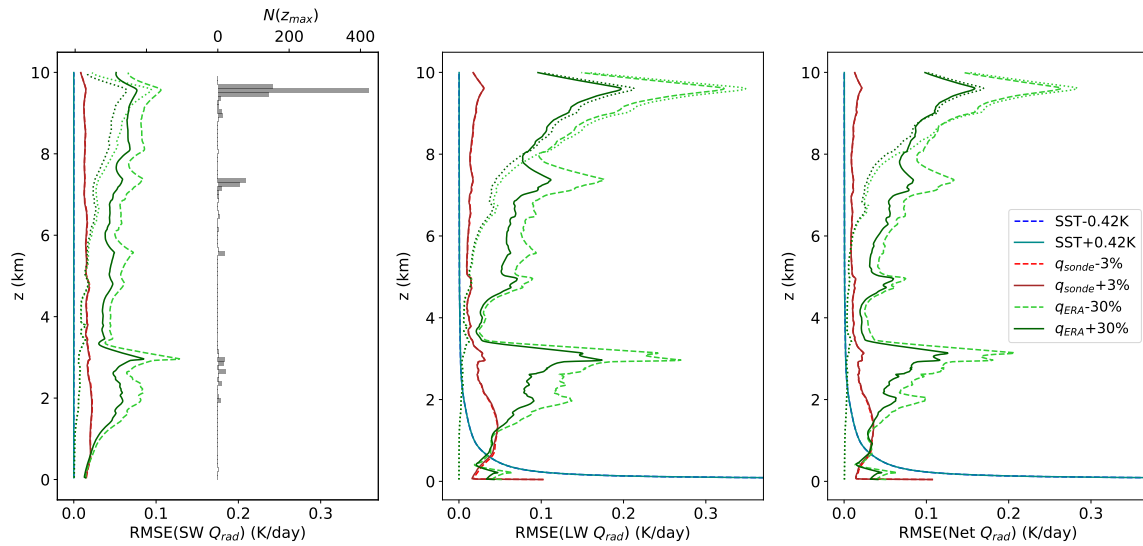


Figure 3-7: Root-mean-square error (RMSE) estimates in shortwave (left), longwave (center) and net heating rates (right) for perturbations in SST_{skin} (blue), ERA5 humidity profiles (green) and sonde humidity measurements (red) for the 1314 daytime profiles that have valid data starting at 40 m. Dashed curves show negative perturbations, solid curves show positive perturbations and dotted green curves show ERA5 humidity perturbations restrained to the 1117 daytime profiles that have valid data at all levels between 40 m and 8 km. The horizontal grey bars on the left panel show the frequency distribution in the maximum level measured (z_{max}).

analysis for the sounding data, we perturb ERA5 3D fields — used as input to the radiative transfer code — by a uniform relative error. Previous studies have shown that ERA5 reanalyses can present biases of various kinds (Nagarajan and Aiyyer, 2004; Dyroff et al., 2015). We compare ERA5 humidity and temperature data with coincident radiosonde measures to obtain an estimate of ERA5 biases up to 100 hPa. From the surface to 100 hPa, the RMSE in temperature between co-located radiosonde soundings and ERA5 is between 0.3 and 0.7 K, with a mean of 0.5 K, and between 5% (at the surface) and 70% (near the inversion) for the specific humidity, with a mean around 30%.

Fig. 3-7 only shows the effect of the ERA5 specific humidity uncertainty, taken at $\pm 30\%$, on radiative profiles, as the temperature has once again a negligible influence. The corresponding green curves (respectively dashed and solid) reveal local maxima in the longwave and net heating rates around 3, 7 and 9.5 km. Again given a median radiative heating value of -1K/day throughout the lower troposphere (Sec. 3.4.1), the errors at these local peaks are between 10–30%. These maxima coincide with the modes in the frequency distribution of the highest level z_{max} measured by the soundings, indicated in grey in the left panel. These peaks suggest that the uncertainty arises from the large discontinuities emerging at the ERA5-sounding junction level when perturbing ERA5 humidity profiles. The results suggest that the corresponding uncertainty mainly occurs in the vicinity of the junction levels. This notion is further confirmed by calculating the RMSE only on profiles which have data between 40 m and 8 km (ie. $z_{min} \leq 40$ m and $z_{max} \geq 8$ km, dotted green curve): the remaining 1117 profiles left do not contain vertical discontinuities in humidity in this range, and we see that the remaining upper-tropospheric discontinuities do not affect heating rates in the lowest troposphere.

Overall, the small uncertainty values given with these tests support the robustness of this data set and gives confidence regarding its use for more detailed investigations in the lower troposphere. The uncertainty from sea surface skin temperature is limited to the first few atmosphere layers, and uncertainty from merging with ERA5 specific humidity is largely contained to the sounding-reanalysis junction point. Uncertainty

associated with observed specific humidity profiles produces localized errors in the cloud and inversion layers below 3 km, though these errors are approximately 5% or less. We recommend that users carefully compare the magnitude of the signal they analyze with the magnitudes of the errors provided here.

3.6 Conclusions

The first objective of this work is to present the method used to calculate clear-sky, aerosol-free radiative profiles from 2580 radiosonde and dropsonde soundings launched during the EUREC⁴A field campaign. These radiative profiles are calculated using a state-of-the-art correlated- k model, RRTMGP, in which ERA5 reanalyses provide lower and upper boundary conditions. We then aggregate the radiative heating profiles at multiple scales to examine temporal and spatial variability in trade wind regimes. We find that radiative heating rates in the wintertime trade-wind environment display significant diurnal and day-to-day variability, and we observe hints that this variability may be associated with different types of mesoscale organization. An uncertainty assessment is further conducted to demonstrate that the influence of uncertainties in the sounding data, and upper and lower boundary conditions, is small relative to the magnitude of estimated radiative heating.

These results present a first overview of how this data set could help answer existing research questions, in particular: 1) What is the role played by radiation in the mesoscale organization of shallow convection? (e.g., Seifert and Heus, 2013; Bretherton and Blossey, 2017b) 2) what is the interplay between the diurnal variability in radiative heating, convection, and cloudiness? (e.g., Gray and Jacobson Jr, 1977; Ruppert Jr and O’Neill, 2019; Vial et al., 2019), and 3) what is the influence of clear-sky radiative cooling gradients on atmospheric circulations? (e.g., Gray and Jacobson Jr, 1977; Mapes, 2001; Emanuel et al., 2014; Thompson et al., 2017; Naumann et al., 2019). Such questions regarding the coupling of clouds, convection, and circulations in trade-wind regimes are at the heart of the EUREC⁴A field campaign, and the radiative profiles presented here complement other EUREC⁴A observations

and data products in forming a toolbox for these investigations.

Chapter 4

Observed subcloud layer moisture and heat budgets in the trades

4.1 Abstract

The trade-wind subcloud layer is an important structural component of the atmosphere. Its thermodynamic variability has long been characterized using simple frameworks, of which mixed layer theory is the simplest kind. Past studies qualitatively support such a description, yet the adequacy of mixed layer theory as a quantitative description has not been tested. Here we use observations collected during the EUREC⁴A (*Elucidating the role of clouds–circulation coupling in climate*) field campaign to test this framework and evaluate our understanding of the trade-wind subcloud layer. We find evidence for a transition layer separating the mixed layer and subcloud layer tops. The presence of such a finitely-thick transition layer with vertical gradients complicates the application of mixed layer theory, which assumes an abrupt gradient, or ‘jump’ at the subcloud layer top. This ambiguity introduces effective parameters and motivates their estimation through a Bayesian methodology. Results from this Bayesian inversion further reflect a finite-depth entrainment zone. We find that subcloud layer moisture and heat budgets close for synoptic variability and a monthly campaign-mean, yielding a campaign-mean residual of 3.6 Wm^{-2} for moisture and 2.9 Wm^{-2} for heat. Surface wind speed variability influences the subcloud layer depth and fluxes, yet thermodynamic variability above the subcloud layer

This chapter is published in the *Journal of the Atmospheric Sciences*.

top emerges as the primary control on subcloud layer moisture and heat variability. Given that this simple theoretical framework can explain observed variability, it offers an appealing framework for evaluating larger-scale models that must parameterize the processes regulating this fundamental part of the atmosphere.

4.2 Introduction

The trade-wind subcloud layer is an important component of the tropical atmosphere. Typically defined as extending from the top of the surface layer (at approximately 50 m) to cloud base (e.g., Malkus, 1958; Stevens et al., 2017), it couples the surface to the trade-wind cloud layer and, in so doing, regulates the import of heat and moisture from the ocean to the atmosphere above (e.g., Malkus, 1958; LeMone and Pennell, 1976; Stevens, 2007). Clouds are influenced by subcloud layer properties, as subcloud moisture variability controls moist static energy variability, which influences convective potential and cloudiness (e.g., Emanuel, 1986, 1993). Clouds also influence the subcloud layer, as they introduce variability in surface fluxes and radiation, influence wind shear, and mix down dry air from aloft that can then be entrained into the subcloud layer (e.g., Stevens, 2006). This subtle interplay between the subcloud and cloud layers ultimately governs the magnitude of latent heat transport from the trades to the equator (e.g., Malkus, 1958). The trade-wind subcloud layer thus forms an important link in the global thermodynamic budget, transporting latent heat to the equatorial belt where it influences large-scale circulations and the global hydrological cycle (Riehl, 1954; Heckley, 1985; Tiedtke, 1989).

To the extent that the subcloud layer influences the cloud layer, the clouds of the trades provide an additional motivation to study the trade-wind subcloud layer. By virtue of their large spatial extent and thus statistical weight, trade-wind cloud regimes have a large influence on the global energy budget and global dynamics (e.g., Bony et al., 2004). Differences in the response of trade-wind cumulus to warming explain large differences in climate sensitivity estimates (e.g., Bony and Dufresne, 2005; Webb et al., 2006; Vial et al., 2013; Myers et al., 2021), some of which have

been shown to relate to how efficiently moisture is exported out of the trade-wind subcloud layer (Sherwood et al., 2014).

Given the importance of the trade-wind subcloud layer, it is useful to understand what controls its properties. To aid this understanding, the subcloud layer has long been characterized using simple frameworks. Turbulence is expected to homogenize subcloud layer thermodynamic variables in the vertical (e.g., Mahrt, 1976; Stull, 2012). Such a well-mixed vertical structure allows for simplification by solving for the vertically-integrated, or bulk, properties of the subcloud layer. Among these the vertically-integrated, or bulk models, the mixed layer model is the simplest case, representing the subcloud layer by a single vertically-averaged value. As reviewed by Stevens (2006), mixed layer models have formed a basis for representing the subcloud layer in larger-scale models (Deardorff, 1972; Arakawa and Schubert, 1974), thermodynamic models of the tropics (Betts and Ridgway, 1989; Miller, 1997), diagnostic studies of surface winds over tropical oceans (Stevens et al., 2002; McGauley et al., 2004), and diagnostic studies of specific regions, including trade-wind regimes (Betts, 1976; Betts and Albrecht, 1987; Neggers et al., 2006), deep convective regions (Emanuel, 1993; Raymond, 1995), or stratocumulus regimes (Kraus, 1963; Lilly, 1968; Wood and Bretherton, 2004). Mixed layer models allow for quantifying the magnitude of different processes that control subcloud layer variability and attributing this variability to changes in the environment.

The adequacy of this mixed layer description of the subcloud layer has, however, only been assessed from relatively few measurements and large-eddy simulations often performed for idealized conditions over small (and usually homogeneous) domains. Past observational studies typically used approximately 100 dropsondes and fixed certain parameters, such as the sea surface temperature and vertical thermodynamic structure above the subcloud layer (Betts, 1976; Betts and Albrecht, 1987; Betts and Ridgway, 1989). Other studies examining large-scale heat and moisture budgets (Augstein et al., 1973; Yanai et al., 1973; Holland and Rasmusson, 1973; Nitta and Esbensen, 1974) considered the layer up to the trade-wind inversion, therefore focusing on different vertical transports than our budgets for the subcloud layer. Aug-

menting subcloud layer thermodynamic analyses with passive remote sensing remains challenging, in particular regarding the boundary layer height, entrainment flux, and vertical motions (e.g., Kalmus et al., 2014). Indeed, tropical moisture variability is poorly quantified by passive remote sensing, especially in the lowest three kilometers, because observed moisture profile features are at scales much finer than the typical weighting functions of even hyperspectral instruments (e.g., Maddy and Barnet, 2008; Chazette et al., 2014; Stevens et al., 2017; Pincus et al., 2017). Output from large-eddy simulations could, conceivably, be used to evaluate mixed layer theory, and mixed layer models have been used to interpret large-eddy simulations (e.g., Neggers et al., 2006; Bellon and Stevens, 2012, 2013; Schalkwijk et al., 2013). Indeed, the apparent realism of large-eddy simulations can suggest a trustworthy representation of nature, yet these simulations use idealized boundary conditions, employ a range of domain sizes and resolutions, and rarely represent the diversity of mesoscale patterns of convection observed in nature, all of which introduce uncertainty into the resultant thermodynamic fields (e.g., Bony et al., 2017). The limitations of both passive remote sensing and large-eddy simulation output render *in situ* observations especially important for testing mixed layer theory as a description of the trade-wind subcloud layer.

As part of the EUREC⁴A (*Elucidating the role of clouds–circulation coupling in climate*) field campaign (Bony et al., 2017; Stevens et al., 2021), we collected the necessary data to investigate the structure and variability of the trade-wind subcloud layer. These data allow us to test whether mixed layer theory is a reasonable and useful theoretical framework for studying the trade-wind subcloud layer. After verifying that the assumptions of mixed layer theory are reasonable relative to observational constraints, we test whether this simple framework is useful for diagnosing the balance of physical processes controlling subcloud layer thermodynamic variability and its large-scale environmental controls. A primary motivation for the EUREC⁴A campaign was to make the first process-based constraint on the trade cumulus feedback, which is undertaken in Vogel et al., in review. The process-based approach in Vogel et al., in review makes use of the mixed layer framework, albeit for the subcloud layer

mass budget. Another motivation for the present paper is therefore to evaluate the adequacy of the mixed layer framework for subcloud layer moisture and heat, in order to assess whether it can be applied to the subcloud layer mass budget and thus the evaluation of trade cumulus feedbacks.

To this end, Section 5.3 presents the EUREC⁴A observations, and Section 4.4 defines subcloud layer variability in terms of five parameters — its height, as well as its means and gradients in specific humidity and potential temperature – and quantifies how each parameter contributes to variability across measurement periods separated by hours to weeks. Section 4.5 introduces the mixed layer theory framework and a Bayesian methodology that is used to jointly constrain uncertain parameters related to entrainment. Section 4.6 then evaluates whether this simple theoretical framework, applied to *in situ* observations, can explain observed synoptic variability and the monthly campaign-mean for moisture and heat. Section 4.7 examines the relationships among subcloud layer properties and large-scale meteorological conditions, and Sec. 4.8 presents discussion and conclusions.

4.3 EUREC⁴A field campaign data

EUREC⁴A field study measurements were made in January and February 2020 in the North Atlantic trade-wind regions, east of Barbados, to study the couplings among clouds, circulations, and their large-scale environment. In both models and observations, clouds and the large-scale environment around Barbados were found to be representative of the Atlantic and Pacific trades (Medeiros and Nuijens, 2016; Rasp et al., 2020), suggesting that many inferences from EUREC⁴A observations are informative of trade-wind regions globally. EUREC⁴A sets itself apart from previous field campaign that are, for instance, reviewed by Garstang et al. (2019), through the intense and unbiased sampling; the use of novel observing strategies combined with improved and novel instrumentation; and the coincidence of satellite measurements with very high spatial resolution and temporal sampling (Bony et al., 2017; Stevens et al., 2021).

Figure 4-1 shows the geographic distribution of the measurements used in this study. Our core data are 810 dropsondes from the German High Altitude and Long Range Research Aircraft (HALO) launched between January 22, 2020 and February 15, 2020 (George et al., 2021; Konow et al., 2021). These dropsondes yield vertical profiles of pressure, temperature, and relative humidity with a manufacturer-stated accuracy of 0.4 hPa, 0.1°C, and 2%, respectively (Vaisala, 2022). We employ level-3 and level-4 dropsonde data, which have been processed and interpolated into a common altitude grid with 10 m vertical resolution (George et al., 2021). We note that George et al. (2021) identify a dry bias in the HALO dropsondes, which they correct with a multiplicative factor of 1.06 applied to relative humidity and all associated moisture quantities from these sondes. We use these corrected data.

One unique aspect of EUREC⁴A is the sampling strategy that provides aggregated, statistical estimates of a larger-scale signal, compared to individual point-wise measurements. During EUREC⁴A, dropsonde measurements were distributed along a fixed flight pattern, the ‘EUREC⁴A circle’ — the EUREC⁴A circle is a circular flight pattern with an approximately 220-kilometer diameter, centered at 13.3°N, 57.7°W, at 9.5 km altitude (Fig 4-1). The spatial scale of the EUREC⁴A circle characterizes the large-scale environment and corresponds to the size of a typical general circulation model gridbox, or what Orlanski (1975) called the meso- β scale (20–200km). Given that measurements did not target specific meteorological conditions (e.g., no ‘cloud-chasing’), they provide unbiased sampling of the large-scale environment.

Following Stevens et al. (2021), one *circle-mean* refers to the mean of typically 12 dropsondes launched over one hour along the EUREC⁴A circle (due to operator and instrument errors, on some circles fewer sondes were launched, but never fewer than seven). A dropsonde is launched for every 30 degree change in heading. Typically each flight incorporated two – temporally well separated – periods of ‘circling’. A *circling-mean* is defined as the mean of three consecutive circle-means (or in two cases, two circle-means), corresponding to 30–36 consecutive soundings aggregated over 210 minutes. Variability on the circling-mean scale captures how the large-scale environment varies across about 3.5-hourly periods, and we refer to variability

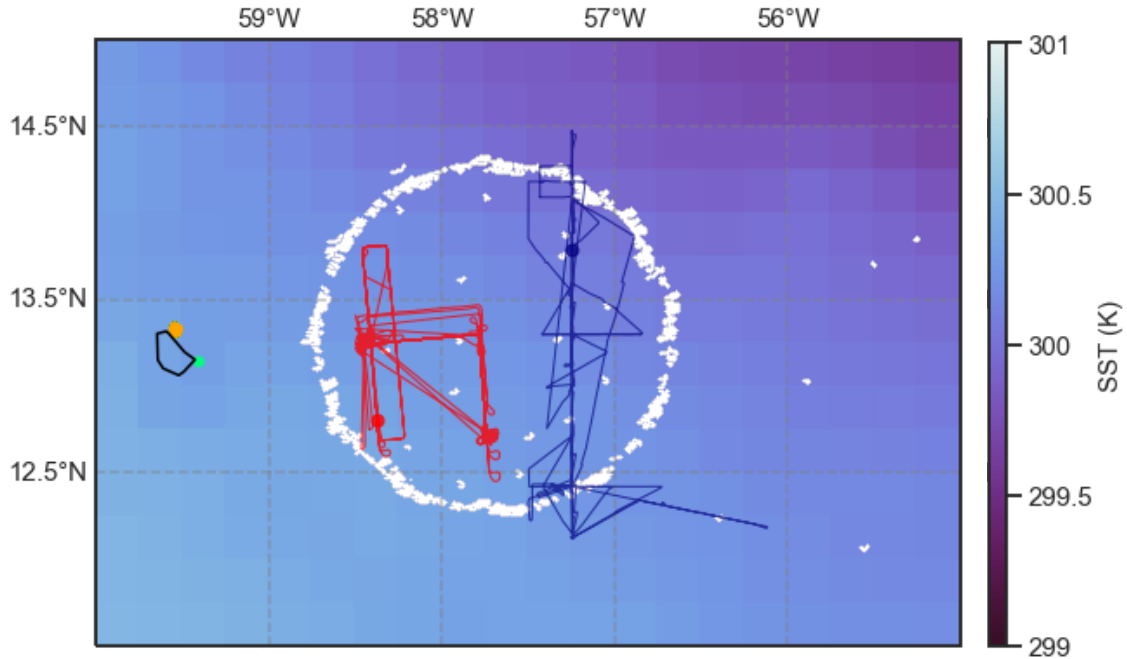


Figure 4-1: Data employed in this study include dropsondes launched in the EUREC⁴A circle (white; 810 HALO dropsonde soundings), subcloud layer thermodynamic measurements from the ATR-42 aircraft (red tracks), and sea surface temperature and surface flux measurements from the R/V Meteor (navy tracks). We also use data from the Barbados Cloud Observatory (green) and subcloud layer thermodynamic measurements from the remotely-piloted aircraft CU-RAAVEN (orange). For illustrative purposes, background sea surface temperatures are ERA5 data at 0.25° resolution, averaged over January and February 2020.

measured on the circling-mean scale as synoptic variability. The *campaign-mean* refers to the mean of 810 dropsondes launched from the HALO aircraft between January 22, 2020 and February 15, 2020, or approximately a monthly-mean. In total, the dropsonde data are aggregated to 69 circle-means, 24 circling-means, and one campaign-mean.

The French ATR-42 aircraft made thermodynamic measurements during 18 flights from January 26 to February 13, 2020. The ATR-42 flew coincident rectangular patterns inside the EUREC⁴A circle (see Fig. 4-1), therefore also providing unbiased measurements of the large-scale environment. Its thermodynamic measurements show good agreement with the HALO dropsonde measurements (Bony et al., 2022). We also make use of smaller-scale thermodynamic measurements between January 24 to

February 15, 2020 below one kilometer from a remotely-piloted aircraft CU-RAAVEN (de Boer et al., 2022). Sea surface temperatures are from the R/V Meteor, with these values extrapolated from the R/V Meteor location to the respective dropsonde location based on fixed zonal and meridional sea surface temperature gradients of $-0.14 \text{ K degree}^{-1}$ of latitude or longitude (Vogel et al., in review). These gradients are estimated from two satellite products (GOES-16 ABI and CLS) and ECMWF Reanalysis of Meteorological data (ERA5, Hersbach et al., 2020), which agree well over the same spatiotemporal domain. To a lesser extent and solely for purposes of comparison with our observations, we use ERA5 data at 0.25° spatial and hourly temporal resolution for January and February 2020, for surface sensible and latent heat fluxes and vertical profiles of specific humidity and potential temperature.

4.4 Describing the subcloud layer structure and its variability

To conceptualize the subcloud layer we first consider a representation in terms of five scalar variables: height or depth (h), mean potential temperature ($\bar{\theta}$), mean specific humidity (\bar{q}), as well as vertical gradients in potential temperature ($\partial\theta/\partial z$) and specific humidity ($\partial q/\partial z$). We hypothesize that knowing these five variables is sufficient to characterize the subcloud layer and how it varies thermodynamically.

4.4.1 Defining the subcloud layer height

We first ask to what extent the subcloud layer height, h , can be defined from observed thermodynamic profiles. Despite its role as a key vertical length scale, there is no consensus on how to define this height (e.g., Seibert et al., 2000). Different methods applied to a single data set have been shown to yield a wide range of heights (e.g., Liu and Liang, 2010; Beyrich and Leps, 2012; Dai et al., 2014), leading to ambiguity in the fundamental question of the depth of the trade-wind subcloud layer.

To estimate h , we use three subcloud height methods, as described here and in

greater detail in Appendix A. Results are summarized in Table 4.1. The first method estimates the depth over which there is no vertical gradient in a conserved variable within a threshold following Canut et al. (2012). This ‘gradient method’ selects the height where a thermodynamic variable exceeds its mean, averaged over the levels below, by a certain threshold ϵ – that is, that height at which the variable is no longer well-mixed vertically. For instance, for specific humidity, the depth is chosen where $|q(z) - \bar{q}_\rho| \leq \epsilon_q$, where $\bar{q}_\rho = \frac{1}{z} \int_{100}^z q(z) dz$ is updated at each vertical level and computed as the density-weighted mean from 100 m to a depth z . We apply this method to q , θ , and virtual potential temperature, θ_v , a proxy for buoyancy. Empirically, we choose a threshold, ϵ , that is one-third of small-scale variability, estimated as within-day variability from 50–550 m depth. These threshold values for q , θ , and θ_v are 0.35 gkg^{-1} , 0.15 K , and 0.20 K , respectively. The second method, following Holzworth (1964), estimates the level at which a hypothetical rising parcel of near-surface air, representing a thermal, reaches its level of neutral buoyancy, based on a cloud-layer θ_v profile, without any overshoot. The third definition finds the peak in the relative humidity profile, given that relative humidity is expected to maximize at the subcloud layer top if specific humidity is constant and temperature decreases with height.

From this analysis, a conceptual picture emerges of two distinct vertical layers. The first layer is a well-mixed layer in q and θ (Fig. 4-2, Fig. 4-9), which also corresponds to the distribution of relative humidity maxima. Averaging these three height methods gives a mean depth of 555 m (Fig. 4-2a,c). A layer that is well-mixed vertically in q and θ has previously been called the mixed layer (e.g., Malkus, 1958; Augstein et al., 1974), and we adopt this same terminology. The buoyancy variable, θ_v , however, remains better-mixed over a deeper layer, to a mean depth of 708 m averaged between the θ_v -gradient and parcel methods. Such a layer that is better-mixed deeper in θ_v than q and θ individually was observed previously (e.g., Malkus, 1958; Augstein et al., 1974; Nicholls and Lemone, 1980; Yin and Albrecht, 2000). This depth also coincides with the mean lifting condensation level (LCL) of 708 m. Each LCL value is the mean of LCL values calculated for air masses from 50–300 m. Note

that the LCL is calculated from circle- or circling-mean air, which averages subcloud layer air from areas that are in regions of clear skies and in regions where clouds form above. If the LCL is, however, calculated from individual dropsonde soundings, the distribution shifts lower, with the moistest parcels having LCL values that align with the mixed layer top (not shown). Historically, the layer that is better-mixed in θ_v and corresponds to the environmental-mean cloud base or LCL level is often called the subcloud layer (e.g., Malkus, 1958; Augstein et al., 1974; Nicholls and Lemone, 1980; Yin and Albrecht, 2000). Although this naming can be confusing, because clouds already start to form *below* the subcloud layer top, we retain this terminology. This height analysis suggests that there is some ambiguity in the determination of the boundary layer depth.

We associate this ambiguous region between the mixed layer top and subcloud layer top with the transition layer (Malkus, 1958). Such a layer is often found in observations (Augstein et al., 1974; Yin and Albrecht, 2000), is used in simple theoretical modeling approaches (e.g., Albrecht et al., 1979), and emerges in simulations (Stevens et al., 2001), yet the processes that give rise to its structure remain little investigated. Here defined as the difference between the subcloud layer top (θ_v -gradient method) and mixed layer top (q -gradient method), the transition layer has thickness 151 ± 77 m in circle-mean data and 152 ± 50 m in circling-mean data. The mixed layer top and subcloud layer top heights, moreover, vary coherently, with a Pearson correlation coefficient of $r=0.86$. Over this interfacial transition layer, q and θ begin to exhibit vertical gradients, albeit in ways that have compensating effects on buoyancy, so that θ_v gradients are less pronounced (e.g., Nicholls and Lemone, 1980; Betts and Albrecht, 1987; Yin and Albrecht, 2000), as illustrated schematically in Fig. 4-2b). The differing vertical structures of the mixed layer and transition layer suggests that they may be controlled by different physical processes, which is the subject of a future study (Albright et al., 2022, being prepared for publication).

In simple modeling studies, an interpretation arose that the transition layer could be modeled as an infinitely-thin layer with ‘jumps’, or abrupt discontinuities, in analogy with the cloud-free convective boundary layer (e.g., Lilly, 1968; Tennekes, 1973;

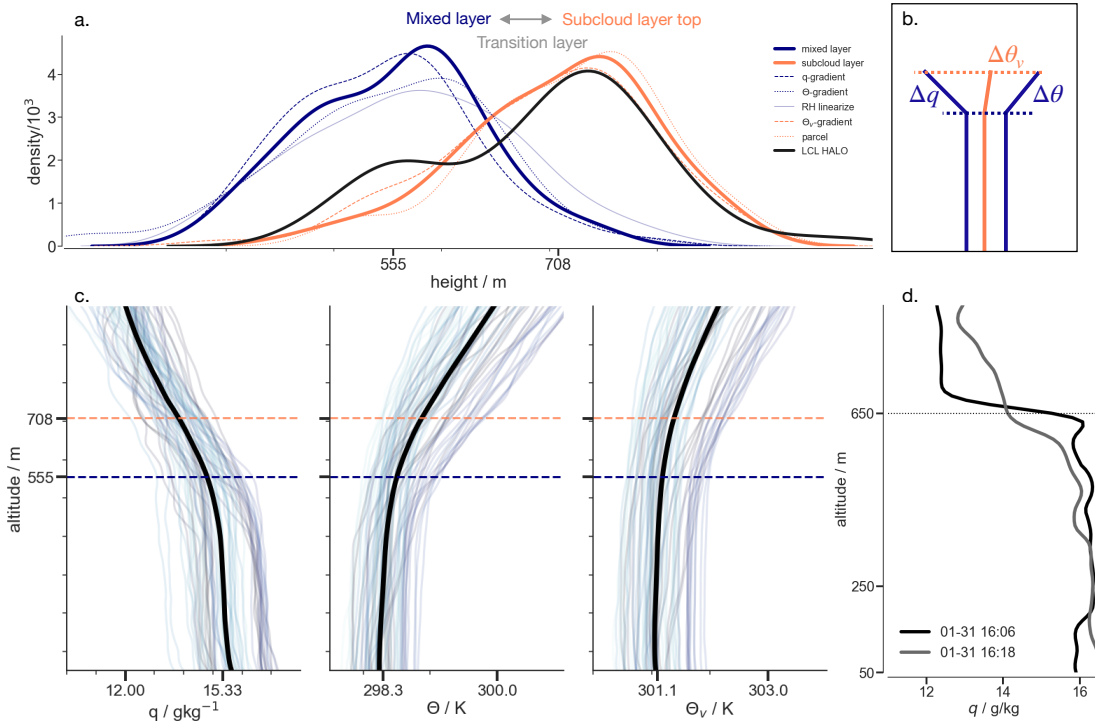


Figure 4-2: (a) Probability distributions from different methods employed to estimate the mixed and subcloud layer heights. We find that three methods based on specific humidity, q , or potential temperature, θ , and relative humidity (blue curves) correspond to the mixed layer top. Two methods using virtual potential temperature, θ_v (the θ_v -gradient method and parcel method, orange profiles) instead correspond to a deeper layer, called the subcloud layer, given its correspondence with the lifting condensation level calculated from environmental-mean air (black). For the mixed layer and subcloud layer top distributions, the thicker line is the mean of distributions calculated using individual height methods. (b) A schematic showing how vertical gradients in q and θ compensate to weaken the vertical gradient in θ_v . (c) 69 circle-mean profiles for q , θ , and θ_v . The black line is the campaign-mean across all profiles, and colored profiles correspond to time (dark to lighter blue over time). Dotted lines mark the mixed layer height and subcloud layer height. The difference between the subcloud layer top and mixed layer top heights indicates the transition layer. (d) Two individual dropsonde profiles: one from January 31, 2020 at 16:06 UTC exhibiting a rare ‘jump-like’ structure (black) and another from January 31, 2020 at 16:18 UTC exhibiting a more typical structure with smoother vertical gradient at the subcloud layer top (grey).

Arakawa and Schubert, 1974; Albrecht et al., 1979; Stevens, 2006). EUREC⁴A measurements do not, however, show the subcloud layer to be a layer defined by a sharp jump or discontinuity at its top, either in aggregated soundings (Fig. 4-2c) or most individual soundings (see one example in Fig. 4-2d). Rarely, in about ten percent of cases, a profile with a sharp jump occurs, such as shown in Fig. 4-2d. The presence of such sharp discontinuities, if rare, does, however, show that smoother profiles are not an artifact of potentially slow dropsonde moisture sensor time responses, and they are instead a physical feature of the atmosphere. The ability of the sondes to measure such sharp profiles is consistent with the manufacturer-stated sensitivities for the Vaisala dropsonde RD41, which have a temperature response time of 0.5 seconds and moisture response time of less than 0.3 seconds at 1000 hPa, 20°C, and the fall speed of the sonde (roughly 6.5 ms⁻¹) (Vaisala, 2022). Indeed, Vömel et al. (2021) show that the new sensors, such as in EUREC⁴A’s RD41 dropsondes, have rapid time constants and do not require time-lag corrections at the warmer temperatures in the lowest kilometers of the atmosphere. A comparison of dropsonde moisture profiles with higher-frequency (1 Hz) moisture measurements from the ATR-42 (not shown) further supports this inference that smooth vertical gradients are not an artifact of slow sensor response times.

The presence of a finite-thickness transition layer introduces ambiguity in the application of the mixed layer theory, whose entrainment closures are based upon a canonical jump-like structure at the subcloud layer top. We address this uncertainty through the introduction of effective parameters estimated through a Bayesian approach, as described in Sec. 4.5.3.

4.4.2 Evidence that vertical thermodynamic gradients are small

Another key assumption in mixed layer theory is that subcloud layer thermodynamic variables can be represented by a single vertically well-mixed value. To test this assumption, we compare the magnitude of vertical gradients relative to variability about vertically-averaged mean values across soundings. We do this in two steps. We first calculate the root mean square error (RMSE) from assuming a vertical, perfectly

well-mixed profile relative to the observed profile up to the mixed layer top. Second, this RMSE is compared with the standard deviation, σ , calculated for all mixed-layer mean values over the campaign (from circle-mean data), as the fractional difference $\left[\frac{\sigma - RMSE}{\sigma}\right] \times 100$. A perfectly well-mixed layer would have values of 100%, and values near 100% indicate that the vertical variability about the mean for a particular sonde is much smaller than the variability among sondes. For q , the fractional difference is $83 \pm 3.2\%$ across circle-mean data, with the values denoting the mean and standard deviation. Similarly, the fractional difference for potential temperature is $76 \pm 6.0\%$, with the smaller value for potential temperature resulting from its smaller variability about the mean value. Fig. 4-9 also illustrates that what we call the mixed layer is indeed well-mixed vertically – with notable exceptions on January 24, 2020 (panels c.,d.), and February 7, 2020 (panels o.,p.), identified as having many cold pools (Touzé-Peiffer et al., 2022), which are expected to cause deviations away from a well-mixed profile. On this basis, we infer that vertical gradients are small and provide initial justification for their omission from the mixed layer description. *A posteriori* support for this conclusion is provided by additional analysis in Sec. 4.6.

Beyond the magnitude of vertical gradients, another question is the extent to which variability in vertical gradients encodes differences in variability among subcloud layers. We find that rank correlations (Kendall and Spearman) and Pearson correlations of $\partial\theta/\partial z$ and $\partial q/\partial z$ with h , $\bar{\theta}$, and \bar{q} are below 0.3, suggesting that the strength of vertical gradients does not strongly differentiate subcloud layers.

4.4.3 Moisture variability is the primary mode of subcloud layer thermodynamic variability

We find that the subcloud layer varies thermodynamically primarily through variability in \bar{q} , and this moisture variability controls nearly all variability in subcloud layer moist static energy (MSE), with a correlation coefficient $r = 0.99$ between \bar{q} and mean subcloud layer MSE. MSE is defined as $c_p T + \ell_v q + gz$ where c_p is the specific heat at constant pressure, T is the absolute pressure in Kelvin, ℓ_v is the specific enthalpy of

vaporization, q is the water vapor specific humidity, g is the gravitational constant, and z is height above the surface. The height of the subcloud layer is defined using the θ_v -gradient method, and subcloud layer means, \bar{q} and $\bar{\theta}$, are defined as the density-weighted means from 50 m to this height.

One way to compare variability in \bar{q} and $\bar{\theta}$ is by diagnosing their contribution to variability in vertical length-scales. In the circle-mean aggregated data, anomalies in \bar{q} relative to the campaign-mean have a Pearson correlation coefficient $r=-0.71$ with h anomalies and $r=-0.97$ with anomalies in the LCL, showing that variability in different vertical heights is strongly associated with \bar{q} variability. Anomalies in $\bar{\theta}$, by contrast, have a Pearson correlation coefficient of only -0.5 with anomalies in the LCL and -0.24 with h anomalies. Warmer temperatures are also associated with increased humidity, which would lower the LCL, so the weak anticorrelation with potential temperature variability could reflect the compensating effects of temperature and humidity on the LCL.

Continuous ERA5 data, which are found to vary coherently with observations despite a dry bias in moisture (see Fig. 4-3a and Bock et al. (2021)), allow for estimating other modes of thermodynamic variability. ERA5 assimilated EUREC⁴A dropsonde and radiosondes, although ongoing analysis of winds shows that the assimilation of local soundings did not strongly influence the reanalysis (Geet George, personal communication). From these continuous ERA5 data, we find the \bar{q} signal, averaged for the same about 220 km-diameter circular domain as the observations (Fig. 4-1), decorrelates after approximately two days, with an autocorrelation coefficient that decreases from 0.98 after one hour to 0.19 after 48 hours (Fig. 4-3d). That moisture is mostly decorrelated after two days aligns well with the mean gap of two days between EUREC⁴A flights, indicating that the research flights sample independent realizations of synoptic moisture variability. The 10 m wind speed is highly autocorrelated, with an autocorrelation coefficient of 0.74 after two days and 0.48 after 8 days (Fig. 4-3d). The wind speed signal decorrelates after ten days with $r=0.04$, demonstrating the dominance of lower-frequency surface wind speed variability.

Another way of analyzing thermodynamic variability is performing fast Fourier

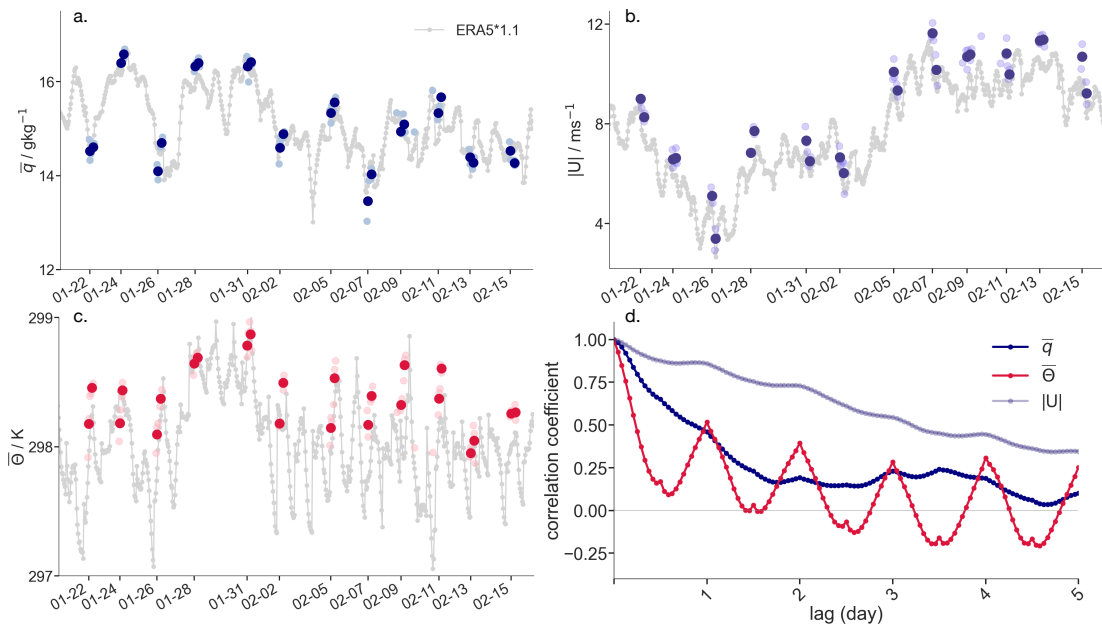


Figure 4-3: Evolution of (a.) subcloud layer mean specific humidity, \bar{q} , (b.) 10 m wind speed, and (c.) subcloud layer mean potential temperature, $\bar{\theta}$ for circle-mean data (lighter circle) and circling-mean data (darker circle), compared with hourly ERA5 data (light grey). Note that ERA5 moisture displays a dry bias (Bock et al., 2021), and here ERA5 specific humidity is multiplied by a factor 1.1. Panel d. shows the autocorrelation coefficients at various time lags calculated from hourly ERA5 data for \bar{q} and $\bar{\theta}$, interpolated to the same heights as the *in situ* data, and the 10 m wind speed.

transformations. The fast Fourier transformation of $\bar{\theta}$ has a strong peak in the power spectral density at a 24-hour frequency, whereas a diurnal signal is not seen in \bar{q} (not shown). Variability in $\bar{\theta}$ is smaller in magnitude (Fig. 4-3c) and appears to be largely diurnal, potentially driven by variability in shortwave radiative heating (Albright et al., 2021a).

4.5 Mixed layer theory for subcloud layer moisture and heat

We first introduce the mixed layer theory framework (Sec. 4.5.1). An important assumption in this theory is that the subcloud layer is well-mixed, which was shown to be the case, at least below the transition layer base (Sec. 4.4.2). The existence of a finite-depth transition layer and its vertical gradients, however, introduces challenges into the application of mixed layer theory, particularly its assumption that the interface between the subcloud layer and cloud layer is vanishingly thin (e.g., Lilly, 1968; Stevens, 2006). EUREC⁴A observations allow us to test the adequacy of this interpretive framework despite the presence of the finite-thickness transition layer.

4.5.1 Theory and closure assumptions

For a subcloud layer scalar, ϑ , after performing a Reynolds decomposition on the conservation equation ($\frac{D\vartheta}{Dt} = Q_\vartheta$, where Q_ϑ is a diabatic source term) and integrating over the depth of the layer, the mixed layer budget of ϑ can be written as,

$$hS_\vartheta = \overline{w'\vartheta'}\Big|_0 - \overline{w'\vartheta'}\Big|_1. \quad (4.1)$$

We neglect the horizontal gradients in $\overline{w'\vartheta'}$, which are small compared to the vertical gradients. S_ϑ includes the contribution of the mean flow to the material derivative, as well as the diabatic source term, Q_ϑ . This diabatic source term Q_ϑ can include radiation or precipitation and evaporation effects, but we set $Q_q = 0$ for moisture, neglecting the influence of evaporating precipitation on the subcloud layer moisture

	units	mean	1 s.d.
h(ML)	m	555	79.0
h(SC)	m	708	83.6
h(LCL)	m	694	105
Δ h(TL)	m	152	50
q_s	gkg^{-1}	22.59	0.189
\bar{q}_{ML}	gkg^{-1}	15.3	0.886
\bar{q}_{SC}	gkg^{-1}	15.1	0.883
SST	K	300.0	0.169
θ_s	K	299.2	0.260
$\bar{\theta}_{\text{ML}}$	K	298.3	0.235
$\bar{\theta}_{\text{SC}}$	K	298.4	0.253
U	m s^{-1}	8.46	2.19
$\partial q/\partial z$ (ML)	$\text{gkg}^{-1}\text{km}^{-1}$	-1.06	0.293
$\partial q/\partial z$ (TL)	$\text{gkg}^{-1}\text{km}^{-1}$	-6.69	2.11
$\partial\theta/\partial z$ (ML)	K km^{-1}	0.424	0.291
$\partial\theta/\partial z$ (TL)	K km^{-1}	2.49	0.644
$\partial\theta_v/\partial z$ (ML)	K km^{-1}	0.233	0.247
$\partial\theta_v/\partial z$ (TL)	K km^{-1}	1.30	0.324

Table 4.1: Campaign-mean and standard deviation of different terms as calculated from the 24 circling-mean data (three-hourly timescale) located in the ‘EUREC⁴A circle’. Various heights are given: h(ML) is the mixed layer top height, h(SC) is the subcloud layer top height, h(LCL) is the lifting condensation level, and Δ h(TL) is the thickness of the transition layer, defined as the difference between the subcloud layer and mixed layer tops. The subscript ‘s’ refers to the surface, and ‘ML’ and ‘SC’ refer to the mixed layer and subcloud layer. The sea surface temperature (SST) values include the cool-skin approximation adjustment – that is, they include the 0.25 K subtracted from R/V Meteor SSTs. U refers to the wind speed at 10 m. Vertical gradients are expressed per kilometer.

budget, but we do account for radiation in the heat budget ($Q_\theta \neq 0$). The equation expresses that the vertical divergence of the turbulent flux balances the sum of the non-turbulent processes, denoted by S_ϑ (e.g., Betts, 1976; Stevens, 2006). The thickness of the layer is h . The subscript 0 denotes values at the lower interface of the bulk layer (ocean-to-subcloud layer interface), and the subscript 1 denotes values at the upper interface (the subcloud-to-cloud layer interface), and w refers to the vertical velocity.

The flux at an interface, i , is given as the product of the velocity relative to the mean flow and a ‘jump’,

$$\overline{w'\vartheta'}|_i = -V_i\Delta_i\vartheta, \quad (4.2)$$

where $\Delta_i\vartheta$ defines the change in ϑ across the interface, from top to bottom, so that $\Delta_1\vartheta = \vartheta_1 - \bar{\vartheta}$ and $\Delta_0\vartheta = \bar{\vartheta} - \vartheta_0$.

With this notation, we can rewrite Eq. (4.1) as,

$$hS_\vartheta = -V_0\Delta_0\vartheta + V_1\Delta_1\vartheta. \quad (4.3)$$

The first term on the right-hand side, $V_0\Delta_0\vartheta$, defines a surface flux wherein the surface exchange velocity, V_0 , denotes the product of the 10 m horizontal wind speed, U (wherein easterly is defined as negative), and a dimensionless parameter, C_d , following surface layer similarity theory (e.g., Stevens, 2006). Note that $-V_0\Delta_0\vartheta$ is positive when surface values are larger than subcloud layer values, which is almost always the case for potential temperature and specific humidity. The dimensionless parameter, C_d , depends on the surface roughness, the structure of the surface layer, and the stability of this layer but is generally taken to be constant and equal to 0.0011 (e.g., Deardorff, 1972; Fairall et al., 2003). In this analysis, we set $C_d = 0.0010$. Our smaller value compensates for the larger difference between the surface and subcloud layer values, compared to the typical difference taken between the surface and 20 m value (e.g., Fairall et al., 2003).

Entrainment closure

V_1 in Eq. (4.3) represents the diabatic growth of the subcloud layer into the overlying fluid and is taken to equal the entrainment rate, E (e.g., Stevens, 2006). The fundamental processes controlling entrainment remain poorly understood and represented (e.g., Fedorovich et al., 2004; Canut et al., 2012). The most basic approach, proposed by Lilly (1968), is to represent the turbulent entrainment flux at the subcloud layer top as a fixed fraction of the surface turbulent flux,

$$E = -\frac{AV_0\Delta_0\theta_v}{\Delta_1\theta_v}. \quad (4.4)$$

This closure is known as the ‘zero-order jump model’ for E , as the jump occurs over a transition layer of zero thickness. A zero-order jump model is made in analogy with the sharp discontinuity seen in stratocumulus mixed layers (e.g., Lilly, 1968; Deardorff, 1972) and dry convective boundary layers (e.g., Tennekes, 1973; Stull, 1976).

The constant A defines the entrainment ‘efficiency’ and varies between 0 and 1. The end member of $A = 0$ refers to total frictional dissipation of the surface buoyancy flux and no entrainment at the layer-top, whereas $A = 1$ refers to zero frictional dissipation, and the entire surface buoyancy flux being available for entrainment (Lilly, 1968). The jump, $\Delta_1\theta_v$, is positive and models the resistance that entrainment feels when tasked with mixing a relatively more buoyant fluid into the turbulent layer.

As discussed in Sec. 4.4.1, the subcloud layer is not, except in rare cases, characterized by such a zero-order jump structure and instead exhibits vertical gradients over a finite depth. Such vertical gradients over a finite thickness are consistent with finite-thickness entrainment zones seen in large-eddy simulations, in what is often called a first-order jump model (e.g., Vanzanten et al., 1999; Canut et al., 2012). The zero- and first-order jump models are contrasted schematically in Fig. 4-4.

We attempt to accommodate the ambiguity from the transition layer by introducing coefficients, C_q and C_θ , which scale jumps at the top of the layer and compensate for possible errors in our choice of the subcloud layer height, h , and uncertainty in the

depth over which the jumps are computed. The scaling coefficient approach is similar to the linear mixing-line model that represents cloud layer air mixing into the mixed layer (Betts and Ridgway, 1989). Whereas our formulation is similar to the ‘transfer coefficient’ approach in Neggers et al. (2006) and Zheng (2019), these studies take differences between values in the free troposphere and the subcloud layer, whereas we consider values across the transition layer. The jumps $\Delta_1 q$, $\Delta_1 \theta$, and $\Delta_1 \theta_v$ are formulated as,

$$\Delta_1 q = C_q(q_{h+} - \bar{q}_{|h-}) \quad (4.5)$$

$$\Delta_1 \theta = C_\theta(\theta_{h+} - \bar{\theta}_{|h-}) \quad (4.6)$$

$$\Delta_1 \theta_v = \Delta_1 \theta + 0.61(\bar{\theta} \Delta_1 q + \bar{q} \Delta_1 \theta) \quad (4.7)$$

The subscript $h+$ refers to the value of q or θ above h , computed as the average from h to $h + 100$ m. $\bar{q}_{|h-}$ or $\bar{\theta}_{|h-}$ are averages from 50 m to the mixed layer top defined from the linearized relative humidity method (see Appendix A), though it is insensitive to defining the mixed layer top using other methods. The choice of averaging up to the mixed layer top, rather than up to h , to calculate these jumps is motivated by the desire to exclude transition layer air in the average. Due to sub-circling variability in h , excluding transition layer air can best be achieved by a conservative (and therefore lower-altitude) choice of averaging height. The choice of averaging from $h + 100$ m is to reduce small-scale variability associated with values at a single altitude. The ultimate magnitude of the entrainment *fluxes* or residuals in the budgets are not affected by selecting values at h , or averaging up to 50 m, 100 m, or 150 m above h , though it does influence the relative magnitudes of the entrainment rate, E , compared to the jumps. Ultimately the budget analysis depends on the product of E times the jump, and so defining the jump over a larger layer increases the jump and decreases E .

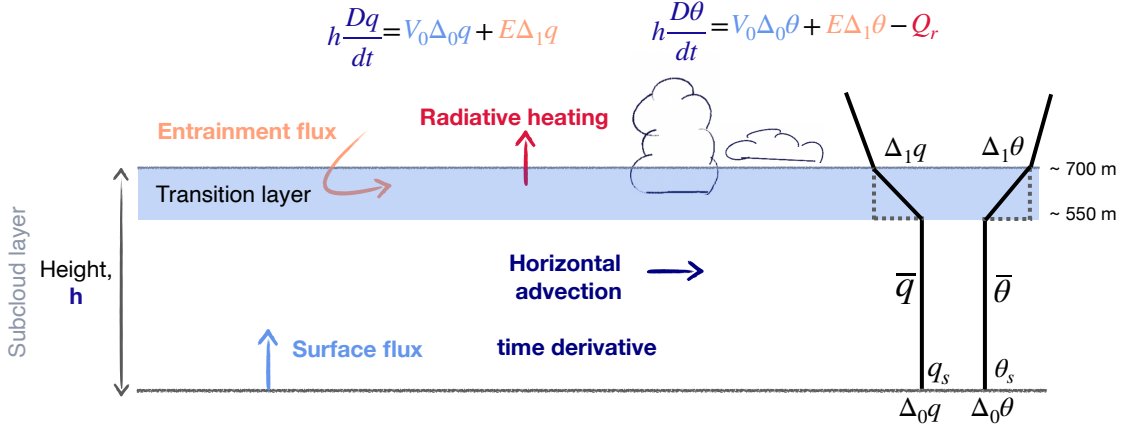


Figure 4-4: Schematic of subcloud layer budgets, as described in Eq. (4.8) and Eq. (4.9). Descriptions of the surface fluxes ($V_0\Delta_0\vartheta$), entrainment fluxes ($E\Delta_1\vartheta$), material derivatives ($\frac{D\vartheta}{dt}$), and clear-sky radiative heating term (Q_r) are given in Sec. 4b and Sec. 4c. The height h refers to the depth of the subcloud layer, which includes both a well-mixed layer and a transition layer. Also shown are idealized profiles of specific humidity, q , and potential temperature, θ in keeping with the zero-order jump model (dotted lines) and the first-order model, similar to what is done in this study (solid lines).

Budget equations for subcloud layer moisture and heat balances

Combining these assumptions, the budget for Eq. (4.1) for specific humidity, \bar{q} , is,

$$h \left[\frac{\partial \bar{q}}{\partial t} + (\bar{\vec{u}} \cdot \nabla \bar{q}) \right] = -C_d U \Delta_0 q - \frac{A_e V_0 \Delta_0 \theta_v}{\Delta_1 \theta_v} \Delta_1 q. \quad (4.8)$$

The \bar{q} balance is between a surface latent heat flux, $-C_d U \Delta_0 q$, which moistens the layer from a saturated ocean surface moisture source, q_s , wherein $\Delta_0 q = \bar{q} - q_s < 0$; an entrainment flux, $-\frac{A_e V_0 \Delta_0 \theta_v}{\Delta_1 \theta_v} \Delta_1 q$, which imports drier cloud layer air into the subcloud layer, wherein E is defined in Eq. (4.4) and $\Delta_1 q < 0$; and large-scale horizontal advection, $\bar{\vec{u}} \cdot \nabla \bar{q}$ and a time-derivative, $\frac{\partial \bar{q}}{\partial t}$, both of which can either moisten or dry the subcloud layer. We neglect phase changes, such as associated with evaporating precipitation within the subcloud layer.

For subcloud layer mean potential temperature, $\bar{\theta}$, the budget equation is,

$$h \left[\frac{\partial \bar{\theta}}{\partial t} + (\bar{\vec{u}} \cdot \nabla \bar{\theta}) \right] = -C_d U \Delta_0 \theta - \frac{A_e V_0 \Delta_0 \theta_v}{\Delta_1 \theta_v} \Delta_1 \theta + h Q_r. \quad (4.9)$$

Eq. (4.9) includes a surface sensible heat flux, $-C_d U \Delta_0 \theta$, which warms the subcloud layer given $\Delta_0 \theta = \bar{\theta} - \theta_s < 0$; an entrainment flux $\frac{-A_e V_0 \Delta_0 \theta_v}{\Delta_1 \theta_v} \Delta_1 \theta$, which brings warmer cloud layer air into the subcloud layer; large-scale horizontal advection $\vec{u} \cdot \nabla \bar{\theta}$, which could either warm or cool the layer; a time-derivative $\frac{\partial \bar{\theta}}{\partial t}$, which is predominantly associated with the diurnal cycle; and a clear-sky radiative heating term Q_r , another cooling term. We again neglect phase changes, such as evaporating precipitation. This heat balance is more difficult to constrain, both because it involves more terms and because the magnitude of individual terms is smaller. Also note that these kinematic fluxes can be converted to dynamic fluxes by multiplying by the air density, ρ , and ℓ_v for specific humidity, and air density and c_p for potential temperature.

The processes in the \bar{q} budget (Eq. (4.8)) and $\bar{\theta}$ budget (Eq. (4.9)) are illustrated schematically in Fig. 4-4.

4.5.2 Observational estimates of terms in mixed layer theory budgets

Here we describe how the different terms in Eq. (4.8) and Eq. (4.9) are calculated from observations, except for entrainment, which is the focus of Sec. 4.5.3. Clear-sky, aerosol-free radiative heating profiles for EUREC⁴A dropsondes and radiosonde profiles are calculated in Albright et al. (2021a). Large-scale horizontal moisture advection, $\vec{u} \cdot \nabla \bar{q}$, and potential temperature advection, $\vec{u} \cdot \nabla \bar{\theta}$, are calculated in George et al. (2021) using the regression method from Bony and Stevens (2019). We estimate the time derivatives or storage terms, $\frac{\partial \bar{q}}{\partial t}$ and $\frac{\partial \bar{\theta}}{\partial t}$, as the ordinary least squares regression slope of the three circle-means per circling-mean. Estimating this derivative as the regression slope for the approximately 30–36 individual soundings per circling yields similar results ($r=0.82$), yet these soundings are more affected by small-scale variability than are circle-means. For uncertainty estimates, we calculate the standard error of the three circle-mean data per circling-mean for all terms in Eq. (4.8) and Eq. (4.9), except for uncertainty on the time-derivative, which we take to be the standard error on the regression slope.

	units	mean	1 s.d.
F_q bulk, dropsondes	Wm^{-2}	166	56
F_q bulk, Meteor	Wm^{-2}	165	48
F_q COARE, dropsondes	Wm^{-2}	162	45
F_q ERA5	Wm^{-2}	178	49
F_θ bulk, dropsondes	Wm^{-2}	6.3	2.7
F_θ bulk, Meteor	Wm^{-2}	6.5	3.8
F_θ COARE, dropsondes	Wm^{-2}	6.0	6.1
F_θ ERA5	Wm^{-2}	10	4.5
E	mm s^{-1}	20.4	7.9
A_e	-	0.43	0.056
C_q	-	1.26	0.34
C_θ	-	1.15	0.31
$\Delta_1 q = C_q(q_{h+} - \bar{q}_{ h-})$	gkg^{-1}	-2.32	0.597
$\Delta_1 \theta = C_\theta(\theta_{h+} - \bar{\theta}_{ h-})$	K	0.782	0.115
$\Delta \theta_v$	K	0.359	0.0297
$E\Delta q$	Wm^{-2}	-128	52.8
$E\Delta \theta$	Wm^{-2}	18.0	6.47
$\overline{\vec{u} \cdot \nabla q}$	$\text{gkg}^{-1}\text{ms}^{-1}$	1.59×10^{-5}	2.12×10^{-5}
$\overline{\vec{u} \cdot \nabla \theta}$	K ms^{-1}	8.51×10^{-3}	8.46×10^{-3}
$Q_{\text{rad,clr}}$	K d^{-1}	-0.853	1.01

Table 4.2: Campaign-mean and standard deviation of different terms as calculated from the 24 circling-mean data (about three-hourly timescale) averaged along the ‘EUREC⁴A circle’ for surface latent and sensible heat fluxes, entrainment fluxes, horizontal advection terms, and net radiative heating. A_e , are from the Bayesian inversion, and the effective jumps are calculated by from Eq. (4.5) and Eq. (4.6) using the mean values of C_q and C_θ . For the surface flux terms, bulk refers to bulk theory formulations, Meteor refers to measurements from the R/V Meteor instead of dropsondes, and COARE refers to the COARE algorithm. Horizontal advection and net radiative heating are values averaged over the subcloud layer depth.

Surface fluxes

Bulk estimates of surface fluxes are calculated as $-C_d U \Delta_0 \vartheta$ (Eq. 4.14 and Eq. 4.15). The difference $\Delta_0 \vartheta$ is taken between the mixed layer mean and surface value and is negative, yielding positive surface fluxes. Estimates are $6.3 \pm 2.7 \text{ Wm}^{-2}$ for the sensible heat flux and $166 \pm 54 \text{ Wm}^{-2}$ for the latent heat flux, with the notation denoting the mean and standard deviation. For the sensible heat fluxes, we subtract 0.25 K from Meteor sea temperatures measured at few-meter depth to account for the ‘cool skin’ effect that sea surface temperatures at the surface are cooler than at few-meter depth (e.g., Fairall et al., 2003). The bulk estimates of surface sensible and latent heat fluxes agree well, both in terms of magnitude and variability, with three alternative, but co-located estimates of these fluxes: bulk estimates from the R/V Meteor, fluxes calculated with the COARE algorithm (Fairall et al., 2003) using HALO dropsonde data, and ERA5 surface fluxes (Table 4.2). Pearson correlation coefficients of our bulk sensible heat flux estimates are $r=0.81$, 0.82 , and 0.72 with these three estimates, respectively. For the latent heat fluxes, the correlations are $r=0.84$, 0.92 , and 0.95 , respectively. These flux values are consistent with climatological values, for instance as shown by Yu et al. (2004) and Bigorre and Plueddemann (2021) (about $160\text{--}170 \text{ Wm}^{-2}$ for the latent heat flux and $6\text{--}8 \text{ Wm}^{-2}$ for the sensible heat flux) with differences being consistent with sampling errors associated with the observations being made for slightly different locations or time periods.

The surface turbulent flux, F_{θ_v} , which is used to compute E , is defined as $F_{\theta_v} = F_{\theta} + 0.608 \bar{\theta} F_q$, wherein 0.608 is a thermodynamic constant that relates the molecular weight of water relative to that of dry air. F_{θ_v} relates to surface buoyancy flux by a factor $\frac{g}{\bar{\theta}}$, which then denotes the time rate of change of turbulent kinetic energy production. F_{θ_v} fluxes estimated from mixed layer theory or bulk methods are $16 \pm 5.2 \text{ Wm}^{-2}$, which agree well with the three other surface flux estimates in magnitude and variability, with correlation coefficients around $r=0.9$.

4.5.3 Bayesian inversion of uncertain terms in entrainment fluxes

The most uncertain terms in Eq. (4.8) and Eq. (4.9) relate to the entrainment fluxes: the effective entrainment efficiency, A_e , and the scaling parameters for the jumps, C_q and C_θ . The entrainment exchange velocity, E (Eq. (4.4)), and fluxes at the subcloud layer top have long been challenging to measure observationally (e.g., Lenschow et al., 1999; Kawa and Pearson Jr, 1989; Stevens et al., 2003b) or estimate from simulations (e.g., Moeng et al., 1999; Bretherton et al., 1999; Vogel et al., 2020).

There are a lack of foregoing constraints on these jumps, and from the trade-wind observations, there are ambiguities associated with how to define the jumps at the upper interface (Fig. 4-2c). Given these uncertainties, we constrain the parameters, $\Theta = \{A_e, C_q, C_\theta\}$, using a Bayesian framework. This approach allows for estimating a joint distribution of parameters, Θ , that are most likely to explain the observed data. The values of C_q , C_θ , and A_e should be physical, and synoptic variability should be explained without having to vary these parameters.

The Bayesian approach is similar to other optimization techniques, yet it yields joint posterior distributions and thus provides an estimate of uncertainty for the constrained parameters. Following Bayes rules, we invert for the joint posterior distribution of Θ ,

$$P(\Theta | y_{\text{obs}}) \propto P(y_{\text{obs}} | \Theta) \cdot P(\Theta). \quad (4.10)$$

Sampled sets of parameter values, Θ , are used with observed estimates of the other terms to model subcloud layer moisture and temperature budgets, y_{obs} , following Eq. (4.8) and Eq. (4.9). We model the likelihood, $P(y_{\text{obs}} | \Theta)$, such that the residuals of the subcloud layer moisture and heat budgets are normally distributed around zero with standard deviations σ_q and σ_θ , respectively. The likelihood $P(y_{\text{obs}} | \Theta)$ is thus formulated based on the multivariate Gaussian distribution of the modeled subcloud layer moisture and temperature budgets,

$$P(y_{\text{obs}} | \Theta) \sim N(0, \Sigma^2(\Theta)). \quad (4.11)$$

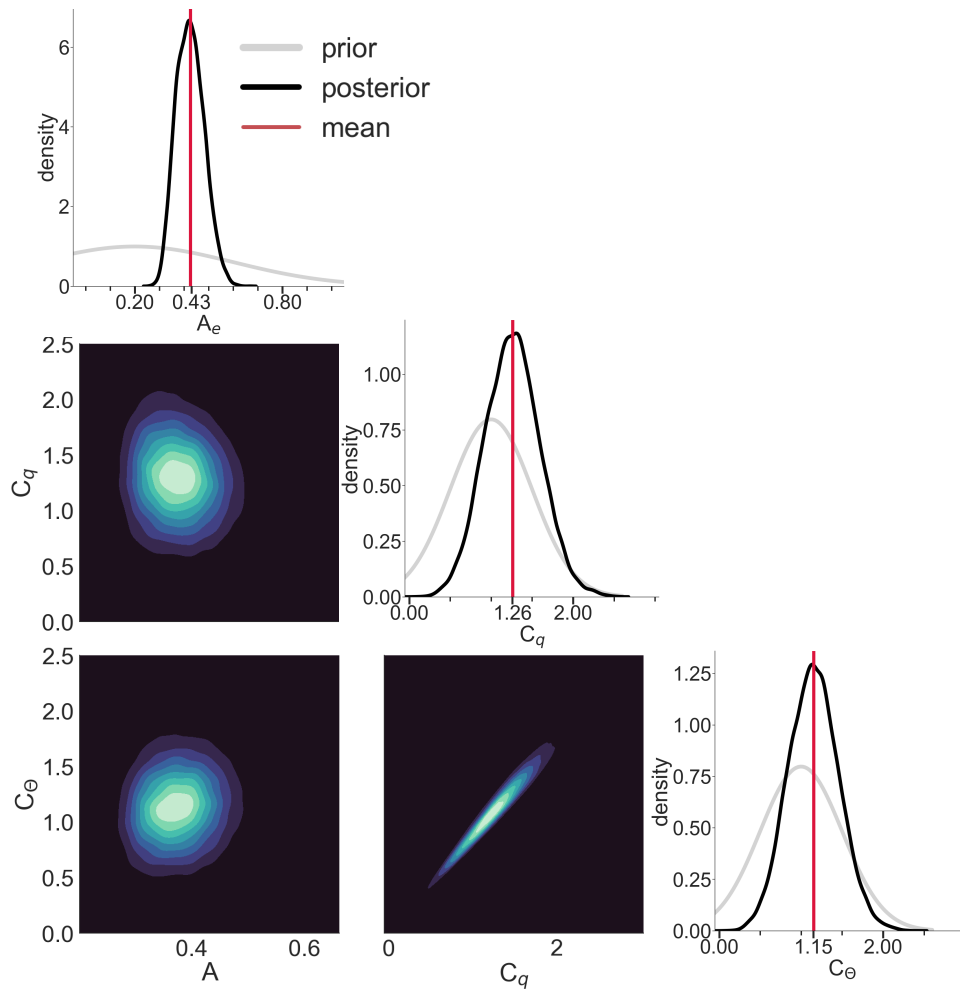


Figure 4-5: Joint posterior distributions for the uncertain entrainment parameters A_e , C_q , and C_θ , with lighter colors referring to more frequently sampled parameter combinations. For the marginal posterior distributions (black), the marginal prior distribution (grey), and mean of the posterior distribution (red) are also shown.

$$\Sigma^2(\Theta) = \begin{bmatrix} \sigma_q^2 & 0 \\ 0 & \sigma_\theta^2 \end{bmatrix}. \quad (4.12)$$

This likelihood expresses the probability of closing the moisture and heat budgets, or jointly obtaining residuals normally-distributed around zero for both budgets given parameters Θ . We set the off-diagonal terms to zero in Eq. (4.12), meaning that there is no covariance between residuals in the moisture and heat budget. We assume a standard deviation σ_q of $1 \times 10^{-8} \text{ kgkg}^{-1}\text{s}^{-1}$, or 17 Wm^{-2} when converted from a kinematic to dynamic flux. For potential temperature, the standard deviation σ_θ is chosen to be $3 \times 10^{-6} \text{ Ks}^{-1}$ or 2.5 Wm^{-2} , though our results are insensitive to these choices. The posterior distribution, $P(\Theta | y_{\text{obs}})$, then represents the distribution of parameter values that are most likely to close the budgets given observed variability.

For the prior distribution $P(\Theta)$ on A_e , we choose a normal prior with mean of 0.2 and standard deviation 0.4, $\mathcal{N}(0.2, 0.4^2)$. A common view of A_e is the ratio of minimum to maximum buoyancy fluxes, when assuming that the minimum buoyancy flux occurs at the subcloud layer top, and that the transition from the negative, minimum to zero buoyancy flux occurs over an infinitely thin layer. Its value is often taken to be 0.2 (Lilly, 1968; Stull, 1976; Tennekes and Driedonks, 1981; Driedonks, 1982; Pino et al., 2003), motivating our choice of normal prior with mean 0.2. Assuming that the source of entrainment is surface buoyancy fluxes (rather than other processes, such as radiative cooling, or evaporative cooling by clouds as in Stevens (2007)), a value of A_e greater than one is energetically inconsistent with our assumptions. Obtaining a posterior distribution of A_e that does not exceed one serves as a physical test of the model. For the scaling parameters, we model the prior distributions for C_q and C_θ as a normal distribution with mean 1 and standard deviation of 0.5.

Sampling is performed using the Metropolis-Hastings algorithm (Metropolis et al., 1953; Hastings, 1970), and we run the model for 60,000 samples, four times (four ‘chains’), though results converge after 30,000 samples. The first 10,000 samples are discarded for each chain, yielding 200,000 samples. Results are consistent among chains, indicating that our model is adequately sampled.

Bayesian inversion results

Notably, the entrainment efficiency, A_e , is well-constrained by the Bayesian inversion and has a maximum likelihood estimate (MLE) posterior value of 0.43 and a 5–95% credible interval of 0.34 – 0.53 (Fig. 4-5). Its marginal posterior distribution is similar regardless of the prior distribution. A_e being larger than 0.2 is consistent with it being an effective parameter that reflects the existence of a finitely-thick transition layer, as previously discussed. Using Sahelian convective boundary layer observations, Canut et al. (2012) also found evidence for an entrainment efficiency larger than 0.2 given a finite-thickness entrainment zone, though in their case wind shear over the entrainment zone contributed to a larger value. Wind shear over the transition layer is, however, small during EUREC⁴A (cf. Fig. 4-10). Whether or not this value of A_e is consistent with direct numerical simulation (Garcia and Mellado, 2014) and large-eddy simulation (Fedorovich et al., 2004) of the convective boundary layer, which suggest values closer to 0.2, is unclear. A larger value of A_e , as in the case of Vanzanten et al. (1999), may result from how we define the jumps and the depth of the layer, whose values are greater than those in idealized LES (as discussed by Fedorovich et al. (2004)). $A_e > 0.2$ could also be indicative of cloud processes within the transition layer contributing to the mixing (cf. Stevens (2007)), an idea we are exploring further in a separate study.

The mean posterior value of C_q is 1.26 with a 5-95% credible interval of 0.74–1.89. The mean posterior value of C_θ is 1.15 with a 5-95% credible interval of 0.65–1.66 (Fig. 4-5). We multiply the mean posterior values of the transfer coefficients by the time-varying values of Δq and $\Delta\theta$ (calculated following Eq. (4.5) and Eq. (4.6)) to obtain specific humidity and potential temperature jumps used to calculate the entrainment flux. The strong covariance between C_q and C_θ , with a Pearson correlation coefficient of $r=0.97$, suggests that the same subcloud layer eddies mix moisture and heat, consistent with physical expectation, and that knowing either C_q or C_θ appears sufficient for scaling the jumps. That the parameters constrained by the Bayesian inversion are physical – namely, an $0.2 < A_e \leq 1$ and scaling coefficients that strongly

covary – acts as a first validation of mixed layer theory.

Our entrainment rates are $20.4 \pm 7.9 \text{ mm s}^{-1}$, with values denoting the mean and standard deviation (Table 4.2). Similar to the surface fluxes, making a direct quantitative comparison with previous studies is difficult given that different regimes are sampled, such as a trade-wind or stratocumulus boundary layer, as well as different vertical levels (e.g., cloud-top versus cloud-base). There are a number of foregoing estimates of cloud-*top* entrainment rates in stratocumulus regimes: during the DYCOMS-II field study southwest of California, Stevens et al. (2003a) find values $3.9 \pm 1 \text{ mm s}^{-1}$; also using *in situ* data but in the southeast Pacific, Caldwell et al. (2005) estimate rates of $4 \pm 1 \text{ mm s}^{-1}$; using satellite measurements for a transect from 35° to 15° N, Kalmus et al. (2014) estimate $3.5 \pm 1.5 \text{ mm s}^{-1}$; and using *in situ* observations from the MAGIC field campaign between California and Hawaii, Ghate et al. (2019) estimated cloud-top entrainment rates of $7.83 \pm 5.23 \text{ mm s}^{-1}$ in closed cellular stratocumulus cloud conditions. The larger entrainment rates during EUREC⁴A are plausible considering the much weaker stability of the capping layer compared to stratocumulus regimes. In the Sahelian boundary layer, Canut et al. (2012) estimate a large range of cloud-top entrainment rates from about 10–150 mm s^{-1} (their Figures 10, 11). In large-eddy simulations of trade-wind regions, Vogel et al. (2020) find a mean entrainment rates of 14 mm s^{-1} , with lower values compared to observed EUREC⁴A values likely due to the coarser vertical resolution leading to a larger $\Delta\theta_v$ -jump.

Justification for larger entrainment efficiency, A_e , from theory

Before presenting the resulting budgets, we present two expository examples that contextualize the larger effective entrainment parameter, A_e , from the Bayesian inversion that accounts for a finitely-thick transition layer.

First, performing a Reynolds decomposition on the conservation equation, $\frac{D\vartheta}{Dt} = Q_\vartheta$, and integrating over a layer above and below h from $h_+ = h + \epsilon$ to $h_- = h - \epsilon$ for

some small ϵ yields an expression for E , wherein θ_{v+} is the value at h_+ , and $\delta h = 2\epsilon$,

$$E = \frac{-AV_0\Delta_0\theta_v}{\Delta_1\theta_v} + \frac{\delta h}{2\Delta_1\theta_v} \left(\frac{d\bar{\theta}_v}{dt} + \frac{d\theta_{v+}}{dt} \right). \quad (4.13)$$

The derivation for Eq. (4.13) is given in Appendix C. Setting Eq. (4.4) and Eq. (4.13) equal for E , we consider that the second term on the right-hand side of Eq. (4.13) is absorbed to increase A in Eq. (4.4), which renders A as an effective parameter, A_e that accounts for jumps occurring over a finite-thickness layer. This second term is what Garcia and Mellado (2014) called the ‘distortion and shape term’, although in their study of a clear-sky convective boundary layer, it was only a small (10%) contribution to a value of $A \approx 0.2$, associated with turbulent mixing.

A second justification is obtained by specifying that A_e is the value yielding the correct vertical flux divergence:

1. Modeling the subcloud layer with an infinitely thin transition layer (zero-order flux-jump model), the rate of warming or drying in the subcloud layer is given by the vertical flux gradient, $\frac{\partial F}{\partial z}$. The vertical flux divergence equals $\frac{F_0(1+A)}{h}$ if $F_h = -AF_0$, where subscripts 0 and h refer to the surface and subcloud layer top, respectively, and F denotes the fluxes.
2. In the case of a finite-thickness transition layer, the flux minimum is not at the top of the subcloud layer, but rather at some height below $h - \delta h$ (first-order flux-jump model; see, for instance, Fig. 1 in Fedorovich et al. (2004) for an illustration). In this case, A is still defined as the ratio of the minimum to maximum flux, and the vertical flux divergence over the layer of depth $h - \delta h$ is $\frac{F_0(1+A)}{(h-\delta h)}$.
3. Setting these two vertical flux divergences equal and replacing A in step (1.) with A_e to introduce an effective parameter into the zero-order flux-jump model is $\frac{F_0(1+A_e)}{h} = \frac{F_0(1+A)}{(h-\delta h)}$, yielding $A_e = \frac{(1+A)h}{(h-\delta h)} - 1$. For example, if $A = 0.2$ as often assumed, and $h = 710$ m, then $A_e = 0.40$ for $\delta h = 100$ m, $A_e = 0.52$ for $\delta h = 150$ m, and $A_e = 0.67$ for $\delta h = 200$ m.

Fedorovich et al. (2004) argue that this apparent increase in A would arise, for instance if the depth of the subcloud layer is chosen to be above the height of the buoyancy flux minimum, which was not measured during EUREC⁴A.

4.6 Resulting moisture and temperature budgets

Adopting the mean parameter estimates from the Bayesian inversion, Fig. 4-6 shows that the bulk theory budgets close to within 3.6 Wm^{-2} for moisture and 2.9 Wm^{-2} for potential temperature for the campaign-mean and can largely explain synoptic variability.

For the moisture budget, the campaign-mean residual is 2.2% of the largest term, the surface latent heat flux. For synoptic variability, the residuals can have larger magnitude, yet uncertainty propagated from the individual terms crosses zero for 20 out of 24 circling-means, suggesting that residuals are unbiased and indistinguishable from zero to within uncertainty. The budgets also close equally well for daytime or nighttime (Fig. 4-6a). In the heat balance, 14 out of 24 residuals are unbiased, with their uncertainty estimates crossing uncertainty, and as for moisture, the heat budget holds equally well for day and night (Fig. 4-6b).

Regarding the relative magnitude of physical processes, for the moisture budget, the dominant balance is between surface latent heat flux ($166 \pm 56 \text{ Wm}^{-2}$) and entrainment drying flux ($-128 \pm 53 \text{ Wm}^{-2}$), with a secondary role for large-scale moisture advection multiplied by h ($-34 \pm 41 \text{ Wm}^{-2}$) and the storage term multiplied by h ($-1.0 \pm 40 \text{ Wm}^{-2}$). The mean ratio between the surface latent heat flux and the entrainment drying flux is 1.39. The advection terms are the product of negative (easterly) winds and a negative difference from taking the difference of a colder, drier value in the east minus a warmer, moister value further west. The net effect of this advection term on the balances is negative because it is subtracted from the left-hand side in Eq. (4.8) and Eq. (4.9).

In the heat budget, the entrainment flux ($18 \pm 6.5 \text{ Wm}^{-2}$) has roughly twice the magnitude of the other terms, which have a similar magnitude of 6–8 Wm^{-2}

(Fig. 4-6b). That the entrainment warming flux has a larger magnitude than the surface sensible heat flux is because the surface latent heat flux contributes strongly to the buoyancy fluxes, i.e., through the F_q contribution to F_{θ_v} . Compared to the moisture budget, wherein surface fluxes balance entrainment fluxes to first-order, there is greater variability in the magnitude of individual terms in the heat budget. In certain cases (e.g., second circling-mean on January 31, 2020), the time-derivative term is larger than the entrainment flux. In the heat balance, radiative cooling of the layer, and the time-derivative and horizontal advection when they are cooling terms, are disproportionately balanced by entrainment warming. In three cases, the magnitude of the heat budget residuals are larger than the largest-magnitude term (second circling-mean on February 2, 2020, second circling-mean on February 7, 2020, second circling-mean on February 13, 2020). Note that setting h to be the *mixed layer top*, rather than the subcloud layer top results in slightly larger residuals, 6.9 Wm^{-2} for the heat budget and 9.6 Wm^{-2} for the moisture budget.

One might be tempted to think that the flexibility afforded by the Bayesian framework allows for closing the budgets by construction. A_e , C_q , and C_θ are assumed to be constant, yet vertical profiles of moisture and potential temperature change across days, such that there is no guarantee that a fixed combination of A_e , C_q , and C_θ allows for budgets to close. We close moisture and heat budgets jointly, which provides a stronger constraint than closing a single budget. That is, in the moisture budget, drying by entrainment balances moistening by surface fluxes, whereas in the heat budget, both entrainment and surface fluxes warm the layer, such that each budget place counteracting constraints on the entrainment rate.

That the budgets close to within small residuals for most cases and the campaign-mean suggests that knowledge of the mean state in Eq. (4.8) and Eq. (4.9) is sufficient to close the budgets, without knowledge of the vertical thermodynamic gradients or incorporating additional processes. The ratios of $\partial\theta/\partial z$ and $\partial q/\partial z$ multiplied by $h/2$ to the jumps at the upper interface are small, with a mean value of 20% for q and 22% for θ , providing further evidence that the influence of vertical gradients on the subcloud layer budgets is small. The correlation of residuals with vertical gradi-

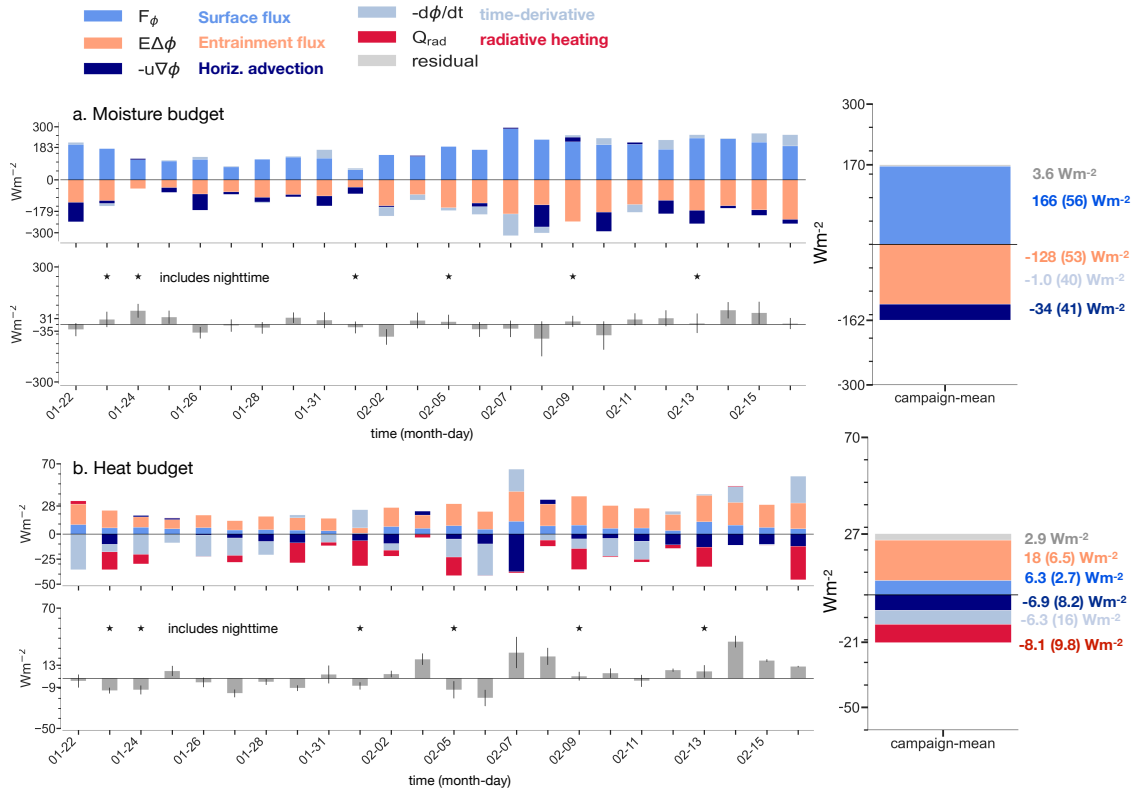


Figure 4-6: Synoptic variation over time and campaign-mean moisture and heat balances, showing the surface flux (blue), entrainment flux (orange), large-scale horizontal advection (dark blue), the time derivative (light blue), clear-sky radiative cooling (red), and the residual term (grey). Note that time is not linear on this axis and refers to the different measurement periods. Black stars flag circling-means that include sondes launched during the nighttime. Panel a. shows the moisture balance whereas panel b. shows the heat budget balance. The black error bar represents uncertainties in quadrature, added together for all terms: the 5-95% Bayesian credible interval on entrainment parameters, and for the other terms, one standard deviation calculated across the three circle-means making up one circling-mean. In the residual panels, the intermediate y-axis ticks (around $30 Wm^{-2}$ and $10 Wm^{-2}$) denote the mean values of positive and negative residuals. For the campaign-mean balance on the right-hand side, values given correspond to the mean and standard deviation of each time across the campaign.

ents, moreover, informs whether the omission of vertical gradients from the budgets is justified. Indeed, correlations of residuals with vertical gradients are small: the correlations of $\bar{\theta}$ residuals with $\partial\theta/\partial z$ and $\partial q/\partial z$ are 0.21 and -0.17 , respectively, and the correlations of the \bar{q} residuals with $\partial\theta/\partial z$ and $\partial q/\partial z$ are 0.33 and -0.25 , respectively.

Is the remaining structure in residuals informative of missing processes?

Structure in the residuals is indicative of observational error, structural issues in our formulations, or missing processes. The entrainment efficiency, A_e , and the scaling coefficients on the jumps, C_q and C_θ , could, in principle, vary on a case-by-case basis with the thickness of the transition layer (compare Eq. (4.13)), which we do not account for in the present analysis by assuming these parameters are constants. That said, the thickness of the transition layer does not strongly correlate with residuals in the moisture ($r=0.38$) or heat budgets ($r=0.20$). Regarding missing processes, we use two proxies for precipitation or precipitation-driven downdrafts, whose influences we neglect: cloud top height estimated from the WALES instrument on-board HALO (Konow et al., 2021), mindful that deeper clouds are more likely to precipitate (e.g., Stevens et al., 2016b), and a cold pool fraction per circling, wherein a cold pool sounding is defined as having θ_v -gradient height less than 400 m (Touzé-Peiffer et al., 2022). The residual structure is, however, not correlated with these proxies. For WALES cloud top height, correlations are $r=0.19$ for \bar{q} residuals and $r=0.16$ for $\bar{\theta}$ residuals. For the cold pool fraction, these correlations are also small, $r=0.23$ for \bar{q} residuals and $r=0.24$ for $\bar{\theta}$ residuals. The weak correlations support our finding that the subcloud layer moisture and heat budgets can close solely by representing small-scale entrainment mixing. These findings, that the influence of downdrafts and other coherent structures is relatively small (at least in the trades) relative to turbulent entrainment mixing, are consistent with Thayer-Calder and Randall (2015), justifying assumptions in many parameterizations, dating back to Arakawa and Schubert (1974).

4.7 How do these subcloud layer properties relate to the large-scale environment?

4.7.1 Wind speed variability

Fig. 4-7 relates variability among U , h , surface fluxes, entrainment fluxes, and the clear-sky radiative cooling, Q_r . A deeper subcloud layer tends to be associated with stronger U , $r=0.62$, consistent with Nuijens and Stevens (2012), though there are outliers with intermediate wind speeds leading to the smallest and largest heights. Naumann et al. (2017) and Naumann et al. (2019) suggest that stronger radiative cooling is associated with a smaller h , while Zheng (2019) finds that stronger radiative cooling deepens the subcloud layer. Unfortunately, our observations do not allow us to resolve this discrepancy. We do not find a simple linear relationship between clear-sky radiative cooling and h (Fig. 4-7, bottom row) or mean thermodynamics. During the night, the wind speed tends to increase, deepening the subcloud layer, which could offset a decrease in the depth of this layer due to stronger nighttime radiative cooling. This compensation highlights the difficulty in disentangling the influence of clear-sky radiative cooling on subcloud layer properties when its variability is aliased onto variability in other variables, such as the surface wind speed.

Surface and entrainment fluxes are strongly associated with U variability, as expected, given their structural dependence on the wind speed. Fixing other parameters at their campaign-mean value and only allowing U to change recovers most variance in surface and entrainment fluxes: 87% of the variance in F_q , 64% of the variance in $E\Delta q$, 74% of the variance in $E\Delta\theta$, though only 22% of the variance in F_θ . If we instead allow only the sea surface temperature to vary, we recover 32% of the variance in F_q , 38% of the variance in $E\Delta q$, 11% of the variance in F_θ , and 35% of the variance in $E\Delta\theta$. The surface wind speed plays a larger role in explaining variability in the fluxes except for F_θ .

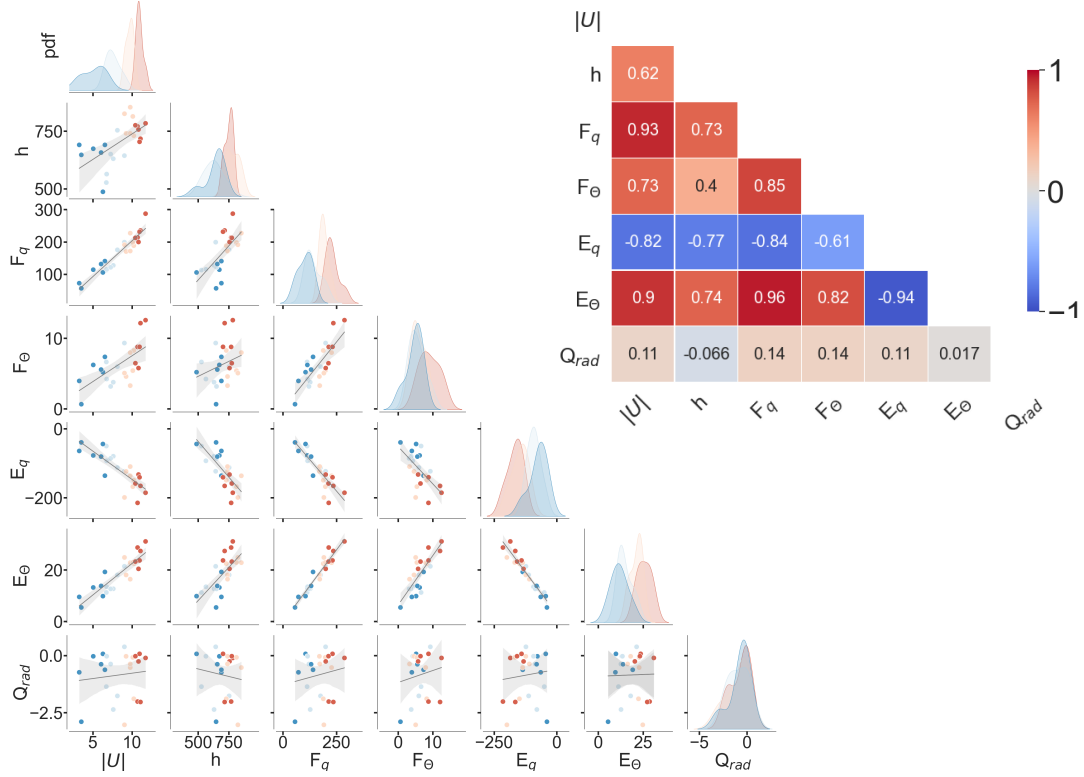


Figure 4-7: Relationships among 10 m wind speed, subcloud layer depth, surface fluxes, entrainment fluxes, and clear-sky radiative cooling. The black line is the ordinary least squares regression, and the grey shading is the 5–95% confidence interval on the regression. Colors correspond to quartiles of the wind speed with increasing wind speed going from blue to red. Note that, along the diagonal, the probability density function (pdf) smooths the four distributions corresponding to quartiles of 10 m wind speed, though these quartiles are non-overlapping: (3.3–6.7], (6.7–9.0], (9.0–10.3], and (10.3–12] ms^{-1} . The inset shows the Pearson correlation coefficients among these variables.

4.7.2 Predictive skill of mixed layer theory

Having established that mixed layer theory is a skillful framework (Sec. 4.6), we can further employ it as a physical mapping to diagnose how boundary conditions, such as the surface wind speed, influence \bar{q} and $\bar{\theta}$. Solving for \bar{q} from Eq. (4.8) yields,

$$\bar{q} = \frac{V_0 q_s + E q_+ - h \left(\frac{\partial q}{\partial t} + \overline{\vec{u} \cdot \nabla q} \right)}{V_0 + E}. \quad (4.14)$$

Similarly, solving for $\bar{\theta}$ from Eq. (4.9) yields,

$$\bar{\theta} = \frac{V_0 \theta_s + E \theta_+ + h Q_r - h \left(\frac{\partial \theta}{\partial t} + \overline{\vec{u} \cdot \nabla \theta} \right)}{V_0 + E}. \quad (4.15)$$

The velocity scale is $V_0 = C_d U$, and q_+ and θ_+ correspond to values 150 m above the subcloud layer top, h , though results are similar for choosing any height between 100–500 m above h . E can, moreover, be rewritten as,

$$E = \frac{A_e F_{\theta_v}}{(\bar{\theta} + 0.61[\bar{\theta}(q_+ - \bar{q}) + \bar{q}(\theta_+ - \bar{\theta})]) - \bar{\theta}_v} \quad (4.16)$$

as function of q_+ and θ_+ .

Predictions of \bar{q} from Eq. (4.14) recover 85% variance in observed \bar{q} , with a correlation coefficient $r=0.92$ (Fig. 4-8b). This simple theoretical framework thus has significant skill for predicting variability in mean subcloud layer humidity. The simple framework has less skill for capturing variations in observed $\bar{\theta}$, with a correlation coefficient of $r=0.48$ between observed $\bar{\theta}$ and $\bar{\theta}$ calculated with Eq. (4.15). The weaker skill for potential temperature is qualitatively consistent with larger residuals in the heat budget. The reduced skill could result from multiple reasons: the smaller magnitude of variability in $\bar{\theta}$ itself compared to \bar{q} (see Fig. 4-3), the smaller magnitude of the terms in the heat budget, and the presence of an additional term of radiative heating in the heat budget, wherein this radiative heating is here only calculated as clear-sky following Albright et al. (2021a). At times, there may be a substantial contribution from clouds, which is not accounted for in our analysis.

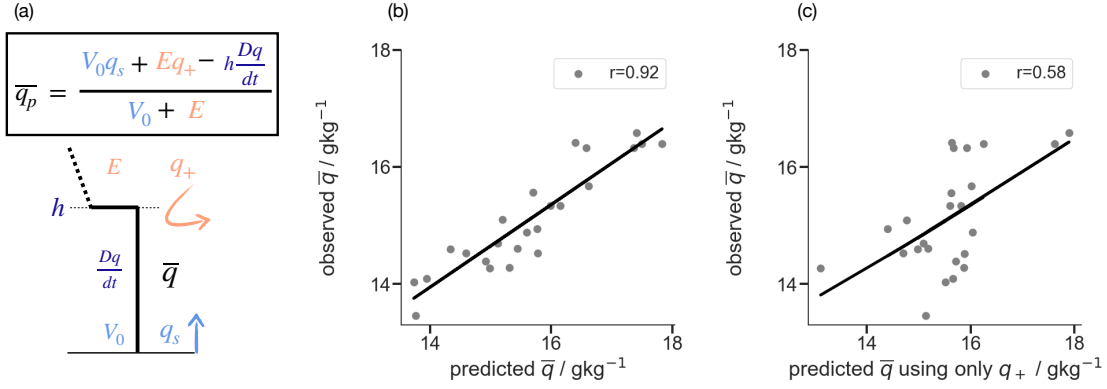


Figure 4-8: (a) Schematic showing the factors influencing mean subcloud layer specific humidity, \bar{q} : V_0 denotes the surface velocity scale, defined as C_d times the 10 m wind speed; h is the subcloud layer height; q_s is the surface (saturated) specific humidity; E is the entrainment rate; q_+ is defined as the mean from h to $h+100$ m; $\frac{Dq}{dt}$ is the total derivative of subcloud layer mean specific humidity. (b) Scatter plot between \bar{q} predicted using Eq. (4.14) and observed \bar{q} , with linear regression and Pearson correlation coefficient. (c) Scatter plot between \bar{q} predicted using Eq. (4.14), but only allowing q_+ to vary and keeping all other terms fixed at their campaign-mean, and observed \bar{q} , with linear regression and Pearson correlation coefficient.

The success of Eq. (4.14) in explaining variability in \bar{q} , however, allows for exploring the influence of different boundary conditions on the mean subcloud layer properties. We externalize different boundary conditions: U , SST, $\vec{u} \cdot \nabla \bar{q}$, $\vec{u} \cdot \nabla \bar{\theta}$, Q_r , q_+ , θ_+ , $\frac{\partial q}{\partial t}$, and $\frac{\partial \theta}{\partial t}$. The terms q_+ and θ_+ are defined as the mean from h to $h+100$ m – that is, air just above the subcloud layer and within the cloud layer and may not be completely independent of the properties of the subcloud layer. Cloud layer moisture variability is likely influenced by processes in the free atmosphere, such as dry intrusions (e.g., Stevens et al., 2021; Villiger et al., 2022).

To test the influence of these conditions, we vary one parameter at a time and fix the other parameters at their campaign-mean value to predict \bar{q} or $\bar{\theta}$ values. Perhaps surprisingly, varying only the surface wind speed to predict \bar{q} yields a weak correlation with observed \bar{q} ($r=-0.2$) or with predicted \bar{q} when allowing all external factors to vary ($r=-0.11$), not only the wind. That the net influence of the wind speed is weak might seem to contradict the previous discussion, but results from its opposing influences, both moistening the layer through surface fluxes and drying it through

entrainment. Whereas the correlation of the surface wind speed with individual fluxes is strong (Fig. 4-7), the correlation of the wind speed with the sum of the surface moistening flux and entrainment drying flux is weak ($r=0.32$). Varying only q_+ , which also influences the entrainment rate through $\Delta\theta_v$, yields the highest correlation with predicted moisture ($r=0.55$) and observed moisture ($r=0.58$, Fig. 4-8c). For heat, we find that θ_+ has a correlation of $r=0.36$ with predicted $\bar{\theta}$ and $r=0.85$ with observed $\bar{\theta}$.

In summary, variability in the fluxes is strongly influenced by U variability. Yet due to opposing influences of the surface and entrainment fluxes on \bar{q} , the surface wind speed does not strongly influence \bar{q} variability. Instead, knowing the humidity above the subcloud layer, q_+ , is the most informative for reconstructing \bar{q} variability. Clouds, however, couple subcloud layer moisture, \bar{q} and q_+ , in which case it is difficult to infer causality. The strong predictive skill of q_+ does point to the importance of understanding what controls dry intrusions into the cloud layer, such as extratropical dry intrusions discussed in Villiger et al. (2022), which can influence the subcloud layer moisture by entraining relatively drier air from the layer above.

4.8 Conclusions

In this analysis, we quantify thermodynamic variability in the trade-wind subcloud layer and test mixed layer theory using extensive *in situ* observations from the EUREC⁴A campaign.

A primary question motivating our analyses is whether mixed layer theory, as a simple and often-employed theoretical framework, is an appropriate and useful way to study how and why the subcloud layer varies. Regarding its appropriateness, a first assumption is that the subcloud layer is well-mixed vertically, and we find that vertical gradients, at least over the mixed layer, are small relative to variability about the mean (Fig. 4-9). Regarding a second assumption about a ‘jump’ at the subcloud layer top, in defining the subcloud layer height, we find evidence for a transition layer that separates the mixed layer top from the subcloud layer top (Fig. 4-2). The transition layer exhibits vertical gradients over finite thickness. The presence of the

transition layer and its vertical gradients introduces ambiguity into the application of mixed layer theory, in particular regarding the formulation of the entrainment rate and entrainment fluxes.

We address this uncertainty through the introduction of effective parameters related to entrainment, which are estimated using a Bayesian methodology. The mean effective entrainment efficiency, $A_e = 0.43$ (Fig. 4-5), is greater than the value of 0.2 as often assumed. Such a large value of A_e is inconsistent with large eddy simulation (Fedorovich et al., 2004) and direct numerical simulation studies (Garcia and Melado, 2014) of idealized convective boundary layers. A large A_e value could arise if other processes are contributing to the energetics of mixing, for instance wind shear, cloud processes, or radiative cooling, or if the depth of the layer is taken to be too deep as compared to the height where the minimum buoyancy flux locates (e.g., Fedorovich et al., 2004; Canut et al., 2012). Applying our inversion technique using the shallower mixed layer depth to specify h does not, however, resolve this discrepancy, nor does wind shear appear to play a role (see Fig. 4-10). This discrepancy leaves a possible disagreement with idealized simulations, or other processes, such as contributions from shallow clouds or radiative cooling in the transition layers, as candidate explanations for a larger A_e . Related to these considerations, there are other open questions regarding the transition layer that we address in a forthcoming publication, particularly, which physical processes give rise to its vertical structure.

Having accounted for the challenges that the transition layer posed for the formulation of entrainment in this theoretical framework, we find that mixed layer theory can explain both synoptic and monthly-mean variability in subcloud layer moisture and heat budgets, with campaign-residuals of 3.6 Wm^{-2} for moisture and 2.9 Wm^{-2} for heat. For synoptic variability across the campaign, the residuals are generally small and unbiased – that is, with uncertainties estimates crossing zero (Fig. 4-6). That the budgets close to within these small residuals suggests that knowledge of the mean state through \bar{q} , $\bar{\theta}$, and h is generally sufficient to close the thermodynamic budgets, without having to include vertical thermodynamic gradients. We also find little evidence that closing moisture and heat budgets requires representing addi-

tional processes, such as precipitation or coherent downdrafts, and we can therefore not distinguish residuals from uncorrelated observational error.

After showing that mixed layer theory is a skillful framework, we use this theory as a mapping between external conditions and subcloud layer thermodynamics. In Sec. 4.4.3, we showed that \bar{q} varies significantly day-to-day and decorrelates after about two days, such that EUREC⁴A research flights sample nearly-independent realizations of large-scale variability. Anomalies in the subcloud layer depth and LCL are, moreover, largely associated with anomalies in \bar{q} . Given its large synoptic variability and influence on subcloud layer vertical length-scales, the primary mode of subcloud layer thermodynamic variability therefore appears to be through \bar{q} variability, motivating our focus on \bar{q} variability. The simple mixed layer theory framework is able to explain significant variability in observed \bar{q} , with a correlation $r=0.92$ between observed and predicted \bar{q} (Fig. 4-8b). Whereas we find strong linear relationships among variability in the surface wind speed and subcloud layer depth, surface fluxes, and entrainment fluxes (Fig. 4-7), variability in the surface wind speed does not explain observed \bar{q} variability due to its compensating influences on both moistening the layer through surface fluxes and drying the layer through entrainment fluxes. Instead, only knowing moisture above the subcloud layer, q_+ , has the most predictive skill for variations in observed \bar{q} ($r=0.58$, Fig. 4-8c) because these are the air masses that are incorporated into the subcloud layer by entrainment.

The ability of mixed layer theory to observationally close subcloud layer moisture and heat budgets gives confidence in using this approach to constrain trade cumulus feedbacks using the subcloud layer mass budget, which is the focus of Vogel et al., in review. In this work, mixed layer theory, combined with novel sampling strategies, are used to perform the first process-level observational test to constrain trade cumulus feedbacks and climate sensitivity (e.g., Rieck et al., 2012; Zhang et al., 2013; Sherwood et al., 2014; Brient et al., 2016; Vial et al., 2016). Given the skill of the mixed layer framework, it would also be worthwhile to apply this framework to representations of the trade-wind subcloud layer by a hierarchy of models, from general circulation to storm-resolving models and large-eddy simulations. Variables analyzed

could include subcloud layer moisture or heat as in this study, momentum (e.g., Holland and Rasmusson, 1973), or isotopes (e.g., Risi et al., 2020). Quantifying the relative magnitudes of different processes, how well the budgets close, and how individual terms vary according to large-scale environmental conditions would serve as a consistent framework for evaluating and comparing how well models represent physical processes, such as surface and entrainment fluxes, relative to novel observational anchoring from the EUREC⁴A field campaign.

4.9 Appendix A: Methodology for various boundary and subcloud layer height estimates

4.9.1 Thermodynamic variable gradient method

The vertical stratification of the tropical atmosphere occurs in all variables, but it is most evident in moisture (Augstein et al., 1974; Stevens et al., 2001). We first define a subcloud layer length scale as the depth over which there is no vertical gradient in specific humidity within a threshold, applying the method from Canut et al. (2012). The method selects the height where the specific humidity becomes greater than the density-weighted mean specific humidity of the levels below by a certain threshold ϵ_q : $|q(z) - \bar{q}| \leq \epsilon_q$, where \bar{q} is updated at each vertical level. We begin at a height of 100 m to minimize the influence of the surface layer. This humidity-jump approach was implicitly adopted in Malkus (1958), and is similar to previous estimates based on discontinuities in observed profiles (e.g. Heffter, 1980; Marsik et al., 1995).

In implementing the q -gradient method, the primary uncertainty is the choice of threshold ϵ_q , which should be large enough not to be biased by small-scale vertical variability, but precise enough to identify the humidity discontinuity at the subcloud layer top. To choose a threshold, we turn to intensive sampling from both the CU-RAAVEN remotely-piloted aircraft and the ATR-42 and HALO aircraft. Empirically, we choose a threshold that is one-third of turbulent, eddy-scale variability, estimated as within-flight variability (compared with day-to-day variability). Calculating the

specific humidity standard deviation below 550 m within a three-hourly flight of the CU-RAAVEN suggests a threshold $\epsilon = 0.3 \text{ gkg}^{-1}$. Calculating the standard deviation in q below 500m from the ATR-42 yields a threshold $\epsilon = 0.35 \text{ gkg}^{-1}$, and for HALO soundings within one flight, one-third of the standard deviation is $\epsilon = 0.27 \text{ gkg}^{-1}$. We use the largest value, $\epsilon = 0.35 \text{ gkg}^{-1}$. The maximum allowable vertical gradient in the boundary layer is thus $0.035 \text{ gkg}^{-1}\text{m}^{-1}$, given a 10m grid spacing. This threshold allows for a certain moisture gradient, or deviation from a perfectly well-mixed profile, noted previously for both the trades and other environments (Malkus, 1958; Mahrt, 1976; Dai et al., 2014) and shown by our analyses. Across the HALO dropsonde soundings, this 0.35 gkg^{-1} threshold corresponds to a 10% difference between mean air in the cloud and subcloud layer, when averaging air masses between 1000–1200m and 100-300m depths. We evaluate this height method and empirically-chosen gradient in Sec. 4.4. Heights from the q -gradient method are $546 \pm 82 \text{ m}$, with values denoting the mean and standard deviation across the 69 circle-mean data.

An advantage of this threshold definition is its straightforward application to other thermodynamic variables like θ and θ_v : $|\theta(z) - \bar{\theta}| \geq \epsilon_\theta$. We use thresholds 0.15 K for θ and 0.20 K for θ_v . The threshold of 0.2K for θ_v is also employed in Touz -Peiffer et al. (2022). These thresholds are similarly chosen from the CU-RAAVEN, ATR-42, and HALO sounding data as one-third of one standard deviation within flights. These thresholds correspond to 10% of differences between cloud and boundary layer air (estimated conservatively as the 1000-1200m minus 100-400m layer-means) for θ and θ_v , respectively. Heights from the θ -gradient are $549 \pm 97 \text{ m}$ and $697 \pm 94 \text{ m}$ for the θ -gradient, with values denoting the mean and standard deviation across the 69 circle-mean data.

4.9.2 Parcel method

Next, we examine the parcel method, also referred to as the ‘Holzworth method’, as introduced by Holzworth (1964), which estimates the level at which a hypothetical rising parcel of surface air, representing a thermal, reaches its level of neutral buoyancy. We compute the level of neutral buoyancy where θ_v surface parcels intersect a

background profile fitted to the cloud layer θ_v profile determined by linear regression. Surface air is defined as 0-50m values; choosing 0-90m air affects the height by $O(1\%)$. We calculate the cloud layer θ_v profile from 100m above the height determined from the q -gradient method to the first inversion base height, defined where the static stability first exceeds 0.1 K/hPa, similar to a definition given in Bony and Stevens (2019).

This parcel method can be viewed as a simplification of the Richardson-number method that neglects the shear contribution (e.g., Seibert et al., 2000; Dai et al., 2014; Zhang et al., 2014). Although the Richardson and gradient Richardson number methods are related to the generation and consumption of mixed layer turbulence and diagnose flow stability (e.g., Garratt, 1994; Stull, 2012), we do not employ this method due to the considerable uncertainty underlying choices in its free parameters (e.g., Zilitinkevich and Baklanov, 2002; Seidel et al., 2012). Heights from the parcel method are 719 ± 85 m.

4.9.3 Linearized relative humidity profile

A third type of definition involves the relative humidity profiles. The relative humidity increases throughout the subcloud layer (e.g., Nuijens et al., 2015b), as the specific humidity q remains largely constant while temperature decreases. In practice, spurious peaks in relative humidity in our circle-mean profiles could arise from the spatial averaging of multiple soundings. For instance, a circle-mean could average between profiles falling through a cloud close to the subcloud layer top, saturated in relative humidity, and drier profiles elsewhere along the EUREC⁴A circle flight path.

To circumvent this bias, we introduce a linearization of the relative humidity profile. We find the first local maximum in relative humidity above 300m and then linearize the relative humidity profile, by ordinary least squares regression, from 50m above the surface to 50m above this first local relative humidity maximum. We then find all local relative humidity maxima below one kilometer and choose the height that minimizes the relative humidity difference between the observed and linearized profiles. Heights from the relative humidity maximum method are 571 ± 96 m.

4.10 Appendix B: Vertical thermodynamic profiles

To further illustrate the vertical structure as described in Sec. 4.4, Fig. 4-9 plots vertical profiles of potential temperature, θ , and specific humidity, q , and Fig. 4-10 plots vertical profiles of virtual potential temperature, θ_v , and zonal wind speed.

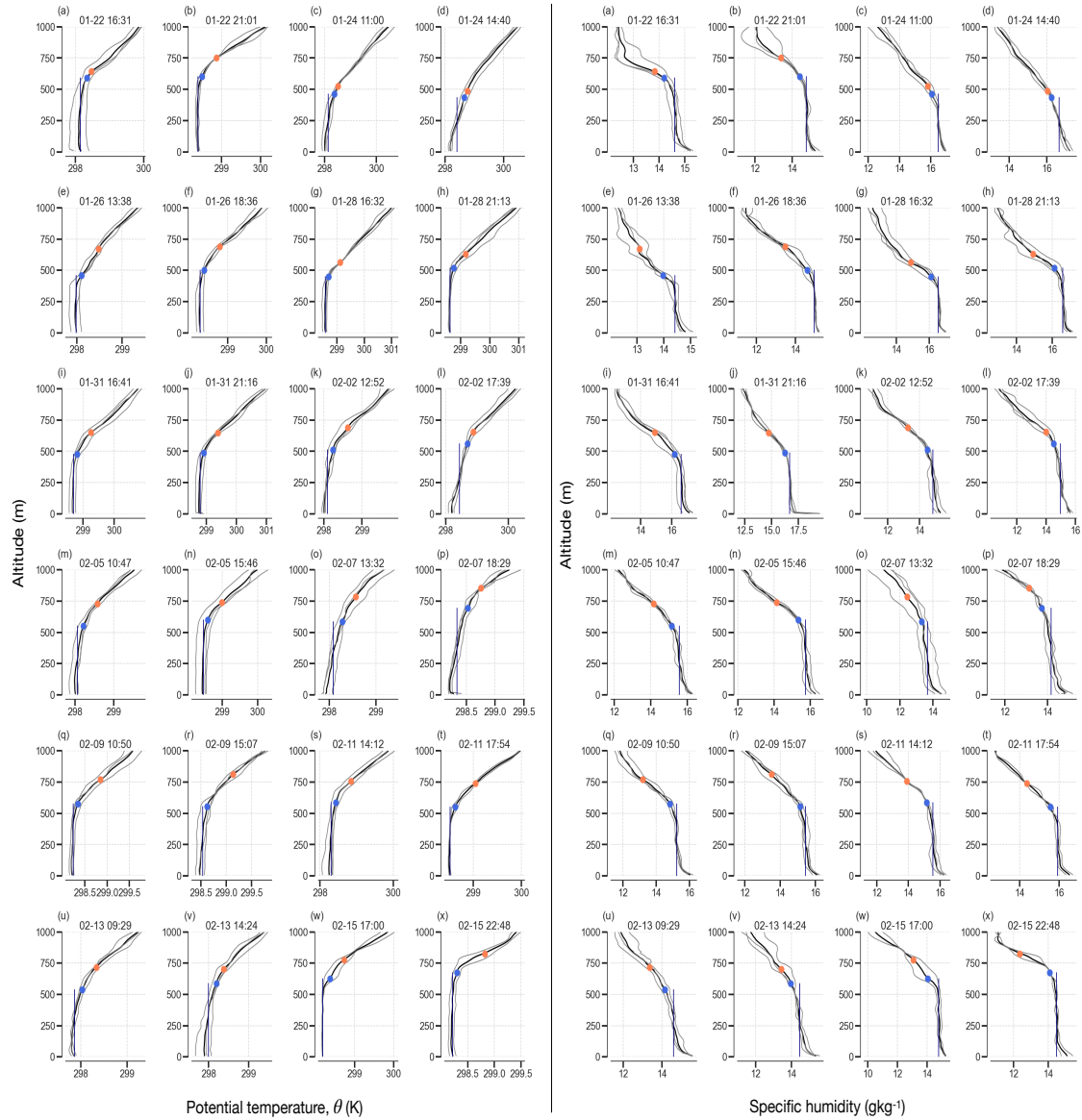


Figure 4-9: The 24 circling-mean profiles (black, aggregate of about 36 dropsondes each) of (left) potential temperature, θ , and (right) specific humidity, q . Each panel also shows the three circle-mean profiles (grey) averaged to estimate each circling-mean. Blue dots correspond to the mixed layer top, estimated with the q -gradient definition, and orange dots denote the subcloud layer top, estimated with the θ_v -gradient definition. The vertical navy line denotes the mixed layer-mean value and demonstrates that the majority of profiles have a vertically well-mixed layer for thermodynamic variables.

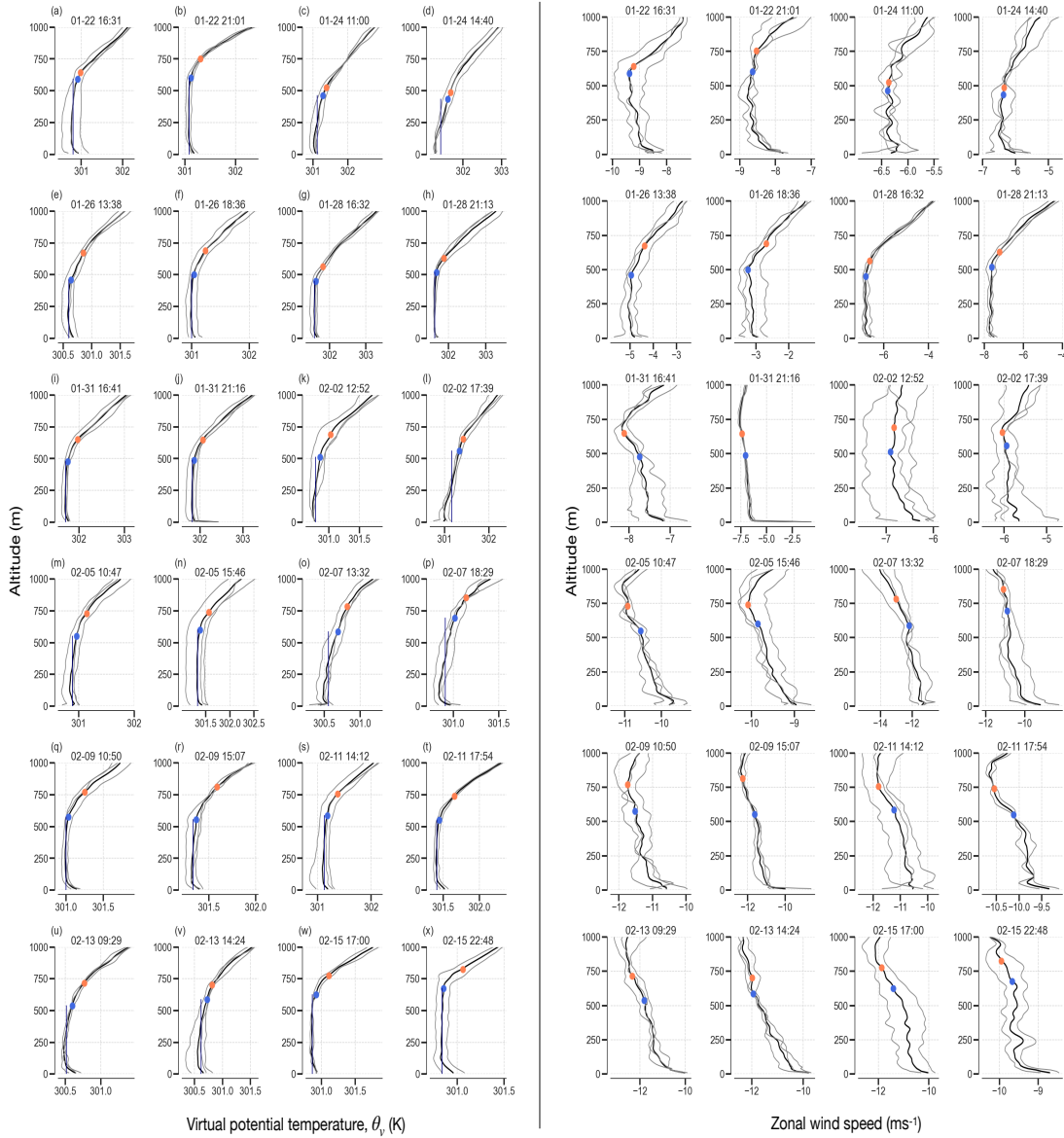


Figure 4-10: The 24 circling-mean profiles (black, aggregate of about 36 dropsondes each) of (left) virtual potential temperature, θ_v , and (right) zonal wind speed. Each panel also shows the three circle-mean profiles (grey) averaged to estimate each circling-mean. Blue dots correspond to the mixed layer top, estimated with the q -gradient definition, and orange dots denote the subcloud layer top, estimated with the θ_v -gradient definition. The vertical navy line denotes the mixed layer-mean value and demonstrates that the majority of profiles have a vertically well-mixed layer for thermodynamic variables (but not the wind speed).

4.11 Appendix C: Derivation for entrainment efficiency parameter, A_e

For a subcloud layer scalar, ϑ , Eq. (4.13) results from integrating the following equation over a thin interfacial layer with lower and upper boundaries $h_- = h - \epsilon$ and $h_+ = h + \epsilon$ and layer-thickness $\delta h = h_+ - h_- = 2\epsilon$,

$$\int_{h_-}^{h_+} \frac{\partial \bar{\vartheta}}{\partial t} dz = - \int_{h_-}^{h_+} \frac{\partial}{\partial z} \overline{w' \vartheta'} dz. \quad (4.17)$$

Applying the Leibniz integral rule for differentiation under integration yields,

$$\frac{d}{dt} [\langle \bar{\vartheta} \rangle_{\delta h} \delta h] - \frac{dh_+}{dt} \vartheta_{h_+} + \frac{dh_-}{dt} \vartheta_{h_-} = -\overline{w' \vartheta'}|_{h_+} + \overline{w' \vartheta'}|_{h_-} \quad (4.18)$$

Assuming that turbulence vanishes at h_+ implies that $\overline{w' \vartheta'}|_{h_+} = 0$. Heights h_+ and h_- are offset from h by a constant, ϵ , such that $h_+ = h + \epsilon$ and $h_- = h - \epsilon$, which means that $\frac{dh_+}{dt} = \frac{dh_-}{dt} = \frac{dh}{dt}$. Assuming that the layer is well-mixed implies that $q_{h_-} = \bar{q}$. With these assumptions, Eq. (4.18) becomes,

$$\frac{d}{dt} [\langle \bar{\vartheta} \rangle_{\delta h} \delta h] - \frac{dh}{dt} \Delta \vartheta = \overline{w' \vartheta'}|_{h_-} \quad (4.19)$$

If δh is constant and $\langle \bar{\vartheta} \rangle_{\delta h}$ is approximately equal to $\frac{\bar{\vartheta} + \vartheta_+}{2}$, with $\bar{\vartheta}$ equaling the mixed layer mean value then Eq. (4.19) becomes,

$$\frac{\delta h}{2} \left[\frac{d\bar{\vartheta}}{dt} + \frac{d\vartheta_+}{dt} \right] - \frac{dh}{dt} \Delta \vartheta = \overline{w' \vartheta'}|_{h_-} \quad (4.20)$$

Note that if assuming that the interfacial layer has zero-thickness, e.g. $\delta h = 0$, Eq. (4.20) becomes,

$$-\frac{dh}{dt} \Delta \vartheta = -E \Delta \vartheta = \overline{w' \vartheta'}|_{h_-}, \quad (4.21)$$

where the growth of the layer, $\frac{dh}{dt}$ is considered the entrainment rate, E .

Replacing ϑ with θ_v yields Eq. (4.13),

$$\frac{\delta h}{2} \left[\frac{d\bar{\theta}_v}{dt} + \frac{d\theta_{v+}}{dt} \right] - \frac{dh}{dt} \Delta\theta_v = \overline{w'\theta'_v} | h_- \quad (4.22)$$

Rearranging to solve for $E = \frac{dh}{dt}$ yields and adopting the formulation for the flux, $\overline{w'\theta'_v} | h_-$, given in Eq. (4.2) and Eq. (4.4) yields,

$$E = \frac{-AV_0\Delta_0\theta_v}{\Delta_1\theta_v} + \frac{\delta h}{2\Delta_1\theta_v} \left(\frac{d\bar{\theta}_v}{dt} + \frac{d\theta_{v+}}{dt} \right). \quad (4.23)$$

The effective A_e can be interpreted as absorbing the second term on the right-hand side in Eq. (4.23).

Chapter 5

A new conceptual picture of the transition layer

5.1 Abstract

The transition layer in the trades has long been observed and simulated, but the physical processes producing its structure remain little investigated. Using extensive observations from the EUREC⁴A (*Elucidating the role of clouds–circulation coupling in climate*) field campaign, we propose a new conceptual picture of the trade-wind transition layer. The majority of cloud bases are observed to form within the transition layer, instead of above it. The theory of cloud-free convective boundary layers suggests a vertical structure with strong jumps at the mixed layer top, yet such strong jumps are only found rarely. Despite cloud fraction near cloud base being small, the cloud-free convective boundary layer structure is infrequent and confined to large ($O(200\text{ km})$) cloud-free areas. We propose that very small clouds, with cloud tops generally below 1.3 km, maintain the transition layer, in analogy with the maintenance of the trade-wind inversion by deeper clouds. This analysis suggests an additional contribution to the energetics of entrainment mixing, which is based on the ability of small clouds to detrain and dissipate condensate into the transition layer, leading to evaporative cooling. Inferences from mixed layer theory and Paluch mixing diagrams, moreover, suggest that the cloudy transition layer structure does not affect the rate of entrainment mixing, but rather the properties of the air incorporated into the mixed

This chapter is in review at the *Journal of the Atmospheric Sciences*.

layer.

5.2 Introduction

The transition layer in the trades has long been observed (e.g., Malkus, 1958; Augstein et al., 1974; Yin and Albrecht, 2000) and simulated (e.g., Stevens et al., 2001), but the physical processes that give rise to its structure are little investigated. This layer is often associated with a thin layer (100–200 m thick) above the turbulent mixed layer (around 500–600 m depth) and is identified from vertical thermodynamic gradients that differ from the nearly-zero vertical gradients in the mixed layer below and the non-zero vertical gradients in the cloud layer above (e.g., Malkus, 1958; Augstein et al., 1974; Yin and Albrecht, 2000).

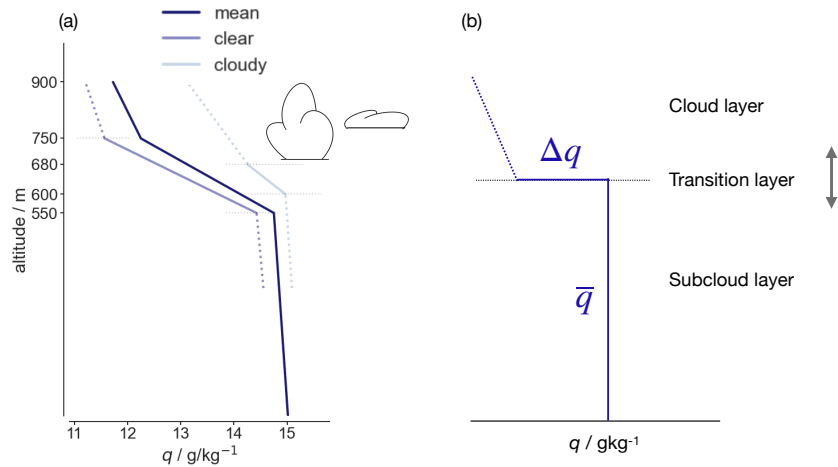
In previous studies, there is, however, substantial ambiguity regarding the transition layer structure and its relation to cloud base. Early observational studies argue that cloud bases form *above* the transition layer top (Malkus, 1958; Augstein et al., 1974). More recent conceptual model studies contend that cloud bases form within the transition layer (Neggers et al., 2009; Gentine et al., 2013), yet their conceptualization of the transition layer remains ambiguous: in Neggers et al. (2009), the mixed layer top and cloud base coincide, but what they call the transition layer is above these two levels; Gentine et al. (2013) call the offset between the mixed layer and cloud layer the ‘dry inversion layer’, with cloud bases occurring somewhere within this layer.

There is also uncertainty whether the transition layer is a ubiquitous feature of the trade-wind atmosphere in both cloudy and non-cloudy areas. Malkus (1958), for instance, examines vertical gradients in 25 trade-wind soundings to conclude that the transition layer was always (100%) present in clear-sky regions and generally (55%) absent in cloudy regions. She also proposes that the transition layer is thicker in clear areas (200 m) than in cloudy areas (80 m), as illustrated schematically in Fig. 5-1a. Augstein et al. (1974), moreover, outlines a qualitative scheme (his Fig. 12) that the trade-wind transition layer is maintained by dry convection and mechanically-

driven turbulence, whereas clouds form and moist convective processes play a role in producing the vertical structure above the transition layer top. The inferences of strong vertical thermodynamic gradients over the transition layer and cloud bases forming above the transition layer top, moreover, established a conceptual picture of the transition layer as a barrier to convection that regulates subcloud to cloud layer transports (e.g., Ooyama, 1971; Augstein et al., 1974; Yin and Albrecht, 2000; Neggers et al., 2006), even though this view stands in contrast to contemporary quasi-equilibrium thinking, which contends that convection occurs in response to larger-scale instabilities rather than local convective inhibition (e.g., Emanuel et al., 1994a).

In the years subsequent to these early observational studies, an interpretation arose in simple modeling studies that the trade-wind transition layer could be modeled as an infinitely-thin layer exhibiting a ‘jump’, or abrupt discontinuity, above the well-mixed layer. This structure is inferred in analogy with stratocumulus regimes (e.g., Lilly, 1968) or cloud-free convective boundary layer (e.g., Stull, 1976; Tennekes, 1973; Arakawa and Schubert, 1974; Albrecht et al., 1979; Stevens, 2006). Such a conceptual view is shown in Fig. 5-1b. A cloud-free direct numerical simulation from Garcia and Mellado (2014) exhibiting strong vertical gradients is reproduced in Fig. 5-1c. These illustrations highlight a layer that is well-mixed by turbulence, topped by a transition layer represented as an abrupt discontinuity, in keeping with expectations from cloud-free boundary layers and stratocumulus regimes. In the trades, the cloud-base cloud fraction is small (e.g., Malkus, 1958; Bony et al., 2022), such that it appears a reasonable approximation to assume that the cloud-free boundary layer structure is the baseline structure, as in Stevens (2006).

Closure schemes for the vertical (rather than lateral) entrainment rate based on cloud-free boundary layers are common features of trade cumulus parametrizations (Betts, 1973; Arakawa and Schubert, 1974; Albrecht et al., 1979). The conceptual view of entrainment in a cloud-free boundary layer is that overshooting plumes entrain filaments of more stratified overlying air into the turbulent layer (e.g., Bretherton, 1997). Such a formulation suggests that clouds are not explicitly agents of turbulent



(c) Reproduced from Garcia, Mellado, 2014

Figure 5-1: (a) Representing specific humidity profiles from Malkus (1958) with the heights and gradients given in that study. The mean profile (dark blue) is the weighted average between 16 clear-sky (averaged in light blue) and 9 cloudy (averaged in medium blue) soundings. The transition layer gradients are shown in solid lines in the clear and cloudy profiles, compared to dashed lines for the mixed and cloud layers. According to this view, clouds start to form above the transition layer top. (b) An idealized profile of specific humidity similar to those in previous conceptual models (e.g., Arakawa and Schubert, 1974; Albrecht et al., 1979; Stevens, 2006). That the infinitely-thin transition layer can vary in height is indicated by the up-and-down arrow. (c) Figure reproduced from Garcia and Mellado (2014) (their Fig. 2), showing the logarithm of the buoyancy gradient (similar to the θ_v gradient) from their direct numerical simulation of a dry convective boundary layer. Colors correspond to increasing values, from black to blue to green.

entrainment mixing, and turbulence and any associated entrainment are instead generated by surface fluxes, wind shear, and radiative cooling (e.g., Bretherton, 1997; Fedorovich et al., 2004).

As part of the EUREC⁴A (*Elucidating the role of clouds–circulation coupling in climate*) field campaign (Bony et al., 2017; Stevens et al., 2021), we collected the necessary data to investigate the structure of the trade-wind transition layer and the physical processes that produce this structure. Using EUREC⁴A observations, the trade-wind subcloud layer is shown to have a nuanced vertical structure that includes a finite-depth transition layer between the well-mixed part of the subcloud layer and subcloud layer top, both in individual and aggregated soundings, contrasting with the jump-like structure expected from cloud-free boundary layers (Albright et al., 2022). Albright et al. (2022), reproduced in Chapt. 4, showed that the presence of the finite-thickness transition layer introduced ambiguity into the application of mixed layer theory for subcloud layer moisture and heat budgets. This ambiguity could, however, be accounted for using effective entrainment parameters constrained using observations and a Bayesian methodology. A larger *effective* entrainment efficiency parameter, $A_e = 0.43$, was found compared to previous studies that contend $A = 0.2$ (e.g., Lilly, 1968; Stull, 1976; Tennekes and Driedonks, 1981; Driedonks, 1982; Pino et al., 2003; Garcia and Mellado, 2014). An effective parameter value of 0.4 is, however, consistent with other large-eddy simulation results (Schalkwijk et al., 2013; Naumann et al., 2017, 2019). An ensuing question then arises, what processes maintain such a finite-thickness transition layer in the trades? Here we provide a first answer to this question.

5.3 EUREC⁴A data

The primary data are similar to those used in Chapt. 4 (published as Albright et al. (2022)), in particular 810 dropsondes from the High Altitude and Long Range Research Aircraft (HALO) launched between January 22, 2020 and February 15, 2020 (Konow et al., 2021). These dropsondes provide vertical profiles of pressure, tem-

perature, and relative humidity, which have been processed and interpolated into a common altitude grid with 10 m vertical resolution (George et al., 2021). As described in Albright et al. (2022), dropsonde measurements were distributed along the ‘EUREC⁴A circle’, defined by a circular flight pattern with an approximately 220-kilometer diameter, centered at 13.3°N, 57.7°W. A ‘circle-mean’ averages about 12 dropsondes along the EUREC⁴A circle. This circular flight pattern was repeated 69 times, over 12 flights. Typically each flight incorporated two – temporally well-separated – periods of circling. A ‘circling-mean’ is defined as the mean of three circle-means. Given that measurements did not target specific meteorological conditions they provide unbiased sampling. The structure of the data collected encourages the definition of 69 circle-means and 24 circling-means.

To estimate cloud *base* heights, we use ceilometer cloud base height estimates from two platforms, the R/V Meteor and the Barbados Cloud Observatory (BCO, Stevens et al., 2016a), at 10-second resolution from January 19, 2020 to February 19, 2020. The Meteor is within the eastern portion of the EUREC⁴A circle, whereas the BCO is about 200 km downstream from the circle center. Data during night times that the HALO aircraft did not fly are dropped. Cloud base heights vary, and to estimate the base of clouds forming from updrafts within the subcloud layer, the first-detected cloud base heights (as in Nuijens et al. (2014): “ cbh_1 , where the superscript 1 denotes it is the first detected base, rather than the second or third”) between 350 and 1000 m are analyzed. These data span the range of the mixed layer lifting condensation levels. We bin data into three-hourly segments and then select the most frequently-sampled value as a representative cloud base (Fig. 5-2). Typically, the first peak corresponds to the absolute peak of the distribution. In the cases where they differ, we select the first peak that is within 50% of the absolute distribution peak. The first peak is chosen because the first decile is biased by rain, whereas higher deciles increasingly reflect cloud side detection from sheared convection or decaying cloud fragments that are not indicative of cloud base (Nuijens et al., 2014). Examples of three-hourly cloud base distributions are given in Fig. 5-2 to illustrate the methodology. In the following analysis, the ceilometer cloud base height distribution refers to the aggregate

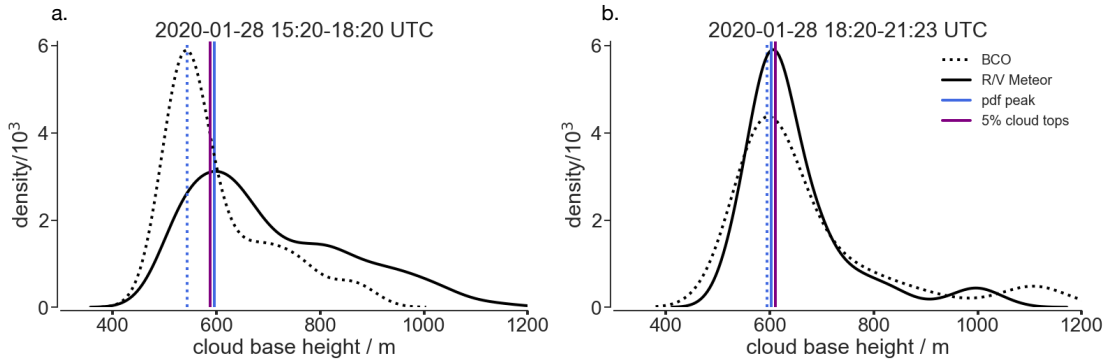


Figure 5-2: Example three-hourly cloud base height distributions from the R/V Meteor (solid) and the Barbados Cloud Observatory ceilometers (dotted), annotated with the first distribution peak (‘pdf peak’, blue vertical line). Also shown is the 5% cloud top height estimate from WALES (purple vertical line) for the same time interval.

of distribution peaks from three-hourly data (e.g., Fig. 5-3c).

Cloud *top* height data are taken from the WALES (*W*ater *v*apor *L*idar *E*xperiment *i*n *S*pace) instrument, a water vapour differential absorption lidar. This lidar operates at four wavelengths around 935 nm to measure water vapor mixing ratio profiles below the HALO aircraft (Wirth et al., 2009; Konow et al., 2021). Data products used are a cloud flag and cloud top height having both a precision and accuracy of about 10 m (Konow et al., 2021). By way of comparison, even high-resolution satellite retrievals from the Advanced Spaceborne Thermal Emission and Reflection Radiometer instrument have a vertical uncertainty of 250–500 m on cloud top height estimates (e.g., Mieslinger et al., 2019), rendering the WALES cloud top height estimates with their high vertical resolution particularly valuable.

5.4 Building a new conceptual picture of the transition layer with EUREC⁴A observations

In Sec. 5.4, we first address the depth (Sec. 5.4.1) and the stability (Sec. 5.4.2) of the transition layer and then the connection to cloud bases and cloud formation (Sec. 5.4.3).

5.4.1 Transition layer depth

The expectation from cloud-free boundary layers is a single layer that varies in height, topped by a discontinuity (e.g., as idealized in Fig. 5-1b). Sampling the undulation of this layer would result in a single Gaussian height distribution (Lilly, 1968). Similarly, averaging multiple soundings with sharp vertical gradients, albeit at different heights, would lead to a mean sounding with a more gradual vertical gradient. To test the idea of a single layer topped by a discontinuity, we perform a vertical length-scale analysis of the convective boundary layer. The methods for calculating various heights are presented in Chapt. 4 (Albright et al., 2022).

The first layer corresponds to a well-mixed layer in q and θ , which also corresponds to the distribution of relative humidity maxima, and has a mean depth of 500 m for individual soundings and 570 m for circle-mean data (Fig. 5-3a,b). A layer that is well-mixed vertically in q and θ has previously been called the mixed layer (e.g., Malkus, 1958; Augstein et al., 1974), and we adopt this same terminology. The buoyancy variable, θ_v , however, remains better-mixed over a deeper layer. Such a layer that is better-mixed deeper in θ_v than q and θ individually was observed previously and referred to as the subcloud layer, given its correspondence with environmental-mean lifting condensation levels (e.g., Malkus, 1958; Augstein et al., 1974; Nicholls and Lemone, 1980; Yin and Albrecht, 2000), even though the naming can be misleading because clouds already start to form *below* the top of this layer (Fig. 5-3c). Indeed, calculating the lifting condensation levels from individual soundings results in a distribution that is closer to the mixed layer top distribution (Fig. 5-3a). This subcloud layer top has a mean depth of 710 m in individual soundings and 708 m in circle-mean data. This height analysis suggests that there is some ambiguity in the determination of the boundary layer depth. Contrary to expectations from cloud-free boundary layers, a conceptual picture emerges from this height analysis of two distinct vertical layers, in individual soundings as well as more aggregated data.

We associate this ambiguous region between the mixed layer top and subcloud layer top with the transition layer (Malkus, 1958) and define it as the difference

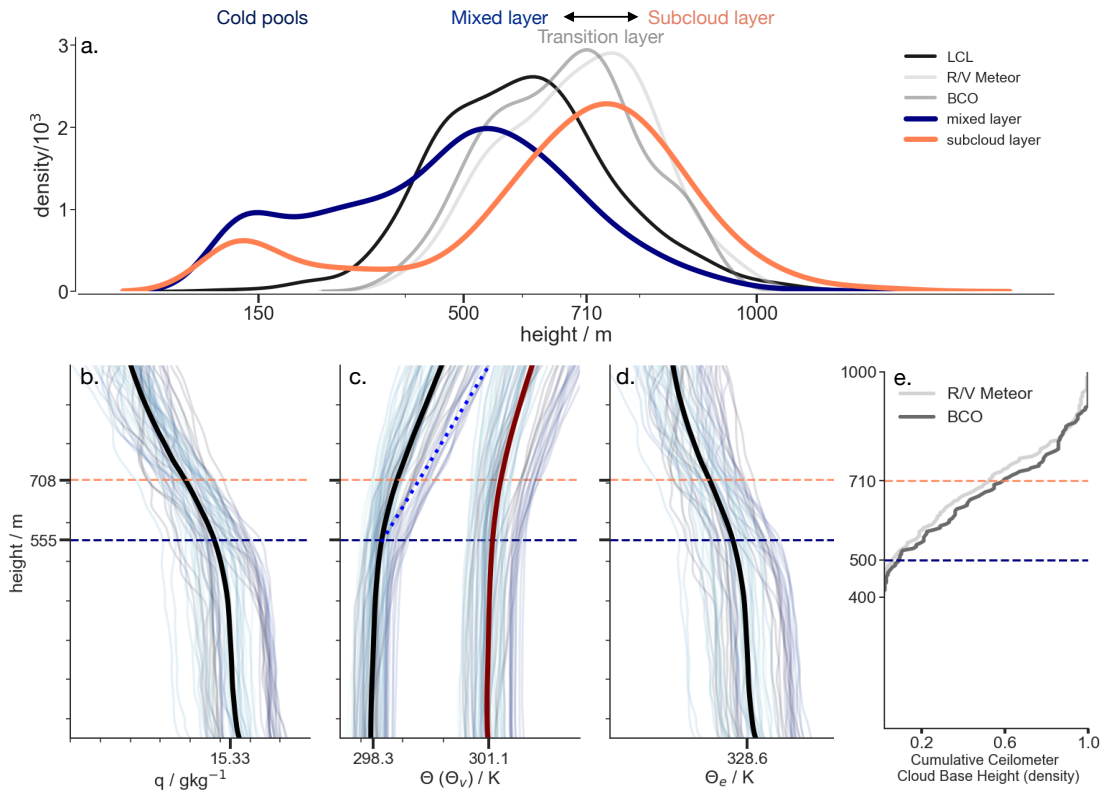


Figure 5-3: Figure adapted from Chapt. 4 (Albright et al., 2022). (a) Distributions of different height methods, as described in Albright et al. (2022) and Sec. 5.4.1, applied to 810 dropsondes to estimate the mixed and subcloud layer heights. Three methods (averaged in the blue curve) based on q and θ , individually and relative humidity correspond to the mixed layer, whereas the θ_v -gradient and parcel method based on θ_v , a proxy for buoyancy correspond to what is often called the subcloud layer height (averaged in the orange curve). Also shown are the distribution of lifting condensation levels calculated for individual dropsonde soundings averaged from 100–300 m air parcels (black) and ceilometer cloud base height estimates from the R/V Meteor and BCO (two grey curves). Cold pool soundings correspond to the distribution around 150 m height. Mixed layer heights lower than 400 m generally correspond to simulations with cold pools (Touzé-Peiffer et al., 2022). Shown in the bottom panels are 69 circle-mean profiles for (b) q , (c) θ , θ_v , and (d) θ_e . The black line is the time-mean across all profiles, and colored profiles go across time (from darker to lighter blue). Dotted lines mark the mixed layer height (blue) and subcloud layer height (orange) calculated using circle-mean data. Their difference indicates the presence of a transition layer. Note that the mixed layer and subcloud layer height values in panel b. are calculated from circle-mean profiles, explaining the difference in heights with panel (a) calculated from individual dropsonde soundings. Shown in panel (e) is the empirical cumulative distribution function (CDF) of aggregated ceilometer cloud base height distributions measured by the R/V Meteor and at the BCO, as described in Sec. 5.3.

between the subcloud layer top and mixed layer top. Using individual dropsondes and taking the difference between the top of the subcloud layer and mixed layer distributions yields a transition layer thickness of 180 ± 207 m, with the values denoting the mean and standard deviation. The values are 151 ± 77 m for circle-mean and 152 ± 50 m for circling-mean data, converging towards a mean depth of about 150 m and smaller standard deviation for increasing scales of averaging. The transition layer therefore appears to have about 100–200 m depth, within the range given in previous observational studies (e.g., Malkus, 1958; Augstein et al., 1974; Yin and Albrecht, 2000), but contrasting with the thin transition layer view from modeling.

5.4.2 Transition layer stability

Previous conceptualizations of the transition layer contend that the transition layer acts as a barrier or cap to convection (Sec. 5.2), which would suggest relatively strong thermodynamic gradients. The transition layer gradients given in Malkus (1958) and Augstein et al. (1974) are a useful point of comparison. Fig. 5-4 shows that transition layer θ_v gradients observed during EUREC⁴A (black line) are, on average, weaker than those in Malkus (1958) and Augstein et al. (1974) (red lines). Specific humidity gradients are similar, and the weaker θ_v gradient in EUREC⁴A is driven by a weaker θ gradient. We speculate that the reason for the greater stability implied by the mean profiles in Malkus (1958) and Augstein et al. (1974) is their smaller sample size and that their sampling was not entirely unbiased, compared to the extensive, unbiased sampling in EUREC⁴A. Malkus (1958), for instance, launch 16 out of their 25 soundings into extended cloud-free regions, whereas the other nine soundings explicitly targeted active cloud cores. Augstein et al. (1974) analyze a larger set of soundings from field campaigns in 1965 and 1969. Soundings are, however, removed when a transition layer was not apparent, which could bias results towards stronger transition layer gradients. During EUREC⁴A, strong gradients with the magnitude of those in Malkus (1958) and Augstein et al. (1974) are seen, but they occur infrequently (Fig. 5-4).

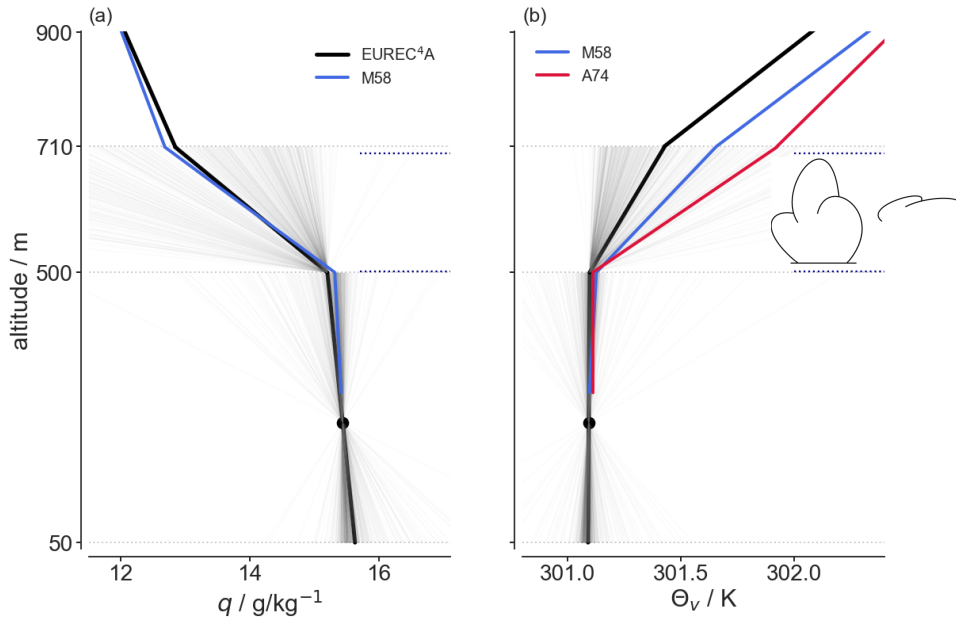


Figure 5-4: Composite profiles of (a) specific humidity, q , and (b) virtual potential temperature, θ_v . The profiles are constructed from the mean mixed layer value; mean gradients over the mixed layer, transition layer, and lower cloud layer; and mean heights of the mixed layer and transition layer top. Heights are estimated from EUREC⁴A sounding data. EUREC⁴A data are plotted in black, both the campaign-mean (thick black line) and individual dropsondes (thin grey lines), with the mixed layer mean value indicated by the black dot. Blue and red profiles use vertical gradients from previous studies; the mean value adjusted to the mean mixed layer value in EUREC⁴A such that transition layer gradients can be more easily compared. M58 (blue) corresponds to Malkus (1958), and A74 (red) refers to Augstein et al. (1974). θ_v gradients are given in Augstein et al. (1974), but for Malkus (1958), θ_v values are calculated from observed temperature, mixing ratio, and pressure profiles in her Fig. 7. Note, moreover, that the visualization in Fig. 5-4 exaggerates the extent of the strongest vertical gradients by extrapolating these strong vertical gradients, which are often found over short distance, over the mean depth of the transition layer. Based on our view, clouds are shown as having their bases at the mixed layer top, rather than the transition layer top as in Augstein et al. (1974) and Malkus (1958). Also shown are the 25th- and 75th-percentile of lifting condensation levels (LCL) calculated from individual dropsondes, averaging LCL values from 100–300 m air parcels (blue dotted lines).

5.4.3 Cloud bases form within the transition layer

Another difference with Malkus (1958) and Augstein et al. (1974) is that the majority of cloud bases are already found *within* the transition layer, instead of above its top. Decreasing θ_e over the transition layer (Fig. 5-3b), a necessary but not sufficient condition for a conditionally unstable layer, hints at a potential role for convective processes in this layer. Examining ceilometer cloud base estimates, about 60% of 3-h-cloud base peaks occur below what is typically called the subcloud layer top height. A cumulative distribution of these cloud base heights is given in Fig. 5-3c, showing that the R/V Meteor has 61% of cloud base peaks below 710 m (55% for BCO). Below 500 m, approximately the mixed layer top height, 6% of clouds measured by the R/V Meteor ceilometer already have their bases (9% clouds at BCO). More recent conceptual modeling studies have also assumed that clouds already have their bases within the transition layer (Neggers et al., 2009; Gentine et al., 2013).

Given that the majority of clouds already have their bases within the transition layer, we conjecture that cloud-mediated processes could play a role in creating its structure. Many clouds may continue to grow above the transition layer, yet a substantial fraction of clouds both form and dissipate within the transition layer. When clouds form, they warm and dry the ambient environment, and when they dissipate, they cool and moisten the environment, such that this air takes on properties that more closely resemble mixed layer air. Such cloud-driven processes could ‘precondition’ the surrounding air and reduce the work to entrain more-buoyant air into the mixed layer. We thus hypothesize that 1) the structure of the transition layer is an important way in which the cloudy boundary layer differs from a cloud-free, or dry boundary layer and 2) these different vertical structures could reflect differences in entrainment and vertical mixing processes. These hypotheses can directly be tested using EUREC⁴A observations.

5.5 Physical origins of transition layer structure

The idea that the presence of clouds changes the transition layer structure is tested through a denial-of-mechanism approach. A distinction is made between a cloud-free convective boundary layer, or a convective boundary layer without clouds at its top over scales much larger than the depth of the layer (e.g., cloud-free over scales greater than 10 km), as compared to cloud-topped convective boundary layers. Large clear-sky areas, rather than simply clear-sky areas in between clouds, are selected because the area between clouds is still influenced by cloud condensate detrainment and mixing from these previous, ‘ghost’ clouds. Such large clear-sky areas are identified in two ways: first, by eye, from GOES-E satellite movies at one one-minute resolution overlain with dropsonde locations and times (Bony et al., 2022); and second, in Sec. 4b, using the cloud flag product from WALES lidar as introduced in Sec. 5.3.

Fig. 5-5 illustrates two case studies, for January 22 (Fig. 5-5a–e) and February 2 (Fig. 5-5f–i), both of which exhibit large clear-sky swaths. In each case, GOES-E satellite movies are used to identify one dropsonde from an extensive cloud-free area, spanning the diameter of the EUREC⁴A circle, and another sonde that is more influenced by clouds. The cloud-free sondes exhibit a well-mixed layer structure topped by a jump. In the non-cloud-free cases, a discontinuity is not visible, and instead there are smoother vertical gradients (Fig. 5-5). Fig. 5-6 shows that large domain large-eddy simulations ($O(100\text{ km})$) exhibit a similar vertical transition layer structure of stronger vertical gradients in large clear-sky areas than in areas influenced by clouds. These simulations further support that smoother vertical gradients in cloudy areas are not spurious observational error (e.g., slower sensor response times if a sonde became wet after passing through clouds, smoothing vertical gradients, cf. Albright et al. (2022)) and represent a physical difference to better understand.

To next test whether the expected difference between cloud-free and cloudy profiles generalizes across the 810 dropsondes, the maximum vertical gradient (over 10 m) is calculated for all dropsonde vertical profiles of specific humidity, q , between 300–800 m. This maximum vertical gradient metric captures the strongest jump that is

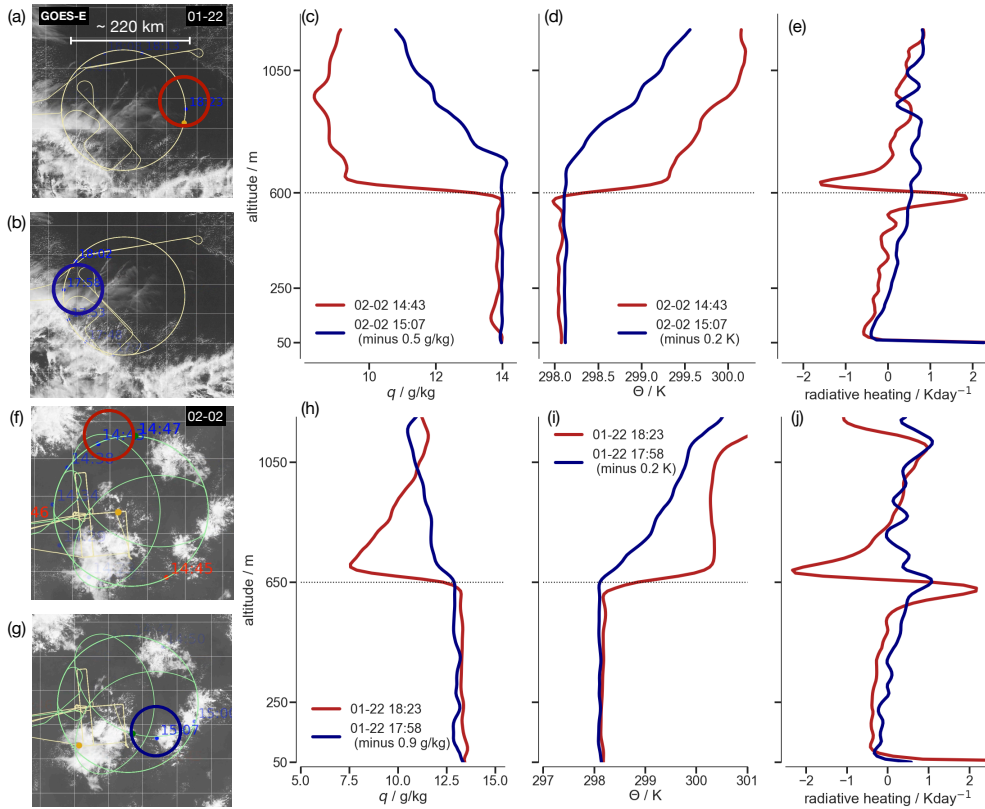


Figure 5-5: Two pairs of dropsonde profiles for specific humidity, q , potential temperature, θ , and net radiative heating wherein one sounding per pair is launched in large clear-sky area (red) and the other in an area influenced by clouds (blue). Pairs of dropsondes are from January 22 (top panels) and February 2 (bottom panels). Also shown are their corresponding GOES-E satellite images (a,b and f,g). The sonde times are given in the legends for dropsonde profiles, and the sonde location (outlined in blue or red circle) is overlain on the satellite image. Note that the vertical profiles are aligned to have approximately the same mixed layer mean value to better compare the transition layer structure; offsets are given in the legend.

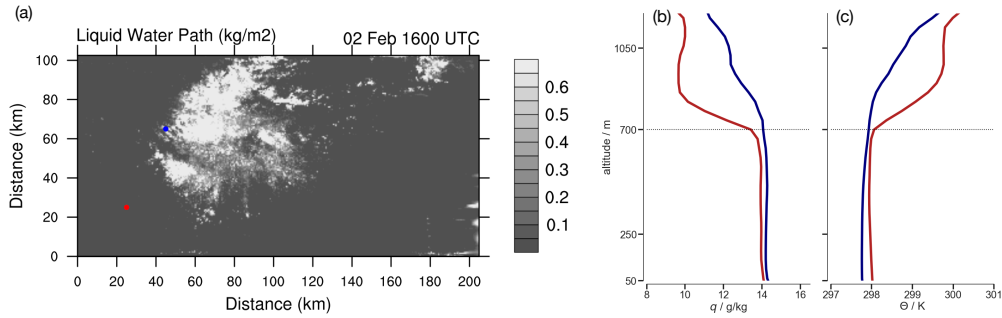


Figure 5-6: Panel (a) shows the liquid water path in a 200x100 km domain simulation of trade-wind cloudiness (‘flower’ pattern) in Dauhut et al. (2022). A representative profile is selected in a large cloud-free area (red) and in an area influenced by cloudiness (blue), whose locations are shown in panel (a). Corresponding specific humidity (b) and potential temperature profiles (c) are also shown. Profiles in different locations around the cloud edge or within the cloud are similar to the selected profile in blue, and other profiles in large cloud-free areas are similar to the red profile.

evident in an observed boundary layer moisture profile. The lower bound of 300 m is chosen to avoid possible surface layer influences, and 800 m acts as a conservative estimate of the mixed layer top. Results are similar for different choices of lower and upper bound. The vertical layering of the atmosphere is present in numerous variables, but particularly evident in moisture (e.g., Augstein et al., 1974), motivating our choice of q , though results are similar for other thermodynamic variables.

Fig. 5-7 shows that the majority of soundings have small values of this maximum vertical gradient metric, corresponding to smooth gradients at the mixed layer top. The 25th-percentile and median values of the maximum vertical gradient are 0.17 and 0.25 gkg^{-1} compared to a standard deviation of 1.06 gkg^{-1} for q averaged from 100–500 m. Examining vertical gradients above the 95th-percentile compared to satellite images, larger values are shown to systematically occur in large clear-sky areas. Fig. 5-7b-e shows satellite images for two days having numerous soundings making up the largest-5% vertical gradient values. On these days, large clear-sky frequently extend across the EUREC⁴A circle. This analysis provides an initial indication of an association between sharp gradients in thermodynamic profiles and large, cloud-free areas.

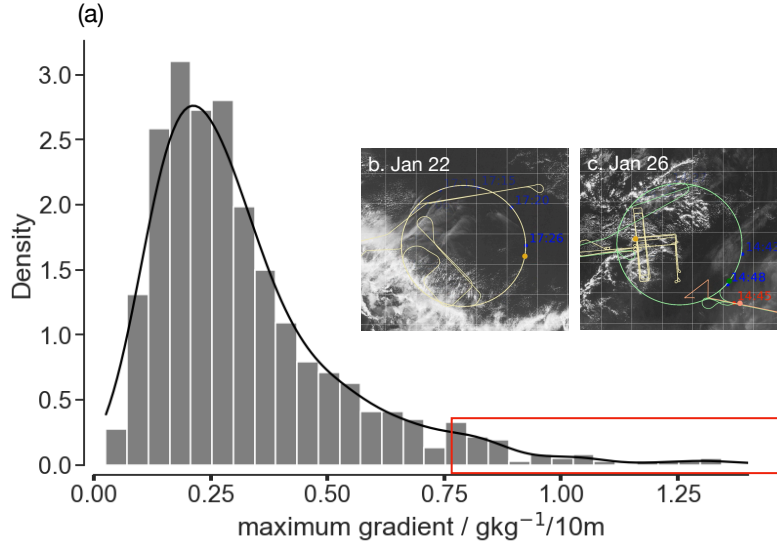


Figure 5-7: Distribution of the maximum vertical gradient (across 10 m) found in a given specific humidity, q , profile between 300–900 m. The red box highlights the largest-5% vertical gradients. Shown in the inset panels (b,c) are two example GOES-E satellite images illustrating large clear-sky swaths from which profiles with the largest-5% vertical gradients are sampled.

5.5.1 Two populations of clouds

A population of clouds is identified that we hypothesize is responsible for changing vertical gradients in the transition layer relative to cloud-free conditions. Fig. 5-8 shows the distribution of cloud top heights estimated from the WALES lidar (Sec. 5.3, cf. Jacob et al. (2020)). This cloud top height distribution is bimodal, with peaks around 850 m and 1900 m. The bimodality in cloud top heights was previously identified (e.g., Genkova et al., 2007; Leahy et al., 2012), but the uncertainty on these early observational estimates (250–500 m) was large compared to the depth of the first cloud population and offset between shallow and deeper clouds, and much larger than the uncertainty in the WALES cloud top height data. There is an apparent scale separation around 1300 m, which also corresponds to the value used to separate two cloud populations simulated at the Barbados Cloud Observatory by large-eddy simulations in Vial et al. (2019). The first peak is associated with shallow, likely non-precipitating clouds, and the second peak is associated with deeper, potentially

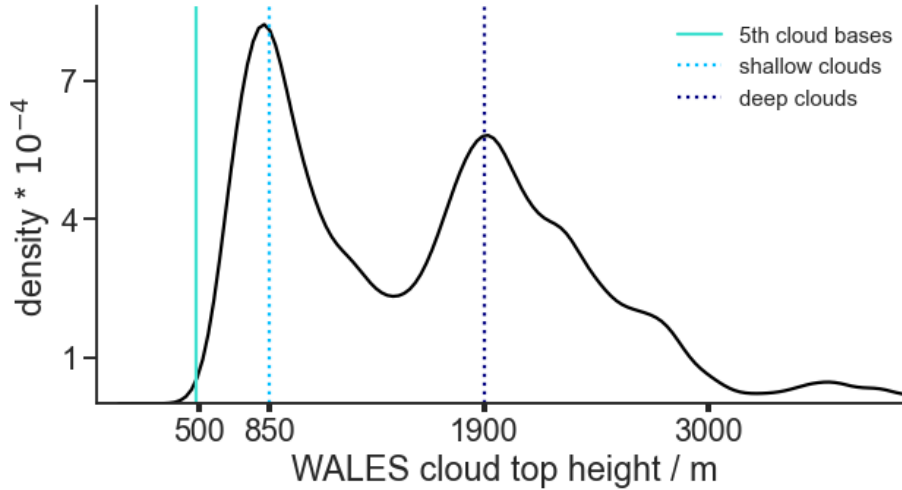


Figure 5-8: Distribution of cloud top heights estimated from WALES lidar data as described in Sec. 5.3. Vertical dashed lines correspond to approximately the peaks in the bimodal distribution, around 850 m for shallower and 1900 m for deeper clouds. The solid turquoise line marks the 5th cloud base heights from R/V Meteor and BCO ceilometers, giving a lower bound of cloud base heights.

precipitating clouds (Lonitz et al., 2015) and stratiform clouds resulting from detrainment near the trade-wind inversion around 2–3 km. Shallow clouds are more frequent than deeper clouds, and they appear to vary relatively little in height, with a standard deviation of 184 m for cloud tops below 1300 m (Fig. 5-8).

5.5.2 Shallow clouds appear to produce transition layer structure

To test how shallow clouds influence the transition layer structure, the maximum vertical gradient distribution (Fig. 5-7) is revisited, but conditioned on scenes using cloud top height estimates. The goal is to isolate large clear-sky swaths that are relatively free from cloud influences and compare the transition layer structure in this cloud-free case versus other cases. Using the WALES cloud flag and cloud top heights, measurements are separated into three categories: large clear-sky areas, cloudy areas with cloud tops below 1.3 km (shallow clouds, e.g. Fig. 5-8), and all areas that are not large clear-sky areas, including cloudy and smaller cloud-free areas (overlapping with the second category). This separation allows us to test whether 1) large clear-sky

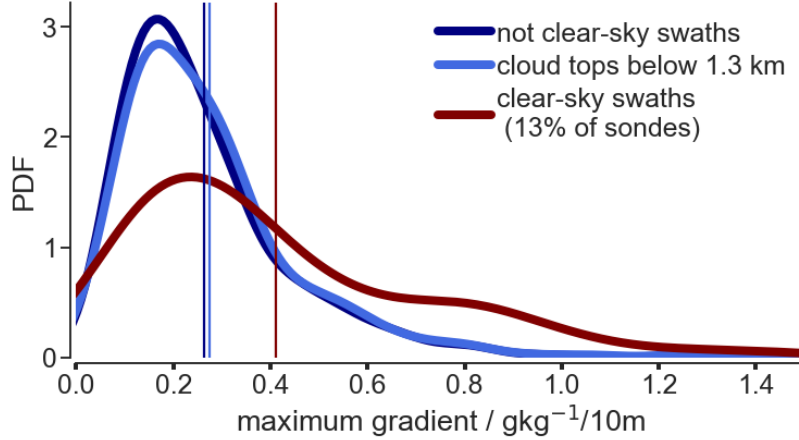


Figure 5-9: Similar to Fig. 5-7, except with distributions conditioned on large clear-sky scenes of at least 15 minutes without encountering a cloud (red), shallow clouds with cloud top heights estimated from WALES lidar data below 1.3 km (light blue), and all areas outside of large clear-sky scenes (dark blue). Each colored vertical line is the mean of the distributions.

areas do systematically exhibit stronger vertical gradients in the transition layer, and 2) the presence of shallow clouds is sufficient to change the transition layer structure from the cloud-free boundary layer case, independent of the influence of deeper clouds.

Large clear-sky areas are selected by first identifying all cloud-free segments using the cloud flag, calculating the 95th-percentile of segment lengths, and then considering segments that are greater than this 95th-percentile as large clear-sky areas. These large cloud-free patches correspond to 15 minutes of flight time without encountering a cloud, or about 180 km at a typical flight speed of 200 m s⁻¹. The associated dropsondes are then selected for these large clear-sky areas, corresponding to 13% of all dropsondes. For cloudy areas, the disjoint set of the large clear-sky swaths is chosen, including clear-sky in between clouds, shallow clouds, and deeper clouds. The category of shallow clouds is selected by removing cases with cloud tops greater than 1.3 km.

The analysis from Fig. 5-7 is then repeated for these three categories. Fig. 5-9 shows that the maximum vertical gradients are indeed stronger in large clear-sky areas than other scenes. The distribution of gradients estimated for shallow clouds is, moreover, nearly identical with the distribution of gradients for all conditions (includ-

ing deeper clouds), suggesting that the presence of shallow clouds is sufficient to cause mixing that smooths vertical gradients relative to cloud-free conditions. From this conditional sampling, a physical picture emerges that the life cycle of shallow clouds forming and dissipating in the transition layer changes vertical gradients relative to cloud-free conditions. The proposed physical mechanism — when shallow clouds dissipate or detrain about 100 m above where they form, they cool and moisten the environment, such that the ambient air more closely resembles the mixed layer properties — is consistent with the observed differences in transition layer structures in Fig. 5-9.

5.6 The effects of a cloudy transition layer

Clouds appear to be responsible for the observed transition layer structure and its deviation from what might be expected for the case of a dry convective boundary layer. It is less clear to what extent the emergence of a cloudy transition layer matters for the evolution of the mixed layer, and hence the net air-sea exchange of energy and moisture.

Using ‘mixing diagrams’ (Paluch, 1979) and mixed layer theory allows for comparing the structure of the lower atmosphere in what was above (Sec. 5.5) called ‘cloud-free’ and ‘cloudy’ profiles. This permits for quantifying the efficiency of mixing in the two cases, and the extent to which differences in the structure the atmosphere above the mixed layer imprints itself on the mixed layer properties, irrespective of the rate of mixing.

5.6.1 Mixing diagrams and mixed layer theory

To answer these questions, it is useful to apply mixed layer theory to mixing diagrams. To introduce the ideas, we first examine the campaign-mean sounding through the lower 3. Fig. 5-10 presents the mixing diagram of this sounding using potential temperature, θ , and specific humidity, q , as thermodynamic coordinates. Each point in this space represents the mean across all 810 dropsondes at a given height. A

mixed layer shows up as a cluster of points around a single value, which in the case of Fig. 5-10 is around $q = 15.4$ and $\theta = 298.3$. Adiabatic mixing between layers of the atmosphere with distinct thermodynamic properties will scatter along a line spanning the space between the points that characterize the respective layers (e.g., Paluch, 1979; Betts and Albrecht, 1987; Heus et al., 2008; Böing et al., 2014). Fig. 5-10 shows that the same mixing line includes both the mixed and transition layers. This structure suggests that air in the transition layer is entrained into the mixed layer. The observed mixing line only changes its slope around 900 m, above the top of the subcloud layer, suggesting that air above this height is no longer directly incorporated into the mixed layer. For reference, Fig. 5-10 also plots the fundamental lines defined by constant θ_v and constant θ_e lines. This visualization shows that the subcloud layer, whose points are roughly aligned with a line of constant θ_v , are better mixed in this quantity than in terms of either q or θ . The constant θ_e line shows the slope that a saturated, cloudy updraft would follow. The mixing line in the cloud layer more closely approaches a constant θ_e line, suggesting that these two fundamental lines could be taken as limiting distributions for the subcloud versus the cloud layers.

A generalized budget equation for the value of a scalar, $\bar{\vartheta}$ within the mixed layer, is derived in Appendix A and can be expressed as,

$$\bar{\vartheta} = \frac{\vartheta'_0 + A^*\vartheta_1}{(1 + A^*)} \quad \text{with} \quad \vartheta'_0 = \vartheta_0 + Q_\vartheta \frac{h}{V_0}. \quad (5.1)$$

This represents two point mixing between air above the boundary layer, whose properties are given by ϑ_1 , and surface values (denoted by ϑ_0) as modified by non-turbulent processes, i.e., advection, storage, or radiative heating. The strength of these non-turbulent processes are measured by Q_ϑ and act on a timescale $\tau = \frac{h}{V_0}$, with h the mixed layer depth and V_0 the surface exchange velocity (drag coefficient-weighted 10 m wind speed, see Appendix A). Eq. 5.1 introduces an important quantity, A^* , a non-dimensional entrainment rate, which defines the non-dimensional entrainment velocity $E = A^*V_0$. It weights the influence of the surface (and non-turbulent processes) and the properties of the air being incorporated into the mixed layer on the

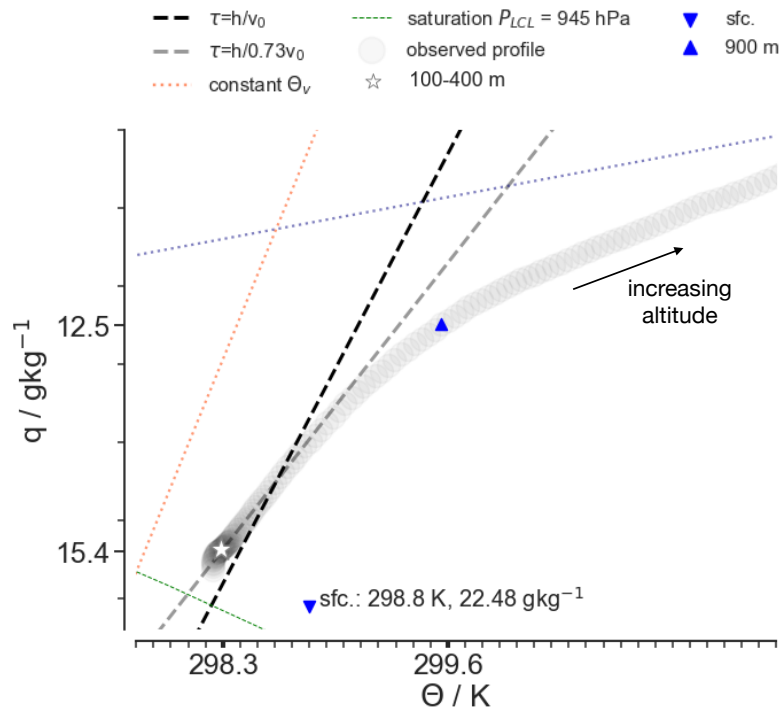


Figure 5-10: Scatter plot of observed q and θ values up to 3 km (grey points) and theoretical mixing lines from the surface to 3 km (black and grey dashed lines). Also shown are the campaign-mean surface value (blue downward triangle), value averaged from 100–400 m (white star), value at 900 m (blue upward triangle), constant lifting condensation level at 945 hPa (green dotted line), constant θ_v line (orange dotted line), and constant θ_e line (dark blue dotted line). Theoretical mixing lines are calculated from Eq. 5.1, as described in Sec. 5. The black dashed line is the theoretical mixing line incorporating air from 10–150 m above the mixed layer layer. The grey dashed line multiplies the surface wind speed by 0.73.

state of the layer.

We use Eq. (5.1) to calculate theoretical mixing lines whose slopes depend on the choices of q_1 and θ_1 and whose end points are given by ϑ'_0 , varying A^* . To calculate ϑ'_0 we used the observed ϑ_0 , Q_ϑ , and $\frac{h}{V_0}$ values from the soundings. We then find the best-fit mixing line to the observations. In Fig. 5-10, demonstrates how the best-fit mixing line to observations coincides with air from 10–150 m above the mixed layer top – that is, it incorporates transition layer air into the mixed layer. Theoretical mixing lines increasingly diverge when deeper air is incorporated into the mixed layer. This analysis suggests that the transition layer is part of the same mixing layer as the mixed layer, and that the mixed layer properties can be conceptualized as two point mixing between air at the top of the transition layer and air imbued with surface properties modified by non-turbulent processes, as measured by Q_ϑ acting on the timescale given by $\frac{h}{V_0}$.

The agreement of this theoretical mixing line, incorporating air from within the transition layer, with the observed values can be empirically improved by increasing $\tau = \frac{h}{V_0}$, for instance by multiplying the wind speed by a factor 0.73 in the V_0 term (Fig. 5-10, grey dashed line). These adjustments suggest potential limitations in how the surface exchange velocity is represented, or the effects of missing source terms, such cloud induced perturbations to the radiative heating. Fig. 5-10a also plots q - θ values corresponding to a constant lifting condensation level at 945 hPa. The observed and best-fit theoretical mixing line are nearly perpendicular to the constant lifting condensation level curve. Whether this is a coincidence, or whether mixing aligns to maximize variance in the lifting condensation level, merits further study.

Effect of a cloudy transition layer on entrainment

Given the mixing line connecting ϑ'_0 with ϑ , the non-dimensional entrainment rate, A^* , can be measured by inverting Eq. 5.1. By deriving A^* from cloud-free and cloudy profiles it should be possible to identify if the presence of a cloud-maintained transition layer leads to substantial changes in the rate of boundary layer deepening, i.e., greater values of A^* .

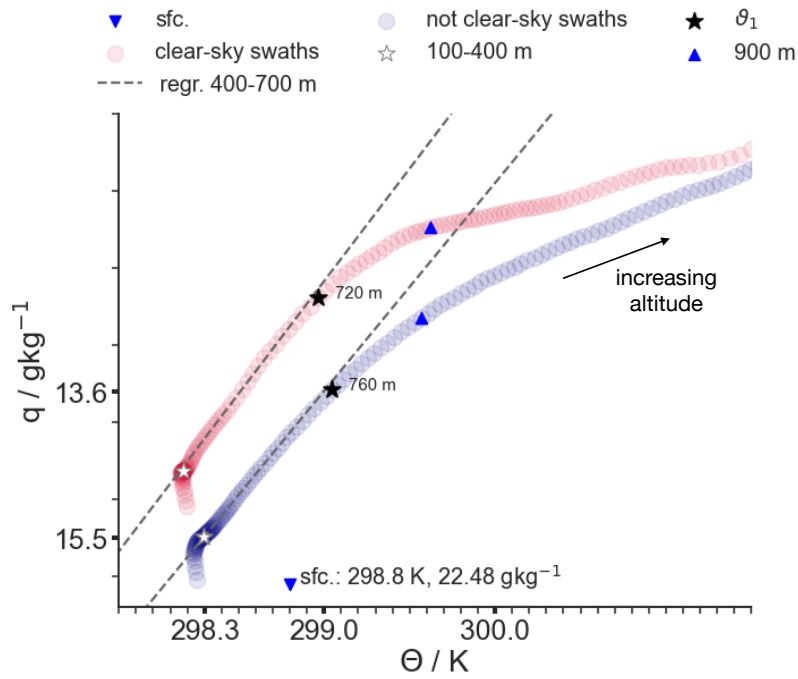


Figure 5-11: As in Fig. 5-10, but for q and θ soundings aggregated for large clear-sky areas (red) and areas influenced by cloudiness (blue, following the conditional sampling in Fig. 5-7). Also shown are the campaign-mean surface value (blue downward triangle), value averaged from 100–400 m (white star), θ_1 value annotated with its height (black star), and value at 900 m (blue upward triangle). Data-derived mixing lines are linear regressions to the observed profile from 400–700 m (grey dotted lines).

To see if clouds influence the value of A^* we compare mixing diagrams for large clear-sky areas and areas influenced by cloudiness (following the sampling in Fig. 5-7). The resulting mixing diagrams are shown in Fig. 5-11. Both seem to show that the cluster of mixed layer points lie at about the same distance along the mixing line, suggesting at least that differences in A^* are subtle. More quantitatively, given $\{\vartheta'_0, \bar{\vartheta}, \vartheta_1\}$, Eq. (5.1) can be inverted for A^* . We follow this procedure for each case, estimating ϑ'_0 by assuming both cases have the same ϑ_0 , but allowing Q_ϑ to vary (giving $\theta'_0 = 297.1\text{K}$ and $q'_0 = 21.1$ for the clear-sky and $\theta'_0 = 297.1\text{K}$ and $q'_0 = 21.4$ for the cloudy profile). In this case, ϑ_1 is chosen as the point where a data-derived mixing line (a linear regression to observations from 400–700 m) departs from the observations by 0.1, a point whose location and height are included on the diagram. This analysis suggests that A^* is slightly larger in the cloudy than cloud-free case. A^* calculated from q equals 3.1 for the clear-sky profile, and $A^*=3.3$ for the cloudy profile; for θ , $A^*=1.5$ for the clear-sky and $A^*=1.7$ for the cloudy profile. This finding remains robust for a range of choices regarding ϑ_1 and data-estimated mixing lines. Mixed layer theory would not lead one to expect differences between A^* calculated with q versus θ ; however the estimates do not diverge as much as they seem. A roughly 0.2 increase in $\bar{\theta}$ leads to commensurate values of A^* , about 3, for both estimates.

That our analysis does not identify a strong change in the deepening rates, A^* , of cloud-free, versus cloudy boundary layers, suggests that the clouds are not influencing the mixing directly. The main difference of the cloud case seems rather to be that it leads to a thicker transition layer — consistent with our previous hypothesis that very shallow clouds maintain the transition layer— and modifies the properties of the air that is being incorporated into the mixed layer.

Effect of a cloudy transition layer on the mixed layer

That the differences in the transition layer state influence the mixed layer and hence surface fluxes is apparent in Fig. 5-11. The mixing line of the cloud-free soundings is clearly distinct from that of the cloud soundings, mostly by virtue of the value of ϑ_1 .

Were this not the case we would expect the value of ϑ_1 to lie on the mixing line of the cloudy soundings, albeit extending to a drier and warmer state. That this is not the case can mostly be attributed to differences in q_1 , suggesting that the main role of the clouds is to moisten the transition layer, rather than to cool it, consistent with the heating-cooling couplet of non-precipitating clouds being within the same mixing layer.

To illustrate this idea, we consider a case of a ‘dry transition layer’. That is, instead of incorporating the campaign-mean transition layer air (averaged between 550–700 m), we incorporate air from higher aloft that is assumed to subside without evaporative cooling of cloud liquid water. This case would imply a stronger jump in the transition layer. To estimate such an example q_1 - θ_1 pair, we consider the campaign-mean specific humidity at 1500 m (having a value of 10.03 gkg^{-1}) and find the corresponding θ value such that the θ_v value at 1500 m equals its mean transition layer value. A constant θ_v is motivated by the idea that gravity waves will remove buoyancy differences at similar levels, e.g., between the observed transition layer value and our ‘dry transition layer’ example. Adopting a q_1 - θ_1 tuple of 10.03 gkg^{-1} and 299.4 K as ϑ_1 values and predicting the mixed layer q - θ pair following Eq. (5.1) yields a predicted mixed layer mean value of 298.9 K and 11.8 gkg^{-1} . We set $A^* = 5$ and otherwise keep terms equal to the values in the adjusted mixing line (grey dashed line in Fig. 5-10). These values are warmer and drier than the prediction using q_1 - θ_1 values in the transition layer, which were 15.44 gkg^{-1} and 298.3 K . This comparison suggests that the presence of a cloudy transition layer leads to a moister and cooler mixed layer. A drier mixed layer would increase surface latent heat fluxes, whereas a warmer mixed layer would decrease surface sensible heat fluxes. These are compensating changes from the point of view of the buoyancy flux. Comparing the predictions in the two example cases, the net influence on the surface buoyancy flux appears, however, to be negligible: the buoyancy flux is 17.69 Wm^{-2} when incorporating air at 1500 m and 17.65 Wm^{-2} when incorporating transition layer air.

5.7 Discussion and conclusions

These analyses suggest that the transition layer structure is predominantly determined by cloudy, not dry processes. An offset exists between mixed and subcloud layer tops in individual soundings, as well as more aggregated vertical profiles, and we associate this offset with a transition layer. Strong vertical gradients at the mixed layer top are only found rarely and when they occur, they tend to occur in scenes that are cloud-free over large ($O(200\text{km})$) areas. In areas influenced by clouds, vertical gradients are instead smoother, extending over a larger depth. Analysis of ceilometer data from several sites suggests that the transition layer is populated by small clouds that have their bases near the top of the mixed layer and tend to only grow a few hundred meters above these bases.

Based on these findings, we propose a conceptual picture of the transition layer maintained by the formation and dissipation of shallow clouds. This layer is in some senses analogous to the maintenance of the trade-wind inversion by deeper clouds, as proposed by Riehl et al. (1951) and derived theoretically by Stevens (2007). Riehl et al. (1951) describe the physical mechanism behind this maintenance of the trade-wind inversion layer by deeper clouds:

“It is well known that the bases of the cumuli have a nearly uniform height, but that the tops are very irregular. Some are found within the cloud layer, many near the inversion base, and some within the inversion layer as active clouds penetrate the base. As shown by visual observation and many photographs, the tops of these clouds break off and evaporate quickly. In this way moisture is introduced into the lower portions of the inversion layer, and the air there situated gradually takes on the characteristics of the cloud layer.”

In this view, overshooting convective plumes collapse or break off and, in the process, inject condensate into the trade-wind inversion layer. The evaporation of this condensate maintains the depth of the cloud layer against compensating subsidence,

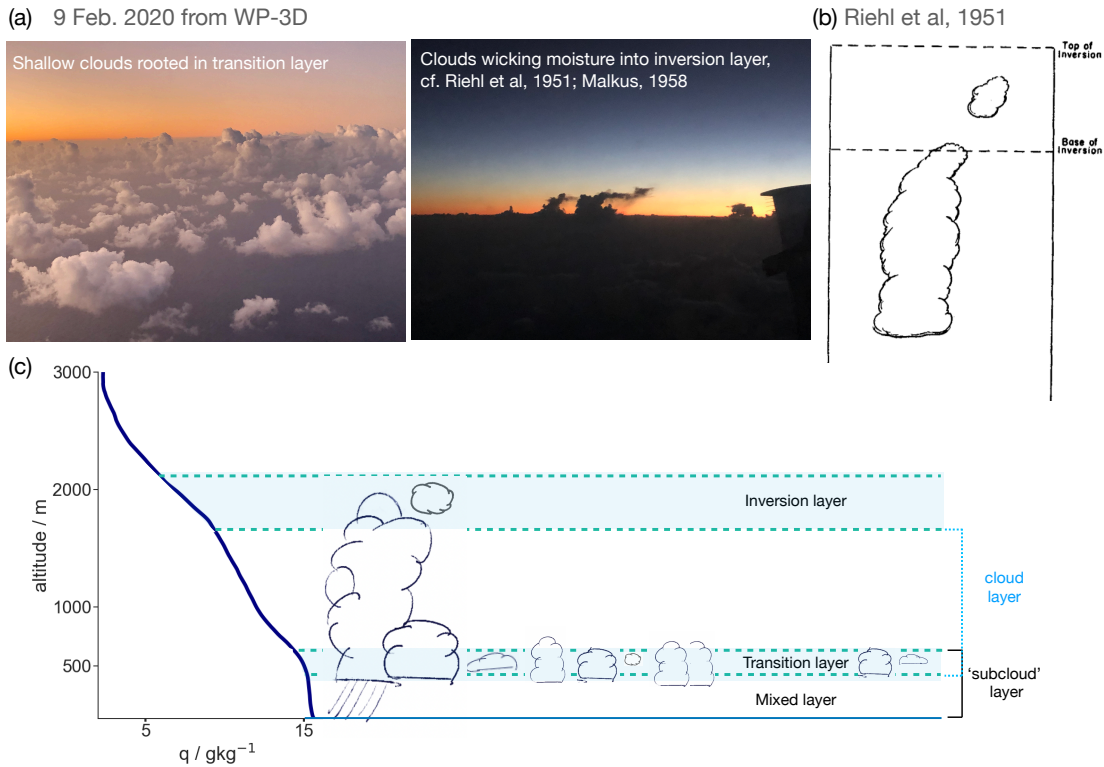


Figure 5-12: (a) Photos taken during a EUREC⁴A flight in the WP-3D aircraft that illustrate the ubiquity of very shallow clouds, often with their bases in the transition layer (left panel), and deeper clouds wicking or injecting moisture to maintain the inversion layer (right panel) as in the mechanism proposed by Riehl et al. (1951). (b) Reproducing a schematic from Riehl et al. (1951) who proposed that the evaporation of deeper clouds maintains the trade-wind inversion layer. (c) Illustration of a conceptual picture suggesting a symmetry between deeper clouds growing and maintaining the trade-wind inversion layer following Riehl et al. (1951) and Stevens (2007), and shallower clouds growing the transition layer. The formation and dissipation of shallow clouds in the transition layer moistens and cools (denoted by the transparent blue area) the transition layer, rendering gradients smoother and weaker compared to the dry boundary layer case.

which dries and warms and shrinks the layer. These ideas are also illustrated by Fig. 5-12b reproduced from Riehl et al. (1951). In a similar way, clouds evaporating in the transition layer grow and maintain the transition layer compared to the abrupt discontinuity observed in the cloud-free boundary layer case. The transition layer then more closely resembles the properties of the mixed layer. These findings suggest a symmetry between shallow and deep clouds, with each population growing its own layer, as illustrated schematically in Fig. 5-12c. These results also suggest that small clouds beget larger clouds. Small clouds ‘precondition’ the large-scale environment and decrease the resistance to convection through weaker vertical gradients in the transition layer, making it easier for deeper clouds to form, similar to the ideas expressed in Neggers (2015), though his preconditioning occurs above what he calls the transition layer in an ‘acceleration-detrainment layer’. Similarly, Janssens et al., in prep show that, in large-eddy simulations, a thicker transition layer with smoothly-varying gradients in q and θ favors the growth of moisture variance that helps promote mesoscale organization of cloudiness.

From this analysis emerges the potential for an additional contribution to the energetics of entrainment mixing, which is based on the ability to detrain condensate whose cooling and moistening lessens the work that needs to be done by entrainment, effectively allowing for values of A_e that are larger than 0.2 (see Fig. 5-13). This view contrasts with the classical view established from dry boundary layers. The classical view of entrainment posits that overshooting plumes must do work on the overlying stratified fluid in order to bring down tendrils or filaments of overlying, more stable fluid and mix it into the turbulent boundary layer below (e.g., Bretherton, 1997) (cf., Fig. 5-13a). Fig. 5-13c, however, highlights how the cloud liquid water dissipation flux allows for more negative ‘effective’ dry buoyancy fluxes and thus larger A_e . The net buoyancy flux is weakly positive in the transition layer due to the compensation between the liquid water flux and more negative dry buoyancy flux. That is, the preconditioning picture of shallow cumuli progressively injecting their moisture and cooling the environment is one of ‘subtle persuasion’ rather than ‘brute force’ entrainment in dry layers. We do not, however, find compelling evidence that

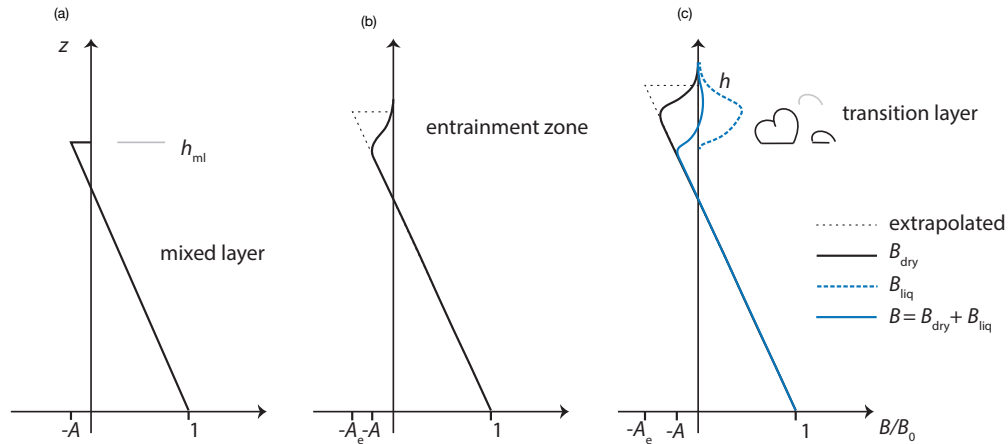


Figure 5-13: Profiles of the ratio of the buoyancy flux to its surface buoyancy flux for different cases, which are used to illustrate the entrainment efficiency, A , or its effective value A_e . Shown in (a) is the classical mixed layer model view of an abrupt discontinuity at the mixed layer top, wherein A is the minimum ratio of the buoyancy flux to its surface value and is found at the layer-top. This view is contrasted with a finite-thickness transition layer in which the minimum buoyancy flux (corresponding to A) is not found at the mixed layer top, but rather A_e extrapolated (in the dotted black line) to the layer-top is the value required to obtain the correct mixed layer heating and cooling rates from the slope of the buoyancy profile. Panel (c) illustrates how the liquid water flux (dotted blue line) can contribute to the net buoyancy flux (solid blue line) and compensate for more negative (extrapolated, dotted black line) dry buoyancy fluxes and larger A_e . The contribution of the liquid water flux can be thought of as an addition ‘boost’ to the energetics of entrainment mixing.

a larger A_e in cloudy conditions implies a greater rate of deepening, but rather that it helps grow an effectively deeper layer.

Building upon findings in Riehl et al. (1951), Stevens (2007), moreover, show that the cloud layer growth could be represented using concepts based on cloud-free, or dry mixed layer theory. He finds that a simple model that is formulated in terms of an ‘effective’ dry buoyancy flux is skillful at predicting the cloud layer growth in large eddy simulations. These findings suggest that cloudy processes can still be represented using cloud-free mixed layer theory if effective parameters are introduced. This result is similar to the findings in Chapt. 4 wherein an entrainment formulation based on mixed layer theory and dry boundary layers was used, but effective parameters were introduced to account for ambiguities resulting from the finite-thickness transition layer, which, as shown here is produced by cloud-mediated processes. Mixed layer theory, with slight modifications, still closes subcloud layer moisture and heat budgets. These considerations highlight that extensive observations from the field, such as from the EUREC⁴A campaign, open the door to revisiting old concepts and testing their applicability when confronted with more extensive new data. This confrontation, in turn, allows for improved understanding of the origins of the characteristic vertical structure of trade-wind air.

Chapter 6

Uncertainty in trade cumulus feedbacks still contributes to uncertainty in global cloud feedbacks in CMIP6

6.1 Outline

In the second part of this thesis, physical understanding developed in chapters 2–5 is applied to the evaluation of general circulation models (GCMs). In previous CMIP ensembles, uncertainties regarding trade cumulus cloud changes were shown to explain large differences in global cloud feedbacks and climate sensitivity (e.g., Bony and Dufresne, 2005; Webb et al., 2006; Vial et al., 2013; Brient and Schneider, 2016). The CMIP6 models have been updated in numerous ways, such as regarding their convection schemes, microphysics schemes, and vertical resolution (e.g., Gettelman et al., 2019; Danabasoglu et al., 2020; Zelinka et al., 2020). It is therefore not *a priori* clear how large a role trade-wind clouds still play in explaining global uncertainties. This chapter uses CMIP6 models to motivate a continued focus on trade cumulus cloud feedbacks. It acts as preparation for Chapt. 7, which presents the first process-based constraint on this trade cumulus feedback. In this chapter and Chapt. 6, Jessica Vial pre-processed the amip and *amip4K* model output and provided valuable

Sec. 6.5 in this chapter contributed to Boucher et al. (2020), published in the *Journal of Advances in Modeling Earth Systems* in May 2020. The remaining analysis is unpublished and served as additional validation for the importance of trade cumulus cloud feedbacks in motivating the EUREC⁴A campaign.

guidance throughout this analysis. The structure of this chapter follows the well-known quip from Winston Churchill (1874–1965) of a ‘riddle wrapped in a mystery inside an enigma’. Here the question is whether the riddle of trade-wind clouds, wrapped in the mystery of tropical clouds, still contribute to enigmas surrounding global cloud feedbacks and climate sensitivity.

6.2 Methods

6.2.1 Estimating equilibrium climate sensitivity

As introduced in Chapt. 1, the equilibrium climate sensitivity (ECS) is one of the earliest metrics for quantifying the climate system response to carbon dioxide (CO₂) forcing (Charney et al., 1979; Cess et al., 1989). As defined in these studies, the top-of-atmosphere (TOA) radiative imbalance, ΔR , can be expressed linearly as the sum of the radiative forcing, F , and the product of a feedback parameter, λ , and the global-mean surface temperature change, ΔT ,

$$\Delta R = F + \lambda \Delta T. \quad (6.1)$$

This product, $\lambda \Delta T$, is also referred to as radiative damping.

The ECS is defined as the global-mean surface temperature change, T_{eq} , that restores a TOA radiative balance, $\Delta R=0$, after a carbon dioxide doubling,

$$ECS = \Delta T_{\text{eq}} = -\frac{F_{2\times\text{CO}_2}}{\lambda}. \quad (6.2)$$

The ECS depends both on the radiative forcing associated with a CO₂ doubling, $F_{2\times\text{CO}_2}$ and the strength of the radiative feedback parameter, λ . A climate system that more effectively reflects shortwave radiation to space, such as through greater low cloud fraction, or more effectively radiates longwave radiation away to space, such through fewer upper-tropospheric clouds, requires less warming, ΔT , to restore a planetary energy balance (e.g., Zelinka et al., 2020; Meehl et al., 2020). A key

assumption is that the radiative damping, $\lambda\Delta T$, in Eq. 6.2 can be expressed as a product of a single, time-invariant feedback parameter, λ , and ΔT . A large body of research has highlighted that the constant λ assumption is imperfect, such as due to different radiative feedbacks actualized on different response timescales (e.g., Armour et al., 2013; Proistosescu and Huybers, 2017) and the state-dependence of feedbacks (e.g., Bloch-Johnson et al., 2015).

Here ECS is estimated following Gregory et al. (2004), similar to Andrews et al. (2012) and Zelinka et al. (2020). Anomalies are calculated as the difference between the first 150 years of global-annual output from *abrupt-4xCO2* simulations (coupled GCM simulations wherein atmospheric CO₂ concentrations are abruptly quadrupled from their preindustrial baseline and then held fixed) and a preindustrial control simulation, *piControl*. Positive radiative fluxes are defined downwards. Note that ECS using 150 years of warming is sometimes referred to as the ‘effective’ climate sensitivity instead of the equilibrium climate sensitivity since the model has not reached equilibrium above 150 years (e.g., Rugenstein et al., 2020; Meehl et al., 2020). Here the two terms are used interchangeably, given the focus on understanding relative differences among models.

Using a subset of 12 CMIP6 models, Fig. 6-1a suggests that there is a bimodal distribution of ECS, with a mean of 4°C and two cluster of models around 3°C and 5°C, which is consistent with the inferences in Zelinka et al. (2020) and Flynn and Mauritsen (2020) who use a larger sample of models. In the following analysis, low and high ECS are defined relative to the CMIP6 mean of 4°C. The second distribution of models having ECS values higher than 5°C was not present in CMIP5, which was unimodal and had a range of 2.1–4.7°C (Taylor et al., 2012; Andrews et al., 2012). As discussed in Sec. 1.2.1, the shift towards higher ECS in the CMIP6 ensemble is thought to result from correcting too-negative extratropical low cloud feedbacks, compared with satellite constraints. This correction then unmasked the consistently too-positive trade cumulus feedbacks, driving high ECS values (Myers et al., 2021).

I explore an additional way of quantifying climate sensitivity that produces a distribution of values and allows for examining the influence of the nonlinear forcing-

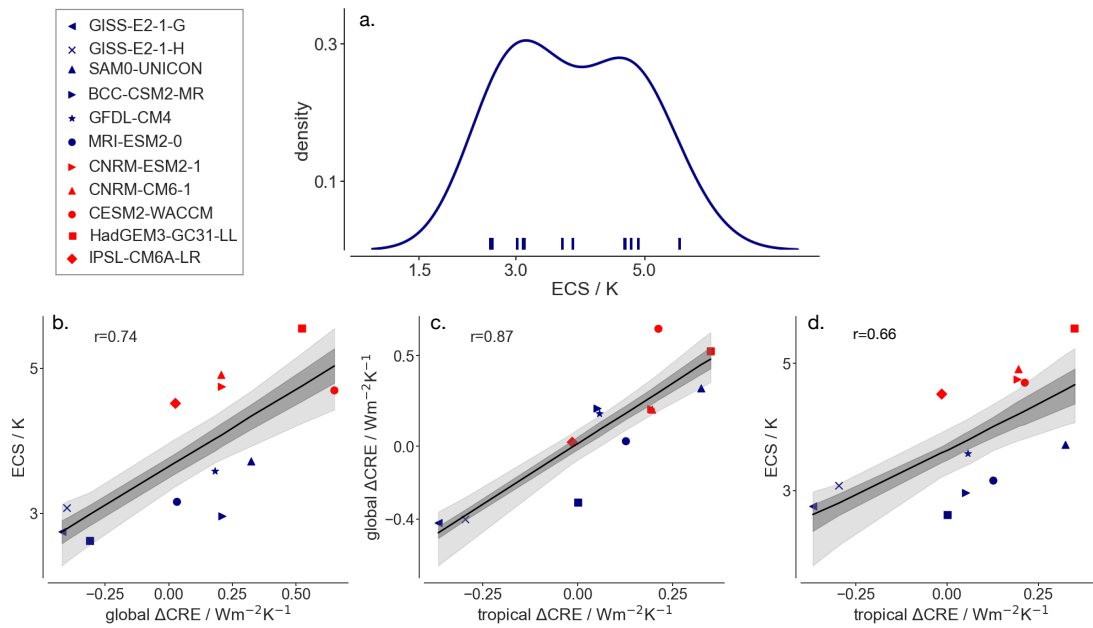


Figure 6-1: (a) Distribution of ECS estimated for the models listed in the legend, and scatter plots of (b) global ΔCRE and ECS (c), tropical ΔCRE and global ΔCRE , and (d) tropical ΔCRE and ECS. High climate sensitivity models, defined as $\text{ECS} > 4^\circ\text{C}$ are red, and low climate sensitivity models ($\text{ECS} < 4^\circ\text{C}$) are blue. 5–95% uncertainty on the linear regression (grey shading) is defined from re-sampling 1000 times with replacement ('bootstrapping').

temperature response relationship. Methodologically, the approach bins annual-mean data, samples one value from each bin, performs a linear regression using one value from each bin, and then repeats this procedure many times (‘bootstrapping’). This ‘binning and bootstrapping’ method contrasts with performing a single linear regression on all data. Binning the data better illustrates a potential nonlinearity in the forcing-response relationship (Fig. 6-2a scatter plot vs. Fig. 6-2b binned data). Repeatedly sampling (for instance 1000 times) yields a distribution, such as for climate sensitivity in Fig. 6-2c. For the IPSL-CM6A-LR model, the mean climate sensitivity from this method is similar to results from the Gregory et al. (2004) regression. Using 300 years of model output, ECS from the Gregory et al. (2004) method is 4.8°C, equal to the mean from the binning and bootstrapping approach. The 5-95% uncertainty from the binning and bootstrapping approach (4.2–5.7 °C) is, however, larger than the 5-95% uncertainty on the regression (4.3–5.2 °C). This larger range in the binning and bootstrapping approach suggests that influences from the nonlinear forcing-response relationship tend to be small but could influence the upper bound, at least for the IPSL-CM6A-LR model as shown in Fig. 6-2. In the following analysis, we, however, return to the Gregory et al. (2004) method for consistency with other studies.

6.2.2 Quantifying cloud radiative responses

In previous ensembles, the spread in cloud feedbacks was the primary driver of the spread in climate sensitivity (e.g., Bony and Dufresne, 2005; Vial et al., 2013; Zelinka et al., 2020). Here we quantify the spread in cloud radiative responses among a subset of models using a simplified metric, the change in the cloud radiative effect (ΔCRE), in order to quantify how much differences in this ΔCRE , globally, in the tropics, and in the trades, contribute to uncertainty in ECS.

The cloud feedback is a component of the radiative feedback, λ , in Eq. (6.1) and Eq. (6.2). A cloud feedback is a change in the top-of-atmosphere radiative flux resulting from a change in cloud albedo (e.g., due to changes in droplet size, water content), fraction, or altitude with warming. A positive feedback denotes that clouds

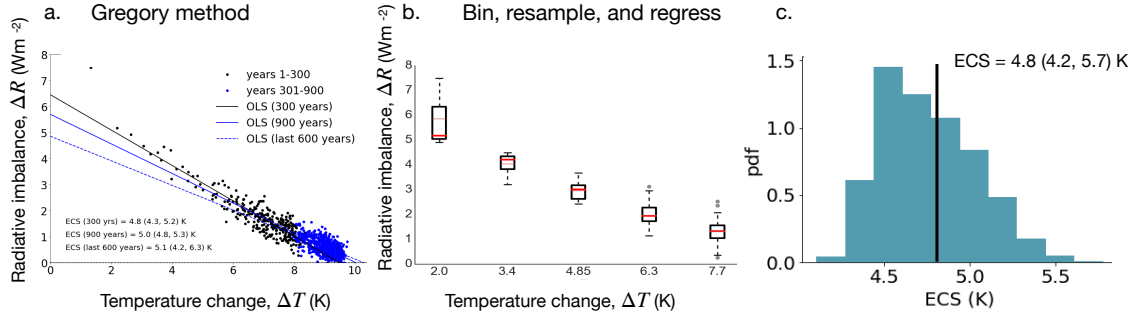


Figure 6-2: (a) Canonical Gregory ordinary least-squares (OLS) regression using different lengths of global-annual data as given in the legend for ΔR and ΔT ; (b) an example of binning 300 years of model output from IPSL-CM6A-LR to better see the concavity in forcing and response; (c) the ECS distribution, with the mean denoted by the vertical line, that results from binning data as in (b) and sampling one value from each bin to perform the least-squares regression and repeatedly (here, 1000 times) performing a regression.

change radiatively in a way that amplifies the initial warming, whereas a negative feedback denotes that clouds change in a way that damps the initial warming. A closely related quantity, the change in the cloud radiative effect (ΔCRE), was shown to be a skillful proxy for intermodel differences in the cloud feedback (e.g., Soden et al., 2008; Vial et al., 2013). CRE is defined as the difference between all-sky (‘all’, with clouds) and clear-sky (‘clr’, clouds artificially removed) net downward radiative fluxes,

$$CRE = R_{\text{all}} - R_{\text{clr}} = (LW_{\text{clr}} - LW_{\text{all}}) + (SW_{\text{all}} - SW_{\text{clr}}) = CRE_{\text{LW}} + CRE_{\text{SW}}, \quad (6.3)$$

with positive radiative fluxes defined downward. In present-day climate, net CRE is negative (about -20 Wm^{-2}) due to $CRE_{\text{LW}} \approx 30 \text{ Wm}^{-2}$, reflecting the longwave warming effect of high clouds, and $CRE_{\text{SW}} \approx -50 \text{ Wm}^{-2}$, due to clouds enhancing the planetary albedo (e.g., Ramanathan et al., 1989). A small change in the cooling effect of clouds (ΔCRE on the order of a few Wm^{-2}) due to global-mean warming, ΔT , could induce a strong feedback, motivating the large, long-standing focus on better constraining the cloud feedback, which is proportional to $\Delta CRE/\Delta T$ (e.g.,

Ramanathan et al., 1989; Bony et al., 2006).

Here ΔCRE is defined as the difference in CRE between a perturbed and control climate simulation. Cloud feedbacks are equal to the ΔCRE with an offset, typically 0.3 Wm^{-2} (e.g., Soden et al., 2008), accounting for the masking effects of clouds on clear-sky fluxes. For instance, removing a high cloud in a dry atmosphere would have a larger influence on the outgoing longwave radiation than would removing such a cloud in an already moist and opaque atmosphere. Whereas the ΔCRE is not a reliable metric of the absolute magnitude of the cloud feedback, it is a skillful proxy for intermodel *spread* in the cloud feedback as calculated from other methods (e.g., Vial et al., 2013; Zelinka et al., 2020). The global ΔCRE calculated for this subset of models has a Pearson correlation coefficient $r=0.99$ with global cloud feedback estimates from Zelinka et al. (2020) using the kernel method. I therefore use ΔCRE as a simplified method for examining the spread in cloud feedbacks.

6.3 Uncertainty in ECS still driven by spread in global and tropical cloud feedbacks

Fig. 6-1b shows that, in this representative subset of models, the spread in the global ΔCRE can explain 55% of the variance in ECS ($r=0.74$). Variability in climate sensitivity is driven more by variance in the shortwave ΔCRE ($r=0.61$) than by variance in the longwave ΔCRE ($r=-0.25$) (not shown). The explanatory power of the global ΔCRE for ECS in this sample is similar to that in the previous CMIP5 ensemble, $r=0.73$ (e.g., Ceppi et al., 2017). The global ΔCRE can result from multiple physical processes, such as rising high clouds (e.g., due to fixed anvil temperature hypothesis), the iris effect (e.g., decreasing anvil cloud fraction with warming), cloud fraction changes in shallow clouds over tropical oceans, and cloud fraction and phase changes in extratropical clouds (e.g., Bony et al., 2006; Ceppi et al., 2017). It is thus not *a priori* clear how large a role the tropics, or cloud fraction changes in the trades, in particular, play in explaining global ΔCRE and climate sensitivity.

Only the *tropical* ΔCRE can, however, still explain 44% of the variance in climate sensitivity ($r=0.66$, Fig. 6-1c) and 76% of the variance in the global cloud feedback ($r=0.87$, Fig. 6-1d). The tropics are defined equatorward of 30° . The extratropical ΔCRE , by contrast, explains only 18% of the variance in ECS ($r=0.42$). While changes in extratropical cloud feedback can explain the shift towards higher mean values from CMIP5 to CMIP6, variance in the tropical ΔCRE can still explain more variance *within* ensembles. The origins of the spread in tropical ΔCRE are therefore examined in greater detail in the following sections.

6.4 Trade-wind cloud responses differ between high and low climate sensitivity models

6.4.1 Conceptualizing the tropical circulation

The tropical cloud responses can further be decomposed using the framework from Bony et al. (2004). The tropical radiation budget depends on the distribution of cloud types, which in turn is controlled, to first-order, by the large-scale atmospheric circulation (Bony et al., 2004). Large-scale atmospheric subsidence favors the formation of shallow clouds, such as trade-wind cumuli and stratocumulus clouds, whereas large-scale ascending motion is associated with deeper convective clouds (Fig. 6-3a). This framework uses the large-scale vertical velocity at 500 hPa, ω_{500} (expressed in hPa/day), as a proxy of the large-scale atmospheric circulation. ω_{500} is the first baroclinic mode of the large-scale circulation in the deep tropics and correlates well with the total diabatic heating of the column, and hence with the precipitation. The tropical circulation can be discretized as a series of dynamical regimes, wherein the ascending branches of large-scale circulations with warm sea surface temperatures correspond to negative values of ω_{500} , and regions of colder sea surface temperatures and large-scale subsiding motions correspond to positive values of ω_{500} . To first order, the signs of negative or positive ω_{500} therefore correspond to large-scale convergence or large-scale divergence. The trades are often identified between 10 to 30 hPa/day

(e.g., Bony et al., 2004; Brient et al., 2016).

The tropical circulation can also be conceptualizing using the large-scale vertical pressure velocity at 700 hPa, ω_{700} , and estimated inversion strength, EIS, more precisely discriminate among low-cloud regimes, such as between the trades and stratocumulus regimes. This approach is similar to Medeiros and Stevens (2011) and Medeiros et al. (2015) using lower tropospheric stability and ω_{500} , and is analogous to the approach in Myers et al. (2021). Following Myers et al. (2021), we identify the trades as areas with climatological annual-mean EIS below 1 K and ω_{700} between 0 and 15 hPa/day.

In the following analysis, ten *amip* models from CMIP5 and CMIP6 are used (see Table 6.1), which are a different sample of models presented above. The *amip* simulations are global simulations of the atmosphere and land surface forced by observed sea surface temperatures (rather than letting these freely evolve as in coupled *piControl* and *abrupt-4xCO2* experiments), sea ice cover, and greenhouse gas concentrations (Gates et al., 1999). *amip4K* models add a uniform 4 K warming to the *amip* simulations. Using observed sea surface temperatures (SST) avoids known biases in coupled models, but there are downsides, such as eliminating feedbacks between the atmosphere and ocean. In coupled models, Liu et al. (2013) show that SSTs are too cold and not variable enough in the Atlantic warm pool compared to observations, and Zhou et al. (2016) show that SSTs are too warm in the eastern equatorial Pacific compared with observed SSTs.

Δ CRE values are calculated as the difference between CRE in *amip4K* and *amip* simulations and then normalized by the 4 K temperature difference in these simulations to give a proxy for the cloud feedback. Qin et al. (2022) find good agreement between cloud feedbacks across geographic locations calculated using coupled (e.g., *abrupt-4xCO2* and *piControl*) and uncoupled, atmosphere-only simulations (e.g., *amip4K* and *amip*), justifying our use of atmosphere-only simulations to analyze the spread of cloud feedbacks. For these *amip* experiments, for heuristic purposes, ECS values are taken from Zelinka et al. (2020), as ECS is calculated using *abrupt-4xCO2* and *piControl* experiments not *amip4K* and *amip* experiments, with low and

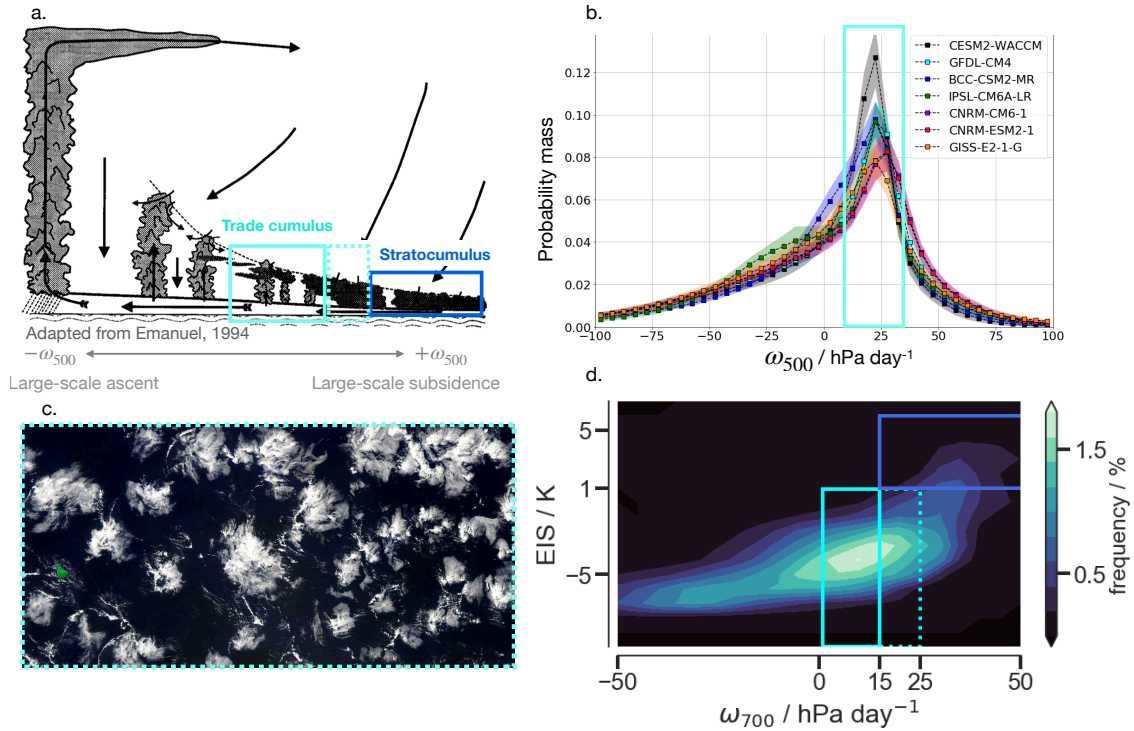


Figure 6-3: (a) An idealization of the tropical circulation as given in Emanuel et al. (1994b), ranging from regions of large-scale ascent and deep convection to regions of moderate large-scale subsidence and trade cumulus clouds (turquoise box) and strong large-scale subsidence and stratocumulus clouds (dark blue box), as well as transition zones between trade cumuli and stratocumuli (dashed turquoise box). (b) The probability density function of ω_{500} in seven CMIP6 *piControl* simulations (listed in the legend), with the colored shading denoting one standard deviation of monthly values around 20-year climatology. The turquoise box denotes trade-wind regions as defined as ω_{500} values from 10–30 hPa/day . (c) A satellite view of ‘flower’ clouds that could represent clouds found in the cumulus-stratocumulus transition zone, the dashed turquoise box in panels a. and d. (d) The mean frequency distribution of tropical dynamical regimes averaged over ten *amip* simulations in EIS and ω_{700} (pressure velocity at 700 hPa) space. Frequency of discretized dynamical regimes is defined as the area covered by these regions, normalized by the total area of the tropics. Following Myers et al. (2021), the trades are defined as areas with climatological annual mean EIS below 1 K and ω_{700} between 0 and 15 hPa/day (turquoise box). Note that this ω_{700} range differs from the ω_{500} range. A potential intermediate zone between cumulus and stratocumulus clouds is extended from 15–25 hPa/day (dashed turquoise box). Also shown are the EIS and ω_{700} values corresponding to stratocumulus regimes (darker blue).

Model acronym	Model	Country
BCC-CSM2-MR	Beijing Climate Center, Climate System Model, version 2	China
CanAM4	Canadian Centre for Climate Modelling and Analysis, Fourth Generation	Canada
CESM2-WACCM	Community Earth System Model (CESM) Whole Atmosphere Community Climate Model	United States
CNRM-ESM2-0	Centre National de Recherches Météorologiques (CNRM) Earth system model, 2 nd gen.	France
CNRM-CM6-1	Centre National de Recherches Météorologiques (CNRM) coupled model, 6 th gen.	France
GFDL-CM4	Geophysical Fluid Dynamics Laboratory (GFDL) Coupled Physical Model 4	United States
GISS-E2-1-G	Goddard Institute for Space Studies (GISS), ModelE Atmosphere/GISS Ocean	United States
GISS-E2-1-H	Goddard Institute for Space Studies (GISS), ModelE Atmosphere//Hycom Ocean	United States
HadGEM3-GC31-LL	Third Hadley Centre Global Environment Model, Global Coupled configuration 3.1	United Kingdom
IPSL-CM5A-LR	Institut Pierre-Simon Laplace (IPSL) coupled model, 5 th generation	France
IPSL-CM6A-LR	Institut Pierre-Simon Laplace (IPSL) coupled model, 6 th generation	France
MIROC6	Model for Interdisciplinary Research on Climate	Japan
MPI-ESM-LR	Max Planck Institute for Meteorology Earth System Model	Germany
MRI-ESM2-0	Meteorological Research Institute Earth System Model version 2.0	Japan
SAM0-UNICON	Seoul National University Atmospheric Model, v.0, Unified Convection Scheme	South Korea

Table 6.1: Additional information for model simulations used in this chapter, as identified by their model acronym.

high ECS again defined relative to the CMIP6 mean of 4°C.

Fig. 6-3b,d shows how the trades are the most common cloud regime in the tropics in these two coordinate systems. In the ensemble-mean frequency distribution (Fig. 6-3d), the trade-wind area covers 32% of the tropics, compared with 4.4% for stratocumulus, using the respective EIS and ω_{700} definitions from Myers et al. (2021) and 39% of the tropics when defining the trades between 10–30 in hPa/day in ω_{500} . The frequency distribution structure is similar for individual models. Perhaps surprisingly, there is also substantial weight in between what Myers et al. (2021) define as either trade-wind or stratocumulus based on the EIS- ω_{700} decomposition. The area from 16–25 hPa/day and EIS < 1 K covers 14% of the tropics and could correspond to transition zones between stratocumuli and trade cumuli, such as when stratocumulus decks recede towards continents. These clouds could perhaps also correspond to clouds named ‘flowers’ by Stevens et al. (2020b) and Bony et al. (2020), which tend to be associated with stronger subsidence (Bony et al., 2020; Schulz et al., 2021).

In geographic space, Fig. 6-4 shows the frequency of occurrence of trade-wind regions in two representative climate models, one having high ECS (IPSL-CM6A-LR) and another with low ECS (BCC-CSM2-MR). Fig. 6-4 shows that trade-wind regions cover wide swaths of tropical oceans. The EUREC⁴A measurement area east of Barbados is nearly always classified as a trade-wind region across the ten models.

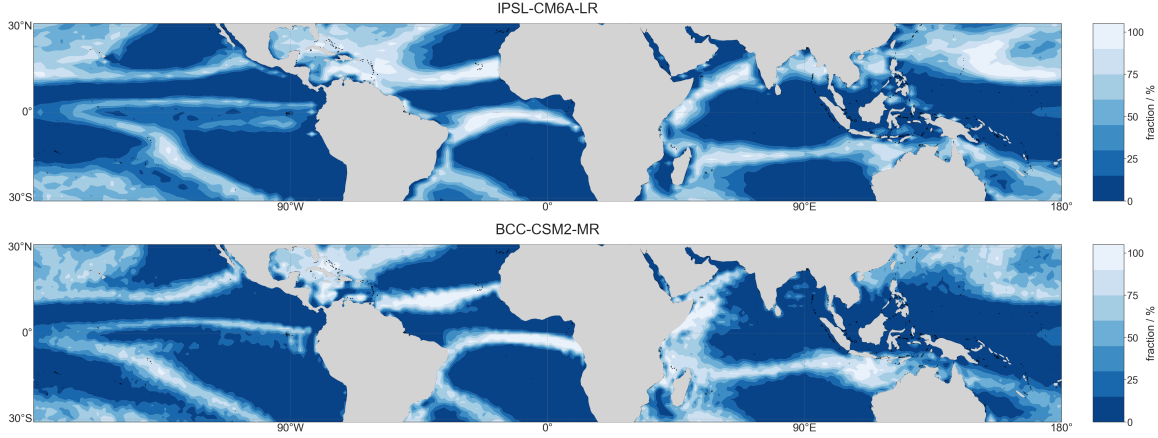


Figure 6-4: Frequency of occurrence of trade-wind regions in geographic space in the IPSL-CM6A-LR model (high ECS) and BCC-CSM2-MR (low ECS) using 30 years of annual model output from *amip* simulations. Trade-wind regions are identified as having $EIS < 1$ and ω_{700} between 0–15 hPa/day, as introduced previously and following Myers et al. (2021).

6.4.2 Different thermodynamic and dynamic cloud radiative responses for high and low ECS models

Clouds are sensitive to changes in both temperature and circulation. The Bony et al. (2004) framework separates these two influences, decomposing a cloud variable, C , such as the ΔCRE , into the sum of a *thermodynamic* component that is related to temperature changes, a *dynamic* component that is related to changes in P_ω , the occurrence frequency of circulation changes, and a *covariance* term that tends to be negligibly small,

$$\overline{\delta C_\omega} = \int_{-\infty}^{+\infty} C_\omega \delta P_\omega + \int_{-\infty}^{+\infty} P_\omega \delta C_\omega + \int_{-\infty}^{+\infty} \delta P_\omega \delta C_\omega. \quad (6.4)$$

Discretizing this equation gives,

$$\overline{\delta C_\omega} = \sum_{\omega} C_\omega \Delta P_\omega + \sum_{\omega} P_\omega \Delta C_\omega + \sum_{\omega} \Delta P_\omega \Delta C_\omega \quad (6.5)$$

The dynamic component, $C_\omega \Delta P_\omega$, represents the effect of changing circulation on the cloud variable, without letting the clouds adjust in response to temperature. The

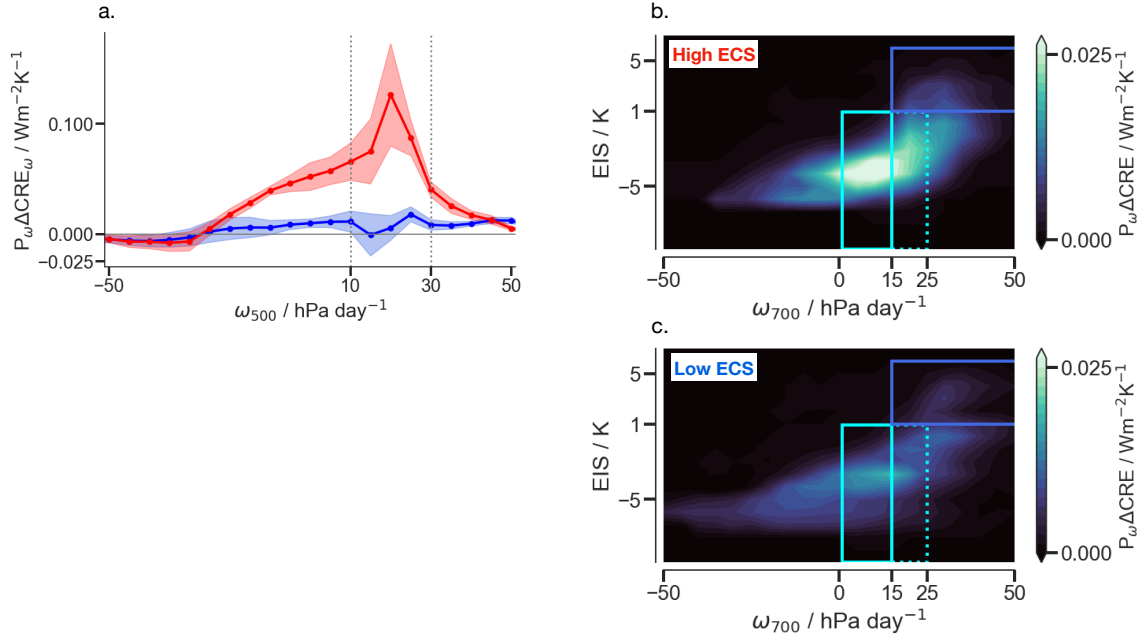


Figure 6-5: (a) The thermodynamic component, $P_\omega \Delta CRE_\omega$, in ω_{500} space for 4 high (red) and 6 low (blue) ECS models, with the mean (solid line) and standard error for the high or low ECS models (shading). In ω_{500} space, trade-wind regions are demarcated by the dashed lines from 10–30 hPa/day. Instead of in ω_{500} space, (b) and (c) show the thermodynamic component in the two-dimensional EIS- ω_{700} space with the boxes defined in the same way as in Fig. 6-3.

thermodynamic component, $P_\omega \Delta C_\omega$, by contrast, quantifies the effect of changing temperature on the cloud response, holding circulation fixed.

To illustrate the association between clouds and circulation, Fig. 6-5 projects the tropical *thermodynamic* cloud radiative response, $P_\omega \Delta CRE_\omega$, resulting only from temperature-induced changes, into the two circulation spaces (EIS- ω_{700} and ω_{500}). A difference emerges between high and low ECS models in the trades. Trade-wind clouds exhibit a moderate radiative sensitivity to temperature change, yet through their ubiquity, or large statistical weight in P_ω , they have a large net influence on the tropical radiation budget. If defining the trades from 10–30 hPa/day in ω_{500} , the fractional contribution of the trades to the tropical ΔCRE is 20% for low ECS models and 46% for high ECS models. In general, the contribution to the spread of

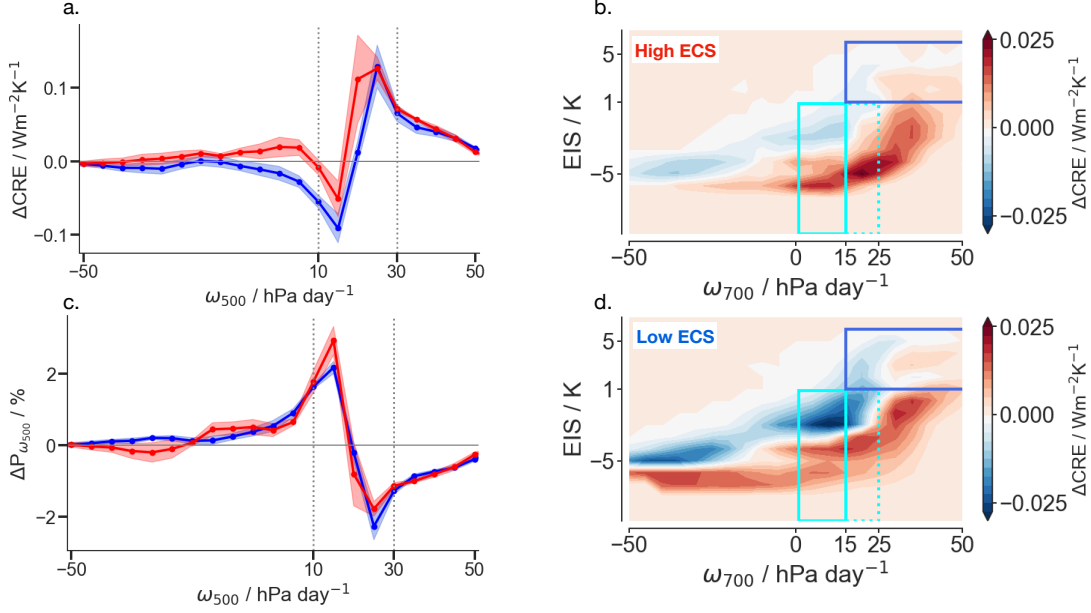


Figure 6-6: (a) The net ΔCRE in ω_{500} space for 4 high (red) and 6 low (blue) ECS models, with the mean and standard error in shading. Trade-wind regions are demarcated by the dashed lines from 10–30 hPa/day. (b) and (d) show the net ΔCRE in EIS- ω_{700} space with the boxes defined in the same way as in Fig. 6-3. (c) shows the change in regime frequency, $\delta P_{\omega_{500}}$ between *amip4K* and *amip* simulations.

a variable, such as ΔCRE , can be quantified as,

$$\frac{\sum_{\omega_{\text{trades}}} (\Delta CRE_{\omega}^{\text{h}} - \Delta CRE_{\omega}^{\text{l}})}{\overline{\Delta CRE}^{\text{h}} - \overline{\Delta CRE}^{\text{l}}}, \quad (6.6)$$

where $\overline{\Delta CRE}$ is the tropical-mean ΔCRE for high (h) or low (l) ECS models. As one example, applying Eq. (6.6) to the thermodynamic ΔCRE and defining the trades from 10–30 hPa/day in ω_{500} , trade-wind regimes contribute to 65% of the spread in the tropical thermodynamic ΔCRE . This contribution is similar for different definitions of the trades: 57% if defining the trades from 10–25 hPa/day, or 78% if defining from 0–30h hPa/day.

Fig. 6-6 shows the tropical net ΔCRE , including both the dynamic and thermodynamic component, and the small covariance term. The correlation between the tropical thermodynamic and net ΔCRE values is $r=0.66$. The change in regime frequency, ΔP_{ω} , (Fig. 6-6c) illustrates the well-established finding that the large-scale

vertical motions associated with tropical circulation weakens with warming. In trade cumulus regimes, weakly-subsiding regions become more frequent at the expense of more strongly-subsiding regimes, with ΔP_ω values crossing zero around 15 hPa/day. The structure and magnitude of the ΔCRE is driven more by the dynamic response to changes in the large-scale circulation than the thermodynamic response. In particular, the dipole structure in the net ΔCRE reflects the influence of the dynamic component of ΔCRE , driven by the dipole structure in ΔP_ω (Fig. 6-6c). Low ECS models have more negative, stabilizing ΔCRE in weakly-subsiding regimes than do high ECS models (Fig. 6-6a,d). In low ECS models, the more stabilizing ΔCRE likely arises from a positive dynamic change in cloud fraction near cloud base and the trade-wind inversion (Fig. 6-8b) and a less-negative thermodynamic component of cloud fraction changes (Fig. 6-8a). These results may suggest that low ECS models simulate stronger estimated inversion strength (EIS) (Wood and Bretherton, 2006) in these weakly-subsiding regimes, whereas high ECS models are associated with weaker EIS, as larger EIS and greater tropospheric stability is associated with increased cloudiness (e.g., Wood and Bretherton, 2006; Myers and Norris, 2013).

6.4.3 Global influence of spread in trade cumulus feedbacks

Fig. 6-7, moreover, shows that these differences in the trade-wind ΔCRE can explain differences in the global ΔCRE and climate sensitivity. Here the trades are selected using the EIS and ω_{700} criteria, but results are qualitatively similar if using the ω_{500} criterion (not shown). Differences in the net trade-wind ΔCRE explain 69% of the variance in the global ΔCRE (Fig. 6-7a) and 25% of the variance in ECS (Fig. 6-7b). Also illustrated are the mean and standard deviation of the marine shallow cloud feedback given in the International Panel of Climate Change’s Sixth Assessment Report (IPCC AR6), which is assessed to be $0.2 \pm 0.16 \text{ Wm}^{-2}\text{K}^{-1}$ from multiple lines of evidence (Arias et al., 2021). The large standard deviation reflects the existing uncertainties associated with different approaches of constraining trade cumulus feedbacks (Arias et al., 2021), as discussed in Chapt. 1.

These trade-wind ΔCRE values and thus correlations are, moreover, relatively

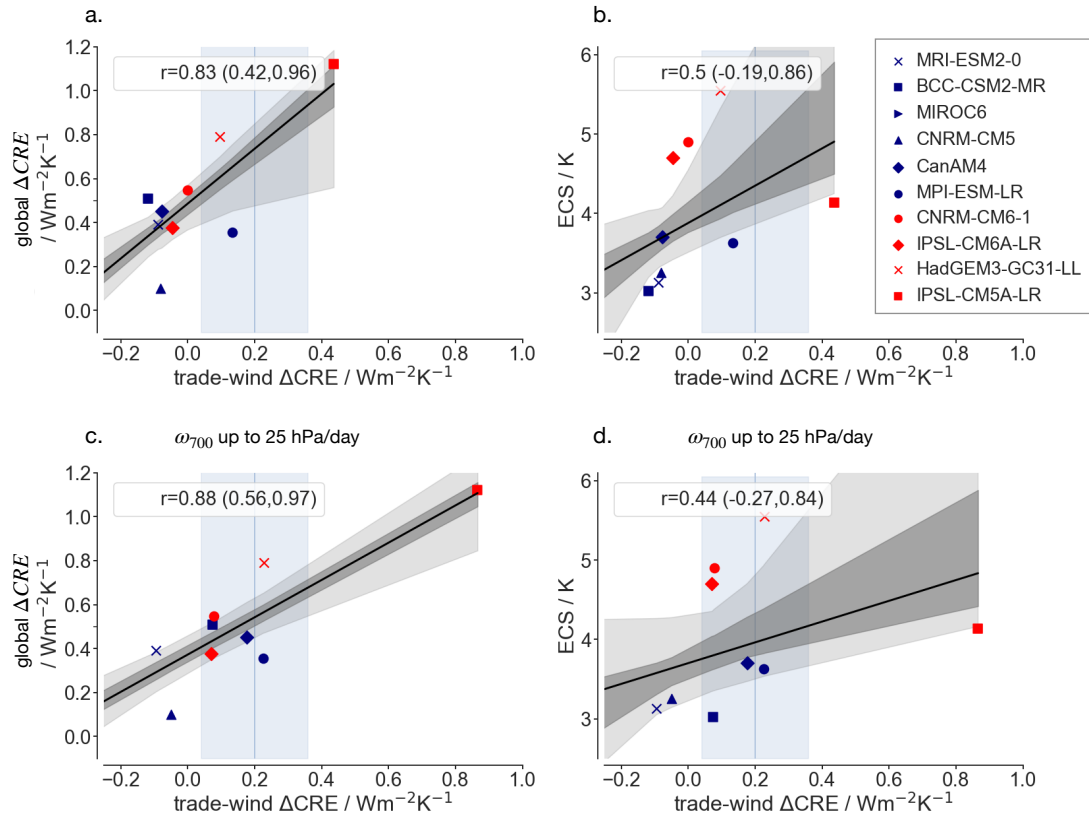


Figure 6-7: Scatter plots between the (a) trade-wind net ΔCRE and global ΔCRE , and (b) trade-wind net ΔCRE and ECS. Trade-wind regions are selected from the EIS- ω_{700} criterion from Myers et al. (2021) as described in the text. Panel (c) and (d) are similar, except with trade-wind regions defined using a slightly modified criterion from Myers et al. (2021), wherein ω_{700} values are less than 25 hPa/day (instead of 15 hPa/day), as a sensitivity test for trade-wind ΔCRE values. Red points denote models with ECS $> 4^\circ\text{C}$, and blue points denote models with ECS $< 4^\circ\text{C}$. Uncertainty on the regression is calculated from bootstrapping, with darker grey corresponding to 25–75% uncertainty and lighter grey to 5–95% uncertainty on the regression. Also shown is the mean (blue vertical line) and standard deviation (blue shading) of the marine shallow cloud feedback as assessed from multiple lines of evidence in the IPCC AR6.

insensitive to different choices of the upper bound of ω_{700} used in identifying trade-wind regions, together with an EIS criterion. As one example, defining the trades using ω_{700} values up to 25 hPa/day, instead of 15 hPa/day as in Myers et al. (2021), following discussions in Sec. 6.4.1, increases the mean trade-wind ΔCRE from a mean of 0.31 to 0.46 $\text{Wm}^{-2}\text{K}^{-1}$. The correlation between the different ΔCRE values is, however, one-to-one, $r=0.996$. The choice of upper bound on ω_{700} therefore does not strongly influence the relative differences among models and their correlations with the global ΔCRE (Fig. 6-7c) and climate sensitivity (Fig. 6-7d). That said, Fig. 6-7 shows that the correlation values are sensitive to the inclusion of individual models, such as the IPSL-CM5A-LR model. For climate sensitivity, the uncertainty range on the correlation crosses zero (Fig. 6-7b,d). The uncertainty range does, however, not span zero for the global ΔCRE (Fig. 6-7a,c).

6.4.4 Vertical cloud fraction changes in high and low ECS models

The change in the vertical cloud fraction in the trades also differs between high and low ECS models, similar to previous ensembles (e.g., Vial et al., 2013; Brient et al., 2016). In previous ensembles, the trade cumulus feedback was shown to largely be governed by changes in cloud fraction near cloud-base, which is, in turn, sensitive to the representation of turbulence, convection, and radiation in models (e.g., Brient et al., 2016; Vial et al., 2016).

Fig. 6-8 shows the change in trade-wind cloud fraction, expressed as the weighted contribution to the net tropical cloud fraction change, which is on the order of one- or two-percent across models. Trade-wind regions are selected from the ω_{700} and EIS criteria as described earlier, but results are similar when selecting on the basis of ω_{500} . The three panels correspond to the thermodynamic change (Fig. 6-8a), dynamic change (Fig. 6-8b), and the net change (Fig. 6-8c). Cloud changes between high and low sensitivity models tend to be most pronounced at two levels – around cloud base at about 930 hPa (~ 700 m) and the inversion base at about 800 hPa (~ 2 km).

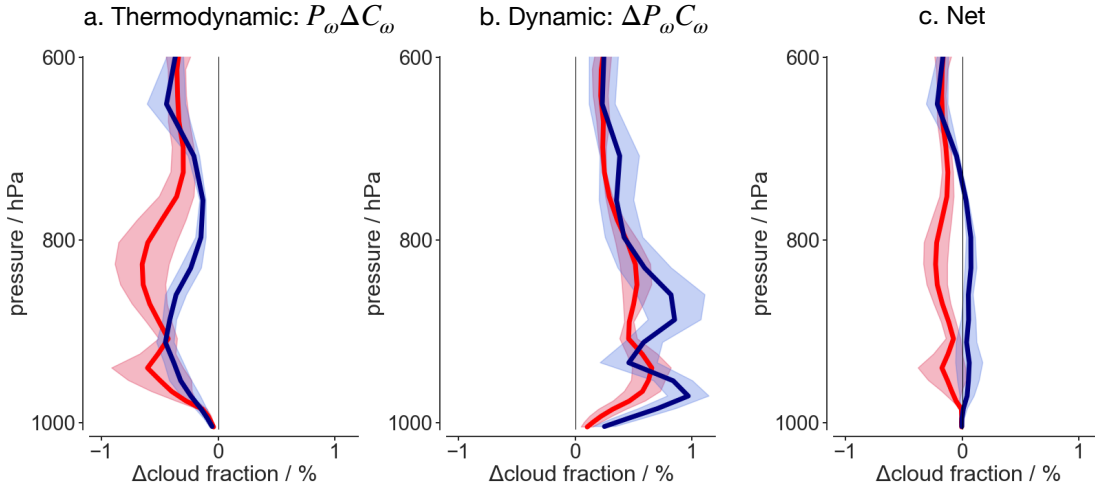


Figure 6-8: Contribution of cloud fraction changes in trades to the tropical cloud fraction change between *amip4K* and *amip* simulations for high (4 models, red) and low ECS models (6 models, blue). Shown are the (a) thermodynamic change, $P_\omega \Delta C_\omega$, (b) dynamic change, $\Delta P_\omega C_\omega$, and (c) net change, $\overline{\delta C_\omega}$, where C_ω refers to cloud fraction. The shading is the standard error. Trade-wind regions are selected from the ω_{700} and EIS criteria, following Myers et al. (2021), as described in the text.

In observations, cloudiness near cloud-base is nearly two-thirds of the total cloud cover in the trades (Nuijens et al., 2014), and in previous model ensembles, cloud-base cloud fraction changes with warming were strongly associated with the spread in trade cumulus cloud feedbacks (e.g., Brient et al., 2016; Vial et al., 2016). These considerations motivate a focus, in the next chapter, on cloud-base cloud fraction and its sensitivity to environmental changes.

6.5 Analysis of climate sensitivity in the IPSL-CM6A-LR model

Before concluding, a more in-depth examination of the causes of higher ECS in the IPSL-CM6A-LR model relative to its predecessor, IPSL-CM5A-LR, is discussed. This analysis contributed to Boucher et al. (2020) (its Sec. 6 on climate sensitivity) and is described below.

When calculated with the Gregory et al. (2004) method, the effective ECS between IPSL-CM5A-LR and IPSL-CM6A-LR increases from 4.0 to 4.5 K using 150 years of data, or from 4.1 to 4.8 K using 300 years of data. The relative contributions to ECS are calculated following Dufresne and Bony (2008) and Vial et al. (2013), and illustrated in Fig. 6-9a. This method decomposes the contributions to ECS into (i) rapid tropospheric and stratospheric adjustments to carbon dioxide and (ii) temperature-mediated feedbacks operating on longer time scales. More specifically, the rapid tropospheric adjustment includes the climate response associated with all tropospheric adjustments (temperature, water vapor, and clouds), surface albedo change, and the small land surface warming due to the CO₂ forcing (Vial et al., 2013). The method also quantifies the relative contributions of the water vapor and temperature lapse rate, surface albedo, and cloud feedbacks. Individual feedbacks are calculated by the radiative kernel method (Bony et al., 2006; Soden et al., 2008; Shell et al., 2008). A radiative kernel acts as a partial derivative, representing the sensitivity of the radiative flux, R , to changes in a climate variable, X , such as water vapor, temperature, and surface albedo. To find the kernel, the radiative code of a climate model is run offline with a standard perturbation, such as 1 K warming at each vertical level, moistening that would occur from warming by 1 K at constant relative humidity, and changing surface albedo by 1%. The radiative kernel, $\frac{\partial R}{\partial X}$, is multiplied by the change in the climate variable of interest diagnosed from a model simulation and then normalized by the global-mean surface temperature change to yield the feedback value,

$$\lambda_x = \frac{\partial R}{\partial X} \frac{\partial X}{\partial T}. \quad (6.7)$$

We employ the same kernels as in Shell et al. (2008) for water vapor, temperature, and surface albedo. The cloud feedback is calculated as a corrected residual term, correcting for a cloud-masking term following Vial et al. (2013), which adds a consistent offset to net cloud feedback value estimated from the cloud radiative effect method (e.g., Andrews et al., 2012). A small residual term reflects nonlinearities in the relationship between radiative perturbation and the temperature response.

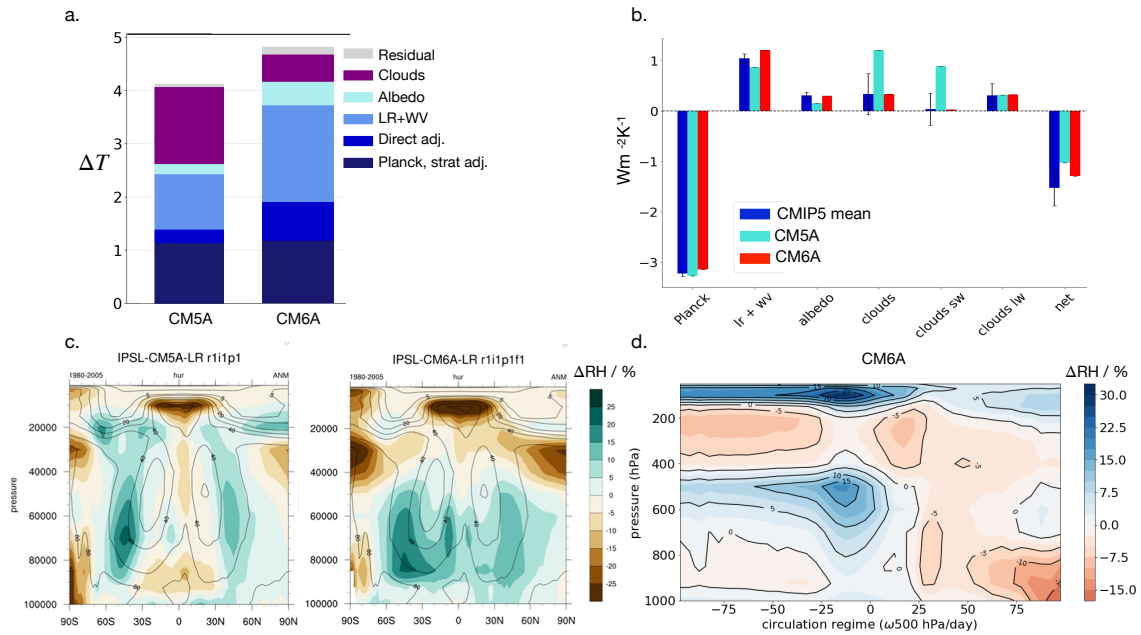


Figure 6-9: (a) Global radiative feedbacks, calculated with the kernel method following Vial et al. (2013) and described in Sec. 6.5, for IPSL-CM5A-LR and IPSL-CM6A-LR models, with each model labelled as either ‘CM5A’ or ‘CM6A’. (b) These feedbacks for the two IPSL versions are also shown relative to the CMIP5 mean feedback values (dark blue) given in Ceppi et al. (2017), showing that the global cloud feedback in the IPSL-CM5A-LR model was much more positive than the CMIP5 mean or the IPSL-CM6A-LR model. Panel (c) shows that a relative humidity bias in the CMIP5 model version (left) increased further in IPSL-CM6A-LR (right) relative to ERA Interim reanalysis. (d) Differences between relative humidity (%) after 150 years of the *abrupt-4xCO2* experiment and values in the *piControl* experiment for the IPSL-CM6A-LR model.

The main drivers of this larger ECS in IPSL-CM6A-LR are, somewhat unexpectedly, more positive rapid tropospheric adjustment to CO₂, and a stronger combined lapse rate and water vapor feedback (Fig. 6-9a), rather than a stronger cloud feedback. We diagnose the strong tropospheric adjustment from *aqua-4xCO2* and *amip-4xCO2* simulations, as well as the *abrupt-4xCO2* simulations, and find that the stronger adjustments come from clear-sky regimes (not shown). The stronger water vapor feedback primarily results from strong moistening tendencies in weakly-ascending regimes around 500 hPa (Fig. 6-9d). We diagnose this moistening tendency in weak ascent regimes by projecting the relative humidity anomalies, defined as the difference between relative humidity after 150 years of the *abrupt-4xCO2* simulation and the *piControl*, into a circulation regime basis, based on ω_{500} (Bony et al., 2004). Relative humidity anomalies reach up to 15% in these weak ascent regimes. The IPSL-CM6A-LR model is, however, also too moist in the historical tropical atmosphere compared with ERA-Interim data (Fig. 6-9c), which suggests the moistening under warming might be exaggerated as well. The net cloud feedback is less positive than in previous model versions (Fig. 6-9a). The IPSL-CM6A-LR model is somewhat of an outlier that predicts a high ECS without a strong global cloud feedback (e.g., Fig. 6-1a.,c).

An anticorrelation between the strength of the cloud and combined lapse rate and water vapor feedback was noted by Huybers (2010) for the CMIP3 ensemble. The two IPSL model versions appear to trade-off in the strength of the combined global lapse rate and water vapor feedback and cloud feedback. In the subset of 12 CMIP6 models analyzed here, such an anticorrelation is also evident ($r=-0.68$), driven more by the water vapor ($r=-0.62$) rather than lapse rate feedback ($r=0.25$). One physical hypothesis is that a mid-tropospheric increase in relative humidity and cloudiness in weakly-ascending regimes could reflect a trade-off between shallow and deep convection schemes. If thermals are not strong enough to trigger deep convection, water vapor and cloudiness accumulate in the mid-troposphere after being transported there by shallow convection, yielding a positive water vapor feedback and negative cloud feedback. This mechanism is, however, confined to a single tropical regime, whereas the feedbacks are global. It would be useful to more systematically examine

potential physical origins of such compensations, such as whether they are tied to a single regime or physical mechanism across models.

6.6 Initial conclusions

In a representative sample of CMIP6 models, differences in trade-wind cloud responses can still discriminate between high and low sensitivity models. The trade-wind thermodynamic and net change in the cloud radiative effect (ΔCRE), as well as vertical changes in cloud fraction, differ between high and low sensitivity models. The trade-wind net ΔCRE can, moreover, explain about 70% of the variance in the *global* cloud feedback. These analyses show that trade-wind cloud feedbacks are still a large source of uncertainty in global cloud feedbacks, even if other regions contribute to the spread in ECS in CMIP6 more so than in previous CMIP ensembles (e.g., Zelinka et al., 2020). These findings are similar to those shown for CMIP5, such as in Vial et al. (2013) and Brient et al. (2016), albeit for a larger number of models.

Three main conclusions are drawn from this chapter that motivate analyses in the following chapter. First, large differences remain in CMIP6 among modeled trade cumulus cloud responses to warming. Second, these differences in trade cumulus cloud responses to warming differ between high and low ECS models. Third, the inability to assess which group of modeled responses are more physically credible highlights a fundamental gap in our understanding of the environmental controls on trade-wind cloudiness. The next chapter tries to improve this understanding with EUREC⁴A observations in order to constrain trade cumulus feedbacks.

Chapter 7

Constraining trade cumulus feedbacks with EUREC⁴A

7.1 Introduction

The skill of mixed layer theory for obsessively closing subcloud layer moisture and energy budgets (Chapt. 4) gives confidence that it can also be applied to the subcloud layer mass budget. In the following chapter, the motivation and key results of Vogel et al. are summarized, with a focus on my contributions. Vogel et al. use mixed layer theory and novel sampling strategies to perform the first observational test of the ‘mixing-desiccation’ hypothesis.

I am the second author on the Vogel et al. study and contributed to the analysis in two main ways. My first contribution was constraining the entrainment rate from the subcloud layer thermodynamic budgets and estimating the subcloud layer depth, as discussed in Chapt. 4. Together with Jessica Vial, my second contribution is analyzing how GCMs represent the mixing-desiccation hypothesis in present-day (Sec. 7.4) and relating these representations to trade-wind cloud radiative responses to warming (Sec. 7.5).

Analysis in this chapter contributed to Vogel et al., which has been accepted in *Nature*.

7.2 Mixing-desiccation hypothesis

EUREC⁴A was originally conceived to observationally constrain trade-wind cloud feedbacks that were shown to explain large differences in climate sensitivity (Bony et al., 2017; Stevens et al., 2021), as introduced in Chapt. 1 and further discussed in Chapt. 6. A substantial chain of research has formulated a specific physical idea about what influences changes in cloudiness with warming. This idea can be expressed as the *mixing-desiccation hypothesis*, or the *cloud fraction vs. mass flux dilemma*. An increased convective mass flux evacuates more mass from the subcloud layer, deepening the cloud layer. This deepening through cloud formation causes mixing at the cloud top, which brings down dry air from the free troposphere. As a result, the moist lower troposphere becomes relatively drier, leading to the evaporation, or desiccation, of clouds near their base. As a result, the mixing-desiccation hypothesis predicts an inverse relationship between convective mixing and cloud-base cloud fraction (e.g., Gettelman et al., 2012; Rieck et al., 2012; Zhang et al., 2013; Sherwood et al., 2014; Tomassini et al., 2014; Brient et al., 2016; Vial et al., 2016; Bony et al., 2017). In a warmer climate, the lower tropospheric humidity gradient increases, following the nonlinear Clausius-Clapeyron relationship. All else equal, vertical mixing even more efficiently dries the environment at cloud-base. The decrease in cloud-base cloudiness is expected to lead to a more positive cloud feedback (e.g., Bony et al., 2017).

Early support for this conceptual picture comes by analogy with the process of stratocumulus breaking up into cumulus. Bretherton and Wyant (1997) use a mixed layer model and find that increasing surface latent heat fluxes, relative to cloud-top radiative cooling, drive the decoupling of the stratocumulus layer. That is, increased surface fluxes, and thus convective mixing (e.g., Tiedtke, 1989), appear to break up stratocumulus into cumulus and reduce cloud fraction. Studies with GCM-ensembles and single GCMs also support the idea that increased convective mixing decreases cloudiness at cloud-base. Sherwood et al. (2014) use 43 GCMs (in CMIP5) to show that differences in the simulated strength of convective mixing between the lower and mid-troposphere in the tropics can explain about 50% of the spread in climate

sensitivity. Stevens et al. (2016b), Tomassini et al. (2014), and Vial et al. (2016) use single climate models run in configurations that differ in their convective mixing parameters and also find evidence that increased convective mixing decreases cloud-base cloudiness.

Other approaches, however, do not find a strong reduction in cloud-base cloudiness with convective mixing. As discussed in Chapt. 1, process-based studies using large-eddy simulations suggest that low clouds are more resilient to changing environmental conditions than many GCM studies suggest (e.g., Blossey et al., 2013; Zhang et al., 2013; Bretherton, 2015; Vogel et al., 2016; Radtke et al., 2021), supporting a neutral or only slightly positive trade cumulus cloud feedback. Using the MIROC model, Kamae et al. (2016) find that differences in lower-tropospheric mixing can explain the spread in low-cloud feedbacks in only half of a perturbed physics ensemble. Myers et al. (2021) and Cesana and Del Genio (2021) use satellite measurements and also find evidence for a near-zero trade-wind cloud feedback. The physical mechanisms behind an apparent robustness of trade-wind clouds to warming are, however, not yet understood.

An alternate null hypothesis is that increased convective mixing *increases* cloud-base cloudiness by moistening the large-scale environment at cloud-base. Such a hypothesis is not the mixing-desiccation hypothesis, but could instead be called the mixing-moistening hypothesis. There are multiple reasons why the mixing-desiccation hypothesis could be wrong. Observed mesoscale vertical velocity is, for instance, larger than the longer timescale-mean values that are typically used in models of varying complexity (Bony and Stevens, 2019; George et al., 2021). This larger variability in vertical velocity could introduce dynamic controls on cloudiness that might be missing in models. It is also not *a priori* clear whether an increased mass flux and entrainment necessarily decrease relative humidity, or could instead increase relative humidity by deepening the subcloud layer (Vogel et al., 2020).

7.3 First observational test of this mechanism

7.3.1 Measurements and methods

To observationally test this hypothesis requires jointly measuring the cloud fraction (C), mass flux (M), and relative humidity (RH) near cloud base. Vogel et al., in prep estimate all of these quantities for the first time at the process level using EUREC⁴A observations. Despite their importance for climate sensitivity and cloud feedback questions, these terms have never been jointly estimated from observations given the challenges of making these measurements. Here the key points related to the measurements and methods are summarized. Additional information is found in Vogel et al., in prep.

To measure the cloud fraction at cloud base, C , the ATR-42 aircraft had horizontally-staring backscatter lidar operating at 355 nm (‘ALIAS’, *Airborne Lidar for Atmospheric Studies*) (Chazette et al., 2020) and horizontally-staring Doppler cloud radar (‘BASTA’, *Bistatic rAdar SysTem for Atmospheric studies*) (Bony et al., 2022). A radar-lidar synergy product of cloud fraction near cloud-base agrees well with independent, coincident estimates (see Fig. 17 of Bony et al. (2022)). The estimate includes drizzle, making it an upper bound on cloud-base cloud fraction.

Vogel et al., in prep consider the mass flux, M , as a proxy for the lower-tropospheric convective mixing. It can be estimated as a residual from the subcloud layer mass budget,

$$\frac{Dh}{dt} = E - M + W. \quad (7.1)$$

The mass balance of the subcloud layer is based on mixed layer theory, as also evaluated in Chapt. 4 for subcloud layer moisture and energy budgets. In the mass balance, the subcloud layer, having a depth h , is controlled by the entrainment rate, E (a mass source), the mass flux, M (a mass sink), and the large-scale vertical velocity, W (either a mass source or sink), as, for instance, described in Stevens (2006). As preparation for EUREC⁴A, Vogel et al. (2020) also evaluated the skill of this mass budget framework using large-eddy simulations. These terms have units of height per

time, such as mm/s. Note that depth, h , multiplied by area and density corresponds to mass.

Vogel et al. show that the time derivative and horizontal advection terms of h are small. If therefore assuming stationarity and homogeneity, $\frac{Dh}{dt}=0$, M can be solved for as the residual of the subcloud layer mass budget. That is, the mass flux is the sum of E and W ,

$$M = E + W. \tag{7.2}$$

Vogel et al., in prep finds that the storage and advection terms are small and unbiased, such that these assumptions are justified. Results are also qualitatively similar when including the total derivative term.

Whereas C is measured from the ATR-42, other terms, such as those to calculate M , are estimated using over 800 dropsondes launched from the coincident HALO aircraft. The subcloud layer height, h , is estimated using the θ_v -gradient method as described in Chapt. 2. The method for calculating the entrainment rate, E , is also described in Chapt. 2. Chapt. 4 constrains uncertain entrainment parameters using a Bayesian inversion of subcloud layer moisture and energy budgets. This approach assesses the skill of mixed layer theory and provides an independent constraint on E for the mass budget in Vogel et al., in prep. The vertical velocity, W , is historically challenging to measure. During two smaller field campaigns in preparation for EUREC⁴A, novel sampling strategies were developed and tested to measure W (Bony and Stevens, 2019). With EUREC⁴A data, George et al. (2021) compute vertical profiles of W by vertically integrating the divergence of the horizontal wind field measured by dropsondes from the surface up to the flight level. These measurements allow for capturing variations in the strength of mesoscale circulations (Bony and Stevens, 2019; George et al., 2021). In this analysis, W is taken at the subcloud layer top, h . Relative humidity, RH , is also estimated from HALO dropsonde measurements at h . Results are similar when considering RH measured by the ATR-42. All terms are computed at the one-hour circle-scale and then aggregated to the three-hourly circling-scale (see terminology in Chapt. 4, Table 1).

7.3.2 Observed relationships

To test the mixing-desiccation hypothesis, Vogel et al., in prep perform a multiple linear regression between cloudiness, C , and mass flux, M , and relative humidity, RH ,

$$C = a_M M + a_{RH} RH + C_0. \quad (7.3)$$

M and RH are not correlated, with a Pearson correlation coefficient $r=-0.075$.

Contrary to the anticorrelation between C and M outlined by the mixing-desiccation hypothesis, the observed correlation between C and M near cloud-base is strong and positive, with $r=0.72$. That is, increased convective mixing is associated with increased, rather than decreased cloudiness. Also including RH further tightens the relationship, giving a correlation between predicted and observed C of $r=0.83$, though the relationship remains driven mostly by M variations. Adding relative humidity presumably improves the correlation because the large-scale moisture conditions influence the persistence of clouds and because not all clouds are active clouds and associated with a mass flux (e.g., Stull, 1985). The physical mechanism will be further discussed in Sec. 7.5, and more thoroughly presented in Vogel et al., in prep.

7.4 Comparison with GCMs

As a point of comparison, we examine how GCMs represent the couplings among the same terms, C , M , and RH . Hourly modeling output at so-called *cfSites*-locations is produced as part of the *Cloud Feedback Model Intercomparison Project* (CFMIP). These 120 locations are sometimes coincident with measurement stations, such as the Barbados Cloud Observatory, and are generally located in areas exhibiting a large spread in intermodel cloud feedbacks (e.g. see Fig. 2 in Webb et al. (2017)). Despite the general notion that GCMs do not produce output in the ‘space of observables’, these point-wise model outputs are more amenable to comparison with *in situ* observations than GCM outputs on larger grid scales.

C , M , and RH are calculated for ten CMIP models (four from CMIP5 and six

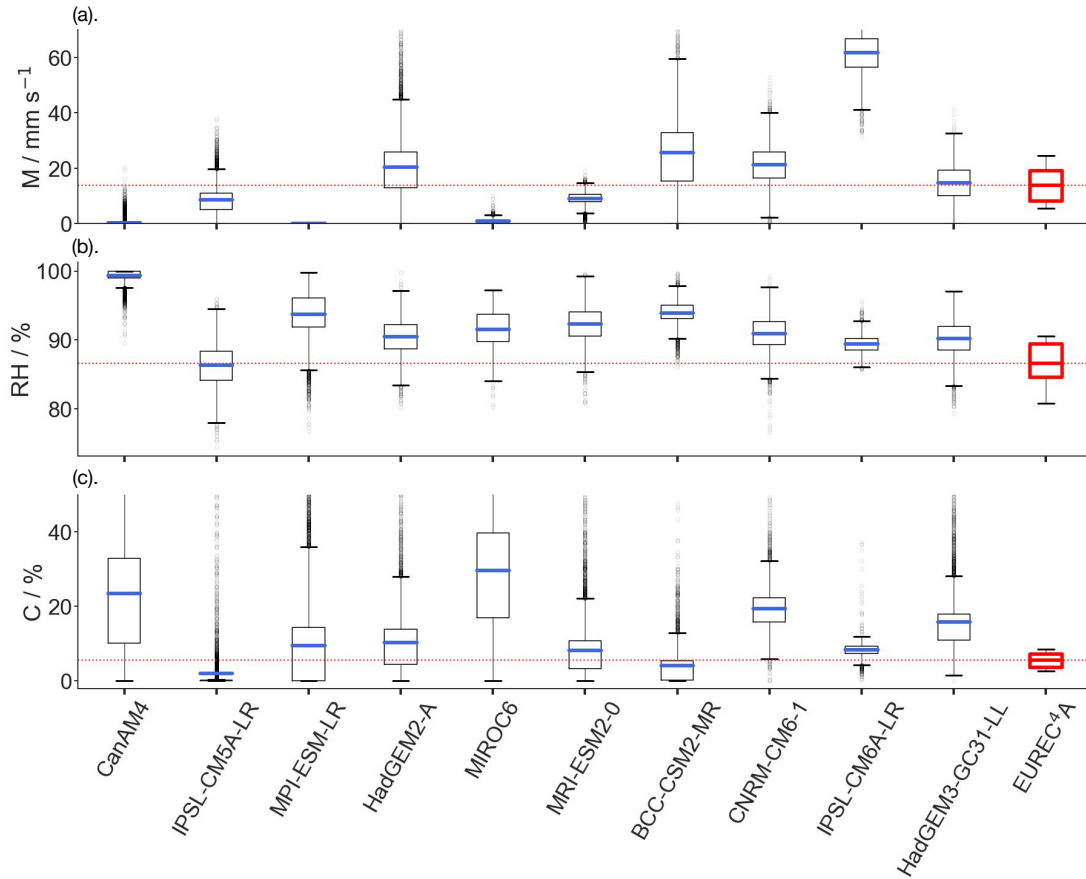


Figure 7-1: Box plots of *cfSite* output from ten *amip* model simulations for (a) mass flux, M , (b), relative humidity, RH , and (c), cloud fraction, C . The box plot corresponds to the interquartile range (from the first quartile to the third quartile), with mean values shown in blue (medians not shown). Whiskers extend from the box by 1.5 times the interquartile range. Flier points are those extending past the whiskers. The interquartile range of observed EUREC⁴A values are outlined in red, and the mean observed value is given by the dotted red line.

from CMIP6) using the *cfSites* output. As in Vial et al., in prep, we use the *amip* configuration from 1979–2008, selecting data in January and February to correspond to EUREC⁴A measurements. For each model, between 2–6 *cfSites* locations are available in the north Atlantic trades between 59–44 °W and 11–16 °N. All profiles with clouds above 600 hPa (about 4.2 km) are dropped to ensure a focus on shallow convection. Values near cloud-base are selected as the first maximum below 850 hPa (about 1.5 km). These vertical levels can differ for cloudiness, mass flux, and relative humidity, but the height differences are, on average, zero. Results are qualitatively similar when constraining all values to occur at the same level. After calculating the near cloud-base values for all sites, we average across the available sites for each model. These spatially-averaged, hourly outputs are then aggregated to the three-hourly timescale, which corresponds to the circling-mean timescale of EUREC⁴A data (see description in Chapt. 4). Hourly outputs are also aggregated to monthly-means for studying longer timescale variability.

Fig. 7-1 shows that these ten models simulate a diversity of cloud-base mass flux, relative humidity, and cloud fraction values for three-hourly data. Across models, the mean M ranges enormously from 1.25×10^{-11} –61.6 mm/s, the mean RH ranges from 86.4–99.4%, and the mean C ranges from 2.06–29.7%. The observed M values is 15.2 ± 6.54 mm/s, with values denoting the mean and standard deviation. Observed RH values are $86.6 \pm 3.06\%$, and observed C values are $5.38 \pm 1.94\%$. Except for one model (IPSL-CM5A-LR), the mean modeled RH value is higher than observed mean RH . Modeled M values vary widely, including by many orders of magnitude. Eight out of ten models predict C values greater than the observed value, and four out of ten models predict C values that are more than twice the observed value.

Among models, the relationships among these variables also differ strongly, both at the three-hourly and monthly timescale. Fig. 7-2a,b plot relationships among C and M and between C and RH using non-standardized data (e.g., not divided by the standard deviation) to show the diversity of simulated relationships. Given the sometimes large differences among modeled values, for instance, in the magnitude of M , values are, however, standardized in the following analysis. As a result of this

standardization, the slope and correlation values are equal. In GCMs, the correlation between standardized C and M ranges from -0.12 to 0.55 in three-hourly data and -0.42 to 0.61 in monthly data. Three of ten GCMs have a negative correlation at the three-hourly timescale and seven GCMs have a weakly positive correlation of $r < 0.3$. The observed correlation between C and M is, by contrast, 0.72, with a 50% confidence interval from 0.65 to 0.82, outside the values spanned by these ten GCMs.

The relationships between C and RH in models also show large variability (Fig. 7-2b), yet these relationships overlap with the observed correlation. In the GCMs, correlations range from 0.097–0.84 in three-hourly model output and 0.21–0.84 in monthly model output. The correlation in three-hourly observed data is 0.36, towards the center of the GCM range, with a 50% confidence interval from 0.16–0.55.

7.5 Can present-day variability constrain future cloud changes?

One condition for the relevance of EUREC4A measurements for evaluating cloud feedbacks, as discussed in Chapt. 2, is that variability expressed on shorter timescales is informative of variability expressed on longer timescales. In the ten GCMs, a strong association emerges between correlations estimated at the three-hourly and monthly timescales, both for the C - M relationship ($r=0.80$, with a 5-95% confidence interval from 0.33–0.95,) and C - RH relationship ($r=0.80$, 0.21–0.96, 5-95% c.i.), as shown in Fig. 7-3. These correlations provide important support that inferences from EUREC4A data are informative about climate scale behaviors. More generally, these correlations suggest that the physical processes underlying the relationships among C , M , and RH are relatively timescale-invariant.

A common approach to narrowing uncertainty in climate variables involves so-called ‘emergent constraints’ (e.g., Eyring et al., 2019; Hall et al., 2019). Emergent constraints relate an observable quantity with an uncertain, non-observable climate response parameter, such as cloud feedbacks or climate sensitivity. If a relationship

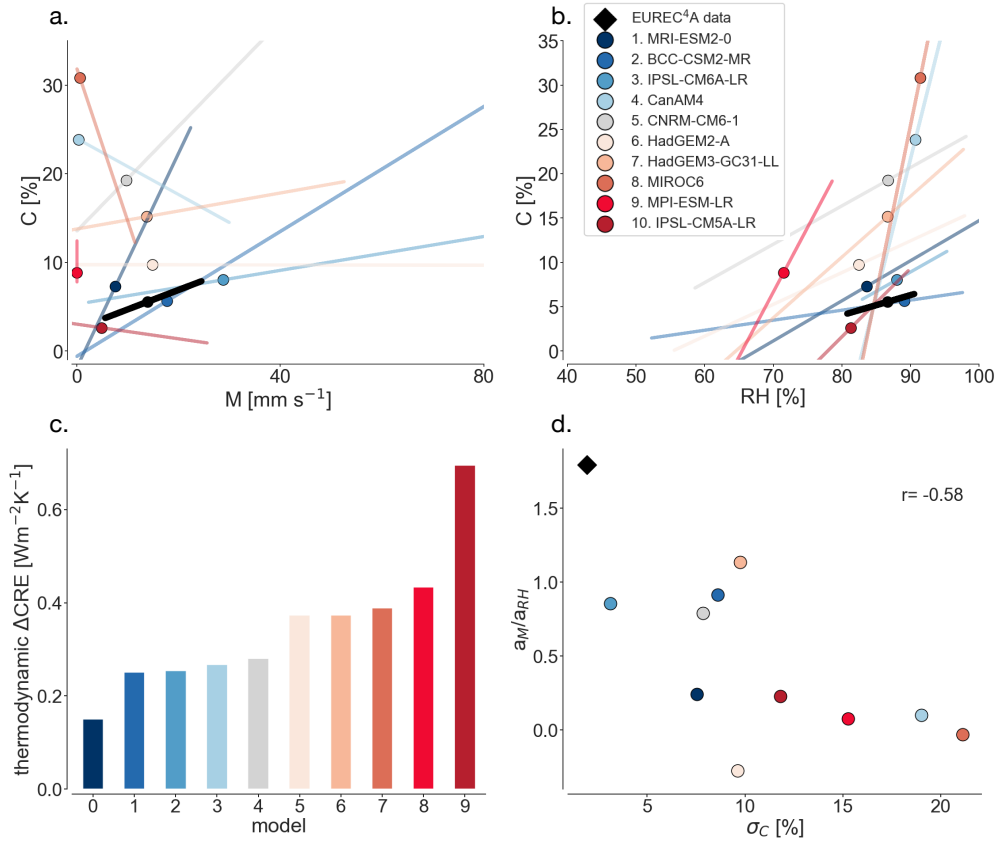


Figure 7-2: Diversity of relationships between (a) C and M and (b) between C and RH . Note that in panels a. and b., data are not standardized (divided by standard deviation) in order to show the variability among models, but the mass flux for the IPSL-CM6A-LR model is divided by three so that its magnitude is comparable to the other models. The circle refers the mean value, and the line is the linear regression fit to model output or observations. Colors are consistent throughout panels and correspond to values of the *thermodynamic* trade-wind ΔCRE , divided by the 4 K change in global-mean surface temperature, with blue to red corresponding to increasing values. Panel c. shows a bar plot of these thermodynamic ΔCRE values. Panel d. plots a_M/a_{RH} versus σ_C as described in Sec. 7.5.

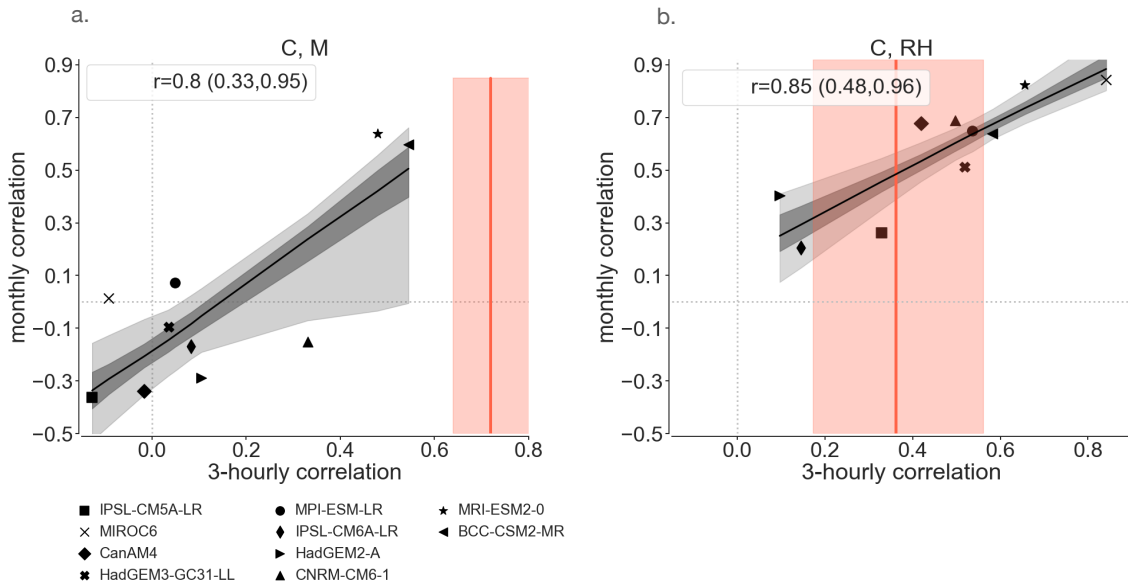


Figure 7-3: Relationship between three-hourly correlation and monthly correlation between cloud fraction and mass flux (a) and between cloud fraction and relative humidity (b). Symbols correspond to models as listed in the legend, and the black line is the ordinary least squares regression. Dark and light grey shading correspond to 50% and 90% confidence interval on the regression, as estimated by bootstrapping, or repeatedly sampling with replacement and performing the regression 1000-times. The (three-hourly) observed correlation is given by the orange vertical line, and orange shading corresponds to 50% uncertainty on the Pearson correlation, as estimated by bootstrapping (rather than the Fisher transformation).

(e.g., linear) emerges between these two variables, estimating the observable quantity provides a ‘shortcut’ to constrain the non-observable variable. Early emergent constraints were proposed for the hydrological cycle (Allen and Ingram, 2002) and snow-albedo feedback and (Hall and Qu, 2006). Regarding Northern Hemisphere snow cover, Hall and Qu (2006) demonstrated that, in 17 CMIP3 models, there is a tight correlation between the amplitude of the seasonal cycle and decrease in snow cover per degree of local warming. This constraint is compelling because it is physically plausible that the same mechanism controls snow cover changes, whether due to seasonal changes or CO₂-mediated radiative forcing. Indeed, this constraint has persisted across multiple climate model ensembles (Qu et al., 2014; Thackeray et al., 2018).

Many other emergent constraints are less robust, casting doubt on the utility of this framework. Caldwell et al. (2018) found that only four of 19 published emergent constraints on climate sensitivity remained plausible when applied to out-of-sample data. Similarly, Schlund et al. (2020b) recalculated previous emergent constraints for the CMIP6 ensemble and found much lower correlations of these metrics with climate sensitivity than with the ensembles for which these constraints were calculated. More generally, the limited sample size of models and near-infinite number of observable quantities implies that some spurious emergent relationships can arise solely due to chance (e.g., Caldwell et al., 2014). The framework is therefore criticized as being the result of ‘data mining’ whose inferences should be treated with caution (e.g., Caldwell et al., 2014, 2018; Lutsko et al., 2021). As GCMs become increasingly sophisticated, multiple factors can explain the spread in global quantities, such as climate sensitivity, (e.g., Zelinka et al., 2020), suggesting that a single metric will no longer have global explanatory power. Emergent constraints should therefore instead target specific physical processes or regions (e.g., Klein and Hall, 2015; Brient and Schneider, 2016), which we adopt as the approach in this work. Such improved physical understanding can then be used to assess the credibility of model representations, or even rule out certain models, whether or not a linear relationship emerges between present-day and future variables.

7.5.1 Observational constraints

We consider three metrics, which can be applied to both three-hourly observations and model output and then related to future cloud changes: (1) the correlation between C and M , as shown in Fig. 7-2a; (2) a_M/a_{RH} , the ratio of the multiple linear regression coefficients of Eq. (7.3); and (3) σ_C , the standard deviation of C .

The first metric quantifies the association between convective mixing and cloud-base cloud fraction. Fig. 7-4 shows that a linear relationship emerges between the correlation between C and M and the change in the trade-wind thermodynamic ΔCRE ($r=-0.71$). There are indications that models simulating a more positive correlation between C and M , in better agreement with observations, predict less-positive thermodynamic ΔCRE values, and vice versa. With the other two metrics, a linear relationship does not emerge with the thermodynamic or net ΔCRE . The correlation with the thermodynamic ΔCRE is -0.19 with a_M/a_{RH} and 0.30 with σ_C .

The two other metrics nonetheless allow for assessing models relative to observational constraints, as modeled metrics both have a large spread and differ from observational metrics. The ratio a_M/a_{RH} quantifies the relative dependence of cloudiness on M , a dynamic control, versus RH , a more thermodynamic control. A greater dependence on RH is, moreover, expected if increasing the mass flux decreases relative humidity, which then decreases cloudiness, in line with the mixing-desiccation hypothesis. Fig. 7-2d shows that all models underestimate a_M/a_{RH} relative to its observed value. This finding suggests that models have a larger dependence on RH (larger a_{RH} regression coefficient) and a weaker dependence on M than observations. Expressed differently, models whose cloudiness depends more on M variations, rather than RH variations are in better agreement with observations. These models, moreover, tend to predict weaker thermodynamic ΔCRE values, though a clear linear relationship does not emerge. These findings suggest that observed clouds are more dynamically controlled, by M , and less thermodynamically controlled, by RH , than clouds in GCMs.

Fig. 7-2d also shows that all models overestimate σ_C , the variability in cloud-

base cloud fraction. Nine of ten models have σ_C values more than three times the observed value. The standard deviation in the IPSL-CM6A-LR (3.2%) is closest to the observed value (1.9%). Both the mean cloud fraction (Fig. 7-1c) and its variability through σ_C are overestimated. Moreover, models that produce a larger mean C also simulate more variation about this mean value, with a correlation $r=0.62$ between the mean C and σ_C . One speculation is that some GCMs represent trade-cumulus clouds more similarly to stratocumulus clouds. The larger mean cloud fraction and larger variability could perhaps be more analogous to stratocumulus decks forming and breaking up than the more scattered trade cumulus fields with lower mean cloud fraction and lower variability.

In terms of obtaining a probabilistic estimate of the trade cumulus feedback, the three metrics co-vary and therefore cannot be treated as fully independent constraints. The correlation between the C and M correlation is 0.49 with a_M/a_{RH} and -0.53 with σ_C . The correlation between a_M/a_{RH} and σ_C is -0.58. These considerations motivate the development of a framework to consider constraints jointly (Sec. 7.6 and Chapt. 8).

7.5.2 Comparison with other cloud feedback estimates

In Fig. 7-5, one metric, the C vs. M correlation is related to the trade cumulus feedbacks estimated from Myers et al. (2021) as a check of consistency. The Myers et al. (2021) trade-wind cloud feedbacks are calculated from different model simulations (*abrupt-4xCO2* rather than *amip4K* simulations), but we use the same regime partitioning based on ω_{700} and EIS as in Myers et al. (2021) to identify the trades as described in Chapt. 6. There are seven models that overlap between our analyses. Fig. 7-5 relates the Myers et al. (2021) trade cumulus feedbacks to the C vs. M correlation for GCMs and observations. The MIROC6 model emerges as an outlier whose trade cumulus cloud feedback is much smaller in the coupled (*abrupt-4xCO2*) than uncoupled (*amip4K*) simulations (Fig. 7-5b). Including the MIROC6 model, the correlation between the Myers et al. (2021) trade cumulus feedback and C vs. M correlation is -0.37. If excluding MIROC6, the correlation is much stronger, $r=-0.92$. The best linear regression fit to GCMs is also extrapolated to the observed correla-

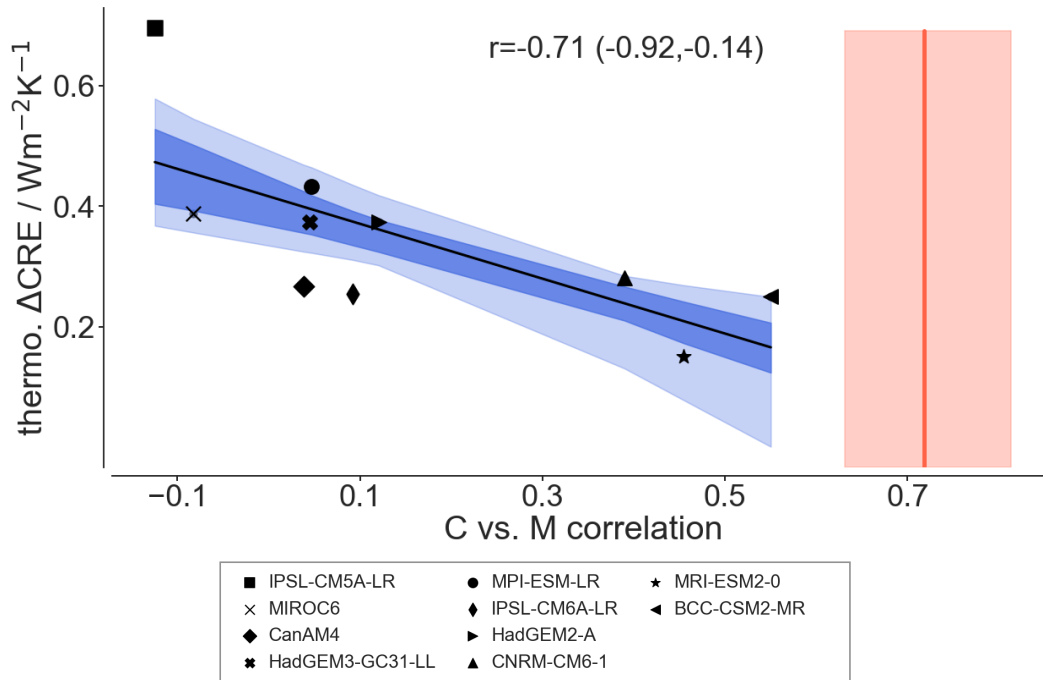


Figure 7-4: Correlation between cloud fraction and mass flux versus trade-wind thermodynamic Δ CRE. As in Fig. 7-3, symbols again correspond to models as listed in the legend, and the black line is the ordinary least squares regression. Dark and light blue shading correspond to 50% and 90% confidence interval on the regression, as estimated by bootstrapping, or repeatedly sampling with replacement and performing the regression 1000-times. The (three-hourly) observed correlation is given in the orange vertical line with shading corresponds to 50% uncertainty on the Pearson correlation as estimated by bootstrapping, rather than the Fisher transformation.

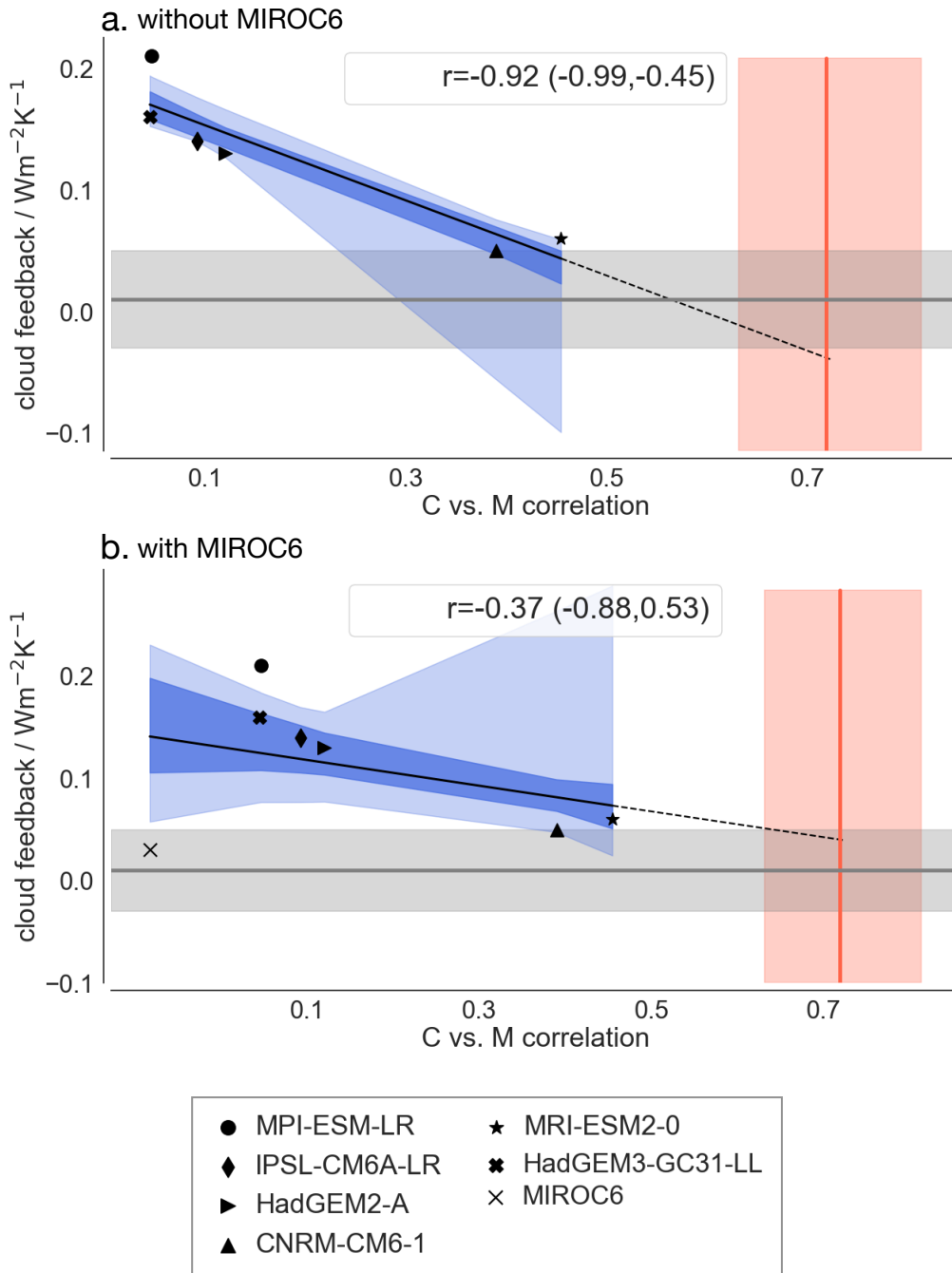


Figure 7-5: As in Fig. 7-4, but with trade-wind cloud feedbacks estimated from Myers et al. (2021) for the six models that overlap with our analysis. Also shown is the best estimate of the trade cumulus feedback (grey horizontal line) and the 90% confidence interval (grey horizontal shading) from Myers et al. (2021), as well as an extrapolation of the best-fit regression line from modeled correlations between the cloud fraction and mass flux to the observed correlation (dashed black line). To highlight the influence of single models, panel (a) includes the MIROC6 model, whereas panel (b) excludes the MIROC6 model.

tion value. The two lines including and excluding MIROC6 span the 90% confidence interval from Myers et al. (2021), as shown in Fig. 7-5, which provides additional support for a weak trade cumulus feedback.

7.6 Discussion and initial conclusions

This chapter described key results of Vogel et al., with a focus on my contributions. Vogel et al. present novel measurements of the convective mass flux, cloud fraction and relative humidity at cloud base from the recent EUREC⁴A field campaign. These measurements allow for performing the first observational test of the mixing-desiccation hypothesis, which is thought to explain large differences in trade cumulus feedbacks and thus equilibrium climate sensitivity.

Instead of the negative relationship between cloudiness and the convective mass flux outlined by the mixing-desiccation hypothesis in climate models, observations show a strong, positive relationship ($r = 0.72$) between cloudiness and the mass flux, consistent with process-based assessments (cf. Chapt. 1). This positive relationship is strengthened by also including relative humidity at cloud base ($r = 0.83$). Observations therefore suggest that cloudiness is principally controlled dynamically through the mass flux, whose variance is controlled equally by the entrainment rate and vertical velocity. In nature, entrainment and mesoscale vertical velocity have compensating influences on relative humidity near cloud-base — entrainment and cloud-base relative humidity are negatively correlated, whereas mesoscale vertical velocity and cloud-base relative humidity are positively correlated. These compensating influences on cloud-base relative humidity prevent the mixing-desiccation mechanism, or a strong desiccation of cloudiness with increased mass flux and convective mixing. An analysis of ten GCMs shows that cloudiness in these models is, by contrast, more controlled thermodynamically by variability in cloud-base relative humidity. GCMs also tend to overestimate both the mean and variability in cloud fraction compared with observations, which could potentially result from a more stratocumulus- than trade cumulus-like representation in GCMs.

We propose three metrics related to these couplings among cloudiness, mass flux, and relative humidity, which can be used to observationally constrain the trade cumulus feedback. Models that simulate a negative coupling between cloudiness and the mass flux, as opposed to the positive observed relationship, tend to produce a stronger thermodynamic cloud feedback (thermodynamic ΔCRE) with warming. Different approaches exist for combining multiple physical constraints in a statistical framework to yield a probabilistic estimate of the trade cumulus feedback, which are discussed in Chapt. 8 as ongoing work.

The findings described in this chapter and more-fully in Vogel et al. provide the first constraint on the trade cumulus feedback at the process-level. The results support a weak trade cumulus feedback, consistent with large-eddy simulations and satellite studies, as discussed in Chapt. 1 and Sec. 7.2. The present work distinguishes itself, however, from these foregoing studies because it also elucidates a physical mechanism behind the robustness of trade cumuli to changes in their environment. Whereas clouds in GCMs are more sensitive to thermodynamic variations, clouds in nature are more robust to thermodynamic variations and instead more controlled by dynamic variations that are not well-represented in GCMs.

Chapter 8

Conclusions and perspectives

Clouds may first strike an observer by their poetry, which sparks the imagination. As introduced in Chapt. 1, clouds have long fascinated the human imagination, and this fascination finds manifold expressions in art. When something is striking, there is often a greater desire to understand it — leading to deeper analysis and deeper appreciation of what we see. The British painter John Constable (1776–1837) contended that “we see nothing truly until we understand it” (Hamblyn, 2002). In this spirit, this thesis can also be interpreted as an attempt to better understand, and therefore to better see the visible and invisible motions that surround us.

This chapter reviews key results from this thesis, organized in two parts (Sec. 8.1), and then discusses new questions that follow from these results (Sec. 8.2). The first part (Chapters 2–5) used EUREC⁴A observations to improve understanding of the characteristic vertical structure of trade-wind air and the processes that determine this structure. Better understanding how the trades vary in the present-day is a necessary condition for evaluating how they will change in the future. In the second part (Chapters 6–7), this improved physical understanding was applied to the evaluation of general circulation models (GCMs) to yield the first process-based constraint on the trade cumulus feedback.

To return to the challenges outlined in Chapt. 1, estimates of future warming, as quantified by the equilibrium climate sensitivity (ECS), disagree by several degrees. One of the largest sources of disagreement is uncertainties about how trade-wind clouds over the oceans will respond to warming (e.g., Bony and Dufresne, 2005; Webb et al., 2006; Vial et al., 2013; Myers et al., 2021). During EUREC⁴A, we collected the necessary data to test whether models predicting large trade cumulus feedbacks

are physically plausible (Bony et al., 2017; Stevens et al., 2021). A single set of measurements cannot disprove a hypothesis, as individual measurements may be biased or non-reproducible. EUREC⁴A, however, brings together a wealth of instruments and approaches. This comprehensive view informed by many coincident observations allows us to propose new conceptual models of the structure of the trade-wind boundary layer and the role of clouds in determining this structure and to conclude that there is little evidence for a strong trade cumulus feedback to warming.

8.1 Summary of key results

8.1.1 Clear-sky radiation in the trades

In the uncertain couplings among clouds, convection, and circulation in the trades, radiative heating plays an important role, yet it is difficult to observe from space. Passive remote sensing cannot capture the sharp vertical moisture gradients, especially in the lower troposphere, that are essential for calculating atmospheric radiative heating profiles (e.g., Maddy and Barnet, 2008; Chazette et al., 2014; Stevens et al., 2017). To fill this gap, we calculate clear-sky radiative profiles from 2580 *in situ* soundings launched during EUREC⁴A, which form the largest radiative profiles data set for the trades (Chapt. 3). An updated radiative transfer code RRTMGP (Rapid Radiative Transfer Model for GCMs, Parallel) from Pincus et al. (2019) is used to calculate the radiative profiles. Variability in radiative heating is evident at multiple scales, such as related to the diurnal cycle, synoptic variability, and mesoscale cloud organization. An uncertainty assessment, moreover, shows that errors resulting from uncertainties in observed sounding profiles and ERA5 reanalysis employed as upper and lower boundary conditions are small. In the context of this thesis, the clear-sky radiative profiles are a necessary component of observationally closing subcloud layer moisture and heat budgets, which is the subject of Chapt. 4.

8.1.2 Observed subcloud layer moisture and heat budgets

The trade-wind subcloud layer is an important structural component of the tropical atmosphere (e.g., Riehl, 1954; Malkus, 1958; Tiedtke, 1989; LeMone et al., 2018), which has long been characterized using simple, bulk frameworks (Betts, 1973; Arakawa and Schubert, 1974; Deardorff, 1972; Stevens, 2006), of which mixed layer models are the simplest kind. The adequacy of the mixed layer description of the subcloud layer has, however, only been assessed from relatively few observations and large-eddy simulations often performed for small domains and idealized conditions (e.g., Stevens, 2006). These limitations render *in situ* observations especially important for testing the skill of mixed layer theory.

Chapt. 4 shows that mixed layer theory, evaluated with EUREC⁴A observations and with uncertain parameters constrained in a Bayesian approach, provides a closed description of subcloud layer moisture and heat budgets. Campaign-residuals are 3.6 Wm^{-2} for moisture and 2.9 Wm^{-2} for heat, and residuals for synoptic variability are small and unbiased. In defining the subcloud layer height using observed thermodynamic profiles, we find evidence for a transition layer that separates the well-mixed part of the subcloud layer from the subcloud layer top. The presence of a transition layer and its vertical gradients introduce ambiguity in the application of mixed layer theory, which are addressed through the introduction of effective parameters estimated through a Bayesian methodology. We find that constrained entrainment parameters reflect mixing over a finitely-thick transition layer. These entrainment parameters, notably a mean effective entrainment efficiency, $A_e = 0.43$, that is greater than 0.2 as often assumed, are consistent with expectations both from theory and direct numerical simulations. The small residuals, moreover, suggest that closing moisture and heat budgets does not require knowledge of additional processes, such as phase changes associated with evaporating precipitation in downdrafts.

Regarding large-scale external influences, we find that the net influence of the surface wind speed on mean subcloud layer moisture is weak due to its compensating influences through surface moistening and entrainment drying. Instead, knowing

moisture and temperature values above the subcloud layer has the most skill for predicting subcloud layer mean moisture and heat, presumably because these are the properties of the air mixed into the subcloud layer by entrainment.

8.1.3 A new conceptual picture of the transition layer

The presence of a finitely-thick transition layer, as discussed in Chapt. 4, contrasts with foregoing theory based on cloud-free convective boundary layers, which have an abrupt discontinuity at their top (e.g., Lilly, 1968). This discrepancy is investigated further in Chapt. 5. The transition layer in the trades has long been observed and simulated, but its origins remain little investigated. This layer is often associated with an 150–200 m stable layer that separates dry turbulent processes in the well-mixed part of the subcloud layer from moist convection in the overlying cloud layer (e.g., Malkus, 1958; Augstein et al., 1974; Yin and Albrecht, 2000). Extensive observations from EUREC⁴A indicate that the majority of clouds are already rooted in the transition layer, and cloud-mediated mixing causes its vertical structure. Strong jumps at the layer top, as expected from the theory of cloud-free convective boundary layers, are only found rarely and when they occur, they tend to occur in large ($O(200\text{km})$) cloud-free areas. A population of small clouds, with their bases beginning around 500 m and growing only a few hundred meters above these bases, is shown to be responsible for smoothing vertical gradients over the transition layer.

These findings lead to a new conceptual picture that the formation and dissipation of shallow clouds maintains the transition layer, in analogy with the maintenance of the trade-wind inversion by deeper clouds as proposed by Riehl et al. (1951) and elaborated by Stevens (2007). Small clouds precondition the large-scale environment and decrease the resistance to convection through weaker vertical gradients in the transition layer, making it easier for deeper clouds to form. This conceptual model suggests that small clouds beget larger clouds. From this analysis also emerges the potential for an alternate view of entrainment mixing, which is based on the ability to detrain condensate into the overlying stable layer and thus induce gentle sinking motion through negative buoyancy. Inferences from mixed layer theory and Paluch

mixing diagrams (e.g., Paluch, 1979) are also used to support inferences of air being sourced from the transition layer for entrainment, rather than being mixed directly from deeper in the cloud layer.

8.1.4 Towards the first process-based constraint on trade cumulus feedbacks

In the second part of this thesis, physical understanding developed in the previous chapters 2–5 is applied to constrain trade-wind cloud feedbacks simulated by GCMs. In CMIP3 and CMIP5, uncertainties in trade-wind cloud responses were the largest source of uncertainty in climate sensitivity (e.g., Bony and Dufresne, 2005; Webb et al., 2006; Vial et al., 2013; Brient and Schneider, 2016).

Chapt. 6 finds that, in a representative sample of CMIP6 models, trade-wind cloud responses still differ between high and low sensitivity models, in the terms of the trade-wind thermodynamic and net change in the cloud radiative effect (ΔCRE), acting as a proxy for the cloud feedback, as well as vertical changes in cloud fraction. The trade-wind net ΔCRE can, moreover, explain about 70% of the variance in the global cloud feedback. These analyses show that trade-wind cloud responses are still a large source of uncertainty in global cloud feedbacks, even if other regions also contribute to the spread in climate sensitivity in CMIP6 (e.g., Zelinka et al., 2020; Flynn and Mauritsen, 2020; Myers et al., 2021). Given the multiple influences on climate sensitivity, efforts should focus on constraining physical processes or regional cloud responses (e.g., Klein and Hall, 2015; Brient and Schneider, 2016; Lutsko et al., 2021), which is the focus of Chapt. 7.

Chapt. 7 presents analysis supporting the first process-based constraint on the trade cumulus feedback. This chapter describes results of Vogel et al., with a focus on my contributions. Vogel et al. present novel measurements from EUREC⁴A of the cloud-base cloud fraction, convective mass flux, and relative humidity. These measurements allow for testing the mixing-desiccation hypothesis, which predicts a negative relationship between convective mixing and cloudiness and is thought to

explain large differences among trade cumulus feedbacks.

Contrary to this hypothesis, observations show a positive relationship between the convective mass flux and cloud fraction ($r=0.72$), which is strengthened by the inclusion of relative humidity ($r=0.83$). Observations indicate that cloudiness is principally controlled dynamically by variations in the mass flux, which is, in turn, influenced by variability in both the entrainment rate and mesoscale vertical velocity. In nature, the compensating effects of entrainment and vertical velocity on relative humidity near cloud-base prevent the mixing-desiccation mechanism, or a strong decrease in cloudiness with increased mass flux.

All components, such as the cloud-base cloud fraction, mesoscale vertical velocity, relative humidity, and the entrainment rate, have, historically, been challenging to estimate with observations and are observational firsts. The entrainment rate is independently constrained in Chapt. 4. Novel sampling strategies during EUREC⁴A provided the most extensive data set to-date of the mesoscale vertical velocity (Bony and Stevens, 2019; George et al., 2021), revealing its influence on cloudiness.

An analysis of ten GCMs, by contrast, indicates that cloudiness in GCMs is more controlled thermodynamically, by relative humidity variations, than dynamically by mass flux variations, as in the observations. We speculate that this dynamical control — both through the entrainment rate that is negatively correlated with cloud-base relative humidity but also through vertical velocity variations that are positively correlated with cloud-base relative humidity — makes clouds in nature more resilient to convective mixing, which has tended to dissipate clouds in GCMs.

To obtain a probabilistic estimate of the trade cumulus feedback, we propose three metrics related to the couplings among cloudiness, mass flux, and relative humidity, which can be applied to both observations and GCMs. In the ten GCMs, a relationship, for instance, emerges between the correlation between the cloudiness and convective mass flux and a proxy for the trade cumulus cloud feedback, the thermo-

This mass flux is also estimated using mixed layer theory. Closing subcloud layer moisture and heat budgets in Chapt. 4 provided an observational assessment of this framework, as well as an independent estimate of the entrainment rate, E , which is used to calculate M in Eq. (7.2).

dynamic Δ CRE. Models predicting the most negative coupling between convective mixing and cloudiness — most inconsistent with observational constraints — are associated with the strongest thermodynamic Δ CRE. This constraint suggests a weak trade cumulus feedback, consistent with large-eddy simulations and satellite studies as discussed in Chapt. 1 and Sec. 7.2. Calculating a probabilistic estimate of the trade cumulus feedback using the three proposed metrics is the subject of ongoing work and described in more detail in Sec. 8.2. The present work, moreover, goes a step further than previous constraints because its aim is to elucidate the physical mechanism behind the resilience of trade-wind cumuli to changes in their environment, with observations indicating that dynamic, rather than thermodynamic controls make clouds in nature more resilient than those in GCMs to changing environment conditions.

8.2 Perspectives

8.2.1 Short-term perspectives

Several projects emerge as relatively logical extensions to ideas proposed in this thesis. Given that mixed layer theory offers a closed description for observations (Chapt. 4), it offers an appealing framework for evaluating larger-scale models that must parameterize the processes regulating this important component of the tropical atmosphere. The mixed layer framework would ensure a consistent definition of different terms and processes and allow for more like-for-like comparisons among terms across models, including GCMs, storm-resolving models, and large-eddy simulations. Such a project would allow the quantification of the relative magnitudes of different processes in these budgets, test how well the budgets close in different models, and examine how individual terms vary according to large-scale environmental conditions. Observations from the EUREC⁴A field campaign, as analyzed in Chapt. 4, act as a novel benchmark for these modeled representations. Numerical simulations are, moreover, continuous in time for variables of interest, such that simulations that are judged as realistic with respect to observational constraints could be used to further improve

process understanding, such as related to entrainment.

A second extension is calculating moist static energy (MSE) budgets, such as for the subcloud layer or the total atmospheric column. It is not immediately clear whether the budgets will close on time- and spatial-scales relevant for EUREC⁴A, such as the three-hourly circling and monthly campaign-mean timescale and about 220 km-diameter EUREC⁴A circle spatial scale. Previous studies used remote sensing observations, but on much larger monthly and annual time scales and continental-wide spatial scales, to observationally constrain water (Rodell et al., 2015) and energy budgets (L’Ecuyer et al., 2015), still with large uncertainties. Inoue and Back (2015) close MSE budgets using TOGA COARE data and Lanczos filters to separate variability with different timescales (about 2-, 5-, 10-day, and Madden–Julian oscillation timescales). Preliminary analysis of EUREC⁴A soundings shows that horizontal and vertical advection terms become increasingly large and variable when approaching the three-hourly circling timescale.

If the total-column MSE budget can, however, be closed to within small residuals using EUREC⁴A observations, this framework could be used to study the interplay of clouds and their environment through an energetic lens. The atmospheric cloud radiative effect (ACRE) emerges as a residual from the total-column MSE budget, yielding an energetic estimate of clouds. It would be useful to compare these estimates of the ACRE with coincident satellite and geometric (i.e. cloud fraction) estimates of cloudiness, as well as examine how the ACRE varies on different scales and relates to large-scale environmental conditions. In a different approach, Brient and Bony (2012) and Brient and Bony (2013) estimate the ACRE from total-column MSE budgets calculated for the IPSL-CM5A-LR model run in a hierarchy of configurations, diagnose the contributions to the ACRE, and conclude that the impact of an external perturbation on low-cloud cover depends on how the perturbation influences the vertical gradient of moist static energy within the boundary layer.

A third, ongoing extension of Chapt. 5 is to compare the transition layer structure in large cloud-free and other regions using large-eddy simulations. A useful first question to answer is whether large cloud-free areas in large-eddy simulations

do exhibit stronger vertical gradients in the transition layer than areas influenced by cloudiness. Whereas the dropsonde observations provide snapshots of the atmospheric state, large-eddy simulations provide continuous data. These simulations could allow for better tracing whether it is the dissipation of shallow clouds that smooth vertical gradients over the transition layer relative to the jump-like structure exhibited in large cloud-free areas. These simulations also provide vertical velocity at high spatial and temporal frequency. The goal is to test whether large cloud-free areas systematically have stronger subsidence, which suppresses convection, than do areas with some cloudiness.

A fourth extension, especially of Chapt. 7, is to combine different observational constraints on the trade cumulus feedback in a physical, statistical framework. Different approaches exist for combining physical constraints, as introduced in Sec. 7.6. Stevens et al. (2016b) propose a quantitative ‘storyline’ approach, which was expanded into the Bayesian statistical framework in Sherwood et al. (2020) to constrain climate sensitivity. Bretherton and Caldwell (2020) discuss an approach that uses multiple physical constraints and an ensemble of GCMs to yield a multivariate Gaussian distribution of an uncertain climate sensitivity proxy. Their approach accounts for observational uncertainties in the different metrics, sampling uncertainties, and covariance among the metrics. One drawback to this approach is an assumption of normality of the underlying variables, which could give overconfidence about the tails of the constrained distribution. Other approaches include the Bayesian approaches of Renoult et al. (2020) and Bowman et al. (2018), and machine learning approach of Schlund et al. (2020a). It is ongoing work to develop a statistical framework to combine the multiple constraints discussed in Chapt. 7 into a single probabilistic estimate of the trade cumulus feedback.

8.2.2 Bias correction using atmospheric radiative profiles from *in situ* measurements and machine learning approaches

Chapt. 3 presented over 2500 radiative profiles derived from *in situ* dropsondes and radiosondes launched during the EUREC⁴A campaign. The soundings more accurately represent fine-scale vertical moisture features, which are critical for calculating atmospheric radiative cooling profiles but are often smoothed in passive remote sensing retrievals and reanalysis data, as for example shown by Prange et al. (2021) and discussed in Chapt. 3. The EUREC⁴A soundings, and therefore the radiative profiles, also have much higher temporal and spatial sampling than the soundings that are typically launched worldwide. The greater accuracy and high sampling intensity of the soundings and radiative profiles provide an opportunity to improve satellite and reanalysis products.

Machine learning is an increasingly common approach for studying clouds and radiation, such as by training on cloud-resolving model output for use in coarser climate models (Rasp et al., 2018; Gentine et al., 2018; O’Gorman and Dwyer, 2018; Beucler et al., 2021, e.g.,). Bias correction is a common problem to which machine learning is applied (e.g., Lary et al., 2016; Karpatne et al., 2018; Mathieu and Aubrecht, 2018). A successful application of machine learning depends primarily on two factors: the machine learning algorithm and a comprehensive training data set (e.g., Mathieu and Aubrecht, 2018; Rolnick et al., 2019; Beucler et al., 2021). The radiative profiles presented in Chapt. 3, and its underlying moisture profiles, would be a useful training set in the application of machine learning, in particular using deep neural networks. The soundings and radiative profiles introduce information about short-term, small-scale features that is missing from passive remote sensing and reanalysis products and therefore has the potential to improve biases in the trades in these products.

8.2.3 How do tropical forests modulate atmospheric moisture transports?

As discussed in Sec. 1.2.1, the trades can be pictured as an expansive river in the sky, advecting moisture into the Intertropical Convergence Zone. A longer-term, broad question is, how and why does the path of water change when it moves over land? An open question is how atmospheric moisture transports work over land where the sources are more variable and the flows more influenced by topography. In other words, how does the broad, moist wave in the trade-wind atmosphere evolve as it snakes and meanders across tropical continents?

One way that land influences atmospheric water flows is through moisture recycling by rainforests, such as the vast rainforests in the Amazon and Congo Rivers. In many tropical regions, moisture appears to be transported in a sort of ‘atmospheric river’, traveling across borders, channeled narrowly in the vertical, but spread out widely in the horizontal, compared to atmospheric rivers in the extratropics, which are narrow in the horizontal and often associated with extreme precipitation (e.g., Gimeno et al., 2014; Rutz et al., 2019). There are many open questions regarding these expansive moisture transports in the tropics and how they differ from atmospheric rivers in the midlatitudes, which are better characterized (e.g., Espinoza et al., 2018). The sources of water, for instance, remain unclear. Jasechko et al. (2013) use isotope measurements to show that transpiration is the largest source of water over continents, representing 80–90% of terrestrial evapotranspiration, though other studies contend that such partitioning is subject to large uncertainties (e.g., Schlesinger and Jasechko, 2014; Ellison et al., 2017). Beyond the origins of the moisture, how do these tropical atmospheric ‘rivers’ move across borders, how variable are their flows, and how do they vary according to large-scale conditions?

These transcontinental moisture flows produce rainfall that feeds lakes and rivers, yet too often such bodies of water are considered as national entities. Political conflicts often find root in river systems, such as Egypt, Sudan, and Ethiopia’s conflicts over the Nile (e.g., Swain, 1997; Carlson, 2013). There is an impression that ‘Egypt is

the Nile’ when examining a map of its population density (e.g., as shown in Fig. 1 of Haars et al. (2016)), illustrating the preeminence of these freshwater sources for human welfare and livelihood. Yet the main source of the Nile is the Ethiopian upper Blue Nile Basin (e.g., Mellander et al., 2013), and rainfall in Ethiopia has its origins, in part, from moisture recycling from rainforests in the Congo.

An ensuing question is, how would deforestation affect these extensive tropical atmospheric rivers? Attributing precipitation changes to such human influences must be treated with caution. Ellison (2018), however, suggest that deforestation in West Africa may have decreased Nile flows from Ethiopia in the last decades of the 20th century. In other African regions, Keys et al. (2016) estimate that up to 40% of sub-Saharan rainfall is presently due to moisture recycled by vegetation. Is the ongoing famine in Madagascar, for instance, in any way connected to ongoing deforestation in the Congo River basin? Similar questions can be asked regarding the influence of deforestation on atmospheric circulations and precipitation in the Amazon (e.g., Coe et al., 2017; Staal et al., 2018), and southeast Asia (e.g., Paul et al., 2016).

Tropical atmospheric moisture flows and their interactions with land are not yet fully understood, and they have never been governed, as would be a river that crosses international borders on land. Storm-resolving models, in concert with remote sensing and *in situ* observations, are a new tool and potentially have advantages for studying these atmospheric moisture flows and precipitation compared to GCMs. There are indications that storm-resolving models may better represent precipitation than GCMs with certain well-documented deficiencies, such as raining too early in the day and too frequently compared to observations (e.g., Palmer and Stevens, 2019; Stevens et al., 2020a). The influences of deforestation on atmospheric water flows could potentially be studied by selectively changing the evaporative capacity over land to reflect how forests modulate water flows compared to deforested areas. Increasing physical understanding of these atmospheric moisture flows and precipitation would provide valuable information for scientists, stakeholders, and policymakers. It therefore seems reasonable to approach these questions with a diversity of tools, and new storm-resolving models complement existing studies using *in situ* observations,

satellite products, and GCMs. Idealized bulk models, similar to those used in this thesis, have provided insights to land-atmosphere couplings (e.g., Betts, 2000; Cronin, 2013) and could also potentially be used in an exploration of the influence of forests on atmospheric moisture variability.

8.2.4 Final thoughts

Behind the apparent steadiness of the trades, as evoked by Pierre Loti, with its “same regular breath, warm, exquisite to breathe; and the same transparent sea, and the same small white clouds”, a more dynamic picture emerges. Ideas in this thesis allow for proposing new conceptual models of the lower trade-wind atmosphere and a more active role for cloud mixing processes in determining its vertical structure, and falsifying a strong trade-wind cloud response to warming, based on clouds being dynamically, rather than thermodynamically controlled. I hope that this thesis was at times enjoyable to read. Participating in EUREC⁴A was a tremendous opportunity to be immersed in the natural environment that I study and approach these questions with first-hand experience, having collected data, watched clouds form and dissipate, and imagined the circulations that fuel these clouds. There remains much to be understood about the trades and how they will evolve with warming. I can only hope that some of the ideas in this thesis can help improve our understanding of the surprises still hidden in the clouds.

Chapter 9

Additional materials

A list of publications as first or co-author is included at the end of this thesis manuscript.

As a final note, another part of my research, developed with Peter Huybers, involves studying aerosols and their multifaceted influences, on radiation and the climate system, as well as on paintings. Regarding the former, our recent paper Albright et al. (2021b) is included in the list of publications, at the end of this thesis after the bibliography. This work uses a Bayesian model of aerosol forcing and Earth’s multi-time-scale temperature response to radiative forcing to understand the origins of different lower bounds on aerosol forcing. We first demonstrate the ability of a simple aerosol model to emulate aerosol radiative forcing simulated by 10 general circulation models. A joint inference of climate sensitivity and effective aerosol forcing from historical surface temperatures is then made over 1850–2019. We obtain a maximum likelihood estimate of aerosol radiative forcing of -0.85 Wm^{-2} (5–95% credible interval from -1.3 to -0.50 Wm^{-2}) for 2010–19 relative to 1750. A relatively tight bound on aerosol forcing is obtained from the structure of temperature and aerosol precursor emissions and, particularly, from the rapid growth in emissions between 1950 and 1980. Obtaining a 5th percentile lower bound on aerosol forcing around -2.0 Wm^{-2} requires prescribing internal climate variance that is a factor of 5 larger than the CMIP6 mean and assuming large, correlated errors in global temperature observations. Ocean heat uptake observations may further constrain aerosol radiative forcing but require a better understanding of the relationship between time-variable radiative feedbacks and radiative forcing.

Regarding the latter, after studying aerosol forcing over the instrumental period,

we look further back in time to study the influence of 19th century air pollution in London and Paris. We present evidence that trends in paintings by J.M.W. Turner and Claude Monet depict trends in historical air pollution. The abstract of this paper, which is in preparation, is reproduced here.

**Paintings by Turner and Monet Depict
Trends in 19th Century Air Pollution**

Abstract: Anthropogenic aerosol emissions increased to unprecedented levels during the 19th century Industrial Revolution, particularly in Western European cities, leading to an optical environment having less contrast and more intensity. Here we show that the trends from more figurative to impressionistic representations in J.M.W. Turner and Claude Monet's paintings in London and Paris over the 19th century render changes in their local optical environment. In particular, we demonstrate that changes in local SO₂ emissions are a highly statistically-significant explanatory variable for trends in the contrast and intensity of Turner, Monet, and others' works, including after controlling for time trends and subject matter. Industrialization altered the environmental context in which painting occurred, and our results indicate that Impressionism contains elements of polluted realism.

Bibliography

- Bruce Albrecht, Virendra Ghate, Johannes Mohrmann, Robert Wood, Paquita Zuidema, Christopher Bretherton, Christian Schwartz, Edwin Eloranta, Susanne Glienke, Shaunna Donaher, et al. Cloud System Evolution in the Trades (CSET): Following the evolution of boundary layer cloud systems with the NSF–NCAR GV. *Bulletin of the American Meteorological Society*, 100(1):93–121, 2019.
- Bruce A Albrecht, Alan K Betts, Wayne H Schubert, and Stephen K Cox. Model of the thermodynamic structure of the trade-wind boundary layer: Part I. theoretical formulation and sensitivity tests. *Journal of Atmospheric Sciences*, 36(1):73–89, 1979.
- Anna Lea Albright, Benjamin Fildier, Ludovic Touzé-Peiffer, Robert Pincus, Jessica Vial, and Caroline Muller. Atmospheric radiative profiles during EUREC⁴A. *Earth System Science Data*, 13(2):617–630, 2021a.
- Anna Lea Albright, Cristian Proistosescu, and Peter Huybers. Origins of a relatively tight lower bound on anthropogenic aerosol radiative forcing from Bayesian analysis of historical observations. *Journal of Climate*, 34(21):8777–8792, 2021b.
- Anna Lea Albright, Sandrine Bony, Bjorn Stevens, and Raphaela Vogel. Observed subcloud layer moisture and heat budgets in the trades. *Journal of the Atmospheric Sciences*, 2022.
- Myles R Allen and William J Ingram. Constraints on future changes in climate and the hydrologic cycle. *Nature*, 419(6903):228–232, 2002.
- Timothy Andrews, Jonathan M Gregory, Mark J Webb, and Karl E Taylor. Forcing, feedbacks and climate sensitivity in CMIP5 coupled atmosphere-ocean climate models. *Geophysical research letters*, 39(9), 2012.
- Akio Arakawa and Wayne Howard Schubert. Interaction of a cumulus cloud ensemble with the large-scale environment, part I. *Journal of the Atmospheric Sciences*, 31(3):674–701, 1974.
- Paola Arias, Nicolas Bellouin, Erika Coppola, Richard Jones, Gerhard Krinner, Jochem Marotzke, Vaishali Naik, Matthew Palmer, G-K Plattner, Joeri Rogelj, et al. Climate Change 2021: The physical science basis. Contribution of working group I to the sixth assessment report of the Intergovernmental Panel on Climate Change; Technical summary. 2021.
- Kyle C Armour, Cecilia M Bitz, and Gerard H Roe. Time-varying climate sensitivity from regional feedbacks. *Journal of Climate*, 26(13):4518–4534, 2013.

- Svante Arrhenius. *Worlds in the making: the evolution of the universe*. Harper & brothers, 1908.
- Ernst Augstein, Herbert Riehl, Feodor Ostapoff, and Volker Wagner. Mass and energy transports in an undisturbed Atlantic trade-wind flow. *Monthly Weather Review*, 101(2):101–111, 1973.
- Ernst Augstein, Heiner Schmidt, and Feodor Ostapoff. The vertical structure of the atmospheric planetary boundary layer in undisturbed trade winds over the Atlantic Ocean. *Boundary-Layer Meteorology*, 6(1-2):129–150, 1974.
- François Bellec. *Marchands au long cours*. Ed du Chêne, 2003.
- Gilles Bellon and Bjorn Stevens. Using the sensitivity of large-eddy simulations to evaluate atmospheric boundary layer models. *Journal of the Atmospheric Sciences*, 69(5):1582–1601, 2012.
- Gilles Bellon and Bjorn Stevens. Time scales of the trade wind boundary layer adjustment. *Journal of the atmospheric sciences*, 70(4):1071–1083, 2013.
- AK Betts. Non-precipitating cumulus convection and its parameterization. *Quarterly Journal of the Royal Meteorological Society*, 99(419):178–196, 1973.
- Alan Betts. Modeling subcloud layer structure and interaction with shallow cumulus layer. *Journal of the Atmospheric Sciences*, 33:2363–2382, 1976.
- Alan K Betts. Thermodynamic classification of tropical convective soundings. *Monthly Weather Review*, 102(11):760–764, 1974.
- Alan K Betts. Idealized model for equilibrium boundary layer over land. *Journal of Hydrometeorology*, 1(6):507–523, 2000.
- Alan K Betts and Bruce A Albrecht. Conserved variable analysis of the convective boundary layer thermodynamic structure over the tropical oceans. *Journal of Atmospheric Sciences*, 44(1):83–99, 1987.
- Alan K Betts and W Ridgway. Climatic equilibrium of the atmospheric convective boundary layer over a tropical ocean. *Journal of the Atmospheric Sciences*, 46(17):2621–2641, 1989.
- Tom Beucler, Imme Ebert-Uphoff, Stephan Rasp, Michael Pritchard, and Pierre Gentine. Machine learning for clouds and climate (invited chapter for the AGU geophysical monograph series ‘clouds and climate’). 2021.
- Frank Beyrich and Jens-Peter Leps. An operational mixing height data set from routine radiosoundings at Lindenberg: Methodology. *Meteorologische Zeitschrift*, 21(4):337–348, 2012.
- Sebastien P Bigorre and Albert J Plueddemann. The Annual cycle of air-sea fluxes in the northwest tropical Atlantic. *Frontiers in Marine Science*, 7:1204, 2021.

- Jonah Bloch-Johnson, Raymond T Pierrehumbert, and Dorian S Abbot. Feedback temperature dependence determines the risk of high warming. *Geophysical Research Letters*, 42(12):4973–4980, 2015.
- Peter N Blossey, Christopher S Bretherton, Minghua Zhang, Anning Cheng, Satoshi Endo, Thijs Heus, Yangang Liu, Adrian P Lock, Stephan R de Roode, and Kuan-Man Xu. Marine low cloud sensitivity to an idealized climate change: The CGILS LES intercomparison. *Journal of Advances in Modeling Earth Systems*, 5(2):234–258, 2013.
- Olivier Bock, Pierre Bosser, Cyrille Flamant, Erik Doerflinger, Friedhelm Jansen, Romain Fages, Sandrine Bony, and Sabrina Schnitt. Integrated water vapour observations in the Caribbean arc from a network of ground-based GNSS receivers during EUREC⁴A. *Earth System Science Data*, 13(5):2407–2436, 2021.
- Steven J Böing, Harm JJ Jonker, Witek A Nawara, and A Pier Siebesma. On the deceiving aspects of mixing diagrams of deep cumulus convection. *Journal of the Atmospheric Sciences*, 71(1):56–68, 2014.
- Sandrine Bony and Jean-Louis Dufresne. Marine boundary layer clouds at the heart of tropical cloud feedback uncertainties in climate models. *Geophysical Research Letters*, 32(20), 2005. doi: 10.1029/2005GL023851.
- Sandrine Bony and Bjorn Stevens. Measuring area-averaged vertical motions with dropsondes. *Journal of the Atmospheric Sciences*, 76(3):767–783, 2019. doi: 10.1175/JAS-D-18-0141.1.
- Sandrine Bony, Jean-Louis Dufresne, Herve Le Treut, Jean-Jacques Morcrette, and Catherine Senior. On dynamic and thermodynamic components of cloud changes. *Climate Dynamics*, 22(2-3):71–86, 2004.
- Sandrine Bony, Robert Colman, Vladimir M Kattsov, Richard P Allan, Christopher S Bretherton, Jean-Louis Dufresne, Alex Hall, Stephane Hallegatte, Marika M Holland, William Ingram, et al. How well do we understand and evaluate climate change feedback processes? *Journal of Climate*, 19(15):3445–3482, 2006.
- Sandrine Bony, Gilles Bellon, Daniel Klocke, Steven Sherwood, Solange Fermepin, and Sébastien Denvil. Robust direct effect of carbon dioxide on tropical circulation and regional precipitation. *Nature Geoscience*, 6(6):447–451, 2013a.
- Sandrine Bony, Bjorn Stevens, Isaac H Held, John F Mitchell, Jean-Louis Dufresne, Kerry A Emanuel, Pierre Friedlingstein, Stephen Griffies, and Catherine Senior. Carbon dioxide and climate: Perspectives on a scientific assessment. In *Climate science for serving society*, pages 391–413. Springer, 2013b.
- Sandrine Bony, Bjorn Stevens, Félix Ament, Sebastien Bigorre, Patrick Chazette, Susanne Crewell, Julien Delanoë, Kerry Emanuel, David Farrell, Cyrille Flamant, Silke Gross, Lutz Hirsh, Johannes Karstensen, Bernhard Mayer, Louise

- Nuijens, James H. Ruppert, Irina Sandu, Pier Siebesma, Sabrina Speich, Frédéric Szczap, Julien Totems, Raphaela Vogel, Manfred Wendisch, and Martin Wirth. EUREC⁴A: A field campaign to elucidate the couplings between clouds, convection and circulation. *Surveys in Geophysics*, 38(6):1529–1568, 2017. doi: 10.1007/s10712-017-9428-0.
- Sandrine Bony, Hauke Schulz, Jessica Vial, and Bjorn Stevens. Sugar, gravel, fish, and flowers: Dependence of mesoscale patterns of trade-wind clouds on environmental conditions. *Geophysical Research Letters*, 47(7):e2019GL085988, 2020.
- Sandrine Bony, Marie Lothon, Julien Delanoë, Pierre Coutris, Jean-Claude Etienne, Franziska Aemisegger, Anna Lea Albright, Thierry André, Hubert Bellec, Alexandre Baron, et al. EUREC⁴A observations from the SAFIRE ATR42 aircraft. *Earth System Science Data Discussions*, pages 1–61, 2022.
- Olivier Boucher, Jérôme Servonnat, Anna Lea Albright, Olivier Aumont, Yves Balkanski, Vladislav Bastrikov, Slimane Bekki, Rémy Bonnet, Sandrine Bony, Laurent Bopp, et al. Presentation and evaluation of the IPSL-CM6A-LR climate model. *Journal of Advances in Modeling Earth Systems*, 12(7):e2019MS002010, 2020.
- Kevin W Bowman, Noel Cressie, Xin Qu, and Alex Hall. A hierarchical statistical framework for emergent constraints: Application to snow-albedo feedback. *Geophysical Research Letters*, 45(23):13–050, 2018.
- Kamau Brathwaite. *Born to Slow Horses*. Wesleyan University Press, 2005.
- C. S. Bretherton and P. N. Blossey. Understanding mesoscale aggregation of shallow cumulus convection using large-eddy simulation. *Journal of Advances in Modeling Earth Systems*, 9(8):2798–2821, 2017a. URL <https://agupubs.onlinelibrary.wiley.com/doi/abs/10.1002/2017MS000981>.
- Christopher S Bretherton. Insights into low-latitude cloud feedbacks from high-resolution models. *Philosophical Transactions of the Royal Society A: Mathematical, Physical and Engineering Sciences*, 373(2054):20140415, 2015.
- Christopher S Bretherton and Peter M Caldwell. Combining emergent constraints for climate sensitivity. *Journal of Climate*, 33(17):7413–7430, 2020.
- Christopher S Bretherton and Matthew C Wyant. Moisture transport, lower-tropospheric stability, and decoupling of cloud-topped boundary layers. *Journal of Atmospheric Sciences*, 54(1):148–167, 1997.
- Christopher S Bretherton, Malcolm K MacVean, Peter Bechtold, Andreas Chlond, William R Cotton, Joan Cuxart, Hans Cuijpers, M Mhairoutdinov, Bronko Kosovic, Dave Lewellen, et al. An intercomparison of radiatively driven entrainment and turbulence in a smoke cloud, as simulated by different numerical models. *Quarterly Journal of the Royal Meteorological Society*, 125(554):391–423, 1999.

- Christopher S Bretherton, Taneil Uttal, Christopher W Fairall, Sandra E Yuter, Robert A Weller, Darrel Baumgardner, Kimberly Comstock, Robert Wood, and Graciela B Raga. The EPIC 2001 stratocumulus study. *Bulletin of the American Meteorological Society*, 85(7):967–978, 2004.
- Christopher S. Bretherton, Peter N. Blossey, Marat Khairoutdinov, Christopher S. Bretherton, Peter N. Blossey, and Marat Khairoutdinov. An Energy-Balance Analysis of Deep Convective Self-Aggregation above Uniform SST. *Journal of the Atmospheric Sciences*, 62(12):4273–4292, dec 2005. ISSN 0022-4928. doi: 10.1175/JAS3614.1.
- CS Bretherton. Entrainment, detrainment and mixing in atmospheric convection. In *The Physics and Parameterization of Moist Atmospheric Convection*, pages 211–230. Springer, 1997.
- CS Bretherton and PN Blossey. Understanding mesoscale aggregation of shallow cumulus convection using large-eddy simulation. *Journal of Advances in Modeling Earth Systems*, 9(8):2798–2821, 2017b. doi: 10.1002/2017MS000981.
- F Brient and S Bony. How may low-cloud radiative properties simulated in the current climate influence low-cloud feedbacks under global warming? *Geophysical Research Letters*, 39(20), 2012.
- Florent Brient and Sandrine Bony. Interpretation of the positive low-cloud feedback predicted by a climate model under global warming. *Climate Dynamics*, 40(9): 2415–2431, 2013.
- Florent Brient and Tapio Schneider. Constraints on climate sensitivity from space-based measurements of low-cloud reflection. *Journal of Climate*, 29(16):5821–5835, 2016.
- Florent Brient, Tapio Schneider, Zhihong Tan, Sandrine Bony, Xin Qu, and Alex Hall. Shallowness of tropical low clouds as a predictor of climate models’ response to warming. *Climate Dynamics*, 47(1-2):433–449, 2016.
- Peter Caldwell, Christopher S Bretherton, and Robert Wood. Mixed-layer budget analysis of the diurnal cycle of entrainment in southeast Pacific stratocumulus. *Journal of the Atmospheric Sciences*, 62(10):3775–3791, 2005.
- Peter M Caldwell, Christopher S Bretherton, Mark D Zelinka, Stephen A Klein, Benjamin D Santer, and Benjamin M Sanderson. Statistical significance of climate sensitivity predictors obtained by data mining. *Geophysical Research Letters*, 41(5):1803–1808, 2014.
- Peter M Caldwell, Mark D Zelinka, and Stephen A Klein. Evaluating emergent constraints on equilibrium climate sensitivity. *Journal of Climate*, 31(10):3921–3942, 2018.

- Guylaine Canut, Fleur Couvreur, Marie Lothon, David Pino, and Frédérique Saïd. Observations and large-eddy simulations of entrainment in the sheared Sahelian boundary layer. *Boundary-layer meteorology*, 142(1):79–101, 2012.
- Guangxia Cao, Thomas W Giambelluca, Duane E Stevens, and Thomas A Schroeder. Inversion variability in the hawaiian trade wind regime. *Journal of Climate*, 20(7): 1145–1160, 2007. doi: 10.1175/JCLI4033.1.
- Andrew Carlson. Who owns the Nile? Egypt, Sudan, and Ethiopia’s history-changing dam. *Origins*, 6(6), 2013.
- K. S. Carslaw, L. A. Lee, L. A. Regayre, and J. S. Johnson. Climate models are uncertain, but we can do something about it. *EOS*, 99, 2018.
- Paulo Ceppi, Florent Brient, Mark D Zelinka, and Dennis L Hartmann. Cloud feedback mechanisms and their representation in global climate models. *Wiley Interdisciplinary Reviews: Climate Change*, 8(4):e465, 2017.
- Grégory V Cesana and Anthony D Del Genio. Observational constraint on cloud feedbacks suggests moderate climate sensitivity. *Nature Climate Change*, 11(3): 213–218, 2021.
- Robert D Cess, Gerald L Potter, JP Blanchet, GJ Boer, SJ Ghan, JT Kiehl, H Le Treut, Z-X Li, X-Z Liang, JFB Mitchell, et al. Interpretation of cloud-climate feedback as produced by 14 atmospheric general circulation models. *Science*, 245 (4917):513–516, 1989.
- Jule G Charney, Akio Arakawa, D James Baker, Bert Bolin, Robert E Dickinson, Richard M Goody, Cecil E Leith, Henry M Stommel, and Carl I Wunsch. *Carbon dioxide and climate: a scientific assessment*. National Academy of Sciences, Washington, DC, 1979.
- P. Chazette, F. Marnas, J. Totems, and X. Shang. Comparison of IASI water vapor retrieval with H₂O-Raman lidar in the framework of the Mediterranean HyMeX and ChArMEx programs. *Atmospheric Chemistry and Physics*, 14(18):9583–9596, sep 2014. ISSN 1680-7324. doi: 10.5194/acp-14-9583-2014.
- Patrick Chazette, Julien Totems, Alexandre Baron, Cyrille Flamant, and Sandrine Bony. Trade-wind clouds and aerosols characterized by airborne horizontal lidar measurements during the EUREC⁴A field campaign. *Earth System Science Data*, 12(4):2919–2936, 2020.
- H Chepfer, S Bony, D Winker, G Cesana, JL Dufresne, P Minnis, CJ Stubenrauch, and S Zeng. The GCM-oriented Calipso cloud product (CALIPSO-GOCCP). *Journal of Geophysical Research: Atmospheres*, 115(D4), 2010.
- Michael T Coe, Paulo M Brando, Linda A Deegan, Marcia N Macedo, Christopher Neill, and Divino V Silverio. The forests of the Amazon and Cerrado moderate

- regional climate and are the key to the future. *Tropical Conservation Science*, 10:1940082917720671, 2017.
- Timothy W Cronin. A sensitivity theory for the equilibrium boundary layer over land. *Journal of Advances in Modeling Earth Systems*, 5(4):764–784, 2013.
- C Dai, Q Wang, JA Kalogiros, DH Lenschow, Z Gao, and M Zhou. Determining boundary-layer height from aircraft measurements. *Boundary-layer meteorology*, 152(3):277–302, 2014.
- Gokhan Danabasoglu, J-F Lamarque, J Bacmeister, DA Bailey, AK DuVivier, Jim Edwards, LK Emmons, John Fasullo, R Garcia, Andrew Gettelman, et al. The Community earth system model version 2 (CESM2). *Journal of Advances in Modeling Earth Systems*, 12(2), 2020.
- Thibaut Dauhut, Fleur Couvreur, Dominique Bouniol, and Coauthors. Flower trade-wind clouds are shallow mesoscale convective systems. *Quarterly Journal of the Royal Meteorological Society*, pages 38–70, 2022.
- Gijs de Boer, Steven Borenstein, Radiance Calmer, Christopher Cox, Michael Rhodes, Christopher Choate, Jonathan Hamilton, Jackson Osborn, Dale Lawrence, Brian Argrow, et al. Measurements from the University of Colorado RAAVEN uncrewed aircraft system during ATOMIC. *Earth System Science Data*, 14(1):19–31, 2022.
- James W Deardorff. Parameterization of the planetary boundary layer for use in general circulation models. *Monthly Weather Review*, 100(2):93–106, 1972.
- Oxford-English Dictionary. Oxford english dictionary.
- Thomas G Dopplick. Radiative heating of the global atmosphere. *Journal of the Atmospheric Sciences*, 29(7):1278–1294, 1972.
- AGM Driedonks. Models and observations of the growth of the atmospheric boundary layer. *Boundary-Layer Meteorology*, 23(3):283–306, 1982.
- Jean-Louis Dufresne and Sandrine Bony. An assessment of the primary sources of spread of global warming estimates from coupled atmosphere–ocean models. *Journal of Climate*, 21(19):5135–5144, 2008.
- Christoph Dyroff, Andreas Zahn, Emanuel Christner, Richard Forbes, Adrian M Tompkins, and Peter FJ van Velthoven. Comparison of ECMWF analysis and forecast humidity data with CARIBIC upper troposphere and lower stratosphere observations. *Quarterly Journal of the Royal Meteorological Society*, 141(688):833–844, 2015. doi: <https://doi.org/10.1002/qj.2400>.
- David Ellison. Forests and water. *Background Analytical Study*, 2, 2018.

- David Ellison, Cindy E Morris, Bruno Locatelli, Douglas Sheil, Jane Cohen, Daniel Murdiyarso, Victoria Gutierrez, Meine Van Noordwijk, Irena F Creed, Jan Pokorny, et al. Trees, forests and water: Cool insights for a hot world. *Global Environmental Change*, 43:51–61, 2017.
- Kerry Emanuel. The effect of convective response time on wishe modes. *Journal of Atmospheric Sciences*, 50(12):1763–1776, 1993.
- Kerry Emanuel, Allison A Wing, and Emmanuel M Vincent. Radiative-convective instability. *Journal of Advances in Modeling Earth Systems*, pages 75–90, 2014. doi: 10.1002/2013MS000270.Received.
- Kerry A Emanuel. An air-sea interaction theory for tropical cyclones. part I: Steady-state maintenance. *Journal of Atmospheric Sciences*, 43(6):585–605, 1986.
- Kerry A Emanuel, J David Neelin, and Christopher S Bretherton. On large-scale circulations in convecting atmospheres. *Quarterly Journal of the Royal Meteorological Society*, 120(519):1111–1143, 1994a.
- Kerry A Emanuel et al. *Atmospheric convection*. Oxford University Press on Demand, 1994b.
- Vicky Espinoza, Duane E Waliser, Bin Guan, David A Lavers, and F Martin Ralph. Global analysis of climate change projection effects on atmospheric rivers. *Geophysical Research Letters*, 45(9):4299–4308, 2018.
- European Centre for Medium-Range Weather Forecasts. ERA5 Reanalysis, 2017.
- Veronika Eyring, Peter M Cox, Gregory M Flato, Peter J Gleckler, Gab Abramowitz, Peter Caldwell, William D Collins, Bettina K Gier, Alex D Hall, Forrest M Hoffman, et al. Taking climate model evaluation to the next level. *Nature Climate Change*, 9(2):102–110, 2019.
- Chris W Fairall, Edward F Bradley, JE Hare, Andrey A Grachev, and James B Edson. Bulk parameterization of air–sea fluxes: Updates and verification for the coare algorithm. *Journal of climate*, 16(4):571–591, 2003.
- Evgeni Fedorovich, Robert Conzemius, and Dmitrii Mironov. Convective entrainment into a shear-free, linearly stratified atmosphere: Bulk models reevaluated through large eddy simulations. *Journal of the atmospheric sciences*, 61(3):281–295, 2004.
- James R Fleming. Joseph fourier, the ‘greenhouse effect’, and the quest for a universal theory of terrestrial temperatures. *Endeavour*, 23(2):72–75, 1999.
- Clare Marie Flynn and Thorsten Mauritsen. On the climate sensitivity and historical warming evolution in recent coupled model ensembles. *Atmospheric Chemistry and Physics*, 20(13):7829–7842, 2020.

- Ž Fuchs-Stone, David J Raymond, and S Sentić. OTREC2019: Convection over the east Pacific and southwest Caribbean. *Geophysical Research Letters*, 47(11): e2020GL087564, 2020.
- L Garand, D S Turner, M Larocque, J Bates, S Boukabara, P Brunel, F Chevalier, G Deblonde, R Engelen, M Hollingshead, D Jackson, G Jedlovec, J Joiner, T Kleespies, D S McKague, L McMillin, J L Moncet, J R Pardo, P J Rayer, E Salathe, R Saunders, N. A. Scott, P Van Delst, and H Woolf. Radiance and Jacobian intercomparison of radiative transfer models applied to HIRS and AMSU channels. *J. Geophys. Res.*, 106(D20):24017–24031, October 2001. doi: 10.1029/2000JD000184.
- Jade Rachele Garcia and Juan Pedro Mellado. The two-layer structure of the entrainment zone in the convective boundary layer. *Journal of the Atmospheric Sciences*, 71(6):1935–1955, 2014.
- John Roy Garratt. The atmospheric boundary layer. *Earth-Science Reviews*, 37(1-2): 89–134, 1994.
- Michael Garstang, Edward Zipser, Robert Ellingson, Kenneth Warsh, Peter Grose, Stanley Ulanski, Ronald Holle, Ward Seguin, David Fitzjarrald, Steven Greco, et al. Three early tropical field experiments. *Bulletin of the American Meteorological Society*, 100(11):2243–2258, 2019.
- W Lawrence Gates, James S Boyle, Curt Covey, Clyde G Dease, Charles M Doutriaux, Robert S Drach, Michael Fiorino, Peter J Gleckler, Justin J Hnilo, Susan M Marlais, et al. An overview of the results of the Atmospheric Model Intercomparison Project (AMIP I). *Bulletin of the American Meteorological Society*, 80(1):29–56, 1999.
- Iliana Genkova, Gabriela Seiz, Paquita Zuidema, Guangyu Zhao, and Larry Di Girolamo. Cloud top height comparisons from ASTER, MISR, and MODIS for trade wind cumuli. *Remote sensing of environment*, 107(1-2):211–222, 2007.
- Pierre Gentine, Alan K Betts, Benjamin R Lintner, Kirsten L Findell, Chiel C Van Heerwaarden, and Fabio D’andrea. A probabilistic bulk model of coupled mixed layer and convection. part II: Shallow convection case. *Journal of the Atmospheric Sciences*, 70(6):1557–1576, 2013.
- Pierre Gentine, Mike Pritchard, Stephan Rasp, Gael Reinaudi, and Galen Yacalis. Could machine learning break the convection parameterization deadlock? *Geophysical Research Letters*, 45(11):5742–5751, 2018.
- Geet George, Bjorn Stevens, Sandrine Bony, Robert Pincus, Chris Fairall, Hauke Schulz, Tobias Kölling, Quinn T Kalen, Marcus Klingebiel, Heike Konow, et al. JOANNE: Joint dropsonde Observations of the Atmosphere in tropical North Atlantic meso-scale Environments. *Earth System Science Data Discussions*, pages 1–33, 2021.

- A Gettelman, JE Kay, and KM Shell. The evolution of climate sensitivity and climate feedbacks in the Community Atmosphere Model. *Journal of Climate*, 25(5):1453–1469, 2012.
- Andrew Gettelman, Cecile Hannay, Julio T Bacmeister, Richard B Neale, AG Pendergrass, G Danabasoglu, J-F Lamarque, JT Fasullo, DA Bailey, DM Lawrence, et al. High climate sensitivity in the Community Earth System Model version 2 (CESM2). *Geophysical Research Letters*, 46(14):8329–8337, 2019.
- Virendra P Ghate, David B Mechem, Maria P Cadeddu, Edwin W Eloranta, Michael P Jensen, Michele L Nordeen, and William L Smith Jr. Estimates of entrainment in closed cellular marine stratocumulus clouds from the MAGIC field campaign. *Quarterly Journal of the Royal Meteorological Society*, 145(721):1589–1602, 2019.
- Luis Gimeno, Raquel Nieto, Marta Vázquez, and David A Lavers. Atmospheric rivers: A mini-review. *Frontiers in Earth Science*, 2:2, 2014.
- William M Gray and Robert W Jacobson Jr. Diurnal variation of deep cumulus convection. *Monthly Weather Review*, 105(9):1171–1188, 1977.
- JM Gregory, WJ Ingram, MA Palmer, GS Jones, PA Stott, RB Thorpe, JA Lowe, TC Johns, and KD Williams. A new method for diagnosing radiative forcing and climate sensitivity. *Geophysical research letters*, 31(3), 2004.
- F. Guichard, D. Parsons, and E. Miller. Thermodynamic and radiative impact of the correction of sounding humidity bias in the tropics. *Journal of Climate*, 13(20):3611–3624, 2000.
- Manuel Gutleben, Silke Martha Groß, and Martin Wirth. Cloud macro-physical properties in Saharan-dust-laden and dust-free north Atlantic trade wind regimes: a lidar case study. *Atmospheric Chemistry and Physics (ACP)*, 19(16):10659–10673, 2019. doi: 10.5194/acp-19-10659-2019.
- Manuel Gutleben, Silke Groß, Martin Wirth, and Bernhard Mayer. Radiative effects of long-range-transported saharan air layers as determined from airborne lidar measurements. *Atmospheric Chemistry and Physics*, 20(20):12313–12327, 2020.
- Christian Haars, EM Lönsjö, Bianca Mogos, and Bram Winkelaar. The uncertain future of the Nile Delta. *NASA/GSFC: Greenbelt, MD, USA*, 2016.
- Alex Hall and Xin Qu. Using the current seasonal cycle to constrain snow albedo feedback in future climate change. *Geophysical Research Letters*, 33(3), 2006.
- Alex Hall, Peter Cox, Chris Huntingford, and Stephen Klein. Progressing emergent constraints on future climate change. *Nature Climate Change*, 9(4):269–278, 2019.
- Richard Hamblyn. *The invention of clouds: How an amateur meteorologist forged the language of the skies*. Macmillan, 2002.

- Dennis L Hartmann, Maureen E Ockert-Bell, and Marc L Michelsen. The effect of cloud type on Earth’s energy balance: Global analysis. *Journal of Climate*, 5(11):1281–1304, 1992.
- W.K. Hastings. Monte Carlo sampling methods using Markov chains and their application. *Biometrika*, 57(1):97—109, 1970.
- William A Heckley. Systematic errors of the ECMWF operational forecasting model in tropical regions. *Quarterly Journal of the Royal Meteorological Society*, 111(469):709–738, 1985.
- Jerome L Heffter. Air resources laboratories atmospheric transport and dispersion model (ARL-ATAD). Technical report, 1980.
- Hans Hersbach, Bill Bell, Paul Berrisford, Shoji Hirahara, András Horányi, Joaquín Muñoz-Sabater, Julien Nicolas, Carole Peubey, Raluca Radu, Dinand Schepers, et al. The ERA5 global reanalysis. *Quarterly Journal of the Royal Meteorological Society*, 146(730):1999–2049, 2020.
- Thijs Heus, Gertjan Van Dijk, Harm JJ Jonker, and Harry EA Van den Akker. Mixing in shallow cumulus clouds studied by Lagrangian particle tracking. *Journal of the Atmospheric Sciences*, 65(8):2581–2597, 2008.
- Joshua Z Holland. Preliminary report on the BOMEX sea-air interaction program. *Bulletin of the American Meteorological Society*, 51(9):809–821, 1970.
- Joshua Z Holland and Eugene M Rasmusson. Measurements of the atmospheric mass, energy, and momentum budgets over a 500-kilometer square of tropical ocean. *Monthly Weather Review*, 101(1):44–55, 1973.
- George C Holzworth. Estimates of mean maximum mixing depths in the contiguous united states. *Mon. Weather Rev*, 92(5):235–242, 1964.
- Peter Huybers. Compensation between model feedbacks and curtailment of climate sensitivity. *Journal of Climate*, 23(11):3009–3018, 2010.
- AJ Illingworth, RJ Hogan, EJ O’connor, Dominique Bouniol, ME Brooks, Julien Delanoë, DP Donovan, JD Eastment, N Gaussiat, JWF Goddard, et al. Cloudnet: Continuous evaluation of cloud profiles in seven operational models using ground-based observations. *Bulletin of the American Meteorological Society*, 88(6):883–898, 2007.
- Kuniaki Inoue and Larissa Back. Column-integrated moist static energy budget analysis on various time scales during TOGA COARE. *Journal of the Atmospheric Sciences*, 72(5):1856–1871, 2015.
- Marek Jacob, Pavlos Kollias, Felix Ament, Vera Schemann, and Susanne Crewell. Multilayer cloud conditions in trade wind shallow cumulus—confronting two ICON model derivatives with airborne observations. *Geoscientific Model Development*, 13(11):5757–5777, 2020.

- Scott Jasechko, Zachary D Sharp, John J Gibson, S Jean Birks, Yi Yi, and Peter J Fawcett. Terrestrial water fluxes dominated by transpiration. *Nature*, 496(7445): 347–350, 2013.
- Nadir Jeevanjee and Stephan Fueglistaler. Simple spectral models for atmospheric radiative cooling. *Journal of the Atmospheric Sciences*, 77(2):479–497, 2020. doi: <https://doi.org/10.1175/JAS-D-18-0347.1>.
- Richard H Johnson, Thomas M Rickenbach, Steven A Rutledge, Paul E Ciesielski, and Wayne H Schubert. Trimodal characteristics of tropical convection. *Journal of climate*, 12(8):2397–2418, 1999.
- Peter Kalmus, Matthew Lebsock, and João Teixeira. Observational boundary layer energy and water budgets of the stratocumulus-to-cumulus transition. *Journal of Climate*, 27(24):9155–9170, 2014.
- Youichi Kamae, Hideo Shiogama, Masahiro Watanabe, Tomoo Ogura, Tokuta Yokohata, and Masahide Kimoto. Lower-tropospheric mixing as a constraint on cloud feedback in a multiparameter multiphysics ensemble. *Journal of Climate*, 29(17): 6259–6275, 2016.
- Anuj Karpatne, Imme Ebert-Uphoff, Sai Ravela, Hassan Ali Babaie, and Vipin Kumar. Machine learning for the geosciences: Challenges and opportunities. *IEEE Transactions on Knowledge and Data Engineering*, 31(8):1544–1554, 2018.
- Seiji Kato, Thomas P Ackerman, Eugene E Clothiaux, James H Mather, Gerald G Mace, Marvin L Wesely, Frank Murcray, and Joseph Michalsky. Uncertainties in modeled and measured clear-sky surface shortwave irradiances. *Journal of Geophysical Research: Atmospheres*, 102(D22):25881–25898, 1997. doi: 10.1029/97JD01841.
- SR Kawa and R Pearson Jr. An observational study of stratocumulus entrainment and thermodynamics. *Journal of the atmospheric sciences*, 46(17):2649–2661, 1989.
- Patrick W Keys, Lan Wang-Erlandsson, and Line J Gordon. Revealing invisible water: moisture recycling as an ecosystem service. *PloS one*, 11(3):e0151993, 2016.
- Stephen A Klein and Alex Hall. Emergent constraints for cloud feedbacks. *Current climate change reports*, 1(4):276–287, 2015.
- Reto Knutti, Maria AA Rugenstein, and Gabriele C Hegerl. Beyond equilibrium climate sensitivity. *Nature Geoscience*, 10(10):727–736, 2017.
- Heike Konow, Marek Jacob, Felix Ament, Susanne Crewell, Florian Ewald, Martin Hagen, Lutz Hirsch, Friedhelm Jansen, Mario Mech, and Bjorn Stevens. A unified data set of airborne cloud remote sensing using the HALO Microwave Package (HAMP). *Earth System Science Data*, 11(2):921–934, 2019.

- Heike Konow, Florian Ewald, Geet George, Marek Jacob, Marcus Klingebiel, Tobias Kölling, Anna E Luebke, Theresa Mieslinger, Veronika Pörtge, Jule Radtke, et al. EUREC⁴A's HALO. *Earth System Science Data Discussions*, pages 1–26, 2021.
- Eric B Kraus. The diurnal precipitation change over the sea. *Journal of Atmospheric Sciences*, 20(6):551–556, 1963.
- Joachim P Kuettner. General description and central program of GATE. *Bulletin of the American Meteorological Society*, 55(7):712–719, 1974.
- David J Lary, Amir H Alavi, Amir H Gandomi, and Annette L Walker. Machine learning in geosciences and remote sensing. *Geoscience Frontiers*, 7(1):3–10, 2016.
- LV Leahy, R Wood, RJ Charlson, CA Hostetler, RR Rogers, MA Vaughan, and DM Winker. On the nature and extent of optically thin marine low clouds. *Journal of Geophysical Research: Atmospheres*, 117(D22), 2012.
- Tristan S. L'Ecuyer, Norman B. Wood, Taryn Haladay, Graeme L. Stephens, and Paul W. Stackhouse Jr. Impact of clouds on atmospheric heating based on the R04 CloudSat fluxes and heating rates data set. *Journal of Geophysical Research: Atmospheres*, 113(D8), 2008. doi: 10.1029/2008JD009951. URL <https://agupubs.onlinelibrary.wiley.com/doi/abs/10.1029/2008JD009951>.
- Margaret A LeMone and William T Pennell. The relationship of trade wind cumulus distribution to subcloud layer fluxes and structure. *Monthly Weather Review*, 104(5):524–539, 1976.
- Margaret A LeMone, Wayne M Angevine, Christopher S Bretherton, Fei Chen, Jimmy Dudhia, Evgeni Fedorovich, Kristina B Katsaros, Donald H Lenschow, Larry Mahrt, Edward G Patton, et al. 100 years of progress in boundary layer meteorology. *Meteorological Monographs*, 59:9–1, 2018.
- Donald H Lenschow, Paul B Krummel, and Steven T Siems. Measuring entrainment, divergence, and vorticity on the mesoscale from aircraft. *Journal of atmospheric and oceanic technology*, 16(10):1384–1400, 1999.
- Douglas K Lilly. Models of cloud-topped mixed layers under a strong inversion. *Quarterly Journal of the Royal Meteorological Society*, 94(401):292–309, 1968.
- Richard S Lindzen and Arthur V Hou. Hadley circulations for zonally averaged heating centered off the equator. *Journal of Atmospheric Sciences*, 45(17):2416–2427, 1988.
- Richard S Lindzen and Sumant Nigam. On the role of sea surface temperature gradients in forcing low-level winds and convergence in the tropics. *Journal of Atmospheric Sciences*, 44(17):2418–2436, 1987.
- Hailong Liu, Chunzai Wang, Sang-Ki Lee, and David Enfield. Atlantic warm pool variability in the CMIP5 simulations. *Journal of climate*, 26(15):5315–5336, 2013.

- Shuyan Liu and Xin-Zhong Liang. Observed Diurnal Cycle Climatology of Planetary Boundary Layer Height. *Journal of Climate*, 23(21):5790–5809, 11 2010. doi: 10.1175/2010JCLI3552.1.
- Norman G Loeb, Bruce A Wielicki, David R Doelling, G Louis Smith, Dennis F Keyes, Seiji Kato, Natividad Manalo-Smith, and Takmeng Wong. Toward optimal closure of the Earth’s top-of-atmosphere radiation budget. *Journal of Climate*, 22(3):748–766, 2009.
- Charles N Long, Sally A McFarlane, A Del Genio, Patrick Minnis, Thomas P Ackerman, J Mather, J Comstock, Gerald G Mace, Michael Jensen, and Christian Jakob. ARM research in the equatorial western Pacific: A decade and counting. *Bulletin of the American Meteorological Society*, 94(5):695–708, 2013.
- Katrin Lonitz, Bjorn Stevens, Louise Nuijens, Vivek Sant, Lutz Hirsch, and Axel Seifert. The signature of aerosols and meteorology in long-term cloud radar observations of trade wind cumuli. *Journal of the Atmospheric Sciences*, 72(12):4643–4659, 2015.
- Edward N Lorenz. *The nature and theory of the general circulation of the atmosphere*, volume 218. World Meteorological Organization Geneva, 1967.
- Bingkun Luo and Peter Minnett. Evaluation of the ERA5 sea surface skin temperature with remotely-sensed shipborne marine-atmospheric emitted radiance interferometer data. *Remote Sensing*, 12(11):1873, 2020. doi: <https://doi.org/10.3390/rs12111873>.
- Nicholas J Lutsko, Max Popp, Robert H Nazarian, and Anna Lea Albright. Emergent constraints on regional cloud feedbacks. *Geophysical Research Letters*, page e2021GL092934, 2021.
- Tristan S L’Ecuyer, Hiroko K Beaudoin, Matthew Rodell, W Olson, B Lin, S Kato, CA Clayson, E Wood, J Sheffield, R Adler, et al. The observed state of the energy budget in the early twenty-first century. *Journal of Climate*, 28(21):8319–8346, 2015.
- Eric S. Maddy and Christopher D. Barnett. Vertical Resolution Estimates in Version 5 of AIRS Operational Retrievals. *IEEE Trans. Geosci. Remote Sensing*, 46(8):2375–2384, August 2008. ISSN 0196-2892. doi: 10.1109/TGRS.2008.917498.
- L Mahrt. Mixed layer moisture structure. *Monthly Weather Review*, 104(11):1403–1407, 1976.
- Joanne Starr Malkus. *On the structure of the trade wind moist layer*. Massachusetts Institute of Technology, 1958.
- Syukuro Manabe and Robert F Strickler. Thermal equilibrium of the atmosphere with a convective adjustment. *Journal of the Atmospheric Sciences*, 21(4):361–385, 1964.

- Syukuro Manabe and Richard T Wetherald. Thermal equilibrium of the atmosphere with a given distribution of relative humidity. 1967.
- B. E. Mapes. Water’s two height scales: The moist adiabat and the radiative troposphere. *Quart. J. Roy. Meteor. Soc.*, 127(577):2353–2366, 2001.
- Frank J Marsik, Kenneth W Fischer, Tracey D McDonald, and Perry J Samson. Comparison of methods for estimating mixing height used during the 1992 Atlanta Field Intensive. *Journal of Applied Meteorology*, 34(8):1802–1814, 1995.
- Pierre-Philippe Mathieu and Christoph Aubrecht. *Earth observation open science and innovation*. Springer Nature, 2018.
- Michael McGauley, Chidong Zhang, and Nicholas A Bond. Large-scale characteristics of the atmospheric boundary layer in the eastern Pacific cold tongue–ITCZ region. *Journal of climate*, 17(20):3907–3920, 2004.
- Brian Medeiros and Louise Nuijens. Clouds at Barbados are representative of clouds across the trade wind regions in observations and climate models. *Proceedings of the National Academy of Sciences*, 113(22):E3062–E3070, 2016. doi: 10.1073/pnas.1521494113.
- Brian Medeiros and Bjorn Stevens. Revealing differences in GCM representations of low clouds. *Climate dynamics*, 36(1-2):385–399, 2011.
- Brian Medeiros, Bjorn Stevens, Isaac M Held, Ming Zhao, David L Williamson, Jerry G Olson, and Christopher S Bretherton. Aquaplanets, climate sensitivity, and low clouds. *Journal of Climate*, 21(19):4974–4991, 2008.
- Brian Medeiros, Bjorn Stevens, and Sandrine Bony. Using aquaplanets to understand the robust responses of comprehensive climate models to forcing. *Climate Dynamics*, 44(7):1957–1977, 2015.
- Gerald A Meehl, Catherine A Senior, Veronika Eyring, Gregory Flato, Jean-Francois Lamarque, Ronald J Stouffer, Karl E Taylor, and Manuel Schlund. Context for interpreting equilibrium climate sensitivity and transient climate response from the CMIP6 Earth system models. *Science Advances*, 6(26):eaba1981, 2020.
- Per-Erik Mellander, Solomon G Gebrehiwot, Annemieke I Gärdenäs, Woldeamlak Bewket, and Kevin Bishop. Summer rains and dry seasons in the upper Blue Nile Basin: the predictability of half a century of past and future spatiotemporal patterns. *PloS one*, 8(7):e68461, 2013.
- W. Paul Menzel, Timothy J. Schmit, Peng Zhang, and Jun Li. Satellite-Based Atmospheric Infrared Sounder Development and Applications. *Bulletin of the American Meteorological Society*, 99(3):583–603, March 2018. ISSN 0003-0007, 1520-0477. doi: 10.1175/BAMS-D-16-0293.1.

- N Metropolis, A Rosenbluth, M Rosenbluth, A Teller, and E Teller. Equation of state calculations by fast computing machines. *Journal of Chemistry and Physics*, 21: 1087–1092, 1953.
- Theresa Mieslinger, Ákos Horváth, Stefan A Buehler, and Mirjana Sakradzija. The dependence of shallow cumulus macrophysical properties on large-scale meteorology as observed in ASTER imagery. *Journal of Geophysical Research: Atmospheres*, 124(21):11477–11505, 2019.
- Theresa Mieslinger, Bjorn Stevens, Tobias Kölling, Manfred Brath, Martin Wirth, and Stefan A Buehler. Optically thin clouds in the trades. *Atmospheric Chemistry and Physics Discussions*, pages 1–33, 2021.
- RL Miller. Tropical thermostats and low cloud cover. *Journal of climate*, 10(3): 409–440, 1997.
- EJ Mlawer, SA Clough, and S Kato. Shortwave clear-sky model measurement inter-comparison using RRTM. In *Proceedings of the Eighth ARM Science Team Meeting*, pages 23–27. Citeseer, 1998.
- Eli J. Mlawer, Vivienne H. Payne, Jean Luc Moncet, Jennifer S. Delamere, Matthew J. Alvarado, and David C. Tobin. Development and recent evaluation of the MT-CKD model of continuum absorption. *Philosophical Transactions of the Royal Society A: Mathematical, Physical and Engineering Sciences*, 370(1968):2520–2556, jun 2012. ISSN 1364503X. doi: 10.1098/rsta.2011.0295.
- Chin-Hoh Moeng, Peter P Sullivan, and Bjorn Stevens. Including radiative effects in an entrainment rate formula for buoyancy-driven PBLs. *Journal of the atmospheric sciences*, 56(8):1031–1049, 1999.
- Kenneth P Moran, Brooks E Martner, MJ Post, Robert A Kropfli, David C Welsh, and Kevin B Widener. An unattended cloud-profiling radar for use in climate research. *Bulletin of the American Meteorological Society*, 79(3):443–456, 1998.
- C. J. Muller and I. M. Held. Detailed Investigation of the Self-Aggregation of Convection in Cloud-Resolving Simulations. *Journal of the Atmospheric Sciences*, 69(8):2551–2565, 2012. ISSN 0022-4928. doi: 10.1175/JAS-D-11-0257.1.
- Timothy A Myers and Joel R Norris. Observational evidence that enhanced subsidence reduces subtropical marine boundary layer cloudiness. *Journal of Climate*, 26(19):7507–7524, 2013.
- Timothy A Myers, Ryan C Scott, Mark D Zelinka, Stephen A Klein, Joel R Norris, and Peter M Caldwell. Observational constraints on low cloud feedback reduce uncertainty of climate sensitivity. *Nature Climate Change*, 11(6):501–507, 2021.
- Badrinath Nagarajan and Anantha R Aiyyer. Performance of the ECMWF operational analyses over the tropical indian ocean. *Monthly weather review*, 132(9): 2275–2282, 2004.

- Ann Kristin Naumann, Bjorn Stevens, Cathy Hohenegger, and Juan Pedro Mellado. A conceptual model of a shallow circulation induced by prescribed low-level radiative cooling. *Journal of the Atmospheric Sciences*, 74(10):3129–3144, 2017.
- Ann Kristin Naumann, Bjorn Stevens, and Cathy Hohenegger. A moist conceptual model for the boundary layer structure and radiatively driven shallow circulations in the trades. *Journal of the Atmospheric Sciences*, 76(5):1289–1306, 2019.
- J David Neelin, Isaac M Held, and Kerry H Cook. Evaporation-wind feedback and low-frequency variability in the tropical atmosphere. *Journal of Atmospheric Sciences*, 44(16):2341–2348, 1987.
- RAJ Neggers. Exploring bin-macrophysics models for moist convective transport and clouds. *Journal of Advances in Modeling Earth Systems*, 7(4):2079–2104, 2015.
- Roel Neggers, Bjorn Stevens, and David Neelin. A simple equilibrium model for shallow-cumulus-topped mixed layers. *Theoretical and Computational Fluid Dynamics*, 20(5):305–322, 2006.
- Roel AJ Neggers, Martin Köhler, and Anton CM Beljaars. A dual mass flux framework for boundary layer convection. part I: Transport. *Journal of the Atmospheric Sciences*, 66(6):1465–1487, 2009.
- Stephen Nicholls and Margaret A Lemone. The fair weather boundary layer in gate: The relationship of subcloud fluxes and structure to the distribution and enhancement of cumulus clouds. *Journal of Atmospheric Sciences*, 37(9):2051–2067, 1980.
- Tsuyoshi Nitta and Steven Esbensen. Heat and moisture budget analyses using BOMEX data. *Monthly Weather Review*, 102(1):17–28, 1974.
- William Nordhaus. Projections and uncertainties about climate change in an era of minimal climate policies. *American Economic Journal: Economic Policy*, 10(3):333–60, 2018.
- Joel R Norris. Low cloud type over the ocean from surface observations. part II: Geographical and seasonal variations. *Journal of climate*, 11(3):383–403, 1998.
- Louise Nuijens and Bjorn Stevens. The influence of wind speed on shallow marine cumulus convection. *Journal of the atmospheric sciences*, 69(1):168–184, 2012.
- Louise Nuijens, Ilya Serikov, Lutz Hirsch, Katrin Lonitz, and Bjorn Stevens. The distribution and variability of low-level cloud in the north Atlantic trades. *Quarterly Journal of the Royal Meteorological Society*, 140(684):2364–2374, 2014.
- Louise Nuijens, Brian Medeiros, Irina Sandu, and Maike Ahlgrimm. The behavior of trade-wind cloudiness in observations and models: The major cloud components and their variability. *Journal of Advances in Modeling Earth Systems*, 7(2):600–616, 2015a.

- Louise Nuijens, Brian Medeiros, Irina Sandu, and Maike Ahlgrimm. Observed and modeled patterns of covariability between low-level cloudiness and the structure of the trade-wind layer. *Journal of Advances in Modeling Earth Systems*, 7(4): 1741–1764, 2015b.
- Kuan-Ting O, Robert Wood, and Hsiu-Hui Tseng. Deeper, precipitating PBLs associated with optically thin veil clouds in the Sc-Cu transition. *Geophysical Research Letters*, 45(10):5177–5184, 2018. doi: 10.1029/2018GL077084. URL <https://agupubs.onlinelibrary.wiley.com/doi/abs/10.1029/2018GL077084>.
- Paul A O’Gorman and John G Dwyer. Using machine learning to parameterize moist convection: Potential for modeling of climate, climate change, and extreme events. *Journal of Advances in Modeling Earth Systems*, 10(10):2548–2563, 2018.
- Katsuyuki Ooyama. A theory on parameterization of cumulus convection. *Journal of the Meteorological Society of Japan. Ser. II*, 49:744–756, 1971.
- Isidoro Orlanski. A rational subdivision of scales for atmospheric processes. *Bulletin of the American Meteorological Society*, pages 527–530, 1975.
- Boutheina Oueslati and Gilles Bellon. Tropical precipitation regimes and mechanisms of regime transitions: Contrasting two aquaplanet general circulation models. *Climate dynamics*, 40(9):2345–2358, 2013.
- Tim Palmer and Bjorn Stevens. The scientific challenge of understanding and estimating climate change. *Proceedings of the National Academy of Sciences*, 116(49): 24390–24395, 2019.
- Ilga R Paluch. The entrainment mechanism in Colorado cumuli. *Journal of Atmospheric Sciences*, 36(12):2467–2478, 1979.
- Supantha Paul, Subimal Ghosh, Robert Oglesby, Amey Pathak, Anita Chandrasekharan, and RAAJ Ramsankaran. Weakening of Indian summer monsoon rainfall due to changes in land use land cover. *Scientific reports*, 6(1):1–10, 2016.
- R Pierrehumbert. Thermostats, radiator fins, and the local runaway greenhouse. *Journal of Atmospheric Sciences*, 52(10):1784–1806, 1995.
- Robert Pincus, Anton Beljaars, Stefan A. Buehler, Gottfried Kirchengast, Florian Ladstaedter, and Jeffrey S Whitaker. The Representation of Tropospheric Water Vapor Over Low-Latitude Oceans in (Re-)analysis: Errors, Impacts, and the Ability to Exploit Current and Prospective Observations. *Surveys in Geophysics*, 38(6): 1399–1423, October 2017. doi: 10.1007/s10712-017-9437-z.
- Robert Pincus, Eli J. Mlawer, and Jennifer S. Delamere. Balancing accuracy, efficiency, and flexibility in radiation calculations for dynamical models. *Journal of Advances in Modeling Earth Systems*, 11(10):3074–3089, 2019. doi: 10.1029/2019MS001621.

- Robert Pincus, Chris W Fairall, Adriana Bailey, Haonan Chen, Patrick Y Chuang, Gijs de Boer, Graham Feingold, Dean Henze, Quinn T Kalen, Jan Kazil, et al. Observations from the NOAA P-3 aircraft during ATOMIC. *Earth System Science Data*, 13(7):3281–3296, 2021.
- David Pino, Jordi Vilà-Guerau de Arellano, and Peter G Duynkerke. The contribution of shear to the evolution of a convective boundary layer. *Journal of the atmospheric sciences*, 60(16):1913–1926, 2003.
- Max Planck. *Scientific autobiography: And other papers*. Open Road Media, 2014.
- Max Popp and Levi G Silvers. Double and single ITCZs with and without clouds. *Journal of Climate*, 30(22):9147–9166, 2017.
- Marc Prange, Manfred Brath, and Stefan Alexander Buehler. Are elevated moist layers a blind spot for hyperspectral infrared sounders? A model study. *Atmospheric Measurement Techniques Discussions*, pages 1–29, 2021.
- Cristian Proistosescu and Peter J Huybers. Slow climate mode reconciles historical and model-based estimates of climate sensitivity. *Science advances*, 3(7):e1602821, 2017.
- Yi Qin, Mark D Zelinka, and Stephen A Klein. On the correspondence between atmosphere-only and coupled simulations for radiative feedbacks and forcing from CO_2 . *Journal of Geophysical Research: Atmospheres*, 127(3):e2021JD035460, 2022.
- Xin Qu, Alex Hall, Stephen A Klein, and Peter M Caldwell. On the spread of changes in marine low cloud cover in climate model simulations of the 21st century. *Climate dynamics*, 42(9-10):2603–2626, 2014.
- Jule Radtke, Thorsten Mauritsen, and Cathy Hohenegger. Shallow cumulus cloud feedback in large eddy simulations—bridging the gap to storm-resolving models. *Atmospheric Chemistry and Physics*, 21(5):3275–3288, 2021.
- VLRD Ramanathan, RD Cess, EF Harrison, P Minnis, BR Barkstrom, E Ahmad, and D Hartmann. Cloud-radiative forcing and climate: Results from the Earth Radiation Budget Experiment. *Science*, 243(4887):57–63, 1989.
- David A Randall and Stephen Tjemkes. Clouds, the Earth’s radiation budget, and the hydrologic cycle. *Global and Planetary Change*, 4(1-3):3–9, 1991. doi: 10.1016/0921-8181(91)90063-3.
- Stephan Rasp, Michael S Pritchard, and Pierre Gentine. Deep learning to represent subgrid processes in climate models. *Proceedings of the National Academy of Sciences*, 115(39):9684–9689, 2018.
- Stephan Rasp, Hauke Schulz, Sandrine Bony, and Bjorn Stevens. Combining crowdsourcing and deep learning to explore the mesoscale organization of shallow convection. *Bulletin of the American Meteorological Society*, 101(11):E1980–E1995, 2020.

- Robert M Rauber, Bjorn Stevens, Harry T Ochs III, Charles Knight, Bruce A Albrecht, AM Blyth, CW Fairall, JB Jensen, SG Lasher-Trapp, OL Mayol-Bracero, et al. Rain in shallow cumulus over the ocean: The RICO campaign. *Bulletin of the American Meteorological Society*, 88(12):1912–1928, 2007.
- David J Raymond. Regulation of moist convection over the west Pacific warm pool. *Journal of Atmospheric Sciences*, 52(22):3945–3959, 1995.
- David J Raymond, GB Raga, Christopher S Bretherton, John Molinari, Carlos López-Carrillo, and Željka Fuchs. Convective forcing in the Intertropical convergence zone of the eastern Pacific. *Journal of the atmospheric sciences*, 60(17):2064–2082, 2003.
- Martin Renoult, James Douglas Annan, Julia Catherine Hargreaves, Navjit Sagoo, Clare Flynn, Marie-Luise Kapsch, Qiang Li, Gerrit Lohmann, Uwe Mikolajewicz, Rumi Ohgaito, et al. A Bayesian framework for emergent constraints: Case studies of climate sensitivity with PMIP. *Climate of the Past*, 16(5):1715–1735, 2020.
- Malte Rieck, Louise Nuijens, and Bjorn Stevens. Marine boundary layer cloud feedbacks in a constant relative humidity atmosphere. *Journal of the Atmospheric Sciences*, 69(8):2538–2550, 2012.
- Herbert Riehl. Variations of energy exchange between sea and air in the trades. *Weather*, 9(11):335–340, 1954.
- Herbert Riehl, TC Yeh, Joanne S Malkus, and Noel E La Seur. The north-east trade of the Pacific Ocean. *Quarterly Journal of the Royal Meteorological Society*, 77(334):598–626, 1951.
- Camille Risi, Caroline Muller, and Peter Blossey. What controls the water vapor isotopic composition near the surface of tropical oceans? results from an analytical model constrained by large-eddy simulations. *Journal of advances in modeling earth systems*, 12(8):e2020MS002106, 2020.
- Matthew Rodell, Hiroko Kato Beaudoin, TS L’Ecuyer, William S Olson, James Stephen Famiglietti, Paul Raymond Houser, Robert Adler, Michael G Bosilovich, Carol Anne Clayson, D Chambers, et al. The observed state of the water cycle in the early twenty-first century. *Journal of Climate*, 28(21):8289–8318, 2015.
- MJ Rodwell and TN Palmer. Using numerical weather prediction to assess climate models. *Quarterly Journal of the Royal Meteorological Society: A journal of the atmospheric sciences, applied meteorology and physical oceanography*, 133(622):129–146, 2007.
- David Rolnick, Priya L Donti, Lynn H Kaack, Kelly Kochanski, Alexandre Lacoste, Kris Sankaran, Andrew Slavin Ross, Nikola Milojevic-Dupont, Natasha Jaques, Anna Waldman-Brown, et al. Tackling climate change with machine learning. *arXiv preprint arXiv:1906.05433*, 2019.

- Maria Rugenstein, Jonah Bloch-Johnson, Jonathan Gregory, Timothy Andrews, Thorsten Mauritsen, Chao Li, Thomas L Frölicher, David Paynter, Gokhan Danabasoglu, Shuting Yang, et al. Equilibrium climate sensitivity estimated by equilibrating climate models. *Geophysical Research Letters*, 47(4):e2019GL083898, 2020.
- James H Ruppert and Richard H Johnson. On the cumulus diurnal cycle over the tropical warm pool. *Journal of Advances in Modeling Earth Systems*, 8(2):669–690, 2016. doi: 10.1002/2015MS000610.
- James H Ruppert Jr and Morgan E O’Neill. Diurnal cloud and circulation changes in simulated tropical cyclones. *Geophysical Research Letters*, 46(1):502–511, 2019. doi: 10.1029/2018GL081302.
- Lynn M Russell, Armin Sorooshian, John H Seinfeld, Bruce A Albrecht, Athanasios Nenes, Lars Ahlm, Yi-Chun Chen, Matthew Coggon, Jill S Craven, Richard C Flagan, et al. Eastern Pacific emitted aerosol cloud experiment. *Bulletin of the American Meteorological Society*, 94(5):709–729, 2013.
- Jonathan J Rutz, Christine A Shields, Juan M Lora, Ashley E Payne, Bin Guan, Paul Ullrich, Travis O’Brien, L Ruby Leung, F Martin Ralph, Michael Wehner, et al. The atmospheric river tracking method intercomparison project (ARTMIP): quantifying uncertainties in atmospheric river climatology. *Journal of Geophysical Research: Atmospheres*, 124(24):13777–13802, 2019.
- Jerôme Schalkwijk, Harmen JJ Jonker, and A Pier Siebesma. Simple solutions to steady-state cumulus regimes in the convective boundary layer. *Journal of the atmospheric sciences*, 70(11):3656–3672, 2013.
- William H Schlesinger and Scott Jasechko. Transpiration in the global water cycle. *Agricultural and Forest Meteorology*, 189:115–117, 2014.
- Manuel Schlund, Veronika Eyring, Gustau Camps-Valls, Pierre Friedlingstein, Pierre Gentine, and Markus Reichstein. Constraining uncertainty in projected gross primary production with machine learning. *Journal of Geophysical Research: Biogeosciences*, 125(11):e2019JG005619, 2020a.
- Manuel Schlund, Axel Lauer, Pierre Gentine, Steven C Sherwood, and Veronika Eyring. Emergent constraints on equilibrium climate sensitivity in CMIP5: do they hold for CMIP6? *Earth System Dynamics*, 11(4):1233–1258, 2020b.
- Timothy J. Schmit, Jun Li, Steven A. Ackerman, and James J. Gurka. High-Spectral- and High-Temporal-Resolution Infrared Measurements from Geostationary Orbit. *Journal of Atmospheric and Oceanic Technology*, 26(11):2273–2292, November 2009. ISSN 1520-0426, 0739-0572. doi: 10.1175/2009JTECHA1248.1.
- Hauke Schulz, Ryan Eastman, and Bjorn Stevens. Characterization and evolution of organized shallow convection in the downstream North Atlantic trades. *Journal of Geophysical Research: Atmospheres*, 126(17):e2021JD034575, 2021.

- Petra Seibert, Frank Beyrich, Sven-Erik Gryning, Sylvain Joffre, Alix Rasmussen, and Philippe Tercier. Review and intercomparison of operational methods for the determination of the mixing height. *Atmospheric environment*, 34(7):1001–1027, 2000.
- Dian J Seidel, Yehui Zhang, Anton Beljaars, Jean-Christophe Golaz, Andrew R Jacobson, and Brian Medeiros. Climatology of the planetary boundary layer over the continental United States and Europe. *Journal of Geophysical Research: Atmospheres*, 117(D17), 2012.
- Axel Seifert and Thijs Heus. Large-eddy simulation of organized precipitating trade wind cumulus clouds. *Atmospheric Chemistry and Physics*, 13:5631–5645, 2013. doi: 10.5194/acpd-13-1855-2013.
- Axel Seifert, Thijs Heus, Robert Pincus, and Bjorn Stevens. Large-eddy simulation of the transient and near-equilibrium behavior of precipitating shallow convection. *Journal of Advances in Modeling Earth Systems*, 7(4):1918–1937, 2015. doi: 10.1002/2015MS000489.
- Karen M Shell, Jeffrey T Kiehl, and Christine A Shields. Using the radiative kernel technique to calculate climate feedbacks in NCAR’s Community Atmospheric Model. *Journal of Climate*, 21(10):2269–2282, 2008.
- SC Sherwood, Mark J Webb, James D Annan, KC Armour, Piers M Forster, Julia C Hargreaves, Gabriele Hegerl, Stephen A Klein, Kate D Marvel, Eelco J Rohling, et al. An assessment of Earth’s climate sensitivity using multiple lines of evidence. *Reviews of Geophysics*, 58(4):e2019RG000678, 2020.
- Steven C Sherwood, Sandrine Bony, and Jean-Louis Dufresne. Spread in model climate sensitivity traced to atmospheric convective mixing. *Nature*, 505(7481):37–42, 2014.
- A Pier Siebesma, Christopher S Bretherton, Andrew Brown, Andreas Chlond, Joan Cuxart, Peter G Duynkerke, Hongli Jiang, Marat Khairoutdinov, David Lewellen, Chin-Hoh Moeng, et al. A large eddy simulation intercomparison study of shallow cumulus convection. *Journal of the Atmospheric Sciences*, 60(10):1201–1219, 2003.
- A Pier Siebesma, Sandrine Bony, Christian Jakob, and Bjorn Stevens. *Clouds and Climate: Climate Science’s Greatest Challenge*. Cambridge University Press, 2020.
- Joseph Smagorinsky. General circulation experiments with the primitive equations: I. The basic experiment. *Monthly weather review*, 91(3):99–164, 1963.
- Brian J Soden. Tracking upper tropospheric water vapor radiances: A satellite perspective. *Journal of Geophysical Research: Atmospheres*, 103(D14):17069–17081, 1998.

- Brian J Soden, Isaac M Held, Robert Colman, Karen M Shell, Jeffrey T Kiehl, and Christine A Shields. Quantifying climate feedbacks using radiative kernels. *Journal of Climate*, 21(14):3504–3520, 2008.
- Roy W Spencer and William D Braswell. How dry is the tropical free troposphere? Implications for global warming theory. *Bulletin of the American Meteorological Society*, 78(6):1097–1106, 1997.
- Arie Staal, Obbe A Tuinenburg, Joyce HC Bosmans, Milena Holmgren, Egbert H van Nes, Marten Scheffer, Delphine Clara Zemp, and Stefan C Dekker. Forest-rainfall cascades buffer against drought across the amazon. *Nature Climate Change*, 8(6):539–543, 2018.
- Claudia Christine Stephan, Sabrina Schnitt, Hauke Schulz, Hugo Bellenger, Simon P de Szoeki, Claudia Acquistapace, Katharina Baier, Thibaut Dauhut, Rémi Laxenaire, Yanmichel Morfa-Avalos, et al. Ship-and island-based atmospheric soundings from the 2020 EUREC⁴A field campaign. *Earth System Science Data Discussions*, pages 1–35, 2020. doi: 10.5194/essd-2020-174.
- Graeme L. Stephens, Juilin Li, Martin Wild, Carol Anne Clayson, Norman Loeb, Seiji Kato, Tristan L’Ecuyer, Paul W. Stackhouse, Matthew Lebsock, and Timothy Andrews. An update on Earth’s energy balance in light of the latest global observations. *Nature Geoscience*, 5(10):691–696, 2012. doi: 10.1038/ngeo1580.
- Nicholas Stern. Stern review: The economics of climate change. 2006.
- Bjorn Stevens. Bulk boundary-layer concepts for simplified models of tropical dynamics. *Theoretical and Computational Fluid Dynamics*, 20(5):279–304, 2006.
- Bjorn Stevens. On the growth of layers of nonprecipitating cumulus convection. *Journal of the atmospheric sciences*, 64(8):2916–2931, 2007.
- Bjorn Stevens and Sandrine Bony. What are climate models missing? *Science*, 340(6136):1053–1054, 2013.
- Bjorn Stevens, Andrew S Ackerman, Bruce A Albrecht, Andrew R Brown, Andreas Chlond, Joan Cuxart, Peter G Duynkerke, David C Lewellen, Malcolm K Macvean, Roel AJ Neggers, et al. Simulations of trade wind cumuli under a strong inversion. *Journal of the atmospheric sciences*, 58(14):1870–1891, 2001.
- Bjorn Stevens, Jianjun Duan, James C McWilliams, Matthias Münnich, and J David Neelin. Entrainment, Rayleigh friction, and boundary layer winds over the tropical Pacific. *Journal of climate*, 15(1):30–44, 2002.
- Bjorn Stevens, Donald H Lenschow, Ian Faloona, C-H Moeng, DK Lilly, B Blomquist, G Vali, A Bandy, T Campos, H Gerber, et al. On entrainment rates in nocturnal marine stratocumulus. *Quarterly Journal of the Royal Meteorological Society: A journal of the atmospheric sciences, applied meteorology and physical oceanography*, 129(595):3469–3493, 2003a.

- Bjorn Stevens, Donald H Lenschow, Gabor Vali, Hermann Gerber, A Bandy, B Blomquist, J-L Brenguier, CS Bretherton, F Burnet, Teresa Campos, et al. Dynamics and chemistry of marine stratocumulus – DYCOMS-II. *Bulletin of the American Meteorological Society*, 84(5):579–594, 2003b.
- Bjorn Stevens, David Farrell, Lutz Hirsch, Friedhelm Jansen, Louise Nuijens, Ilya Serikov, Björn Brüggmann, Marvin Forde, Holger Linne, Katrin Lonitz, et al. The barbados cloud observatory: Anchoring investigations of clouds and circulation on the edge of the itcz. *Bulletin of the American Meteorological Society*, 97(5):787–801, 2016a.
- Bjorn Stevens, David Farrell, Lutz Hirsch, Friedhelm Jansen, Louise Nuijens, Ilya Serikov, Björn Brüggmann, Marvin Forde, Holger Linne, Katrin Lonitz, and Joseph M. Prospero. The Barbados Cloud Observatory: Anchoring investigations of clouds and circulation on the edge of the ITCZ. *Bulletin of the American Meteorological Society*, 97(5):787–801, 2016b. doi: 10.1175/BAMS-D-14-00247.1.
- Bjorn Stevens, Hélène Brogniez, Christoph Kiemle, Jean-Lionel Lacour, Cyril Crevoisier, and Johannes Kiliani. Structure and dynamical influence of water vapor in the lower tropical troposphere. *Surveys in Geophysics*, 38(6):1371–1397, 2017. doi: 10.1007/s10712-017-9420-8.
- Bjorn Stevens, Claudia Acquistapace, Akio Hansen, Rieke Heinze, Carolin Klinger, Daniel Klocke, Harald Rybka, Wiebke Schubotz, Julia Windmiller, Panagiotis Adamidis, et al. The added value of large-eddy and storm-resolving models for simulating clouds and precipitation. *Journal of the Meteorological Society of Japan. Ser. II*, 2020a.
- Bjorn Stevens, Sandrine Bony, Hélène Brogniez, Laureline Hentgen, Cathy Hohenegger, Christoph Kiemle, Tristan S L’Ecuyer, Ann Kristin Naumann, Hauke Schulz, Pier A Siebesma, et al. Sugar, gravel, fish and flowers: Mesoscale cloud patterns in the trade winds. *Quarterly Journal of the Royal Meteorological Society*, 146(726):141–152, 2020b.
- Bjorn Stevens, Sandrine Bony, D Farrell, and 293 co authors. EUREC⁴A. *Earth System Science Data*, 2021.
- Claudia J Stubenrauch, William B Rossow, Stefan Kinne, S Ackerman, G Cesana, H Chepfer, L Di Girolamo, B Getzewich, A Guignard, A Heidinger, et al. Assessment of global cloud datasets from satellites: Project and database initiated by the GEWEX radiation panel. *Bulletin of the American Meteorological Society*, 94(7):1031–1049, 2013.
- Roland B Stull. The energetics of entrainment across a density interface. *Journal of the atmospheric sciences*, 33(7):1260–1267, 1976.
- Roland B Stull. A fair-weather cumulus cloud classification scheme for mixed-layer studies. *Journal of Applied Meteorology and Climatology*, 24(1):49–56, 1985.

- Roland B Stull. *An introduction to boundary layer meteorology*, volume 13. Springer Science & Business Media, 2012.
- Ashok Swain. Ethiopia, the Sudan, and Egypt: the Nile river dispute. *The Journal of Modern African Studies*, 35(4):675–694, 1997.
- D Sylvester. René magritte: Catalogue raisonné. Antwerp, 1992.
- Karl E Taylor, Ronald J Stouffer, and Gerald A Meehl. An overview of CMIP5 and the experiment design. *Bulletin of the American meteorological Society*, 93(4):485–498, 2012.
- H Tennekes and AGM Driedonks. Basic entrainment equations for the atmospheric boundary layer. *Boundary-Layer Meteorology*, 20(4):515–531, 1981.
- Hendrik Tennekes. A model for the dynamics of the inversion above a convective boundary layer. *Journal of Atmospheric sciences*, 30(4):558–567, 1973.
- Chad W Thackeray, Xin Qu, and Alex Hall. Why do models produce spread in snow albedo feedback? *Geophysical Research Letters*, 45(12):6223–6231, 2018.
- K Thayer-Calder and David Randall. A numerical investigation of boundary layer quasi-equilibrium. *Geophysical Research Letters*, 42(2):550–556, 2015.
- David W. J. Thompson, Sandrine Bony, and Ying Li. Thermodynamic constraint on the depth of the global tropospheric circulation. *Proceedings of the National Academy of Sciences*, 114(31):8181–8186, 2017. ISSN 0027-8424. doi: 10.1073/pnas.1620493114.
- Michael Tiedtke. A comprehensive mass flux scheme for cumulus parameterization in large-scale models. *Monthly weather review*, 117(8):1779–1800, 1989.
- Richard SJ Tol. The economic effects of climate change. *Journal of economic perspectives*, 23(2):29–51, 2009.
- Lorenzo Tomassini, Aiko Voigt, and Bjorn Stevens. On the connection between tropical circulation, convective mixing, and climate sensitivity. *Quarterly Journal of the Royal Meteorological Society*, 141(689):1404–1416, 2014.
- Ludovic Touzé-Peiffer, Raphaela Vogel, and Nicolas Rochetin. Cold pools observed during EUREC⁴A: Detection and characterization from atmospheric soundings. *Journal of Applied Meteorology and Climatology*, 61(5):593–610, 2022.
- Vaisala. RD41 Technical data. Technical report, University Corporation for Atmospheric Research, 2018.
- Vaisala. Vaisala dropsonde RD41 datasheet in english, 2022.

- Margreet C Vanzanten, Peter G Duynkerke, and Joannes WM Cuijpers. Entrainment parameterization in convective boundary layers. *Journal of the atmospheric sciences*, 56(6):813–828, 1999.
- Jessica Vial, Jean-Louis Dufresne, and Sandrine Bony. On the interpretation of inter-model spread in CMIP5 climate sensitivity estimates. *Climate Dynamics*, 41(11):3339–3362, 2013. doi: 10.1007/s00382-013-1725-9.
- Jessica Vial, Sandrine Bony, Jean-Louis Dufresne, and Romain Roehrig. Coupling between lower-tropospheric convective mixing and low-level clouds: Physical mechanisms and dependence on convection scheme. *Journal of Advances in Modeling Earth Systems*, 8(4):1892–1911, 2016.
- Jessica Vial, Sandrine Bony, Bjorn Stevens, and Raphaela Vogel. Mechanisms and model diversity of trade-wind shallow cumulus cloud feedbacks: a review. *Shallow clouds, water vapor, circulation, and climate sensitivity*, pages 159–181, 2017.
- Jessica Vial, Raphaela Vogel, Sandrine Bony, Bjorn Stevens, David M Winker, Xia Cai, Cathy Hohenegger, Ann Kristin Naumann, and H el ene Brogniez. A new look at the daily cycle of trade wind cumuli. *Journal of advances in modeling earth systems*, 11(10):3148–3166, 2019. doi: 10.1029/2019MS001746.
- Leonie Villiger, Heini Wernli, Maxi Boettcher, Martin Hagen, and Franziska Aemisegger. Lagrangian formation pathways of moist anomalies in the trade-wind region during the dry season: two case studies from EUREC⁴A. *Weather and Climate Dynamics*, 3(1):59–88, 2022.
- Raphaela Vogel, Louise Nuijens, and Bjorn Stevens. The role of precipitation and spatial organization in the response of trade-wind clouds to warming. *Journal of Advances in Modeling Earth Systems*, 8(2):843–862, 2016.
- Raphaela Vogel, Sandrine Bony, and Bjorn Stevens. Estimating the shallow convective mass flux from the subcloud-layer mass budget. *Journal of Atmospheric Sciences*, 77(5):1559–1574, 2020.
- Holger V omel, Mack Goodstein, Laura Tudor, Jacquelyn Witte,  zeljka Fuchs-Stone, Stipo Senti c, David Raymond, Jose Martinez-Claros, Ana Jura c c, Vijit Maithel, et al. High-resolution in situ observations of atmospheric thermodynamics using dropsondes during the organization of tropical east pacific convection (OTREC) field campaign. *Earth System Science Data*, 13(3):1107–1117, 2021.
- Gernot Wagner and Martin L Weitzman. *Climate shock*. Princeton University Press, 2016.
- Mark J Webb, CA Senior, DMH Sexton, WJ Ingram, KD Williams, MA Ringer, BJ McAvaney, R Colman, Brian J Soden, R Gudgel, et al. On the contribution of local feedback mechanisms to the range of climate sensitivity in two GCM ensembles. *Climate Dynamics*, 27(1):17–38, 2006.

- Mark J Webb, Timothy Andrews, Alejandro Bodas-Salcedo, Sandrine Bony, Christopher S Bretherton, Robin Chadwick, H el ene Chepfer, Herv e Douville, Peter Good, Jennifer E Kay, et al. The cloud feedback model intercomparison project (CFMIP) contribution to CMIP6. *Geoscientific Model Development*, 10(1):359–384, 2017.
- Peter J Webster and Roger Lukas. TOGA COARE: The coupled ocean–atmosphere response experiment. *Bulletin of the American Meteorological Society*, 73(9):1377–1416, 1992.
- Martin L Weitzman. Fat-tailed uncertainty in the economics of catastrophic climate change. *Review of Environmental Economics and Policy*, 5(2):275–292, 2011.
- Martin L Weitzman. Fat tails and the social cost of carbon. *American Economic Review*, 104(5):544–46, 2014.
- Keith D Williams, Alejandro Bodas-Salcedo, Michel D equ e, Solange Fermepin, B Medeiros, M Watanabe, Christian Jakob, Stephen A Klein, Catherine A Senior, and David L Williamson. The Transpose-AMIP II experiment and its application to the understanding of Southern Ocean cloud biases in climate models. *Journal of Climate*, 26(10):3258–3274, 2013.
- Martin Wirth, Andreas Fix, Peter Mahnke, Horst Schwarzer, Friedrich Schrandt, and Gerhard Ehret. The airborne multi-wavelength water vapor differential absorption lidar WALES: system design and performance. *Applied Physics B*, 96(1):201–213, 2009.
- R Wood, CS Bretherton, D Leon, AD Clarke, P Zuidema, G Allen, and H Coe. An aircraft case study of the spatial transition from closed to open mesoscale cellular convection over the Southeast Pacific. *Atmospheric Chemistry and Physics*, 11(5):2341–2370, 2011.
- Robert Wood. Stratocumulus Clouds. *Monthly Weather Review*, 140(8):2373–2423, 2012. ISSN 0027-0644. doi: 10.1175/MWR-D-11-00121.1.
- Robert Wood and Christopher S Bretherton. Boundary layer depth, entrainment, and decoupling in the cloud-capped subtropical and tropical marine boundary layer. *Journal of Climate*, 17(18):3576–3588, 2004.
- Robert Wood and Christopher S Bretherton. On the relationship between stratiform low cloud cover and lower-tropospheric stability. *Journal of climate*, 19(24):6425–6432, 2006.
- Robert Wood, Kuan-Ting O, Christopher S Bretherton, Johannes Mohrmann, Bruce A Albrecht, Paquita Zuidema, Virendra Ghate, Chris Schwartz, Ed Eloranta, Susanne Glienke, et al. Ultraclean layers and optically thin clouds in the stratocumulus-to-cumulus transition. part I: Observations. *Journal of the Atmospheric Sciences*, 75(5):1631–1652, 2018a. doi: 10.1175/JAS-D-17-0213.1.

- Robert Wood, Hsiu-Hui Tseng, et al. Deeper, precipitating PBLs associated with optically thin veil clouds in the Sc-Cu transition. *GRL*, 45(10):5177–5184, 2018b. doi: 10.1029/2018GL077084.
- Michio Yanai, Steven Esbensen, and Jan-Hwa Chu. Determination of bulk properties of tropical cloud clusters from large-scale heat and moisture budgets. *Journal of Atmospheric Sciences*, 30(4):611–627, 1973.
- Bingfan Yin and Bruce A Albrecht. Spatial variability of atmospheric boundary layer structure over the eastern equatorial pacific. *Journal of climate*, 13(9):1574–1592, 2000.
- Lisan Yu, Robert A Weller, and Bomin Sun. Mean and variability of the WHOI daily latent and sensible heat fluxes at in situ flux measurement sites in the Atlantic Ocean. *Journal of climate*, 17(11):2096–2118, 2004.
- Mark D Zelinka, Timothy A Myers, Daniel T McCoy, Stephen Po-Chedley, Peter M Caldwell, Paulo Ceppi, Stephen A Klein, and Karl E Taylor. Causes of higher climate sensitivity in CMIP6 models. *Geophysical Research Letters*, 47(1):e2019GL085782, 2020.
- Minghua Zhang, Christopher S Bretherton, Peter N Blossey, Phillip H Austin, Julio T Bacmeister, Sandrine Bony, Florent Brient, Suvarchal K Cheedela, Anning Cheng, Anthony D Del Genio, et al. Cgils: Results from the first phase of an international project to understand the physical mechanisms of low cloud feedbacks in single column models. *Journal of Advances in Modeling Earth Systems*, 5(4):826–842, 2013.
- Y Zhang, Z Gao, D Li, Y Li, N Zhang, X Zhao, and J Chen. On the computation of planetary boundary-layer height using the bulk Richardson number method. *Geoscientific Model Development*, 7(6):2599–2611, 2014.
- Youtong Zheng. Theoretical understanding of the linear relationship between convective updrafts and cloud-base height for shallow cumulus clouds. part I: Maritime conditions. *Journal of the Atmospheric Sciences*, 76(8):2539–2558, 2019.
- Chen Zhou, Mark D Zelinka, Andrew E Dessler, and Stephen A Klein. The relationship between interannual and long-term cloud feedbacks. *Geophysical Research Letters*, 42(23):10–463, 2015.
- Chen Zhou, Mark D Zelinka, and Stephen A Klein. Impact of decadal cloud variations on the Earth’s energy budget. *Nature Geoscience*, 9(12):871–874, 2016.
- Sergej Zilitinkevich and Alexander Baklanov. Calculation of the height of the stable boundary layer in practical applications. *Boundary-Layer Meteorology*, 105(3):389–409, 2002.

List of publications

1. **Albright, A.L.**, Proistosescu, C. and Huybers, P., 2021. [Origins of a Relatively Tight Lower Bound on Anthropogenic Aerosol Radiative Forcing from Bayesian Analysis of Historical Observations](#). *Journal of Climate*, 34(21), 8777-8792.
2. **Albright, A.L.**, Fildier, B., Touzé-Peiffer, L., Pincus, R., Vial, J. and Muller, C., 2021. [Atmospheric radiative profiles during EUREC4A](#). *Earth System Science Data*, 13(2), 617-630.
3. **Albright, A.L.**, Bony, S., Stevens, B., and Vogel, R., 2022. [Observed subcloud layer moisture and heat budgets in the trades](#). *Journal of the Atmospheric Sciences*.
4. **Albright, A.L.**, Stevens, B., Bony, S., and Vogel, R., 2022. [A new conceptual picture of the trade-wind transition layer](#). In review in *Journal of the Atmospheric Sciences*.
5. **Albright, A.L.** and Huybers, P., 2022. Paintings by Turner and Monet depict trends in 19th century air pollution. In preparation.
6. Boucher, O., Servonnat, J., **Albright, A.L.**, Aumont, O., Balkanski, Y., Bastrikov, V., Bekki, S., Bonnet, R., Bony, S., Bopp, L. and Braconnot, P. et al, 2020. [Presentation and evaluation of the IPSL-CM6A-LR climate model](#). *Journal of Advances in Modeling Earth Systems*, 12(7), p.e2019MS002010.
7. Stevens, B., Bony, S., and the EUREC4A team (including **Albright, A.L.**), 2021. [EUREC4A](#). *Earth System Science Data*, 13(8), 4067-4119.
8. Lutsko, N.J., Popp, M., Nazarian, R.H. and **Albright, A.L.**, 2021. [Emergent constraints on regional cloud feedbacks](#). *Geophysical Research Letters*, p.e2021GL092934.
9. Bony, S. and the ATR team (including **Albright, A.L.**), 2022. [EUREC4A observations from the SAFIRE ATR-42 aircraft](#). *Earth System Science Data*, 14(4), 2021-2064.
10. Vogel, **Albright, A.L.**, Vial, J., George, G., Stevens, S., and Bony, S. Strong cloud-circulation coupling explains weak trade cumulus feedback. Accepted (Sept. 2022) in *Nature*.
11. Vial, J., **Albright, A.L.**, Vogel, R., Musat, I. and Bony, S. The daily cycle of trade-wind cumuli: a process-based constraint for cloud feedbacks. In review at *PNAS*.
12. Quaas, J., Jia, H., Smith, C., **Albright, A.L.**, Aas, W., Bellouin, N., Boucher, O., Doutriaux-Boucher, M., Forster, P.M., et al., 2022. [Robust evidence for reversal in the aerosol effective climate forcing trend](#). *Atmospheric Chemistry and Physics Discussions*, 1-25.